Oil & Natural Gas Technology

Final Scientific Report: CONTROLS ON METHANE EXPULSION DURING MELTING OF NATURAL GAS HYDRATE SYSTEMS: TOPIC AREA 2

Type: Final Scientific Report

Reporting Period Start Date: October 1, 2012
Reporting Period End Date: January 14, 2016

Principal Author: Peter B. Flemings
Date Report issued: February 2016
DOE Award No.: DE-FE0010406

Peter B. Flemings
The University of Texas at Austin
101 East 27th Street, Suite 4.300
Austin, TX 78712-1500
e-mail: pflemings@jsg.utexas.edu
Phone number: 512-475-9520

Office of Fossil Energy

CONTROLS ON METHANE EXPULSION DURING MELTING OF NATURAL GAS HYDRATE SYSTEMS: TOPIC AREA 2
FINAL SCIENTIFIC REPORT

Contents

1. Executive Summary

1.1. Project Goal

The project goal is to predict, given characteristic climate-induced temperature change scenarios, the conditions under which gas will be expelled from existing accumulations of gas hydrate into the shallow ocean or directly to the atmosphere. When those conditions are met, the fraction of the gas accumulation that escapes and the rate of escape shall be quantified. The predictions shall be applicable in Arctic regions and in gas hydrate systems at the up dip limit of the stability zone on continental margins. The behavior shall be explored in response to two warming scenarios: longer term change due to sea level rise (e.g. 20 thousand years) and shorter term due to atmospheric warming by anthropogenic forcing (decadal time scale).

1.2. Project Objectives

During the first budget period, the objectives are to review and categorize the stability state of existing well-studied hydrate reservoirs, develop conceptual and numerical models of the melting process, and to design and conduct laboratory experiments that dissociate methane hydrate in a model sediment column by systematically controlling the temperature profile along the column. The final objective of the first budget period shall be to validate the models against the experiments.

In the second budget period, the objectives are to develop a model of gas flow into sediment in which hydrate is thermodynamically stable, and conduct laboratory experiments of this process to validate the model. The developed models shall be used to quantify the rate and volume of gas that escapes from dissociating hydrate accumulations. In addition, specific scaled simulations characteristic of Arctic regions and regions near the stability limit at continental margins shall be performed.

1.3. Project Background and Rationale

The central hypothesis proposed is that hydrate melting (dissociation) due to climate change generates free gas that can, under certain conditions, propagate through the gas hydrate stability zone and vent at the seafloor. Gas venting through the regional hydrate stability zone is accomplished by alteration of the regional equilibrium conditions (creation of three phase conditions) by increased salinity and heat due to hydrate formation, due to gas fracturing, or a combination of both. This research will explore the controls on whether methane reaches the seafloor (or atmosphere) as the original hydrate deposit dissociates and what the magnitude of these fluxes are. This hypothesis has significant implications for the forcings and feedbacks associated with climate change. It is described below the observations and models that have led to formulating this hypothesis.

2. Summary of Research

2.1. Task 1: Project Management and Planning

A. Goal:

The Recipient shall execute the project in accordance with the approved Project Management Plan covering the entire project period. The Recipient shall manage and control project activities in accordance with their established processes and procedures to ensure subtasks and tasks are completed within schedule and budget constraints defined by the Project Management Plan. This includes tracking and reporting progress and project risks to DOE and other stakeholders.

B. Activities Phase 1:

1. An initial web-based kick off meeting was held on 11/07/2012.
2. Twice-monthly telephone conferences with all of our participants have been organized and held.
3. We recruited one post-doctoral scientist for the project (Dr. Kehua You) who arrived from Texas A&M on June 15, 2013.
4. We recruited 4 graduate students for the project.
5. Dylan Meyer (geoscience, started F 2012), Kris Darnell (geoscience, Fall 2012), Jason Sanford (geoscience, Spring 2014), Imran Khan (petroleum engineering, Spring 2014).
6. We organized travel and supported experiment at LBNL
    a. Peter Polito, LBNL visit, Jan 2 – 4, 2013
    b. Peter Polito, LBNL visit, July 7 - 12, 2013
    c. Kehua You, LBNL visit, Sept 22 – 27, 2013
    d. Steve Bryant, 2013 NCGC Symposium, Oct 29 – 30, 2013
    e. Peter Polito & Dylan Meyer, LBNL visit, Dec 16 – 20, 2013
7. Completed Reports (as of the end of budget period one):
    a. 5 Quarterly Research Performance Progress Reports
    b. 17 Cost Accrual Reports
    c. 5 SF-425 Federal Financial Reports
8. We purchased equipment for construction of a thermistor string. The thermistor string consists of ten 10 kΩ resistors epoxied ten centimeters apart inside a 0.25” OD stainless steel tube. External circuitry converts the temperature-controlled resistance drop in each loop to a DC voltage, which is recorded and converted to temperature by a LabVIEW program.

C. Activities Phase 2:

1. Coordinated the overall scientific progress, administration and finances of the project
2. Communicated with project team and sponsors
    a. Organized regular team meetings
    b. Actively monitored project risks and as needed reported to project team and stakeholders.

c. Managed SharePoint site to facilitate online communication and collaboration
d. Managed email list serves for key project teams
e. Completed Reports:
    i. Quarterly Research Performance Progress Reports
    ii. Monthly Cost Accrual Reports
    iii. Monthly SF-425 Federal Financial Reports

2.2. Task 2: Conceptual and Numerical Model Development -1D (Complete)

Milestone 1.A 1-D simulation of gas hydrate dissociation in natural systems.

Milestone 1.B 1-D Simulation of gas hydrate dissociation in laboratory

Milestone 1.C Model-based determination of conditions required for gas not to reach seafloor/atmosphere from dissociating hydrate accumulation.

A. Goal:

The Recipient shall modify and integrate existing dynamic models of hydrate formation based on phase stability and transport of mass and energy (Behseresht and Bryant, 2011a; Behseresht and Bryant, 2011b; Behseresht et al., 2008a; Behseresht et al., 2008b; Liu and Flemings, 2006, 2007) to be applicable to hydrate melting. The Recipient shall modify their existing 1D code to be able to input initial conditions that reflect realistic hydrate concentrations, pore water salinities, etc. The Recipient shall modify the code by applying boundary conditions to allow for the ability to supply changes in surface temperature and pressure through time. The Recipient shall apply the modified codes to laboratory scale experiments and to natural hydrate systems such as suboceanic and Arctic subpermafrost systems.

Subtask 2.1 - Dissociation of 1D vertical hydrate accumulation

The Recipient shall focus on the dynamics within an accumulation of hydrate subjected to a perturbation in temperature. The Recipient shall integrate their existing three components (methane, water, salinity) three phase (gaseous, aqueous, hydrate) stability model with an existing multiphase (gaseous, aqueous) transport model. The Recipient shall extend the integrated model to account for pressure buildup during hydrate disassociation. The phase transport model shall be used to account for the dissipation of pressure by viscous flow, by buoyancy and by saturation gradients (capillarity). The model shall allow for general boundary conditions (prescribed pressure and saturations or prescribed fluxes), so in this first stage of the model development, any fluid that leaves the hydrate-bearing sediment will not be modeled after it leaves. (The fate of gas phase which leaves the hydrate-bearing sediment is critical to the overall research objective and will be the focus of Task 5). The Recipient shall couple the extended phase stability/transport model to salinity transport by advection and by diffusion. This in turn shall be coupled to enthalpy transport by advection and conduction, allowing for general boundary conditions

(prescribed temperature or prescribed heat flux). The Recipient shall ensure the numerical stability of the extended model across a wide range of relative rates of hydrate dissociation and pressure dissipation.

Subtask 2.2 - Apply 1D model to laboratory experiment

As the capabilities of the model developed in Task 2.1 are added, the Recipient shall use the model to predict the behavior of the laboratory experiments of controlled hydrate dissociation which will be conducted simultaneously in Task 4. The Recipient shall use the results of the experiments in Task 4 to validate the model and to gain insight into the coupled transport processes during hydrate dissociation.

Building on the preliminary work reported in Bryant and Juanes (2012), the Recipient shall augment the model as needed to account for conditions peculiar to the experiment; for example, the Recipient shall simulate a closed system with an external reservoir so that total masses of brine and of methane are constant and overall system pressure can change with time. Input to the model shall be the permeability, porosity and capillary characteristic curves for the sand(s) used to pack the column, and the initial distribution of phases (brine, hydrate, gas) within the column. The Recipient shall use the model to predict saturation distribution with space and time and the rates and volumes of fluid phases leaving the column. The Recipient shall compare the predictions to measurements to examine the validity of the conceptual and physical basis of the model. The Recipient shall determine the underlying processes that result in differences between the simulator and experiments, and revise the model as needed during this validation exercise.

Subtask 2.3 - 1D models of natural examples

The Recipient shall use the model to predict the behavior of natural gas hydrate systems subjected to a temperature perturbation to determine under what conditions gas is predicted to escape from the hydrate-bearing sediment. For these conditions the model shall provide a worst-case estimate of gas flux to seafloor or atmosphere, since gas that leaves the hydrate-bearing sediment is in effect assumed to migrate unhindered through any overlying sediment.

Subtask 2.3.1 Hydrate accumulations below permafrost

The Recipient shall apply the model to subpermafrost accumulations of hydrate for depths ranging from those present at Mallik (hydrate interval starting at 900 mbsf) to those characteristic of Mt. Elbert (e.g. 900 mbsf) and for two warming scenarios (rapid vs. slow increase in the temperature at top of accumulation). The Recipient shall use the well-characterized Mt. Elbert and Mallik accumulations as examples of deep hydrates. The Recipient shall closely examine the conditions under which the model predicts that gas can migrate upward through the various capillary barriers present in these particular accumulations. The Recipient shall determine the conditions under which the theoretical limiting case of

zero upward migration applies; in this situation the dissociation would simply restore the original, pre-global-cooling accumulation of gas. The Recipient shall use the model to examine the sensitivity of whether gas escapes to variations in grain size distribution (and hence to variation in capillary curves, permeability and relative permeability to gas and brine phases especially in the presence of hydrate) with depth in the hydrate bearing sediment. The Recipient shall also study the sensitivity with respect to depth of the accumulation, as the competition between gas pressure induced fracturing and gas-pressure induced drainage shifts with the in-situ stress.

The Recipient shall conduct this analysis for two limiting-case initial conditions. In one, the hydrate-bearing sediment shall be assumed to be in three phase equilibrium (gas, brine, hydrate) throughout the accumulation. In the other, the hydrate above the base of the gas hydrate stability zone shall be assumed to be within the L+H (brine, hydrate) with the extent of the distance from the three-phase equilibrium point increasing with elevation above the base of gas hydrate stability. This part of the Task shall address one of the key hypotheses of this research, namely whether the predicted upward migration of gas depends upon the manner in which the hydrate accumulation formed.

Subtask 2.3.2 - 1D model application to deposits near up-dip limit of stability zone on continental margins

The Recipient shall repeat the activities of Subtask 2.3.1 for prototypical accumulations of hydrate along continental margins for a depths ranging from 10 to 100 meters below seafloor. . The Recipient shall determine the conditions (if any) under which zero gas migration is predicted. The Recipient shall closely examine the sensitivity to competition between fracturing and drainage. For scenarios in which upward migration of gas is predicted, the Recipient shall tabulate the predicted fluxes as worst-case values for comparison with models of gas expulsion to be developed in Phase 2 of the project.

B. Activities Phase 1:

Task 2 is was completed in Phase 1. Significant accomplishments include that we completed development of two models: 1) An analytical ‘box’ model to describe hydrate formation in a specific volume; and 2) a one dimensional, fully coupled, transient numerical transport model that describes hydrate formation and multi –phase (gas and water) flow. The ‘box’ model is used to design our experimental approach and to then understand the experimental results. The numerical model is used to simulate hydrate formation and dissociation both at the experimental and geological scales. A major computing challenge that was overcome was to stabilize and make more efficient the numerical model that we completed. We applied the ‘numerical’ and ‘box’ model to simulate the behavior we pursued in our laboratory experiments. The match between theory and observation was remarkable. We applied the coupled model to predict the effect of seafloor warming on marine hydrate deposits (2.3.2). A

significant finding was that given a sufficient initial hydrate deposit, the methane that was disassociated would self-propagate through the hydrate stability zone and vent to the ocean.

Analytical 'box' model

Here we derive an analytical solution to calculate the maximum hydrate saturation and methane gas consumption during hydrate formation in sediments partially saturated with water and flooded with methane gas. We present examples where the pore fluid is assumed to both saline and fresh. This model is based on thermodynamic equilibrium among liquid phase, vapor phase and hydrate phase. Three components, water, salt and methane, are considered in the model. The calculations are based on mass conservations of water, salt and methane in the 'box'.

Case 1: Saline solution

Figure 1 shows the schematic diagram for this model. Initially, the sediment is filled with $S_{g,i}$ methane gas (dimensionless, gas saturation) and $S_{w,i}$ water (dimensionless, water saturation) with a salinity of $X^s_{w,i}$ (wt.%). The initial pressure and temperature in the system is P_i (Pa) and T_i (°C), respectively. Methane hydrate starts to form when the system pressure and temperature decrease to the hydrate stable zone P_f (Pa) and T_f (°C), respectively. During hydrate formation, methane gas is allowed to freely flow into the sediment while no water reservoir is connected to the sediment.

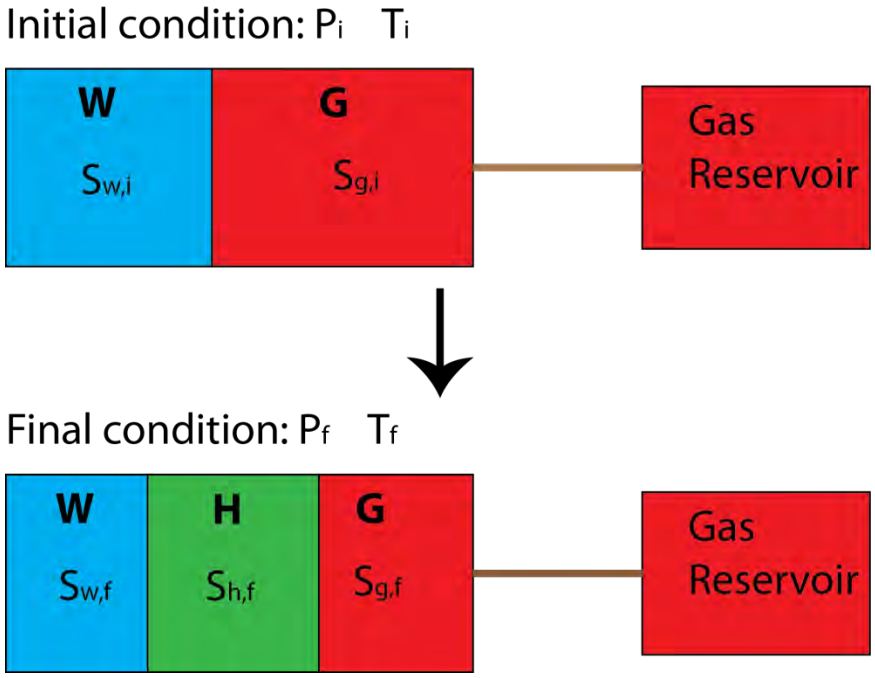

Figure 1: Schematic diagram of the 'box' model. G is gas or vapor phase. W is water or liquid phase. H is hydrate phase. P_i and T_i are the initial pressure and temperature, respectively. P_f and T_f are the final equilibrium pressure and temperature, respectively. $S_{g,i}$ and $S_{w,i}$ are the initial gas and water saturations, respectively. $S_{g,f}$, $S_{w,f}$ and $S_{h,f}$ are the final equilibrium gas, water and hydrate saturations, respectively.

Since salt is transported by water flow and there is no water flow that enters or leaves the system during the experiment, the total amount of salt initially in the sediment should equal that after hydrate formation. Therefore, one has

$$V_{tot}\phi S_{w,i}\rho_{w,i}X^{s}_{w,i} = V_{tot}\phi S_{w,f}\rho_{w,f}X^{s}_{w,e}\,, \qquad \text{Eq 1}$$

where V_{tot} is the total volume of the sediment (m^3); ϕ is porosity (dimensionless); $X^{s}_{w,e}$ is the mass fraction of salt in brine at three phase equilibrium condition (wt.%) , which can be calculated from the phase boundary curves of brine, gas and methane hydrate using P_f and T_f (Liu and Flemings, 2007); $\rho_{w,i}$ and $\rho_{w,f}$ are the initial and final brine density in the sediment, which can be calculated using the initial and final pressure, temperature and salinity values, respectively (Liu and Flemings, 2007). We reorganize Eq. (1) and obtain the final water saturation as

$$S_{w,f} = \frac{S_{w,i}\rho_{w,i}X^{s}_{w,i}}{\rho_{w,f}X^{s}_{w,e}}\,. \qquad \text{Eq 2}$$

The maximum hydrate saturation is calculated from the mass conservation of fresh water in the sample. The initial mass of the fresh water in the brine should equal the final mass of the fresh water in the brine plus that in the hydrate, therefore, one has

$$V_{\text{tot}}\phi S_{w,i}\rho_{w,i}\left(1-X^{s}_{w,i}\right)\left(1-X^{m}_{w,i}\right) = V_{\text{tot}}\phi S_{w,f}\rho_{w,f}\left(1-X^{s}_{w,f}\right)\left(1-X^{m}_{w,e}\right) + \frac{V_{tot}\phi S_{h,f}}{M_h/\rho_h}NM_w\,, \qquad \text{Eq 3}$$

where $X^{m}_{w,i}$ and $X^{m}_{w,f}$ are the initial and final solubility of methane in the water (wt.%) As in Liu and Flemings (2007), the solubility of methane in water in presence of hydrate is calculated using the model of *Henry et al.* (1999) , while the solubility of methane in water in absence of hydrate is calculated using the model of *Duan et al.* (1992). M_w and M_h are the molar weight of water (kg mol^{-1}) and methane hydrate (kg mol^{-1}), respectively; ρ_h is the methane hydrate density, and we used the value of 912 kg m^{-3} in this study; N is the stoichiometric hydration number, which is assumed to be constant and equal to 5.75 in this study. We restate Eq. (3) and obtain the maximum hydrate saturation of

$$S_{h,f} = \frac{\left[S_{w,i}\rho_{w,i}\left(1-X^{s}_{w,i}\right)\left(1-X^{m}_{w,i}\right) - S_{w,f}\rho_{w,f}\left(1-X^{s}_{w,f}\right)\left(1-X^{m}_{w,e}\right)\right]M_h}{NM_w\rho_h}\,. \qquad \text{Eq 4}$$

The final gas saturation can be written as

$$S_{g,f} = 1 - S_{w,f} - S_{h,f}\,. \qquad \text{Eq 5}$$

Mass conservation of methane is used to calculate the methane gas consumption in the sample. Initially, the methane is distributed in water and gas phase. At three phase equilibrium condition, the methane is distributed in water, gas and hydrate phases, therefore, one has

$$\Delta m = m^m_{w,f} + m^m_{g,f} + m^m_{h,f} - m^m_{w,i} - m^m_{g,i}\,, \quad \text{Eq 6}$$

where Δm is the mass of methane gas consumed during hydrate formation (kg); $m^m_{w,f}$, $m^m_{g,f}$, $m^m_{h,f}$ are the mass of methane (kg) in the final water, gas and hydrate phases, respectively; $m^m_{w,i}$ and $m^m_{g,i}$ are the mass of methane (kg) in the initial water and gas phases, respectively. They are calculated as

$$m^m_{w,f} = V_{tot}\phi S_{w,f}\rho_{w,f}X^m_{w,f}\,, \quad \text{Eq 7}$$

$$m^m_{g,f} = V_{tot}\phi S_{g,f}\rho_{g,f}\,, \quad \text{Eq 8}$$

$$m^m_{h,f} = \frac{V_{tot}\phi S_{h,f}\rho_h}{M_h}M_m\,, \quad \text{Eq 9}$$

$$m^m_{w,i} = V_{tot}\phi S_{w,i}\rho_{w,i}X^m_{w,i}\,, \quad \text{Eq 10}$$

$$m^m_{g,i} = V_{tot}\phi S_{g,i}\rho_{g,i}\,, \quad \text{Eq 11}$$

where M_m is the molar weight of methane (kg mol^{-1}); $\rho_{g,i}$ and $\rho_{g,f}$ are the initial and final gas density (kg m^{-3}), respectively, which can be calculated from the initial and final temperature and pressure, respectively (Liu and Flemings, 2007). Substitute Eqs. (7)-(11) into Eq. (6), one can obtain the methane gas consumption during methane hydrate formation at the final pressure and temperature of P_f and T_f, respectively.

Case 2: Fresh water

In this case, methane hydrate is formed in a sediment column initially partially saturated with fresh water and flooded with the methane gas. Under the same three phase equilibrium pressure and temperature condition for saline water P_f and T_f as discussed above, the fresh water system reaches liquid and hydrate stable zone. However, since the sediment is connected with a methane gas reservoir, and water is limited, theoretically all the water initially in the sediment should be converted to hydrate. Therefore, one has

$$S_{w,f} = 0\,. \quad \text{Eq 12}$$

By conservation of water mass, we find

$$V_{tot}\phi S_{w,i}\rho_{w,i}\left(1 - X^m_{w,i}\right) = \frac{V_{tot}\phi S_{h,f}}{M_h/\rho_h}NM_w\,. \quad \text{Eq 13}$$

We reorganize Eq. (13) and obtain the maximum hydrate saturation for the case of fresh water

$$S_{h,f} = \frac{S_{w,i}\rho_{w,i}\left(1 - X^m_{w,i}\right)M_h}{NM_w\rho_h}. \qquad \text{Eq 14}$$

The final gas saturation is calculated by Eq. (5). According to the mass conservation of methane, one can calculate the methane gas consumption for the fresh water case as follows

$$\Delta m = m^m_{g,f} + m^m_{h,f} - m^m_{w,i} - m^m_{g,i}. \qquad \text{Eq 15}$$

$m^m_{g,f}$, $m^m_{h,f}$, $m^m_{w,i}$ and $m^m_{g,i}$ can be calculated by Eqs. (8)-(11), respectively.

Matlab programs SH_BRINE and SH_FRESH have been developed to assist the above calculations for the saline water and fresh water cases, respectively.

Numerical model

This numerical model considers the fully coupled multiphase, multicomponent fluid flow, solute transport and heat flow. It was originally developed by *Liu* (2006) and has been described in *Liu and Flemings* (2007) . The downward direction is set as positive direction. This model is based on local thermodynamic equilibrium among the liquid, vapor, and hydrate phases. Three components, water, salt and methane, are considered in the model. Fluid flow in the system includes viscous flow (pressure driven), capillary flow (saturation-gradient driven) and gravity flow (buoyancy driven). Heat is transported by conduction and advection.

The following assumptions are used in the model: (1) Darcy's law describes multiphase fluid flow in the uniform porous media. (2) There is no sedimentation and erosion. (3) There is no in situ biogenic methane. (4) Methane is the only hydrate-forming gas. (5) Salt is confined to the liquid phase. (6) Methane is assumed to be the only component in the gas phase. (7) Hydrate is a solid phase and only two-phase (vapor+liquid) capillary pressure is considered. (8) The temperature among each phase is locally in equilibrium.

Appling mass conservation to each component, one can get the mass balance equation for methane as

$$\phi\frac{\partial\left(\sum_{\beta=l,v,h}\rho_\beta S_\beta X^m_\beta\right)}{\partial t} - \sum_{\beta=l,v}\nabla\left\{\frac{kk_{r\beta}}{\mu_\beta}\left(\nabla P_\beta - \rho_\beta g\right)\rho_\beta X^m_\beta\right\} - \nabla\left\{\phi^2 D^m_{l0}\rho_l\nabla X^m_l\right\} - q^m = 0. \qquad \text{Eq 16}$$

The mass balance equation for water is

$$\phi\frac{\partial\left(\sum_{\beta=l,h}\rho_\beta S_\beta X^w_\beta\right)}{\partial t} - \sum_{\beta=l}\nabla\left\{\frac{kk_{r\beta}}{\mu_\beta}\left(\nabla P_\beta - \rho_\beta g\right)\rho_\beta X^w_\beta\right\} - \nabla\left\{\phi^2 D^w_{l0}\rho_l\nabla X^w_l\right\} - q^w = 0. \qquad \text{Eq 17}$$

The mass balance equation for salt is

$$\phi\frac{\partial\left(\sum_{\beta=l}\rho_\beta S_\beta X_\beta^s\right)}{\partial t}-\sum_{\beta=l}\nabla\left\{\frac{kk_{r\beta}}{\mu_\beta}\left(\nabla P_\beta-\rho_\beta g\right)\rho_\beta X_\beta^s\right\}-\nabla\left\{\phi^2 D_{l0}^s\rho_l\nabla X_l^s\right\}-q^s=0. \qquad \text{Eq 18}$$

In the above three equations, the superscripts m, w and s denote methane, water and salt, respectively. The subscripts *l*, *v* and *h* denote liquid, vapor and hydrate phases, respectively.

ϕ is porosity (dimensionless). *t* is time (sec). *k* is sediment permeability (m^2). ρ_β, S_β, μ_β, P_β and $k_{r\beta}$ are the density (kg m^{-3}), saturation (dimensionless), dynamic viscosity (Pa sec), pressure (Pa) and relative permeability of β phase, respectively. X_β^m, X_β^w and X_β^s are the mass fractions of methane, water and salt in β phase, respectively. *g* is acceleration due to gravity (m s^{-2}). D_{l0}^m, D_{l0}^w and D_{l0}^s are the molecular diffusion coefficient (m^2 s^{-1}) of methane, water and salt, respectively. q^m, q^w and q^s are the sources or sinks of methane, water and salt, respectively.

The energy balance equation (superscript *e*) is

$$\frac{\partial\left(\left(1-\phi\right)\rho_R C_R T+\sum_{\beta=l,v,h}\phi\rho_\beta S_\beta u_\beta\right)}{\partial t}-\sum_{\beta=l,v}\nabla\left\{\frac{kk_{r\beta}}{\mu_\beta}\left(\nabla P_\beta-\rho_\beta g\right)\rho_\beta h_\beta\right\}-\nabla\left\{\lambda\nabla T\right\}-q^e=0, \qquad \text{Eq 19}$$

where the subscript *R* denotes the solid grain. *T* is temperature (°C). λ is the bulk thermal conductivity of the porous media (W m^{-1} °C^{-1}), and $\lambda=\left(1-\phi\right)\lambda_R+\phi\sum_{\beta=l,v,h}S_\beta\lambda_\beta$. λ_β, u_β and h_β are the thermal conductivity (W m^{-1} °C^{-1}), specific internal energy (J kg^{-1}) and specific enthalpy (J kg^{-1}) of phase β, respectively.

Duan et al.'s (1992) model is used to calculate the methane solubility in water in absence of methane hydrate. Henry et al.'s (1999) model is used to calculate the methane solubility is water in presence of methane hydrate. The Leverett J-function is used to describe the relationship between capillary pressure and pore fluid saturation (Bear, 1972). Corey's model is used to calculate the relative water and gas permeability (Bear, 1972).

Porosity is defined as the pore volume fraction filled with fluid phases (liquid and vapor). As hydrate forms, porosity is reduced as $\phi=\phi_0(1-S_h)$, where ϕ_0 is the porosity (dimensionless) in absence of hydrate. The decrease of porosity leads to the decrease of intrinsic permeability, which is described by the model of *Kleinberg et al.* (2003), where hydrate is assumed to form in the center of the pores. The decrease in porosity and permeability can change the capillary pressure, which is calculated as $P_c=\sqrt{k_0\phi/\phi_0 k}P_{c0}$, where k_0 and P_{c0} are the intrinsic permeability (m^2) and capillary pressure (Pa) in absence of hydrate, respectively.

The numerical model is solved by fully implicit block-centered finite-difference method. Upstream weighting is used to calculate the phase mobility, and harmonic weighting is used to calculate the intrinsic permeability. Newton_Raphson method is used to iteratively solve the nonlinear equations. Primary variables switching method is used in case of the appearance or disappearance of phases.

The Matlab program originally developed by *Liu* (2006) for this numerical model can only simulate the case when the sediment is initially 100% saturated with water. We modified the input files and the files calculating the Jacobian and residual matrixes for solving the nonlinear equations to extend the program to more general cases of any arbitrary initial water, gas or hydrate saturations. Besides, we added a dynamic time-step choice to improve the numerical stability. With the dynamic time-step choice, the simulation starts with a big time-step value. This value will be cut down to a smaller one whenever the calculation cannot be converged or when it is converged to unreasonable situations, for example, when the saturations are less than zero or greater than 100%. At the new time, the time-step will get back to the original big value to guarantee the efficiency of the simulation. We also added the choice of manually controlling the sediment temperature and fixed gas pressure boundary condition to simulate the laboratory experiment.

Laboratory Experiment

This section is to simulate the laboratory experiment described in section 4.1 using the analytical 'box' model and the fully coupled numerical model described above. Initially, the 12.7 cm long F110 sand sample is saturated with 49 vol.% methane gas and 51 vol.% brine having a salinity of 3.5 wt.%. The F110 sand sample has a porosity of 35%, an intrinsic permeability of 8.3×10^{-13} m^2 and capillary entry pressure of about 0.02 MPa. The initial temperature for the sample is 17 ^{o}C, and the initial gas pressure is 6.94 MPa. We fix the gas pressure at the upstream end of the sample to be 6.94 MPa by connecting it to a constant pressure pump, which allows methane gas to freely enter or leave the sample upon the pressure change in the sample. We set a closed boundary at the downstream end of the sample. For the convenience of space discretization in the numerical model, we set the sample length to be 12 cm. But the displayed results here have been corrected by this volume change from the real sample (12.7 cm in length).

Figure 2 shows the accumulated methane gas consumption during the hydrate formation and dissociation predicted by the analytical (blue line) and numerical models (yellow line). The numerically predicted gas consumption is slightly less than the analytically predicted value (yellow line is slightly below blue line). This is because the analytical model neglects the capillary pressure and treats the water pressure as equaling the gas pressure. The predicted Gas consumptions increase from nearly zero to greater than 1 g when temperature is decreased to 8 ^{o}C. Methane hydrate is predicted to form when the temperature is decreased to 8.4 ^{o}C at the pressure of 6.94 MPa and salinity of 3.5 wt.%. After that the predicted gas consumptions increase stepwise as temperature is decreased for hydrate formation, and then decrease stepwise as temperature is increased for hydrate dissociation. The black line with

rectangle markers is the laboratory measured methane gas consumption, which will be discussed in detail in Task 4.

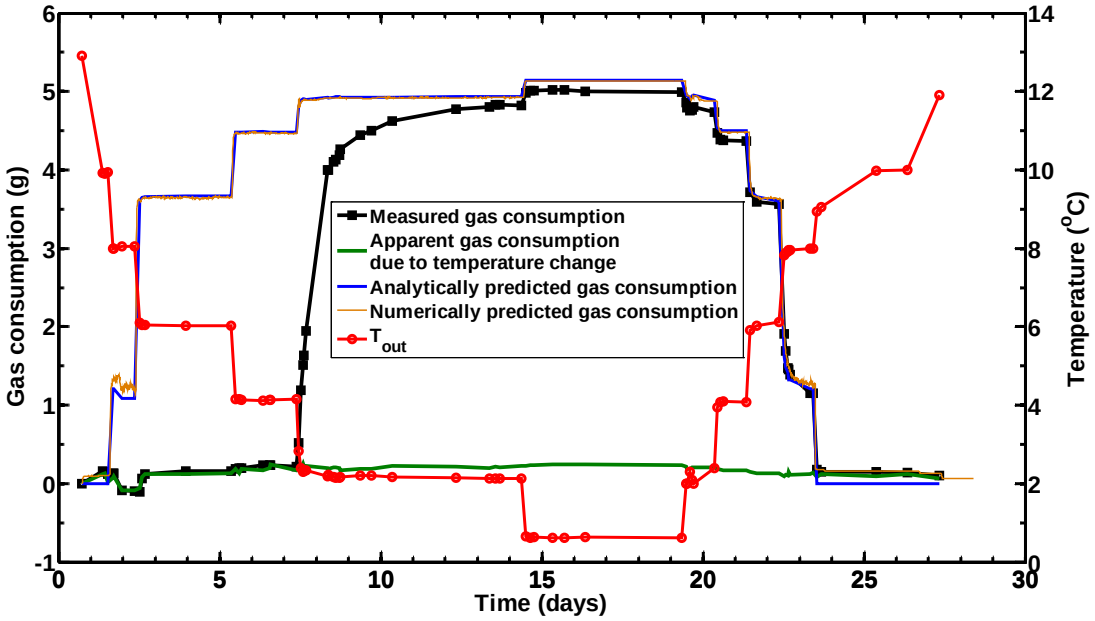

Figure 2: Comparison of measured and predicted methane gas consumption during hydrate formation and dissociation. T2 is the temperature measured on the out radius of the sample. The sample is initially filled with sediment of porosity 35%, and water saturation of 51%. Gas is allowed to flow into or out of the sample. Pressure is held constant by connecting the upstream end of the sample to a constant pressure pump.

Figure 3 shows the distribution of the water, gas and hydrate saturation in the sample calculated by the numerical model at Day 1, 11, 17, 22 and 23 when the sample temperature is 17 (room temperature), 2.2 and 0.6 °C during hydrate formation, and 4.1 and 6 °C during hydrate dissociation, respectively. The sample is initially homogeneously saturated with 49 vol.% methane gas and 51 vol.% water. Therefore, the simulated saturations are quite homogeneous across the sample. Hydrate saturation increases as temperature decreases.

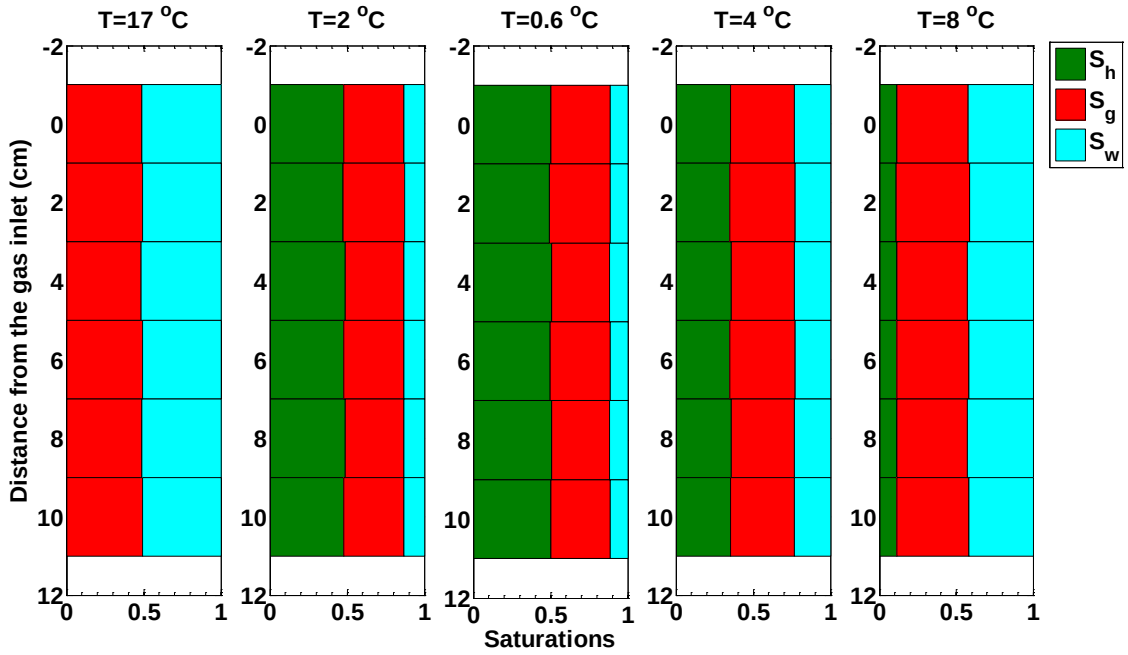

Figure 3: Distribution of saturations at Day 1, 11, 17, 22 and 23 when the sample temperature is 17 (room temperature), 2, 0.6, 4 and 8 °C, respectively.

Figure 4 shows the predicted water, gas and hydrate saturations and salinity using the analytical (lines) model. The predicted results by the numerical model are not shown here because they are undistinguishable from the predicted results by the numerical model. As temperature is decreased to below 8.4 °C, hydrate saturation increases while water and gas saturation decreases stepwise as temperature is decreased for hydrate formation. At the same time, salinity increases and stabilizes to a fixed value at each temperature. As temperature is increased from Day 19 for hydrate melting, hydrate saturation decreases while water and gas saturation increases stepwise. Salinity decreases stepwise as hydrate dissociates. Each point on the curves is three-phase equilibrium when hydrate saturation is greater than zero.

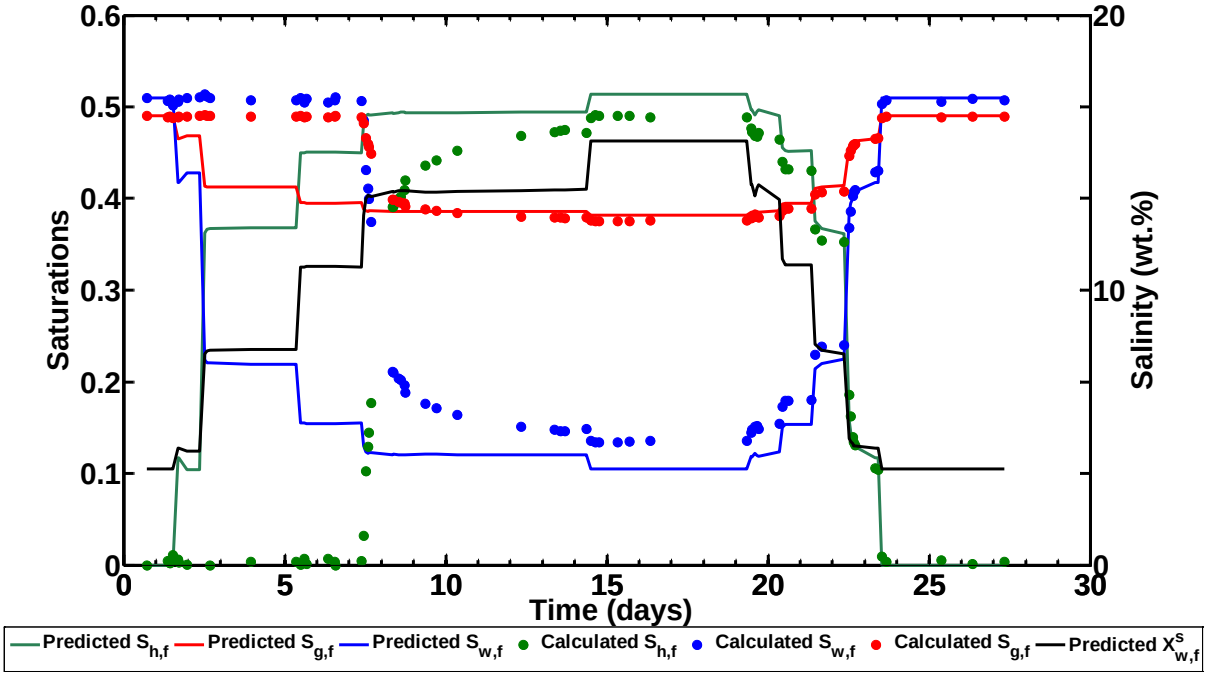

Figure 4: Comparison between the calculated water (blue), gas (red) and hydrate bulk saturations (green) using the measured methane gas consumption (dots) and the predicted saturations using the analytical solutions (lines).

1D model application

We use the dynamic, multiphase flow model of (Liu and Flemings, 2007) to investigate the sensitivity of natural hydrate systems to warming perturbations. Our simulations aim to test the hypothesis that hydrate systems close to three-phase equilibrium1) are most sensitive to warming, 2) are the sources of high methane release, and 3) may exhibit transient behaviors as the warming signal propagates into the sediment column. We test these hypotheses by considering one specific case study modeled after (Reagan and Moridis, 2008), who in their 'Case III' simulate a cold, shallow hydrate deposit typical of the arctic continental shelf. We model a one-dimensional, vertical geometry that initially only contains seawater and hydrate, and captures, both, the regional hydrate stability zone (RHSZ) and the sediment below the RHSZ. We force the system with small, instantaneous temperature perturbations (+ 0.22C) and analyze the evolution over long time scales (~10kyr).

Using this general framework, we show that hydrate is melted at the base of the RHSZ (BRHSZ) and that the dissociated gas migrates upward creating its own three-phase equilibrium pathway. The upward migrating gas reforms hydrate once it enters into the new hydrate stability zone. However, the gas can self-propagate through the overlying hydrate stability zone and breach the seafloor if the initial hydrate saturation is sufficiently large for a given level of warming.

The generic result from the hydrate dissociation simulation is as follows. Warming at the seafloor diffusively propagates downward eventually elevating the temperature at the hydrate deposit to the

local stability temperature. This causes dissociation at the base of the deposit. The temperature throughout the deposit remains fixed at the stability temperature during dissociation, but adjusts according to dissociation-induced changes in pressure and salinity at depth. Once enough hydrate dissociates, the gas buildup can freely flow upward and a zone with gas and hydrate exists. This vertical gas transport and basal hydrate dissociation continues until the gas reaches the new location for the BRHSZ. At the new BRHSZ, the gas re-solidifies as hydrate raising the temperature of the surrounding deposit through the release of latent heat. This latent heat release warms the overlying sediment above the stability temperature and raises the salinity during hydrate formation-driven salt expulsion. This allows concurrent hydrate formation and vertical gas flow. In this way, the free gas propagates upward in three-phase equilibrium despite being in the RHSZ. This self-propagation moves all the way to the seafloor. Eventually, hydrate formation shuts down due to methane depletion at the seafloor, and this shutdown propagates downward. The final deposit is shifted upward according to the new P-T conditions and contains less methane than the initial deposit due to venting at the seafloor.

These simulation results contrast previous work, which has suggested that free gas does not migrate through the hydrate stability zone, but instead migrates laterally along the dissociating BRHSZ. The transient venting events described above are a new phenomenon that has not previously been discussed or analyzed within models. The remainder of this section will address the conditions under which this behavior is applicable and the implications for natural systems worldwide.

Model Setup

We simulate a deposit below the seafloor with an overlying water column of 320 m, a seafloor temperature of 0.4 C, and a geothermal gradient of 0.03 C / m. Our simulation domain contains a grid above the seafloor where sh=0 and the pressure is hydrostatically fixed. This is an open boundary in which we monitor outward fluxes of gas and water. The bottom boundary is at 120 mbsf. We initiate the model with a hydrate deposit 60 m in depth with the top of the deposit at 40 m below the seafloor. The BRHSZ is 100 mbsf before the temperature perturbation. The deposit has a hydrate saturation of 10% by volume. We assess the implications that the new behavior has on natural systems, with special attention to the inherent dependence on hydrate saturation.

At time = 0 years, we introduce a warming at the seafloor that is instantaneous and held fixed throughout time. We analyze two cases, where Case 1 has a 0.1 C perturbation, and Case 2 has a 0.22 C perturbation. All else remains constant between the two cases. Furthermore, neither of these temperature perturbations is sufficient to eliminate the RHSZ. The expectation is that all gas remains within the system and should eventually all be contained in hydrate, albeit with a BRHSZ that has shoaled substantially.

In Case 1, we expect the BRHSZ to shoal 20 m. And in Case 2, we expect the BRHSZ shoal of 35 m.. Finally, in Case 3 the HSZ is completely eliminated with all available methane vented into the ocean. These three cases demonstrate different behaviors and illuminate a new scenario for venting.

Simulation Results

Case 1:

In Case 1, the hydrate at the base melts once the temperature perturbation has reached the BRHSZ. The bottom-most layer entirely dissociates, then the gas moves freely upward and reforms hydrate directly above, at the depth of the new RHSZ. During the dissociation of the hydrate, the warming signal ceases its propagation and the temperature at the dissociation depth is held fixed at the three-phase equilibrium temperature. The hydrate formation increases the salinity due to the expulsion of salt in the hydrate structure. However, these effects are insufficient to alter the state of the system further. Instead, all of the methane that is mobile is converted to hydrate at its lowest possible depth. Once all of the mobile methane is re-converted to hydrate, the salt diffuses away from the source of the formation and the heat slowly diffuses away as well. The final hydrate deposit sits at the expected location and total methane losses are minimal and restricted to pressure induced water flux into the ocean within the dissolved phase.

Case 2:

In Case 2, the hydrate at the base also melts once the temperature perturbation has propagated through the deposit. However, the upward migrating gas does not immediately reform hydrate. Instead, the overlying hydrate also undergoes dissociation and the free gas creates a pressure buildup. The pressure buildup forces gas migration. The gas at the new RHSZ does begin to reform some hydrate, but this additional heat and salinity is too much forcing for the overlying hydrate. These combined effects create a high salinity, high temperature pathway that 'burns' through the overly hydrate. Thus, a free gas pathway exists with venting into the ocean. This persists until the gas column loses its buoyancy driven mobility. Then, the top-most gas reforms hydrate capping additional free gas flow. The formation signal then propagates downward, depleting all of the available, mobile methane within the RHSZ. At the end of the simulation, there is a hydrate deposit situated where one would it expect it to be based on a static, thermodynamic analysis. However, the dynamic adjustment drives ~25% of the original methane quantity (by volume) into the ocean. We show results below for Case 2.

Case 3:

In Case 3, the system behaves very similarly to Case 2 until hydrate begins dissociating. Once dissociation begins, the entire deposit quickly undergoes dissociation with upward gas propagation. A vent develops within 1 kyr. Eventually all methane is vented into the ocean at a rate much greater than that observed in Case 2.

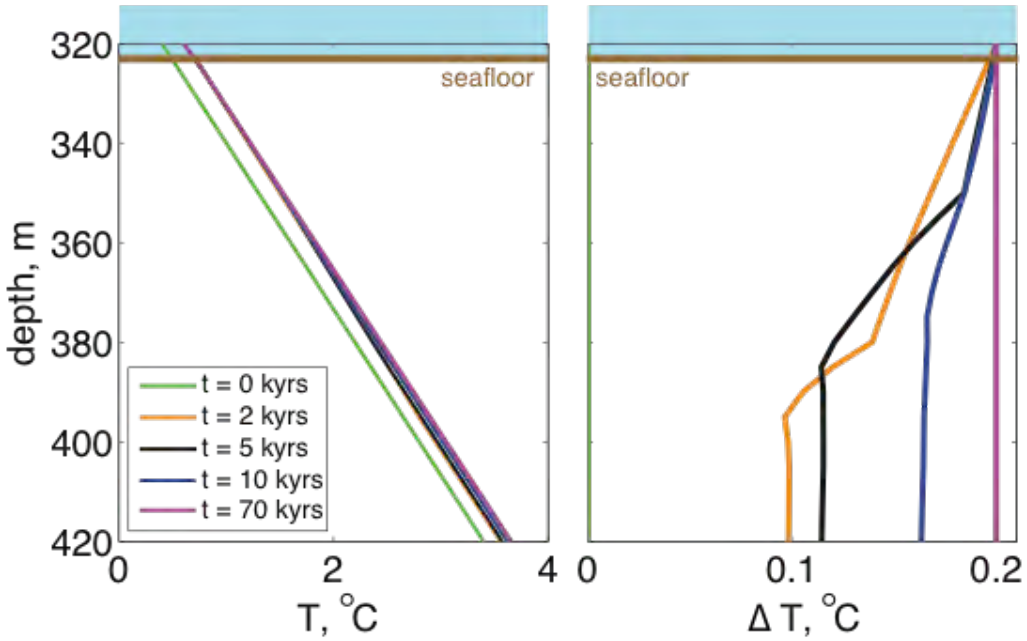

Figure 5: (Left) The temperature evolution from Case 2. The initial temperature profile does not include the temperature perturbation. This is applied directly after and held constant. (Right) The temperature difference from the initial.

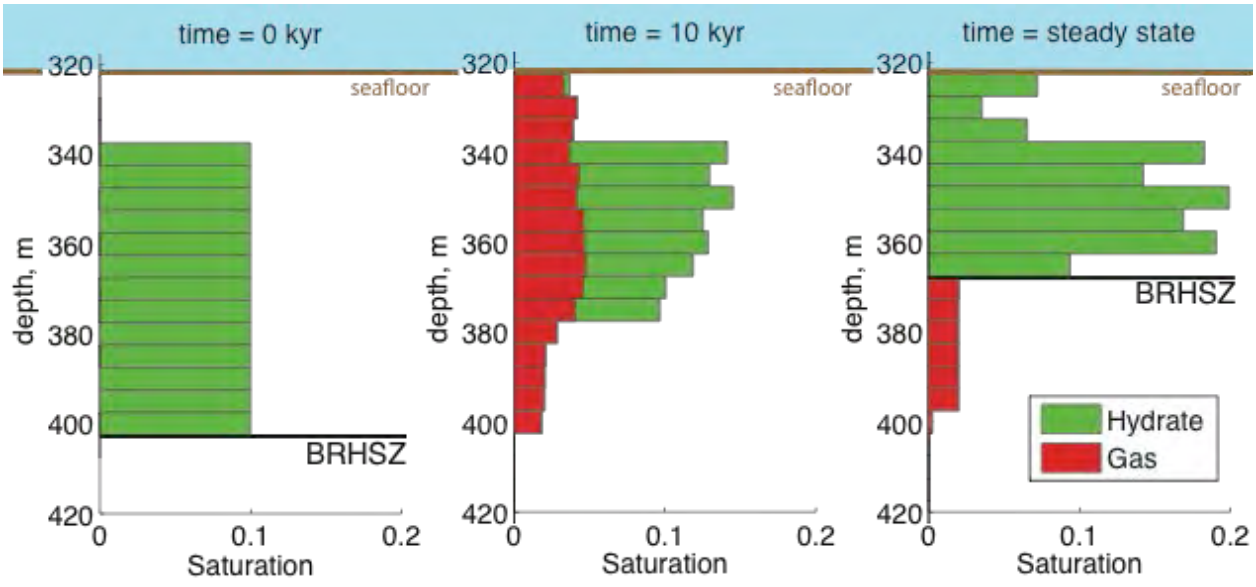

Figure 6: Saturation evolution from Case 2. The time progression goes from left to right. Green represents hydrate and red represents gas. The base of the regional hydrate stability zone is indicated with a horizontal line.

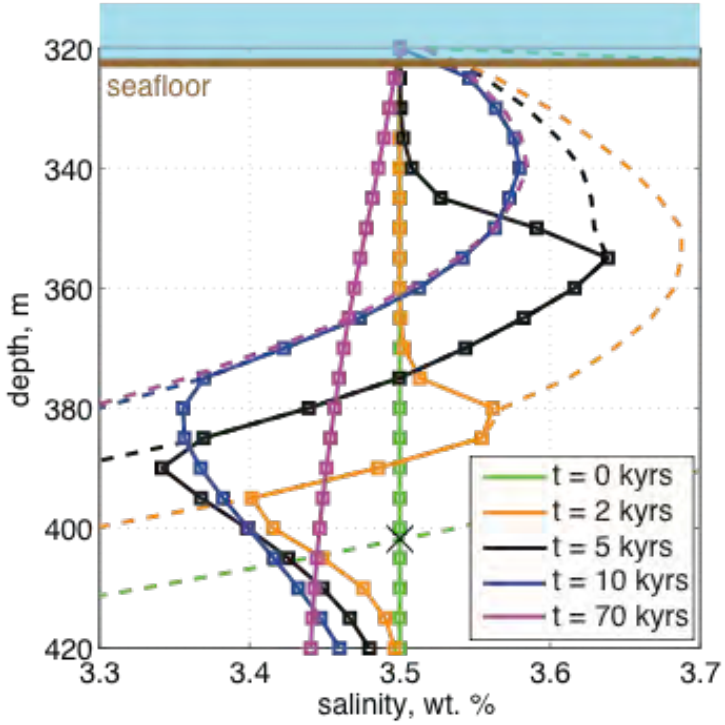

Figure 7: The salinity evolution in Case 2. The salinity at the time slice is plotted as a line with squares. The salinity required to achieve three-phase equilibrium is plotted as a dashed line. There is a source of fresh water where dissociation occurs, and there is a source of salt where secondary hydrate formation occurs.

Salinity effects:

The general hydrate deposit evolution can be seen in Figure 7, which shows the salinity profiles at the same time slices as before. During dissociation, the salinity decreases due to the release of fresh water. During formation, the salinity increases from the expulsion of salt in the hydrate structure. These salinity changes are largely responsible for the unique venting behavior shown in Case 2. The hydrate stability temperature is a function of pressure and salinity, with lower salinity raising the stability temperature and with higher salinity lowering the stability temperature. In this way, the hydrate formation is a self-limiting process. With continued hydrate production, the pore-water will eventually become too saline and free gas will be stable in the presence of hydrate.

Venting:

We also show graphically how the gas venting varies over time in Figure 8. For Case 1, no venting occurs, whatsoever. However, as previously discussed, there is a transient pulse of gas that vents into the ocean in Case 2. This venting behavior is characterized by a sharp increase to a peak value followed by slightly less sharp decrease. This a pulse that dissipates and is not sustained throughout time. This behavior occurs over a ~5 kyr period. In Case 3, the venting occurs much sooner and at a much larger rate.

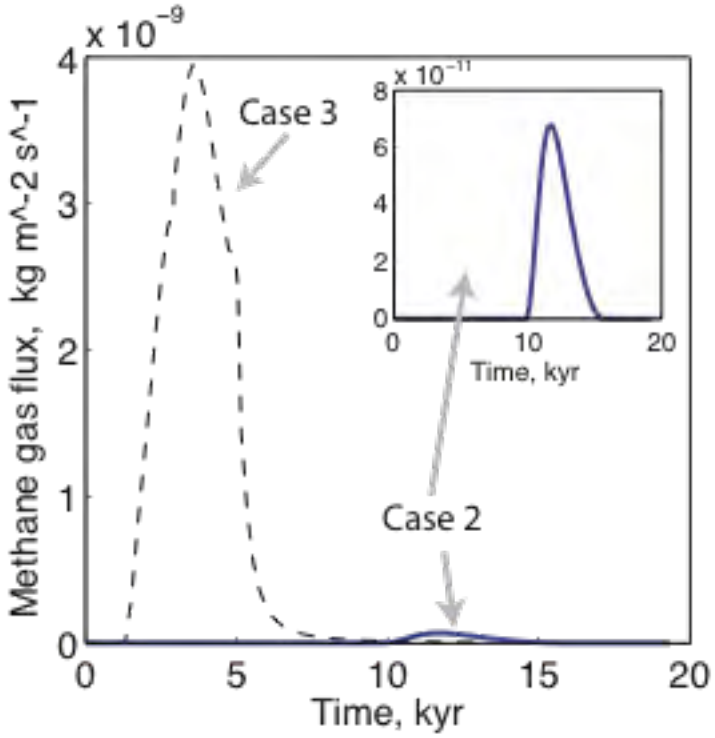

Figure 8: Gas flux venting into the ocean at the seafloor as a function of time. No gas flux for Case 2. There is a transient pulse of gas flux for Case 2 lasts ~5 kyr. In Case 3, all of the methane is vented.

Implications and Extensions

The simulation results presented show that for a given hydrate deposit there are methane losses into the ocean that are driven by the consequences of the phase changes. The volume expansion during hydrate dissociation drives gas flow upward, while the heat release and salinity increase during hydrate formation drives anomalous hydrate dissociation within the RHSZ.

We have extended the results from Case 2 to a generic environment. Our analysis shows that the behavior in Case 2 is a consequence of the changes in volume that occur during the re-organization of the system. We have shown that salinity increase that occurs during the secondary hydrate formation is the control on the three-phase behavior. Thus, we can simply calculate the changes in the hydrate stability zone from a given warming, and assess the hydrate re-organization. The threshold for transient venting as we have shown happens when the amount of dissociated hydrate exceeds the amount of hydrate required to elevate the salinity in the shortened hydrate stability zone to the three-phase equilibrium. This basic analysis demonstrates that the transient venting is a potential mechanism for

venting across a wide range of water depths and temperature changes.

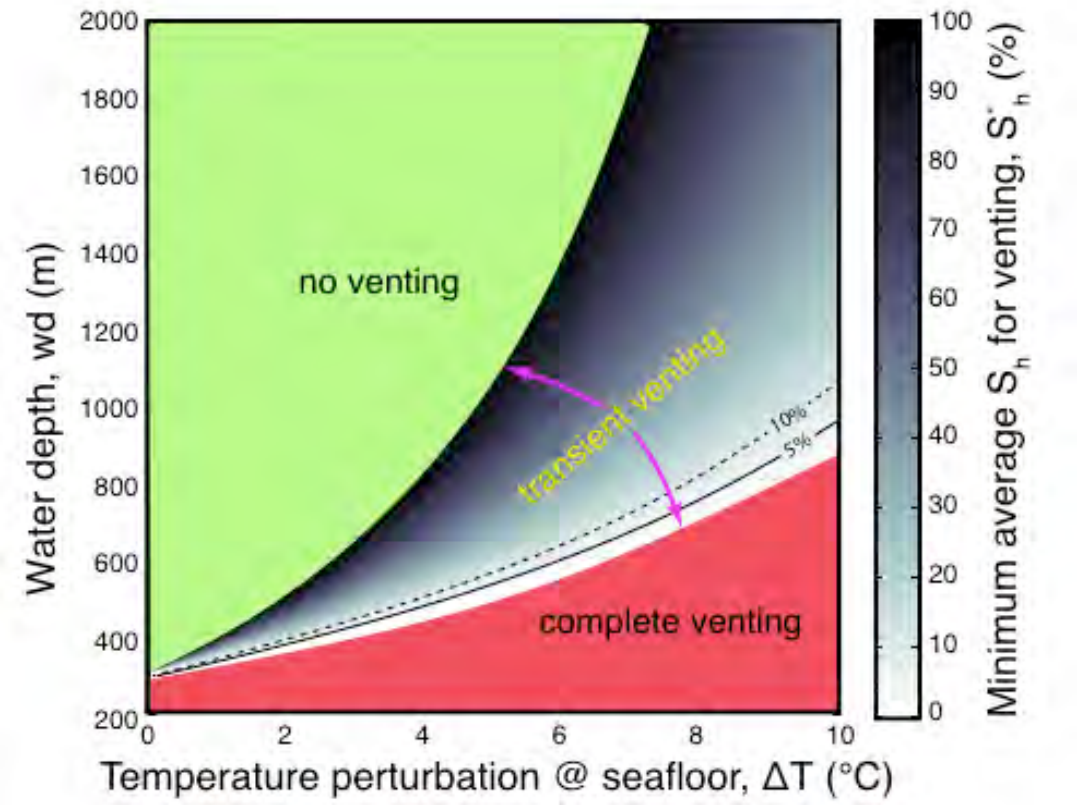

Figure 9: Gas venting potential under a given temperature increase (from assumed 0 C) and at a given water depth. The gradient shows the minimum hydrate saturation within the dissociated zone necessary to produce transient venting.

2.3. Task 3: Categorize Stability of Known Hydrate Reservoirs (Complete)

Milestone 1.D Determination of What Hydrate Reservoirs are at Three-Phase Equilibrium.

A. Goal:

The Recipient shall review and categorize the stability state of existing well-studied hydrate reservoirs, including but not limited to the Cascadia margin at Sites 1249 and 1250 (ODP Leg 204) and U1328 (IODP Exp. 311), offshore India (e.g. the Krishna-Godavari (K-G) Basin and the Ulleung Basinm, and the Mallik, and Mt. Elbert deposits, to determine and catalogue their thermodynamic state, i.e. their location relative to the three-phase equilibrium surface. Specifically, the Recipient shall study well-documented examples where pore fluid salinity, temperature, and hydrate saturation are independently measured (e.g. by pore water sampling, and geophysical logs, respectively). The Recipient shall calculate the in-situ pore fluid salinity and shall calculate whether, given the observed temperature, pressure and salinity, the reservoir is at the three phase equilibrium or within the brine-hydrate region (L+H). The Recipient shall develop a public and broad database of well understood examples where the thermodynamic state can be described.

B. Activities Phase 1:

We constrained the in situ temperature, pressure, and salinity at 4 locations: 1) ODP Site 1249A (offshore Oregon), 2) IODP Site U1328A (offshore Vancouver), 3) NGHP Site 01-10A (Krishna-Godavari Basin, off the eastern coast of India), and 4) at Mallik Site 5L-38 (Mackenzie River Delta in the Northwestern Territories, Canada). ODP Site 1249A and NGHP Site 01-10A have elevated in situ salinities near or at the three-phase boundary for a large portion of the GHSZ, indicating that portions of these systems are at three-phase equilibrium. Mallik has locally elevated salinities documenting three-phase equilibrium within the GHSZ. IODP Site U1328A has elevated salinities, but only for a small portion of the GHSZ and it does not appear that any portion of the sediment within the GHSZ is at three-phase equilibrium. A significant discovery is that we have shown that there are examples both on land and in the ocean basin where there is evidence within the gas hydrate stability zone (GHSZ) that the system is at three phase stability: salinity is elevated enough that gas, water, and hydrate can be present.

Introduction

Gas hydrate is a chemical compound consisting of a gas trapped within the crystalline lattice of ice. Hydrate is stable at high pressures and low temperatures and salinities (Figure 10) and can contain various types of low molecular weight gases, though in natural systems it is primarily occupied by methane (Kvenvolden, 1988). Hydrate systems have been identified in submarine sediments along continental margins around the world, primarily through the presence of a bottom-simulating reflector (BSR), but also in recovered cores (Kvenvolden, 1993; Shipley et al., 1979). The combined volume of methane gas stored globally in these hydrate systems is estimated to range from 1 to 5×10^{15} m^3, at standard temperature and pressure (Milkov, 2004).

Along with the potential economic importance of a methane reservoir this size, the possible release of the methane from these systems due to climate change (Dickens, 2003; Wright et al., 2005) has both environmental and geohazard implications. The release of large amounts of methane, a potent greenhouse gas, into the ocean could cause a significant rise in atmospheric concentrations, exacerbating the effects of global warming (Archer et al., 2004; Dickens, 2003; Kvenvolden, 1988). Also, the introduction of large amounts of free gas into submarine sediments could significantly destabilize continental slopes and could cause an increased frequency and severity of tsunamogenic submarine landslides (Kayen and Lee, 1991; Mienert et al., 2005; Nixon and Grozic, 2007; Paull et al., 1996).

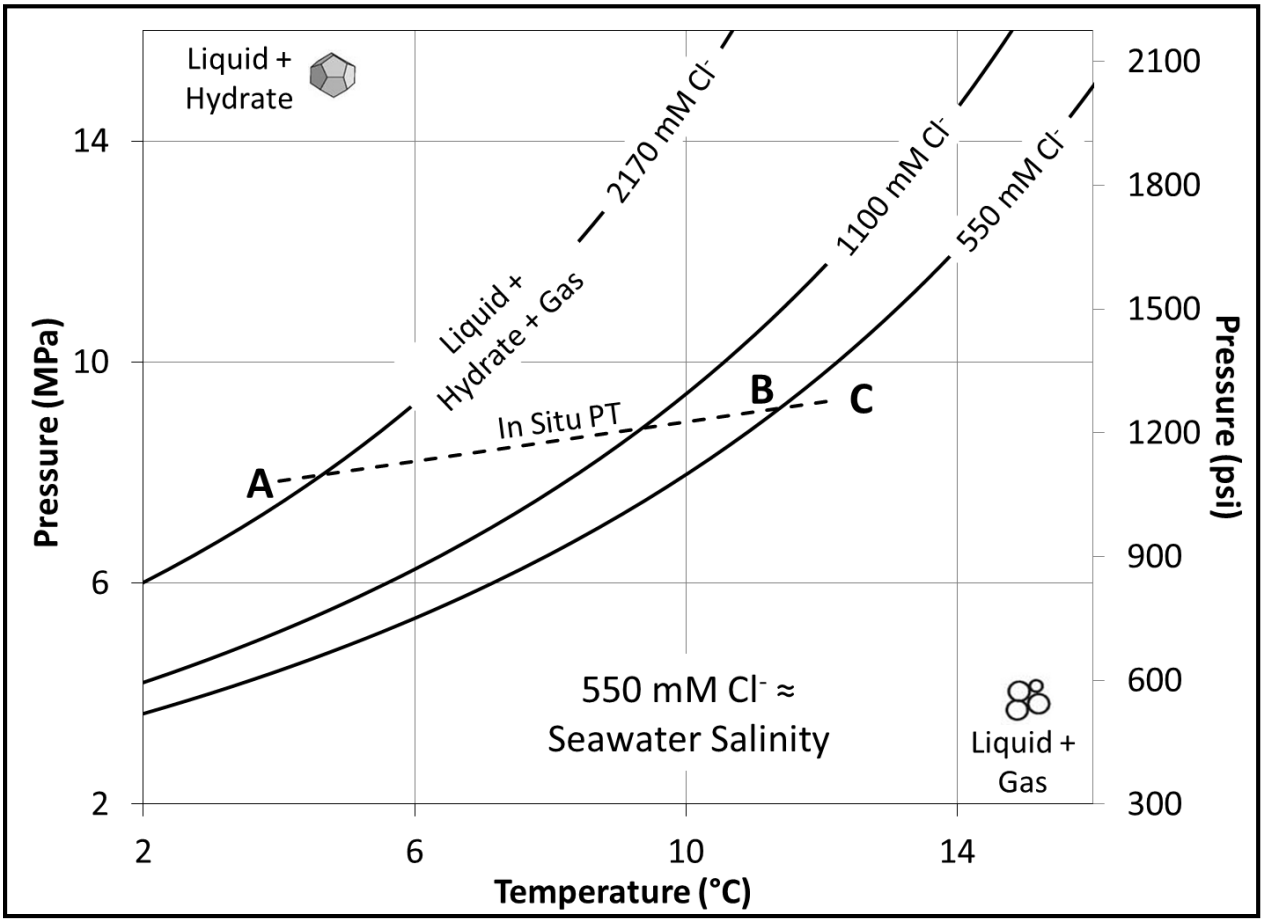

Figure 10: Phase diagram for Structure I methane hydrate. Plots pressure-temperature (PT) conditions required for three-phase equilibrium at various pore-water salinities. Dashed line is an example PT profile where depth increases from A to C and B marks the phase transition boundary as seawater salinity. As salinity increases, the three-phase equilibrium conditions change to high pressures and lower temperatures, moving up the in-situ PT profile.

Commonly, the in-situ conditions of the gas hydrate stability zone (GHSZ) are described by assuming constant geothermal and hydrostatic gradients and pore-water salinity within the system (Figure 11a, b, and c). The intersection between the in-situ salinity and the thermodynamically-defined three-phase salinity marks the depth to the base of the GHSZ. As a result, the traditional concept of submarine gas hydrate systems consists of a three-layer model (Figure 11d). The top layer extends from the seafloor to the base of the GHSZ where hydrate and water (L + H) are stable. The bottom layer consists of all the sediment below the GHSZ where free gas and water (L + G) are stable. The middle layer defines the three-phase boundary where hydrate, free gas, and water (L + G + H) are all stable. This boundary is commonly identified by the BSR (Schmuck and Paull, 1993).

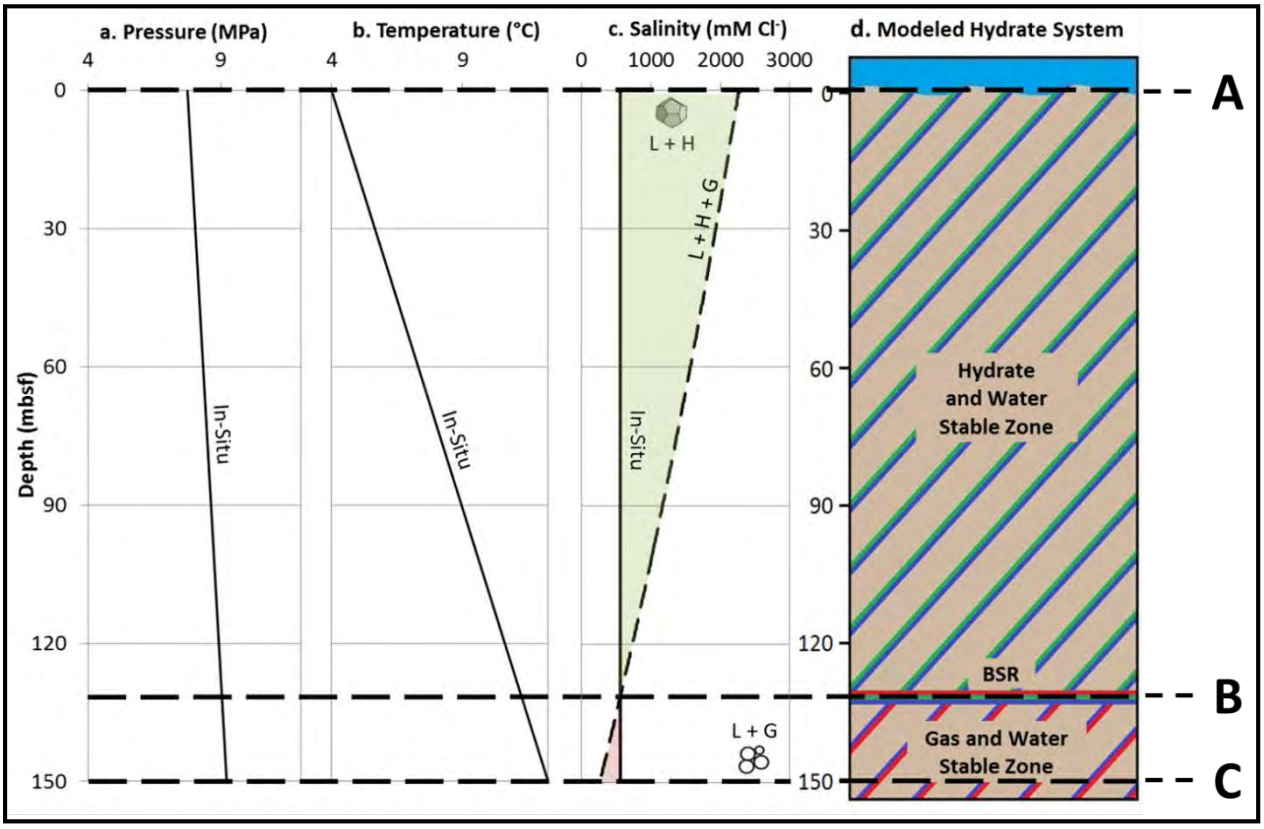

Figure 11: Traditional model of a submarine hydrate system. Solid lines mark the assumed in-situ conditions. Dashed line marks the salinity required for three-phase equilibrium. Intercept between these lines indicates the depth to the base of the GHSZ, marked by the BSR. Depths marked A, B, and C refer to the in-situ PT profile in Figure 1. a) In-situ pore pressure is determined by assuming a constant hydrostatic pressure gradient and no overpressure development. b) In-situ temperature is determined by assuming a constant geothermal gradient, controlled by the conduction of heat from below where heat flow and the thermal conductivity of the sediment are constant. c) In-situ salinity of the pore-water is assumed to be constant and equal to seawater salinity. d) Modeled structure of a hydrate system with these assumed conditions. Two 2-phase regions separated by a three-phase boundary.

The occurrence of seafloor gas vents at many sites (Haeckel et al., 2004; Heeschen et al., 2003; Torres et al., 2011; Tréhu et al., 2004) requires the presence of gas within the GHSZ and indicates that the thermodynamic conditions may vary from the classic model described above. These observations have led researchers to further explore the in-situ conditions of these systems. Haeckel, et al. (2004) identified the presence of anomalously high salinities from cores taken at Hydrate Ridge, offshore Oregon, despite hydrate dissociation and subsequent "freshening" of the pore-waters (Lu et al., 2005; Wright et al., 2005). Milkov, et al. (2004) degassed a pressure core from 14 meters below the seafloor (mbsf) at this site and determined that the in-situ salinity at that depth was approximately 1630 mM Cl^- (~3 times greater than seawater). Torres, et al. (2011) discussed six sites in the Krishna-Godivari Basin, Ulleung Basin, and offshore Vancouver Island, similar to Hydrate Ridge, that also recorded elevated core-derived salinities. These studies suggest that assuming a constant, sea water salinity with depth

may not accurately represent the in-situ salinity. Elevated salinities within the GHSZ can cause the three-phase equilibrium boundary to migrate toward higher pressures and lower temperatures (Figure 10), altering the thermodynamic state of the system.

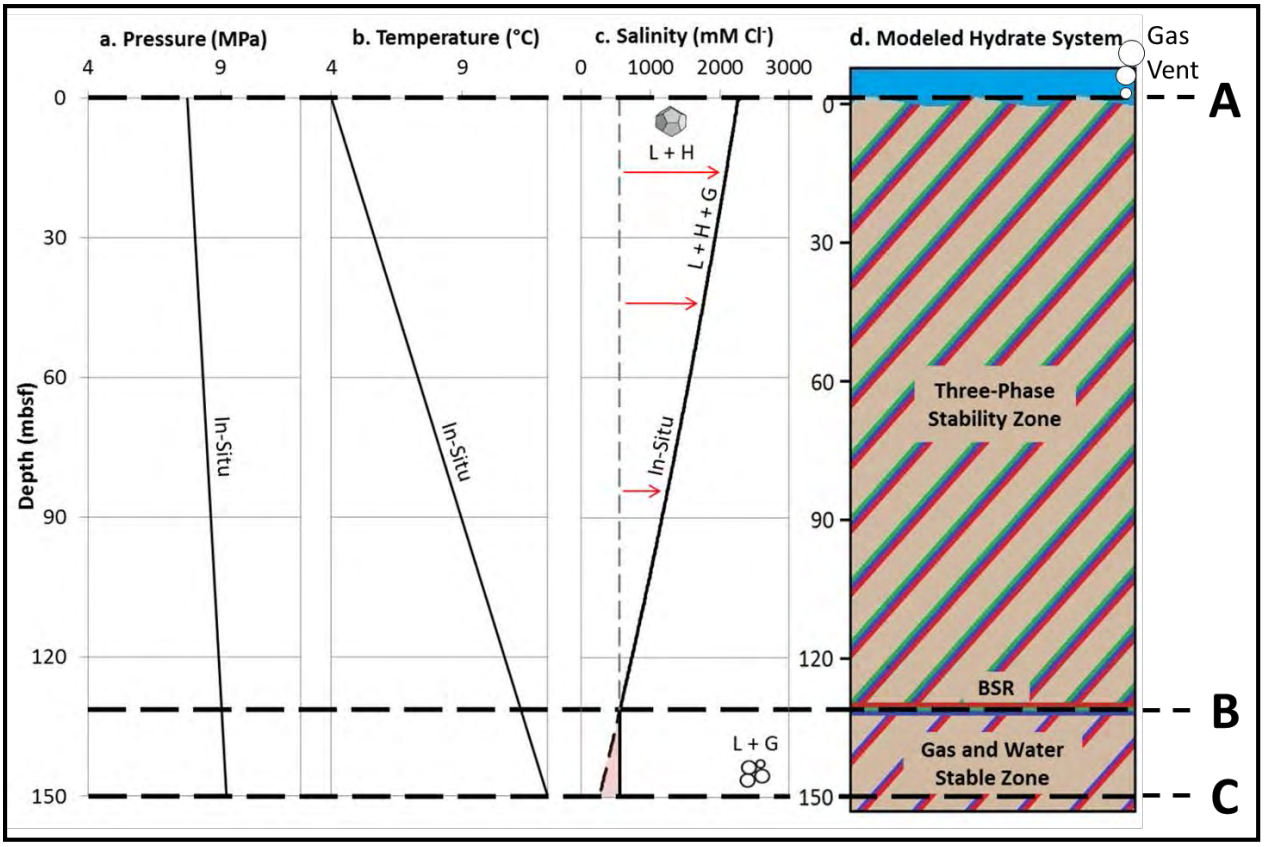

Figure 12: Alternative model of a submarine hydrate system that includes the effect of elevated salinities on in-situ thermodynamic state. Solid lines mark the assumed in-situ conditions. Dashed line marks the salinity required for three-phase equilibrium. Intercept between these lines indicates the depth to the base of the GHSZ, marked by the BSR. Depths marked A, B, and C refer to the in-situ PT profile in Figure 1. a) In-situ pore pressure is determined by assuming a constant hydrostatic pressure gradient and no overpressure development. b) In-situ temperature is determined by assuming a constant geothermal gradient, controlled by the conduction of heat from below where heat flow and the thermal conductivity of the sediment are constant. c) In-situ salinity of the pore-water is variable throughout the GHSZ and will elevate to the three-phase equilibrium as hydrate forms. d) Modeled structure of a hydrate system with these assumed conditions. Elevated salinities create three-phase equilibrium conditions throughout the GHSZ, such the system now consists of a three-phase region, below which hydrate is not stable.

The mechanism behind the observed hypersaline environments in these hydrate systems is likely salt exclusion during hydrate formation (Hesse and Harrison, 1981). This process alters the relative concentrations of water and salts in the pore space by incorporating water into the hydrate structure while forcing salt back into the remaining pore-water. Theoretically, with enough hydrate formation and subsequent increase in salinity, three-phase equilibrium could be maintained through a significant

portion of the GHSZ. In this state, the BSR would no longer mark a thin, distinct boundary at three-phase equilibrium, as in the traditional model, but the base of a relatively thick three-phase zone within the GHSZ (Figure 12), explaining the presence of gas within the GHSZ.

We constrain the in situ temperature, pressure, and salinity at each study site to estimate the phases that can be present based on equilibrium thermodynamic calculations. We report the in situ salinity and hydrate saturation and evaluate the thermodynamic state within the GHSZ at four locations. Two of the sites have elevated in situ salinities near or at the three-phase boundary for a large portion of the GHSZ, indicating that portions of these systems are at three-phase equilibrium. One site has locally elevated salinities documenting three-phase equilibrium within the GHSZ. The final site has elevated salinities, but only for a small portion of the GHSZ and not near the three-phase boundary.

Determination of in situ hydrate saturation and pressure, temperature, and salinity conditions

In order to assess the overall thermodynamic state of a hydrate system, the in-situ pressure, temperature, and salinity must be determined throughout the GHSZ. The in-situ pressure and temperature are used to define the salinity required for three-phase equilibrium, which marks the boundary between the hydrate stable and gas stable zones. The in-situ salinity can then be compared to the three-phase salinity to determine the thermodynamic state of the hydrate system with depth.

Determination of in-situ pressure and temperature

We follow the common assumption of previous research and assume a hydrostatic gradient and that no overpressure is developing within the sediments. Therefore, we calculate pore pressure (u) at a particular depth within the GHSZ using Equation 20:

$$u = (\rho_{sw} \cdot g \cdot Z_{wd}) + (\rho_{pw} \cdot g \cdot Z) = \rho_{sw} \cdot g \cdot (Z + Z_{wd}) \quad \text{Eq 20}$$

Z_{wd} is the water depth at the site, Z is the depth within the GHSZ, ρ_{sw} is the average density of seawater (1.023 g/cm^3), g is gravitational acceleration (9.81 m/s^2), and ρ_{pw} is the assumed density of the pore-water. The density of water can vary depending on its salinity and temperature. The potential effect of this density change on the pore pressure, however, is relatively small, so we assume that the pore-water density is equal to seawater density.

We calculate the in-situ temperature (T) at a particular depth within the GHSZ using Equation 21:

$$T = T_b + (Z \cdot G_g). \quad \text{Eq 21}$$

T_b is the temperature at the seafloor, and G_g is the geothermal gradient for the site. Geothermal gradient is controlled by the thermal conductivity and heat flow of the material below the seafloor (Henninges et al., 2005) and can be determined using downhole temperature probes.

Determination of in-situ salinity

The core-derived salinities are usually presumed to equal the in-situ values. The presence of hydrate, however, can result in elevated in-situ salinities. The dissociation of that hydrate releases fresh water back into the pore space, decreasing the salinity and invalidating this assumption. In this case, we determine the in-situ salinity using a method similar to that implemented by Malinverno, et al. (2008), which calculated the in-situ hydrate saturation from pore-water freshening. We assume a two-phase system where only free water, of saturation S_w, and hydrate, of saturation S_h, exist, such that:

$$S_h = 1 - S_w. \quad \text{Eq 22}$$

We also assume that the total pore volume does not change with hydrate formation and that the system is closed to diffusion and advection, meaning that the salt is immobile (Liu and Flemings, 2006). With these assumptions, we calculate the in-situ salinity ($C_{in\text{-}situ}$) with a volumetric correction (Eq. 23) between the core-derived salinity (C_0) and the water saturation:

$$C_{in-situ} = \frac{C_0}{1 - S_h} = \frac{C_0}{S_w}. \quad \text{Eq 23}$$

2.3 Determination of in-situ water saturation

We determine the water saturation using Archie's Law (Archie, 1942):

$$S_w = \sqrt[N]{\frac{a \cdot \rho_w}{n^m \cdot \rho_t}}. \quad \text{Eq 24}$$

N is the saturation exponent, a is the tortuosity coefficient, ρ_w is the pore-water resistivity, n is the porosity, m is the cementation exponent, and ρ_t is the formation resistivity. We use the RING resistivity log from the Logging-While-Drilling (LWD) data as a good estimate of the true formation resistivity (Cook et al., 2012). Porosity is calculated using a density equation:

$$n = {(\rho_m - \rho_b)}\Big/{(\rho_m - \rho_f)}. \quad \text{Eq 25}$$

Where ρ_m is the average grain density derived from the core moisture and density data, ρ_f is the assumed constant fluid density for each study site, and ρ_b is the bulk density derived from the LWD density log.

The pore-water resistivity is dependent upon the temperature and salinity of the water and is calculated using Arps' Equation (Arps, 1953):

$$\rho_w = 0.0123 + \left(\left(\frac{3647.5}{C^{0.955}}\right) \cdot \frac{45.4}{(T_f + 21.5)}\right) \quad \text{Eq 26}$$

Where T_f is the fluid temperature, determined using Equation 21, and C is the salinity of the water.

We determine the tortuosity coefficient (*a*) and cementation exponent (*m*) for each site based on resistivity and porosity measurements where water is the only phase present (S_w = 1). With this assumption, Equation 24 simplifies to:

$$F = \frac{\rho_t}{\rho_w} = a \cdot n^{-m} . \qquad \text{Eq 27}$$

Where *F*, termed the formation factor, is the ratio of formation resistivity to pore-water resistivity. A power law regression is taken from a cross-plot between porosity and formation factor (Pickett plot) and is used to infer the values of *a* and *m*. We limited the values of *a* and *m* to be between 0.5 – 1.5 and to be greater than 1, respectively (Crain, 2013).

To ensure that the points chosen to determine *a* and *m* are from material that is fully water saturated, we only use data points that are from below the GHSZ and that are not associated with anomalously low log-derived density. We also remove data points that have a bulk density correction log greater than ±0.25 g/cm^3 or a caliper log that exceeds the bit diameter by greater than 1 cm (0.394 in). These conditions are applied not only to ensure that the points represent water-saturated sediments, but also to remove points where borehole conditions may have compromised the log data accuracy.

The value of the saturation exponent in hydrate-saturated sediments is a topic of considerable debate. Pearson, et al. (1983) shows that *N* was equal to approximately 2 for various water-saturated sandstones. Hydrate-bearing sediment, however, experiences physical changes as hydrate precipitates and therefore does not act like a clean, water-saturated sandstone. Spangenberg (2001) suggested that *N* can range from 0.5 to 4 and that the value was dependent on many factors, including: whether hydrates are isopachous or pore-filling, the degree of hydrate saturation, and the significance of capillary effects. Spangenberg suggests that, regardless of the other factors, *N* increases at greater hydrate saturations. We assume an *N*-value of 4 for all study sites, because our region of interest is associated with significant hydrate saturations.

We use an iterative application of Archie's Law (Eq. 24) and the salinity correction (Eq. 23) to determine the in-situ water saturation and salinity. The water saturation is calculated for the first iteration using the core-derived salinity. This salinity is then corrected and used in the following iteration to recalculate the water saturation. The saturation from the current iteration is then used to re-correct the core-derived salinity for the following iteration. This process is repeated for 10 iterations, though we found that the calculated water saturation and in-situ salinity leveled off (ΔS_w < 1%) after 4 to 5 iterations.

During this procedure, linear interpolation was required to account for the different sampling resolutions of the log and core-derived data. The logged data resolution ranged from 3.05 – 15.24 cm (1.2 – 6 in), depending on the site and logging tool, while the core was sampled every 208 – 493 cm (81.9 – 194.1 in). To account for this difference, this iterative application of Archie's law is run using two modes of linear interpolation at each site. The first mode interpolates between the core-derived salinities to determine a unique salinity value for each resistivity data point. This method produces a hydrate saturation and salinity curve at the same resolution as the resistivity data. The second mode interpolates between the resistivity measurements to determine a unique resistivity value for each salinity sample. This mode produces a hydrate saturation and salinity profile for each available salinity

data point. The results from both of these interpolation modes are shown in the results for each site as gray or black lines for the resistivity resolution data and red dots for the salinity resolution data.

Determination of three-phase salinity

We calculate the salinity necessary to maintain three-phase equilibrium throughout the GHSZ for the interpreted temperature and pressure profiles at each study site. At any particular depth, we define this salinity as the point where the solubility of methane gas in water in a liquid-gas phase system (Duan et al., 1992) and liquid-hydrate phase system (Henry et al., 1999), at the unique in-situ pressure and temperature conditions, are equal. This model was described by Liu and Flemings (2006) and showed good agreement with stability conditions produced by the CSMHYD hydrate program (Sloan, 1998).

Study Sites

Analysis of well log and core-derived data

Each study site was chosen for the availability of necessary log and core data as well as the confirmed presence of hydrate within the logged portion of the well. The standard suite of log data included the gamma ray, caliper, resistivity, bulk density, photoelectric factor, and neutron porosity tools. Some logs were not essential to our calculations and are therefore are not displayed in the well log montages. We analyze the LWD and core data to infer the presence of hydrate and the dominant lithology and to determine if salt diffusion or advection is significantly affecting the in-situ salinity.

Hydrate presence is inferred using the resistivity and bulk density logs. Gas hydrate is a highly resistive material that complicates the conductive pathway, increasing tortuosity and the measured resistivity (Collett and Ladd, 2000; Cook et al., 2010; Pearson et al., 1983). Also, gas hydrate has a density equal to approximately 0.925 (Collett et al., 2012), which is less than seawater. The formation of gas hydrate could result in a decrease in measured bulk density as the greater density pore fluid is replaced by the significantly less dense hydrate. Therefore, we infer the presence of hydrate wherever the resistivity increases and bulk density decreases together.

The general lithological trends within a well are determined from the gamma ray log and core samples. The gamma ray tool responds to changes in grain size distribution, recording larger gamma ray values (GAPI) in finer-grained sediment (Serra, 1984). This information is used to identify interbedded fine-grained and coarse-grained material and directional-fining sequences. The core samples allow for a more complete characterization of the lithology, but sacrifice data resolution. These data are used to calibrate and confirm the analysis performed on the gamma ray log.

We determine the validity of the “closed system” assumption from the core-derived salinities. In an open system, the excess in-situ salt will be reduced back to baseline values through diffusion and advection, while in a closed system it will remain in the pore space. When the core is removed from the in-situ conditions and hydrate dissociates, fresh water will flow back into the pore space, freshening the

pore-water. With open conditions the core-derived salinities would be significantly below seawater, while with closed conditions the pore-water would freshen back to the baseline salinity. Therefore, we interpret the system to be "closed" if the core-derived salinities are around seawater.

ODP Site 1249A

ODP Site 1249A (Figure 13) was drilled on the southern summit of Hydrate Ridge, offshore Oregon (44º 34.237'N, 125º 8.841'W) to determine the abundance and distribution of gas hydrate resources at in the region and to investigate the processes that allow free gas to exist within the GHSZ. Site 1249A is located approximately 220 km southwest of Portland, Oregon in 788.5 meters of water. The well was drilled to a total depth of 90 mbsf, stopping short of the base of the GHSZ (115 mbsf) for safety concerns (Shipboard Scientific Party, 2003). A standard suite of LWD tools was run for the entire well; the relevant LWD and core-derived data from this borehole are presented in Figure 14. The baseline density and resistivity values and Archie parameters for this site were determined using LWD data from ODP Site 1250A, 305 meters to the southwest, because this hole penetrated the base of the GHSZ (Shipboard Scientific Party, 2003). Archie's parameters, *a* and *m*, were determined to equal 1.50 and 1.89, respectively (Table 1, Figure 15).

The resistivity log for ODP Site 1249A has a baseline value of 1.1 ohmm. From 0 – 21 mbsf, the resistivity increases log-linearly from the baseline to 110 ohmm. Between 21 – 47 mbsf, the resistivity is consistently elevated to an average of 88 ohmm with a maximum value of 214 ohmm at 34 mbsf. From 47 mbsf to the total depth, the resistivity decreases exponentially towards an average value of 2.3 ohmm. The density log has a baseline value of 1750 kg/m^3. From 0 – 47 mbsf the density is consistently lower than the baseline, ranging between 1060 – 1670 kg/m^3 and averaging 1590 kg/m^3. From 47- 64 mbsf, the density increases log-linearly from 1450 – 1750 kg/m3. From these analyses, we conclude that hydrate likely exists within the entire cored region of this well, with high saturations concentrated in the region between 21 – 47 mbsf. The presence of gas hydrate was confirmed through the occurrence of soupy or "mousse-like" textured sediments, caused by hydrate dissociation, infrared images, and from whole-round cores where hydrate samples were preserved (Shipboard Scientific Party, 2003).

The gamma ray log for Site 1249A increases from 40 to 60 GAPI log-linearly throughout the well, indicating a relatively consistent lithology. The low range in gamma ray measurements suggests that the lithology at this site consists of fine-grained sands and coarse-grained silty material. Core samples, however, defined two lithological units, both of which consisted of silty-clay material with thin, interbedded sandy layers. The lower section (Unit II) contained a higher frequency of thin sand layers (Shipboard Scientific Party, 2003).

At Site 1249A, the core-derived salinities range from 354 – 1008 mM Cl^-, averaging 556.6 mM Cl^- with a standard deviation of ±44.6 mM Cl^-, excluding the values above 15 mbsf, where borehole washout could be affecting the pore fluid. The close proximity of the salinities to the baseline salinity indicates that the system was closed during hydrate formation.

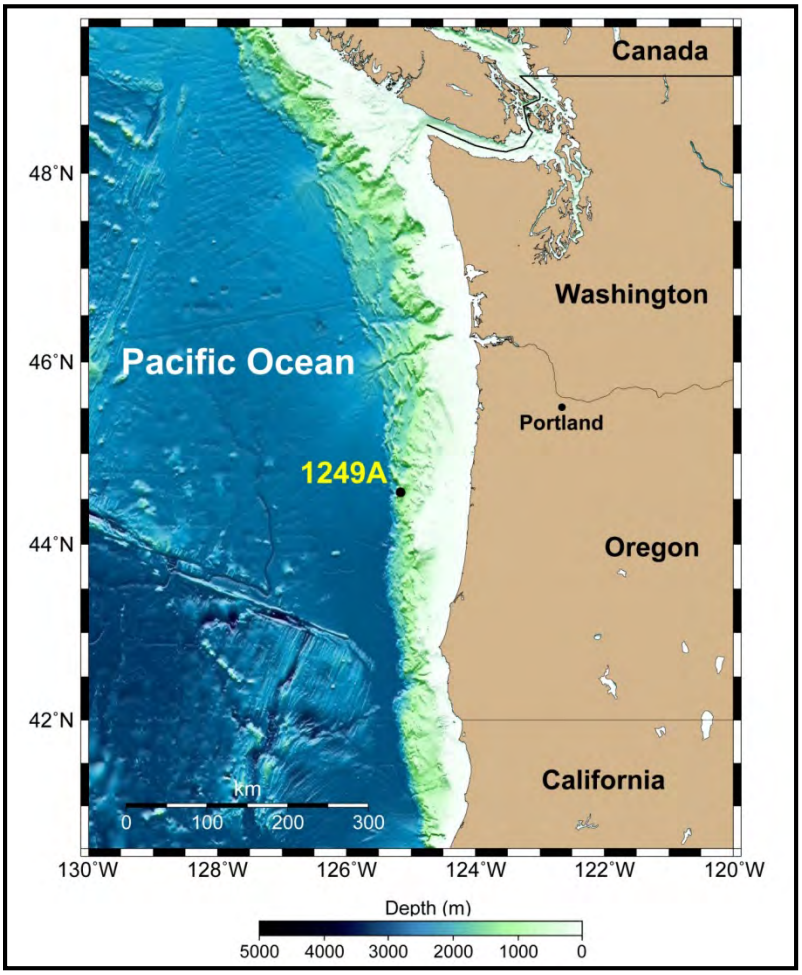

Figure 13: ODP Site 1249A is located approximately 220 km southwest of Portland, Oregon, in about 790m of water. Bathymetry data from IOC, et al. (2003).

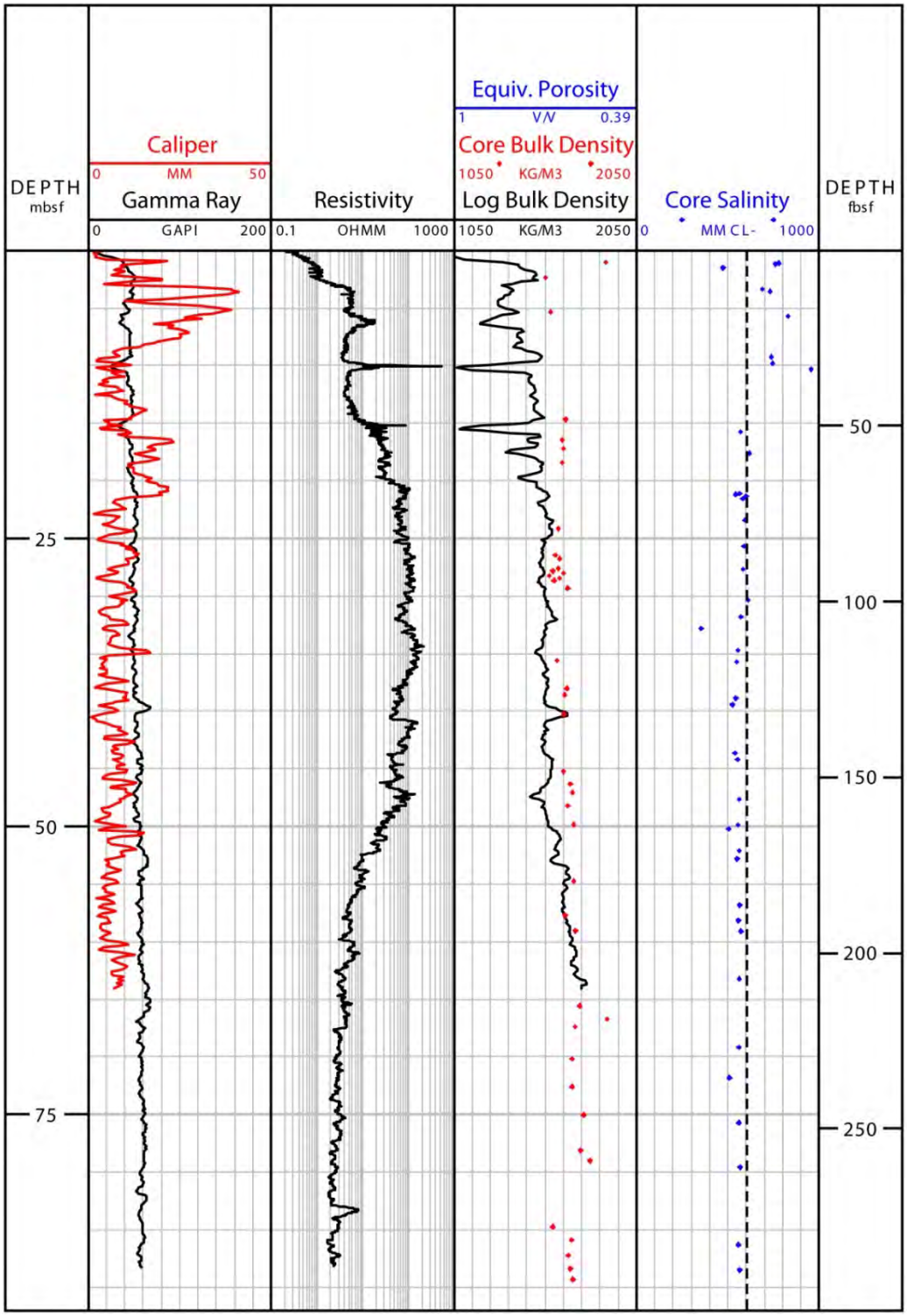

Figure 14: Montage of core and LWD data from ODP Site 1249A at Hydrate Ridge. Track 1: Gamma ray and differential caliper log; Track 2: RING resistivity log; Track 3: Core-derived and LWD bulk density. Equivalent porosity scale (assuming ρg = 2.70 g/cm3 and ρw = 1.05 g/cm3) is included for reference; Track 4: Core-derived chloride concentration. Dashed line represents average salinity of 607.7 mM Cl-.

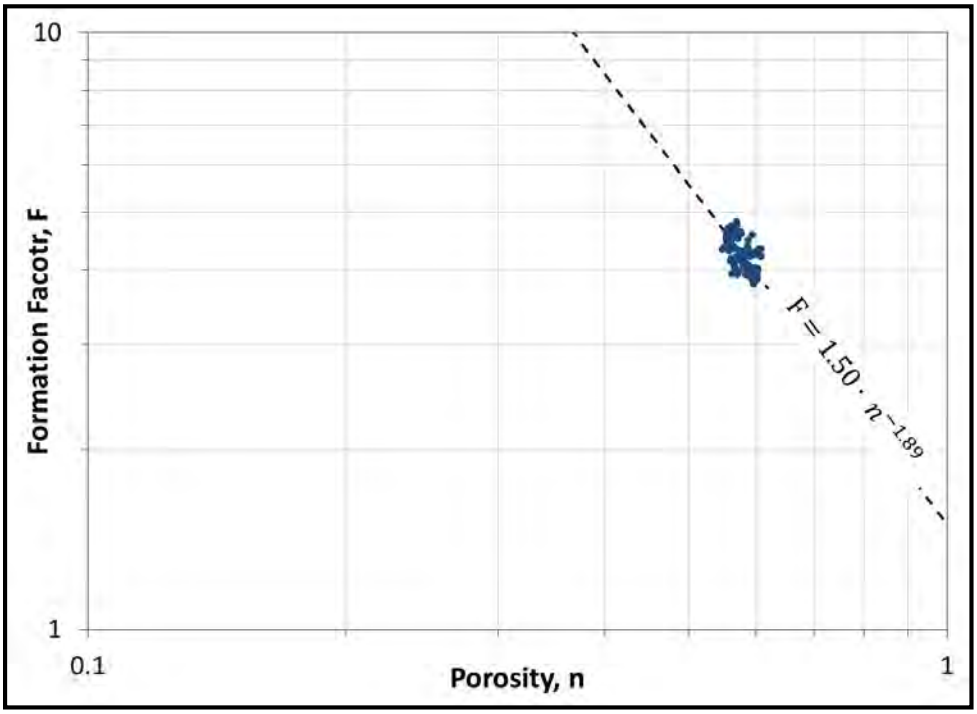

Figure 15: Pickett plot for ODP 1249A. The best fit linear regression line using water-saturated points yields the cementation exponent (m = 1.89) and tortuosity coefficient (a = 1.50).

IODP Site U1328A

IODP Site U1328A (Figure 16) was drilled on the mid-continental slope off of Vancouver Island (38º 40.057'N, 126 º 51.043'W) in a water depth of 1267.7 m to a total depth of 300 mbsf, penetrating the base of the GHSZ at 219 mbsf. The stratigraphy in this region is dominated by silty-clay with interbedded coarser-grained material. The presence of gas hydrate was confirmed through infrared temperature data as well as the incidence of soupy or "mousse-like" textured sediment caused by hydrate dissociation (Expedition 311 Scientists, 2006). The standard suite of LWD instruments were deployed throughout the cored section of the well (Figure 17). Archie's parameters, *a* and *m*, were determined to equal 1.48 and 1.4, respectively (Table 1, Figure 18).

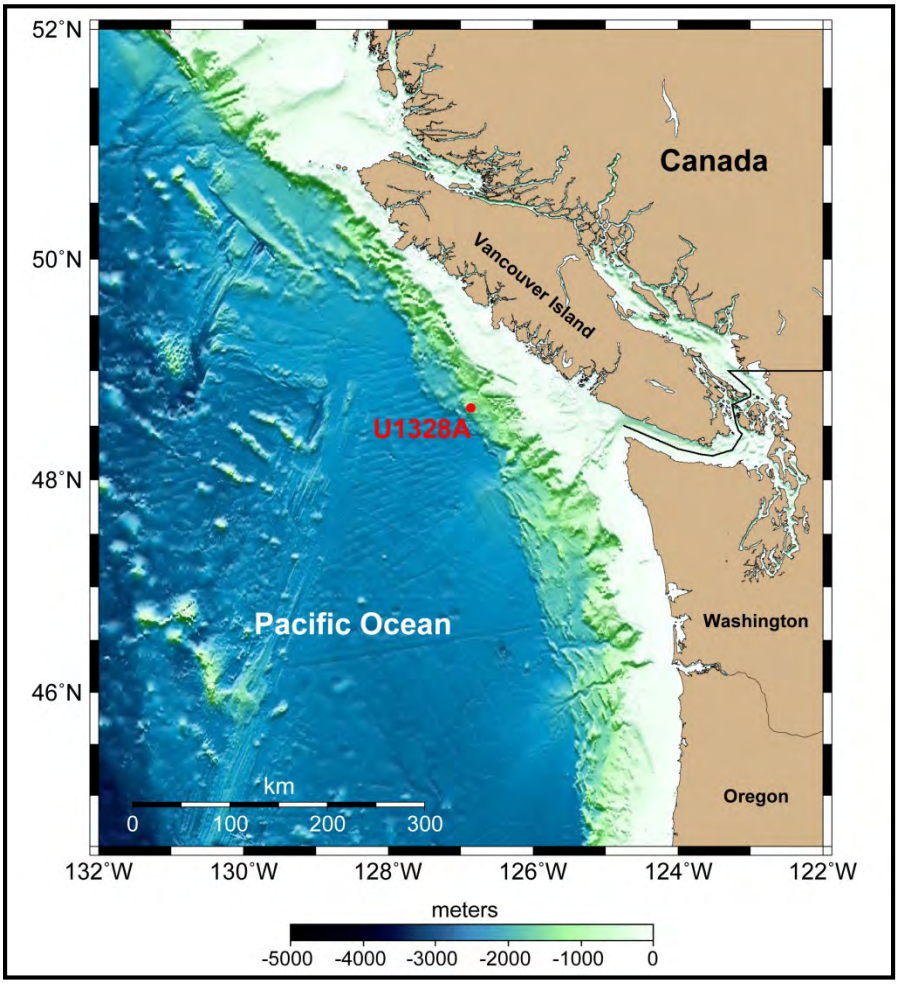

Figure 16: IODP Site U1328A is located approximately 100 km offshore Vancouver Island to the southwest, in about 1270m of water. Bathymetry data from IOC, et al. (2003).

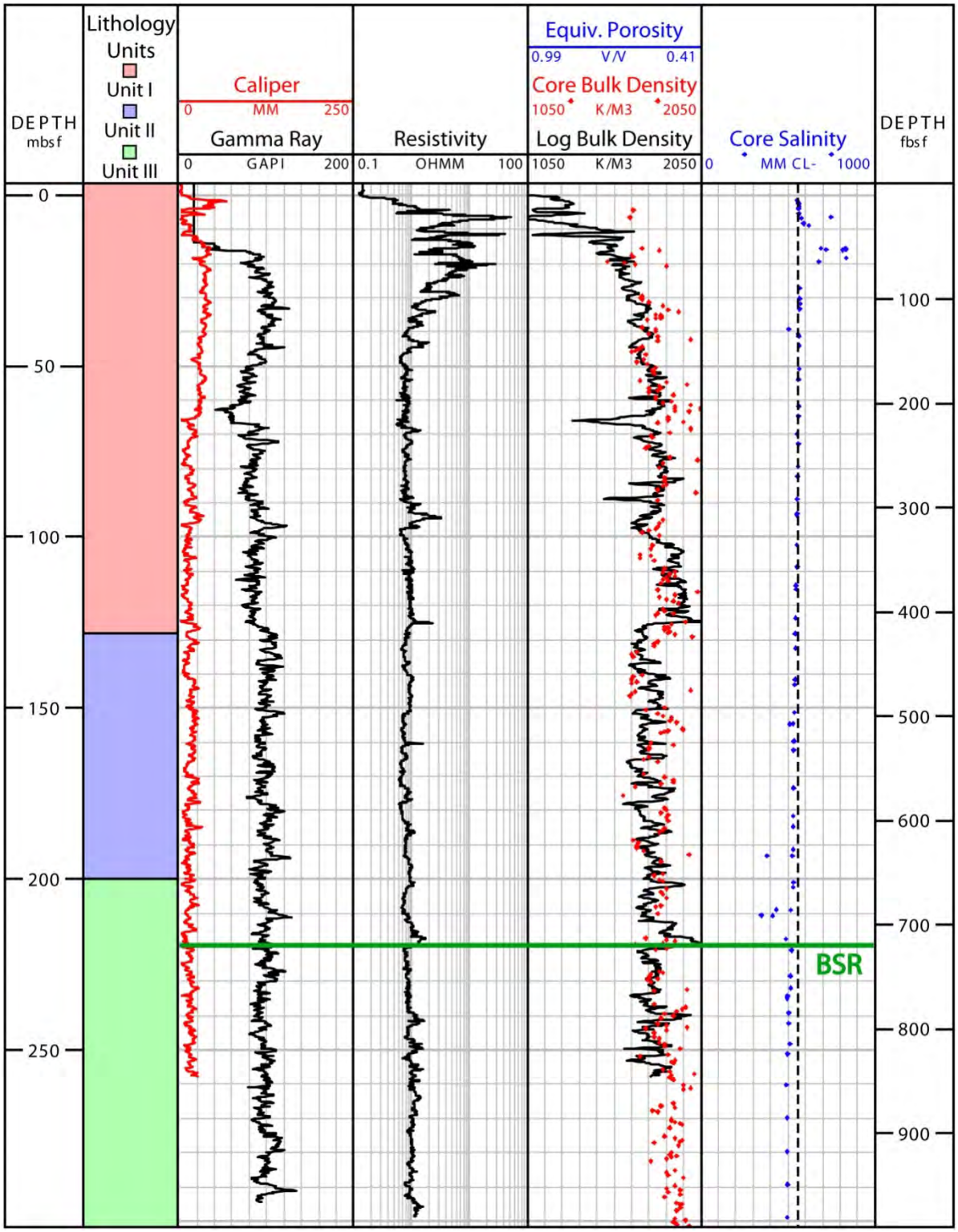

Figure 17: Montage of core and LWD derived data from IODP Site U1328A offshore Vancouver Island. Track 1 – Gamma ray and differential caliper log; Track 2 – RING resistivity; Track 3 – Core-derived and logged bulk density

and equivalent porosity assuming ρ_g = 2.76 g/cm^3 and ρ_w = 1.03 g/cm^3; Track 4 – Core-derived chloride concentrations compared to the concentrations required for three-phase equilibrium.

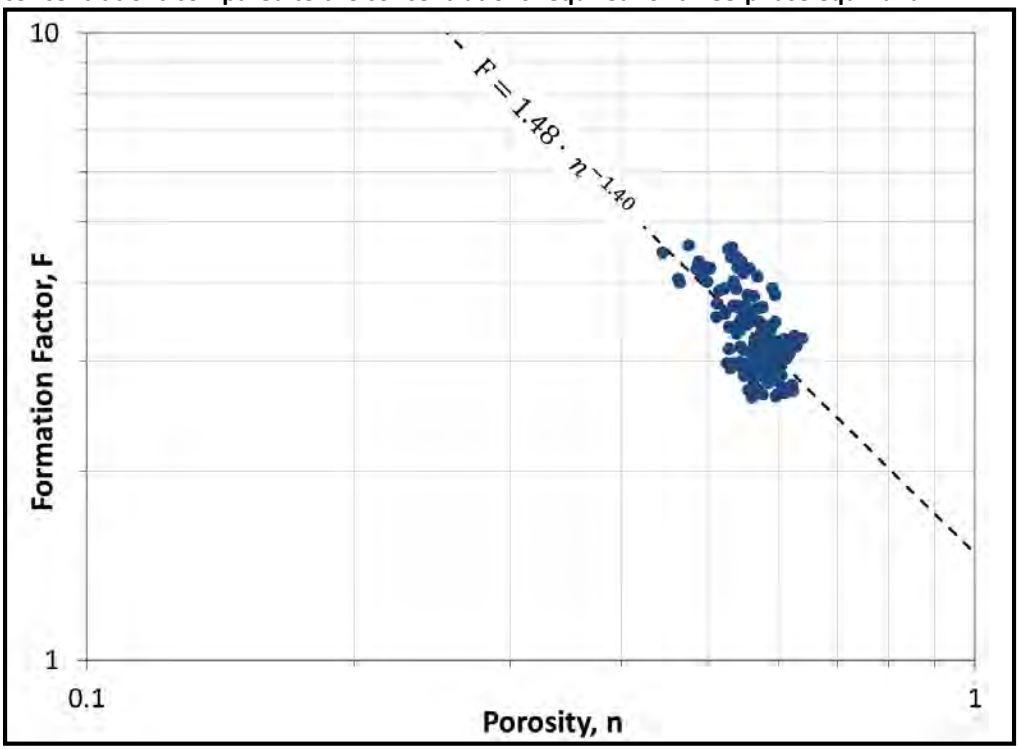

Figure 18: Pickett plot for IODP Site U1328A. The best fit linear regression line using water-saturated points yields the cementation exponent and tortuosity coefficient. At this site, *a* = 1.48 and *m* = 1.40.

NGHP Site 01-10A

NGHP Site 01-10A (Figure 19) was drilled in the Krishna-Godavari Basin, off of the eastern coast of India (15º 51.857'N, 81º 50.079'E) to investigate the distribution of methane hydrate resources available in that region. Site 10A is located approximately 150 kilometers southeast of Guntur, India in 1049.3 meters of water. The well was drilled to a total depth of 205.5 mbsf and penetrated the BSR at 160 mbsf (NGHP Expedition 01 Scientists, 2007). A standard suite of LWD tools was run for the entire well; the relevant LWD and core-derived data from this borehole are presented in Figure 20. Archie's parameters, *a* and *m*, were determined to equal 1.50 and 1.62, respectively (Table 1, Figure 21). To avoid washout near the seafloor, the first 30 mbsf of the hole were drilled with low flow, rotation, and penetration rates. After 30 mbsf, the flow rate was increased until all LWD tools were activated (NGHP Expedition 01 Scientists, 2007). As a result, the data required for our calculation was only available below 22 mbsf.

The resistivity log for Site 10A increases from a baseline value of 0.94 ohmm starting at 28 mbsf, reaching a maximum value of 130 ohmm at 48 mbsf. Between 48 – 160 mbsf, the resistivity drops log-linearly from the peak value back to the baseline, excluding the region between 89 – 125 mbsf, where the resistivity drops an average of 8.3 ohmm below the this trend. Where data was available, the bulk density log ranges from 1240 – 1820 kg/m^3 with a baseline density of 1800 kg/m^3. Above the BSR, the bulk density decreased significantly from the baseline between 22 – 89 and 125 – 160 mbsf. Below the

BSR, the density alternated between the baseline and a bulk density of approximately 1500 kg/m^3, which could either indicate the presence of free gas or be the result of poor borehole conditions. These data indicate that hydrate exists between 28 – 160 mbsf, but that greater saturations of hydrate occur between 45 – 90 and 125 – 160 mbsf. The occurrence of hydrate at Site 10A was confirmed in core sample cuts, infrared imaging data, and the occurrence of soupy or "mousse-like" textured sediment as a result of hydrate dissociation in core samples. Gas hydrate was observed as solid nodules, disseminated throughout the pore space, and within high-angle fractures (NGHP Expedition 01 Scientists, 2007).

The gamma ray log for Site 10A ranges between 60 -100 GAPI from 28 – 160 mbsf, with an average value of 82 GAPI, indicating that the lithology is primarily fine-grained material. The lithology from recovered cores supports this interpretation, defining a single lithological unit consisting of a clay matrix with varying occurrence of nannofossils. The core lithology also indicated the presence of authigenic carbonate cements in large portions on the well (NGHP Expedition 01 Scientists, 2007).

The core-derived salinities for NGHP Site 10A range from 397.6 – 634 mM Cl^-, averaging 526.6 mM Cl^- with a standard deviation of ±65.3 mM Cl^-. The range of salinity values are relatively well distributed throughout the well, showing no particular trends correlated with lithology or hydrate presence. The close proximity of the salinities to the baseline salinity indicates that the system was closed during hydrate formation.

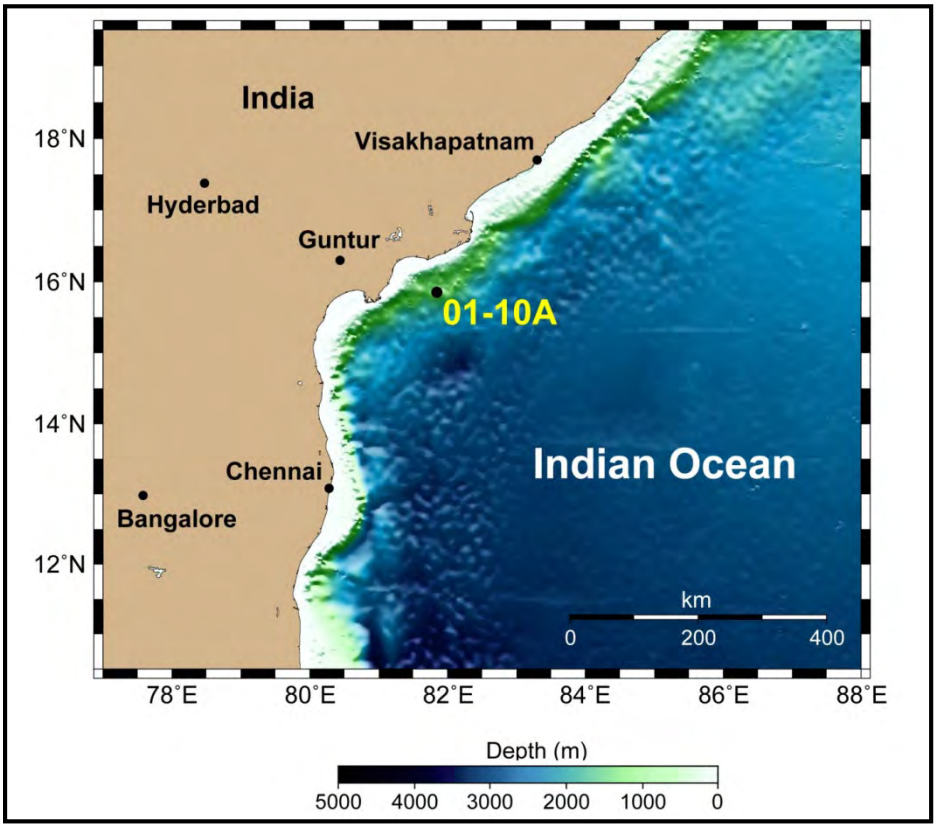

Figure 19: NGHP Site 01-10A is located approximately 150 km southeast of Guntur, India in about 1050m of water. Bathymetry data from IOC, et al. (2003).

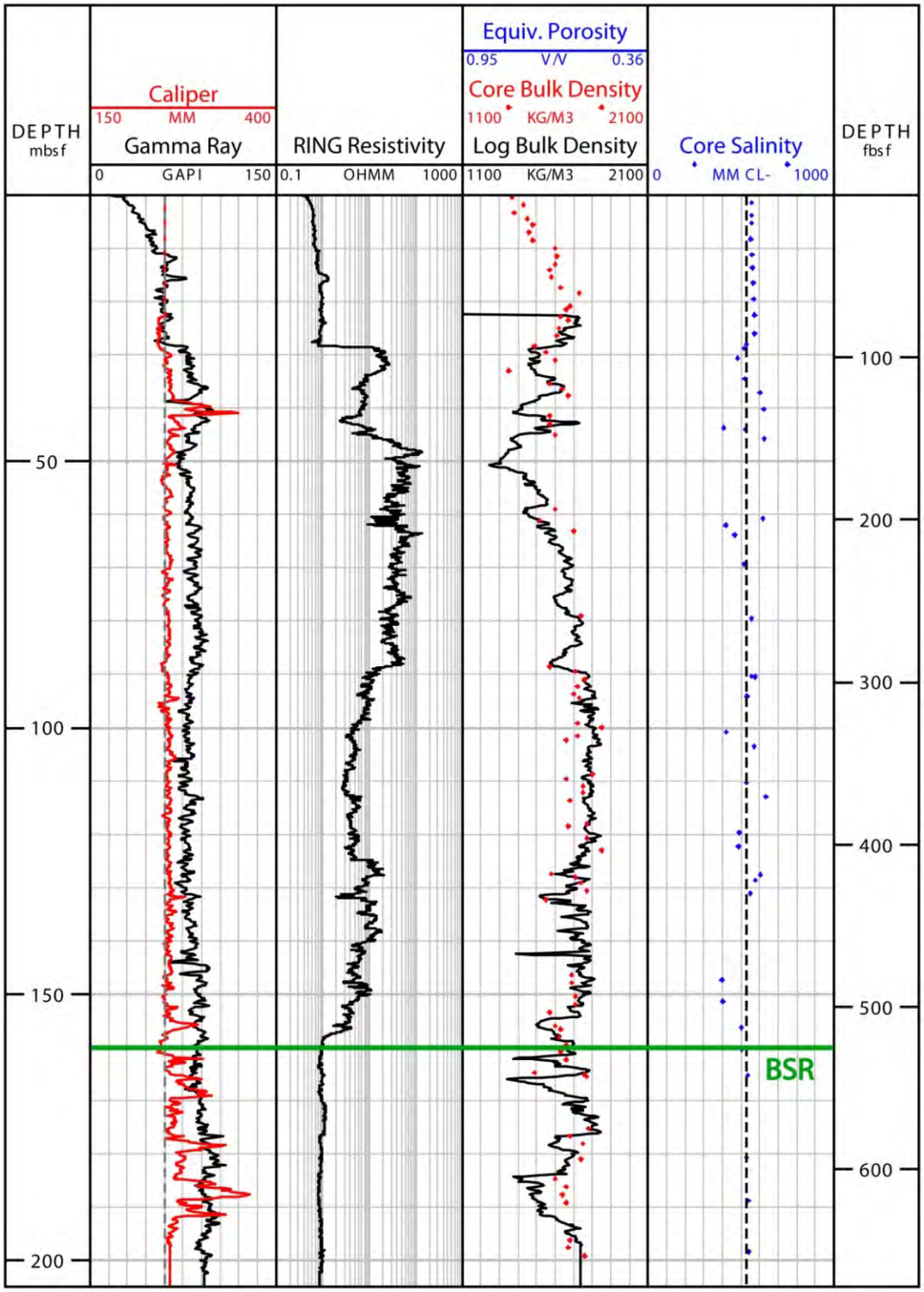

Figure 20: Montage of core and LWD data from NGHP Site 01-10A in the Krishna-Godavari Basin. Track 1: Gamma ray and caliper log (dashed line indicates bit size); Track 2: RING resistivity log; Track 3: Core-derived and LWD bulk density. Equivalent porosity scale (assuming ρg = 2.72 g/cm3 and ρw = 1.023 g/cm3) is included for reference; Track 4: Core-derived chloride concentration. Dashed line represents average salinity of 526.4 mM Cl-.

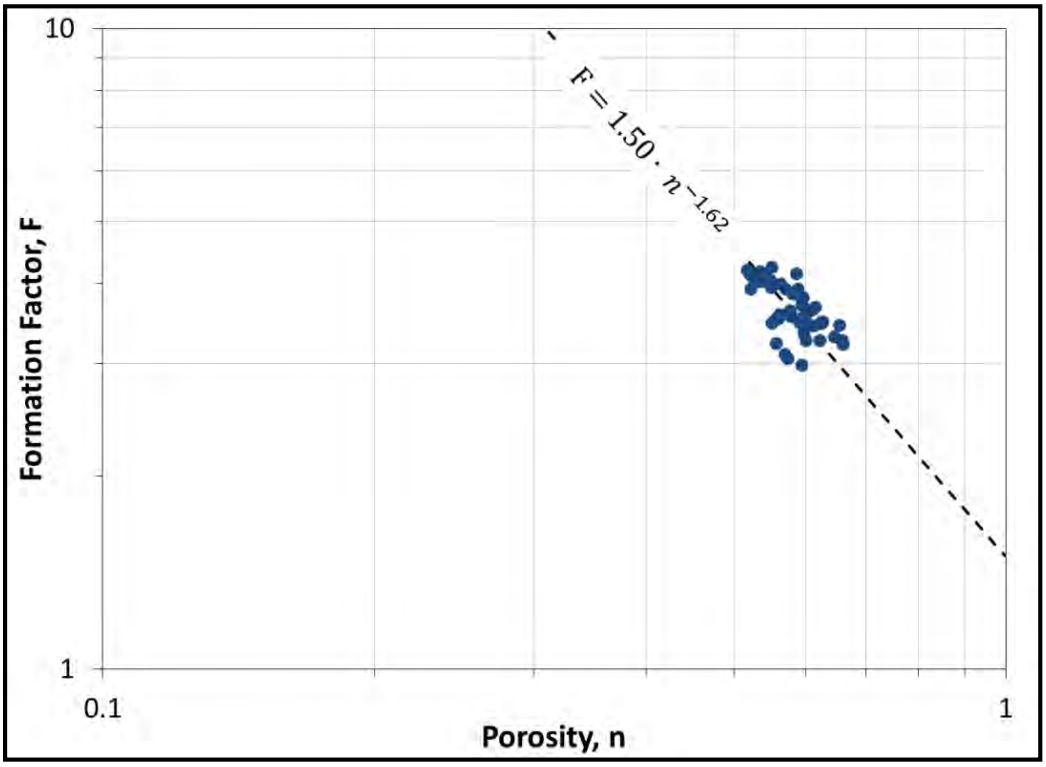

Figure 21: Pickett plot for NGHP 01-10A. The best fit linear regression line using water-saturated points yields the cementation exponent (m = 1.62) and tortuosity coefficient (a = 1.50).

Mallik Site 5L-38

Mallik Site 5L-38 (Figure 22) was drilled in the Mackenzie River Delta in the Northwestern Territories, Canada (69º 27.655'N, 134 º 39.648'W). The site was drilled in a water depth of 1 m to a total depth of 1166 mbsf. The upper 676.5 mbsf consists of permafrost-cemented sediment, underlain by water saturated sediment in which hydrate formed between 891 and 1107 mbsf (Collett et al., 2005; Takahashi et al., 2005). The stratigraphy within the GHSZ consists of 4 thick layers of sandy material (5 – 52 meters) seperated by thick, fine-grained silt layers (Medioli et al., 2005). The presence of gas hydrate in the area was previously confirmed in 1972 and 1998 (Bily and Dick, 1974; Collett and Dallimore, 1998; Dallimore et al., 1999) during the drilling of the Mallik L-38 and 2L-38, respectively, and was also confirmed at the 5L-38 well through the presence of hydrate in recovered cores and use of pressure core samples to specifically recover hydrate samples (Lu et al., 2005). This well was divided up into 4 distinct zones based upon the values for core-derived chloride concentrations in Matsumoto, et al. (2005) and supported by the lithology in that same study. There was an extensive wireline logging program implemented within the GHSZ at this site; the pertinent well log and core data is shown in Figure 23. Archie's parameters, *a* and *m*, were determined to equal 0.75 and 2.052, respectively (Table 1, Figure 24).

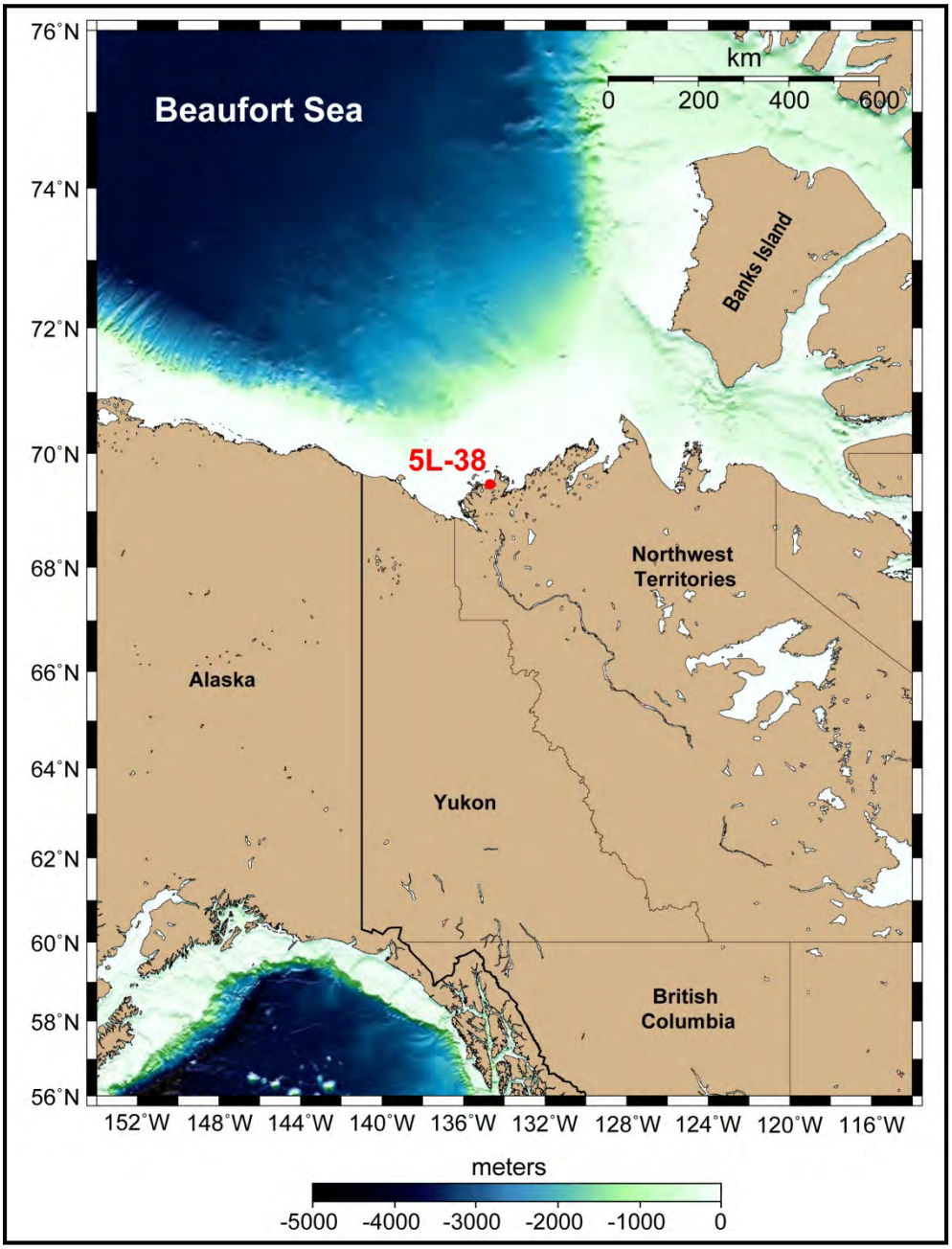

Figure 22: Mallik Site 5L-38 is located in the Mackenzie River Delta, Northwestern Territories, Canada in about 1m of water. Bathymetry data from IOC, et al. (2003).

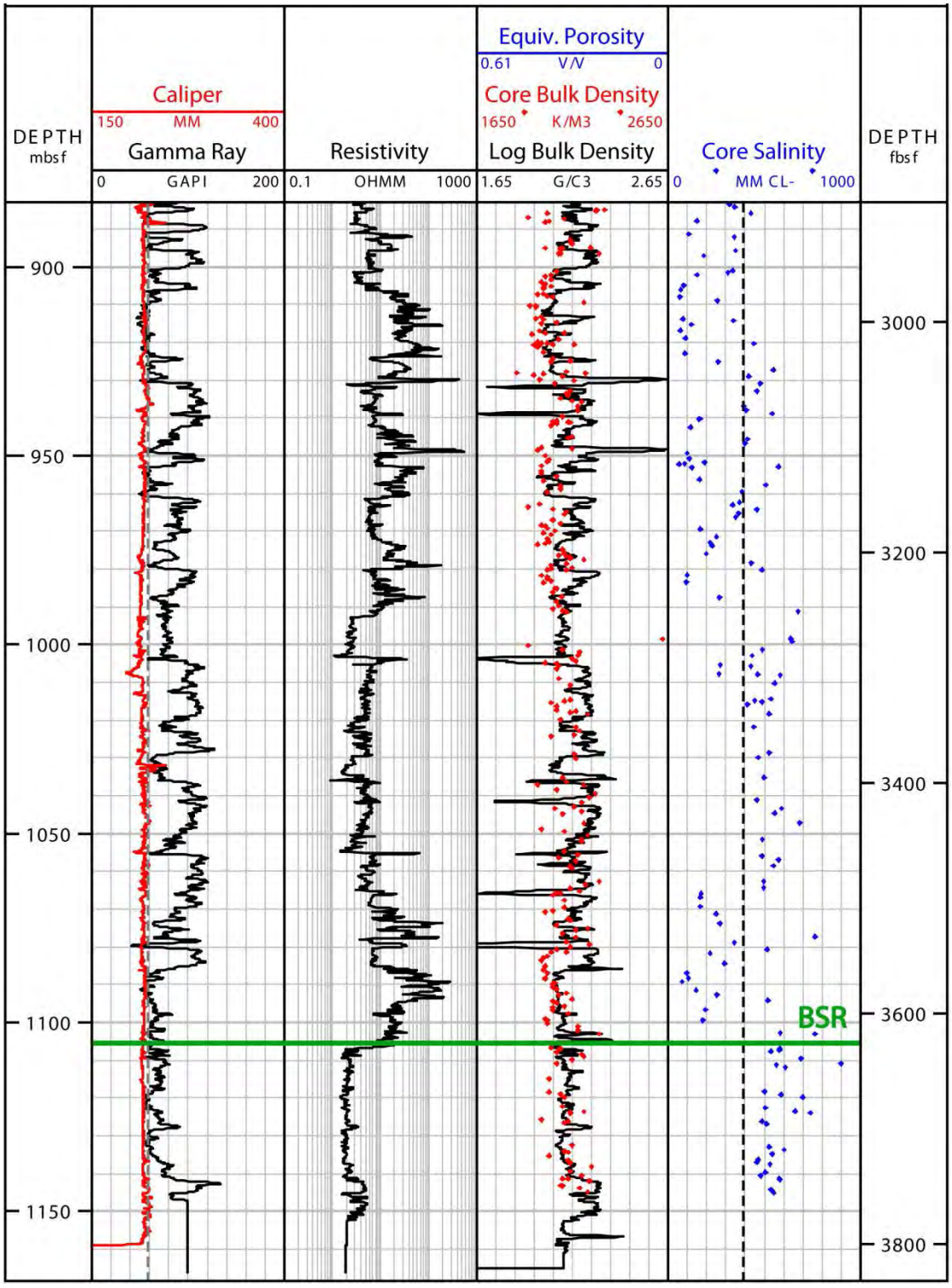

Figure 23: Montage of core and wireline derived data from Mallik Site 5L-38 in the Mackenzie Delta. Track 1 – Gamma ray and caliper log (dashed line represent the bit size for this section); Track 2 – Focus mode 5 (deep) resistivity; Track 3 – Core-derived and logged bulk density and equivalent porosity assuming ρg = 2.65 g/cm3

and ρw = 1.01 g/cm3; Track 4 – Core-derived chloride concentrations compared to the concentrations required for three-phase equilibrium.

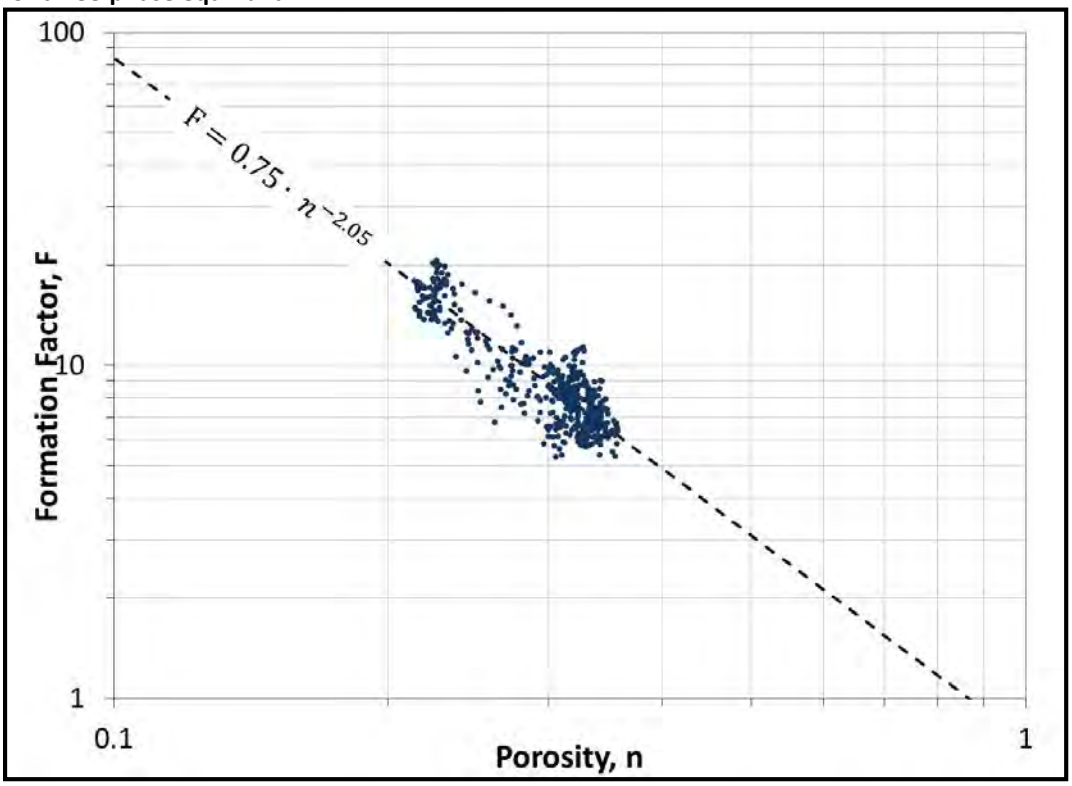

Figure 24: Pickett plot for Mallik Site 5L-38. The best fit linear regression line using water-saturated points yields the cementation exponent and tortuosity coefficient. At this site, *a* = 0.75 and *m* = 2.05.

Results

ODP Site 1249A

At Site 1249A, the hydrate saturation averages 0.484 between 2 – 15 mbsf, excluding two peaks at 6.3 and 10 mbsf with saturations of 0.695 and 0.89, respectively. The highest hydrate saturation exists between 15 – 47 mbsf, with saturations ranging from 0.514 – 0.814 with an average of 0.733. Below 47 mbsf, the hydrate saturation reduces exponentially to an average of 0.192 in the bottom 11 meters of the well (Figure 25; Track 2).

The calculated in-situ salinities are well correlated with the hydrate saturations. An average salinity of 1580 mM Cl^- exists between 2 – 15 mbsf, approximately 2.6 times greater than the baseline salinity, excluding the two anomalous peaks at 6.3 and 10 mbsf with salinities of 2985 and 7742 mM Cl^-, respectively. Between 15 – 47 mbsf, the in-situ salinity ranges from 1316 to 2996 mM Cl^- and averages 2154 mM Cl^-, 3.54 times greater than the baseline salinity. Below 47 mbsf, the salinity decreases exponentially from 2700 mM Cl^- back to 1.25 times greater than the baseline (Figure 25; Track 3). The pressure core sample taken at 14 mbsf was determined to have an in-situ salinity of 1630 mM Cl^-

(Milkov et al., 2004), which correlates well with the salinity we calculated for that depth and supports the other in-situ salinities we determined.

We qualitatively identify one thick region, between 15 – 47 mbsf, and two thin layers, from 9.8 – 10.5 mbsf and 5.7 – 7 mbsf, where the in-situ salinities are near to or exceed the three-phase boundary (Figure 25; Track 3), and interpret these regions to be at three-phase equilibrium. We believe that the two thin layers are associated with the presence of free gas, because they are both associated with a drastic decrease in bulk density and increase in resistivity that is uncharacteristic of the surrounding sediment. We still interpret these regions to be at three-phase equilibrium, however, because the salinity indicates this thermodynamic state.

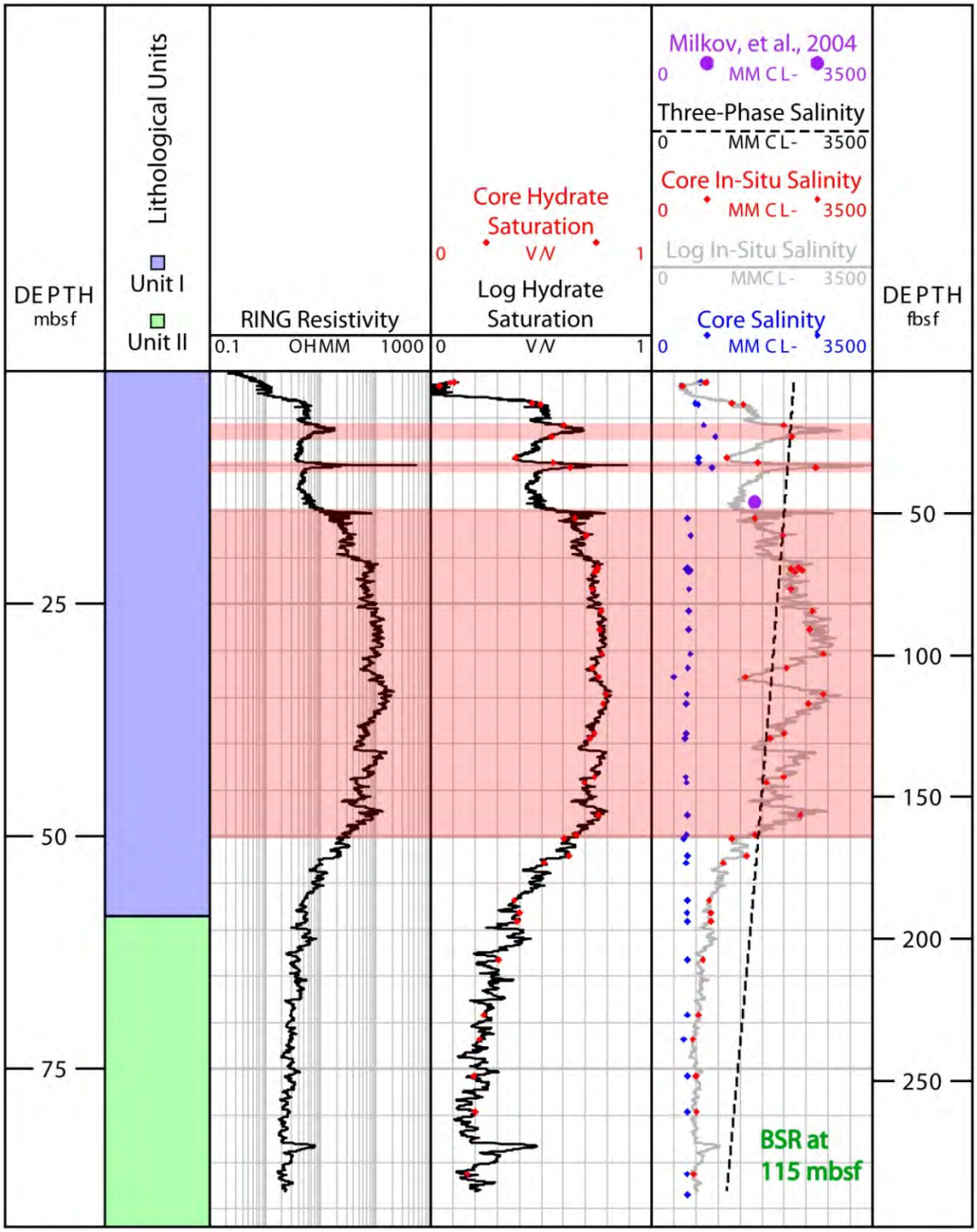

Figure 25: Results from ODP Site 1249A. Track 1: Core-derived lithological units, descriptions can be found in the scientific reports (Shipboard Scientific Party, 2003). Track 2: RING resistivity log; Track 3: Resistivity- (black line) and salinity-interpolated (red dots), Archie-derived hydrate saturation; Track 4: Core-derived salinity (Shipboard Scientific Party, 2003), resistivity- (gray line) and salinity-interpolated (red dots) in-situ salinities, and the salinity required for three-phase equilibrium (dashed line). Red shading shows qualitatively interpreted three-phase equilibrium zones.

IODP Site U1328A

We identify a relatively thin region of the GHSZ (0 – 30 mbsf) with high hydrate saturation, which decreases rapidly to essentially no hydrate for the rest of the GHSZ (Figure 26; Track 1). This zone of high hydrate saturation is correlated with elevated salinities near the top of the GHSZ, but do not reach the three-phase boundary (Figure 26; Track 2). These results suggest that no portion of this system is at three-phase equilibrium.

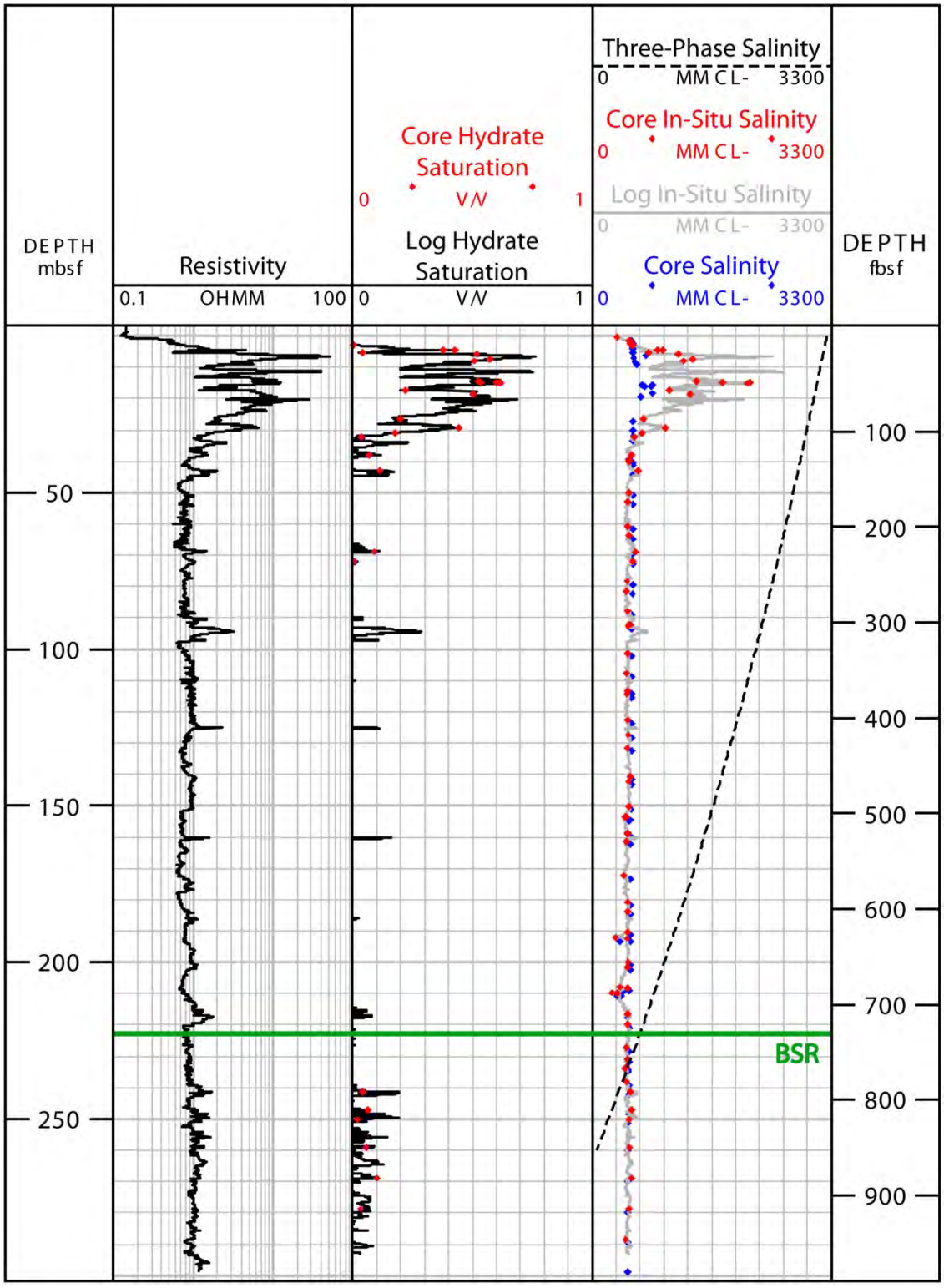

Figure 26: Results from IODP Site U1328A. Track 1 – RING resistivity log; Track 2 – Resistivity (black line) and salinity (red dots) interpolated, Archie-derived hydrate saturations; Track 3 – Core-derived salinity (Expedition

311 Scientists, 2006), resistivity (black line) and salinity (red dots) interpolated in situ salinities, and the salinity required for three-phase equilibrium (dashed line).

NGHP Site 01-10A

At Site 10A, there are four distinct zones of varying hydrate saturation: Zone 1, from 28 – 45 mbsf; Zone 2, from 45 – 90 mbsf; Zone 3, from 90 – 123 mbsf; and Zone 4, from 123 – 160 mbsf. These zones are identified by significant changes in the average value of the hydrate saturations between zones. Zone 1 – 4 have average hydrate saturations of 0.526, 0.7, 0.382, and 0.413, respectively, with a peak saturation of 0.817 at 48.4 mbsf (Figure 27; Track 3). The hydrate saturations in Zones 2 and 4 are consistently high and follow a relatively linear decline in value with depth. The hydrate saturation drops rapidly from 0.40 – 0 in the last 3 meters above the BSR. Zones 1 and 3 exhibit lower hydrate saturations relative to the proximal zones as well as a similar decrease in saturation with depth. Elevated salinities are identified throughout zones 1 – 4, averaging 1181, 1922, 876.6, and 872 mM Cl^-, respectively, ranging between 1.66 – 3.65 times greater than the baseline salinity (Figure 27; Track 4).

We qualitatively interpret Zones 2 and 4, where in-situ salinities are at or exceed the three-phase salinity, to be near to or at three-phase equilibrium. Between 46 – 57 mbsf, the in-situ salinities calculated at the log data resolution (gray line) were far greater than the three-phase salinity. At the pressure and temperature conditions at this depth, hydrate would not be stable under these conditions. We attribute these anomalously high values to the lack of core-derived salinities within this section. The interpolation of salinity values between the available salinity data above and below this region results in an average salinity 94.6 mM Cl^- greater than the baseline. If the baseline salinity were used in this region, the in-situ salinities would decrease by between 270 – 530 mM Cl^-.

Seven pressure cores were recovered while drilling sites 10B and 10D and were used to determine the in-situ hydrate saturation. The resulting saturation values from these analyses are plotted with the calculated hydrate saturations in Figure 11. Two of the cores, 10B-28P (175.1 mbsf) and 10B-25P (164.1 mbsf), were taken below the base of the GHSZ. The volume of gas released from these cores was either below the saturation point of methane in water or would result in a small volume of free gas in the core. The other five pressure cores, 10B-08Y (50.1 mbsf), 10B-15P (98.2 mbsf), 10B-18Y (117.4 mbsf), 10D-12E (77.8 mbsf), and 10D-22E (145.1 mbsf), were taken above the base of the GHSZ. Core 10D-12E, however, had substantial mechanical complications during recovery and storage that resulted in significant hydrate dissociation and gross underestimation of in-situ hydrate saturation (NGHP Expedition 01 Scientists, 2007).

Core 10B-08Y had significant air voiding caused by hydrate dissociation or gas devolution during handling, which significantly reduced the amount of core available to determine hydrate saturation. Also, the micro CT scanner used to quantify hydrate saturation had a resolution two orders of magnitude greater than the pore size, reducing its ability to detect disseminated hydrate (Rees et al., 2011a). These handling complications and methodological limitations could have caused significant underestimation of the hydrate saturation.

The other three pressure cores were all associated with varying amounts of hydrate dissociation during recovery that resulted in lower calculated in-situ hydrate saturation (NGHP Expedition 01 Scientists, 2007). Despite these complications, however, the saturations derived from these three pressure cores are correlated relatively well with the Archie-derived hydrate saturations we present here. The average saturation of these pressure cores was 16.3 percent lower than calculated, which can be attributed to the dissociation of hydrate during recovery and handling.

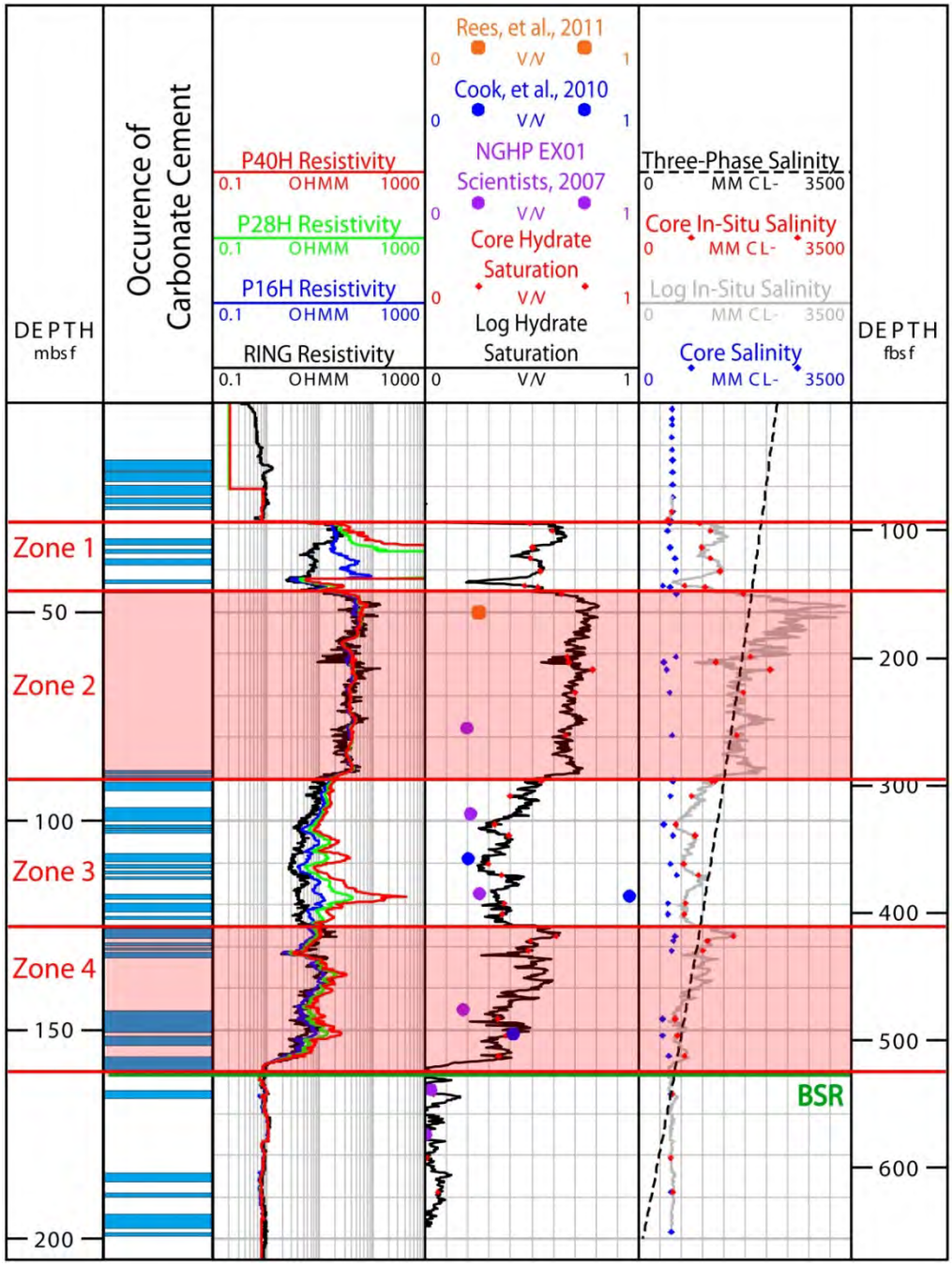

Figure 27: Results from NGHP Site 01-10A. Track 1: Occurrence of carbonate cement derived from recovered cores (NGHP Expedition 01 Scientists, 2007); Track 2: RING (black line) and propagation resistivity curves (colored lines) at 2MHz and depths of investigation ranging from 16 – 40 inches; Track 3: Resistivity- (black line) and salinity-interpolated (red dots), Archie-derived hydrate saturation, pressure core-derived hydrate saturations (NGHP Expedition 01 Scientists, 2007; Rees et al., 2011a), and modeled hydrate saturations incorporating resistivity anisotropy (Cook et al., 2010); Track 4: Core-derived salinity (NGHP Expedition 01 Scientists, 2007), resistivity- (gray line) and salinity-interpolated (red dots) in-situ salinities, and the salinity required for three-phase equilibrium (dashed line). Red shading show quantitatively interpreted three-phase equilibrium zones.

Mallik Site 5L-38

Hydrate formation at Mallik 5L-38 is limited to Zones 1 and 3, with decreasing hydrate saturation towards the seafloor (Figure 28; Track 1). Our calculated hydrate saturations correlate well with the saturations determined from the pressure core sampling program (Lu et al., 2005). These zones of high saturation are associated with elevated in situ salinities, however, the salinities only approach or cross the three-phase boundary in Zone 3 (Figure 28; Track 2). From these results, we interpret three-phase equilibrium to exist betnween 1060 – 1107 mbsf.

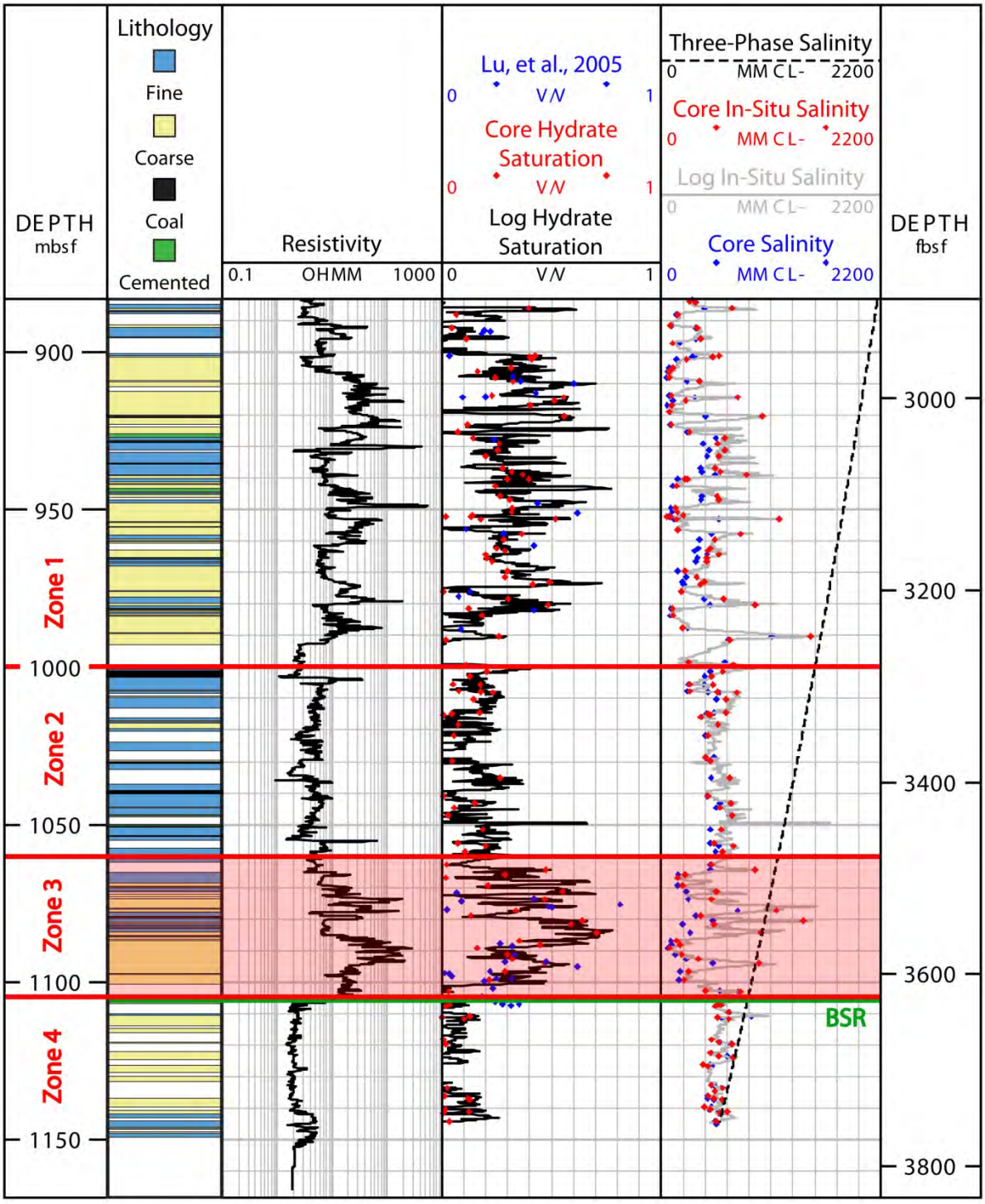

Figure 28: Results from Mallik 5L-38. Track 1 – Core-derived, generalized core lithology; Track 2 – RING resistivity log; Track 3 – Resistivity (black line) and salinity (red dots) interpolated, Archie-derived hydrate saturation and hydrate saturations determined from pressure core samples (Lu et al., 2005). Track 4 – Core-derived salinity (Matsumoto et al., 2005), resistivity (black line) and salinity (red dots) interpolated in situ salinities, and the

salinity required for three-phase equilibrium (dashed line). Red boxes indicate zone interpreted as being at three-phase equilibrium.

Study Site	Water Depth (mbsf)	Depth to BSR (mbsf)	Bottom Temperature (ºC)	Geothermal Gradient (°C/km)	Grain Density (g/cm^3)	Fluid Density (g/cm3)	Archie Parameters		
							a	m	N
ODP 1249A	788.5	115	4.0	55	2.70	1.050	1.50	1.89	4
IODP U1328A	1267.7	219	3.5	52	2.76	1.030	1.48	1.40	4
NGHP 01-10A	1049.4	160	6.5	45	2.72	1.023	1.50	1.62	4
Mallik 5L-38	1.0	1107	5.7	30	2.65	1.010	0.75	2.05	4

Table 1: Parameters used to determine in situ hydrate saturation and salinity at each study site. Archie's parameters, a and m, were determined for each site from the LWD data. N was assumed to be constant for all sites. All parameters were taken from the initial and scientific reports for each site (Collett et al., 2005; Expedition 311 Scientists, 2006; Henninges et al., 2005; NGHP Expedition 01 Scientists, 2007; Shipboard Scientific Party, 2003).

Discussion

Limitations on hydrate formation and distribution

Within the regions interpreted to be at three-phase equilibrium, hydrate formation is buffered by the in-situ salinity. Salinity increases as hydrate forms until it reaches the value required for three-phase stability, which is controlled by the in-situ pressure and temperature conditions. In the zones interpreted to be at two-phase equilibrium, however, hydrate formation could be limited by an absence of gas or by the presence of carbonate cements.

The structure and stability of hydrate is dependent upon the gas composition and flux (Sloan, 1998). Studies have suggested that free gas migrates laterally from ODP Site 1250 to Site 1249, intersecting Site 1249A at approximately 50 mbsf (Liu and Flemings, 2006), resulting in an absence of free gas below this depth. This limits the gas available to form hydrate either to that dissolved in the pore-water or to biogenically produced gas, which explains the lower hydrate saturations observed in this region.

At both study sites, the core was used to identify major lithological units throughout the well according to grain size distribution and the presence of biogenic material. At NGHP Site 01-10A, the core was also used to identify the presence of carbonate cements (Figure 11; Track 1), which frequently complicates the pore structure and decreases permeability (Lucia, 1983). From 0 – 90 mbsf, Zones 1 and 2, core recovery was 64.6 percent and carbonate occurrence was reported in 26.4 percent of the core. Between 90 – 160 mbsf, Zones 3 and 4, core recovery was 67.4 percent with reported carbonate occurrence in 66.1 percent of the core (NGHP Expedition 01 Scientists, 2007). The lower hydrate saturations in Zones 3 could be related to the increased presence of carbonate cements. Either the decreased permeability is reducing the gas saturation and limiting hydrate formation, or it is increasing capillary effects, which decrease hydrate stability (Clennell et al., 1999; Liu and Flemings, 2011) and the three-phase salinity.

Resistivity anisotropy from hydrate-filled fractures

Both of the study sites have been associated with the presence of high-angle, hydrate-filled fractures (Cook et al., 2010; Lee and Collett, 2009; Weinberger and Brown, 2006). It has been suggested that these fractures create an anisotropic medium that could result in overestimates of hydrate saturation, when using isotropic petrophysical methods (Kennedy and Herrick, 2003; Lee and Collett, 2009). In isotropic media, the measured resistivity is the same regardless of the direction in which the measurement is taken. In the presence of alternating layers of materials with distinctly different resistivities, however, the measured resistivity perpendicular ($R_{\perp}$) to the layers tends to be far greater than the resistivity parallel ($R_{\parallel}$) to the layers (Cook et al., 2012; Kennedy and Herrick, 2003). With an isotropic model, this increase in resistivity is attributed to greater hydrate saturation, despite the fact that hydrate-filled fractures contribute little additional hydrate saturation to the sediment. We critically evaluate the distribution and character of the fracture network at each study site to determine if fractures are affecting our results.

Hydrate-filled fractures are identified from recovered core samples and from the Resistivity-At-Bit (RAB) images and the propagation resistivity data collected during LWD acquisition. In the core samples, curators observe concentrated hydrate in fractures and identify the massive presence of hydrate using thermal infrared imaging to detect negative thermal anomalies (NGHP Expedition 01 Scientists, 2007; Shipboard Scientific Party, 2003). The RAB imaging system records the resistivity of the borehole wall in all directions, creating a three-dimensional look at how resistivity changes across the borehole. Hydrate-filled fractures appear as sinusoidal layers with high resistivity, because the fracture intersects the borehole wall at two different depths along the strike orientation. The dip of the fracture (ϑ) can be calculated from the borehole diameter (D) and amplitude of the fracture (A) on the RAB image (Weinberger and Brown, 2006):

$$\theta = tan^{-1}\left(\frac{A}{D}\right). \quad \text{Eq 28}$$

The propagation resistivity tool records the phase-shift and attenuation resistivity at two frequencies and three source-receiver spacings and has been used to infer information about $R_{\parallel}$ and $R_{\perp}$ in the borehole (Ellis and Singer, 2007). Fractures are identified in the phase-shift propagation resistivity data from separation between the resistivity curves, caused by increasing resistivity at greater depths of investigation. Greater separation between the propagation resistivity curves indicates more anisotropic conditions, potentially due to the presence of fractures (Cook et al., 2010). This tool is not only used to identify the presence of fractures, but also provides a qualitative assessment of the degree to which anisotropy is affecting the bulk resistivity measurement.

At ODP Site 1249A, fractures were only identified through the core samples and RAB imaging data; interpretation of these data is limited to the scientific reports. Using the infrared scanner, hydrate was identified in 49 core samples taken from Site 1249F. Only eight of those samples, starting at 47 mbsf,

were associated with hydrate in veins or fractures. In the RAB image, the highest concentration of hydrate is between 24 – 50 mbsf, where 20 fractures identified within this region (Shipboard Scientific Party, 2003). This information indicates that the fractures are likely creating anisotropy in the sediment that is causing an increase in resistivity. The resistivity of the sediment, however, is similar to that of the fractures, which diminishes the effects of anisotropy. Therefore, between 24 – 50 mbsf, the bulk resistivity is less affected by the presence of hydrate-filled fractures and using an isotropic model could still be acceptable.

At NGHP Site 01-10A, the infrared scanner identified large amounts of hydrate distributed throughout the well, though none of these occurrences were associated with fractures. The RAB image revealed the presence of hydrate-filled fractures concentrated between 90 – 124 mbsf, with sporadic fractures in other regions of the well (Cook et al., 2010; NGHP Expedition 01 Scientists, 2007). The phase-shift propagation resistivity curves (Figure 11; Track 2) show separation in Zones 1, 3, and 4, with concentrated separation in Zone 3. This indicates the presence of resistive fractures in these regions, supports the results from the RAB image, and suggests that Zone 2 can be considered isotropic.

Cook, et al. (2010) used a one-dimensional forward fracture model to predict the bulk hydrate saturation at three depths, incorporating the effects of resistivity anisotropy. Two of the saturations predicted from this model correlated well with our Archie-calculated saturations (Figure 11; Track 3), suggesting that Archie's law could be valid in anisotropic conditions (Lee and Collett, 2009). These results suggest that the hydrate saturation and salinity we calculated in Zones 2 and 4 accurately represent the in-situ conditions and that, although the conditions at Zones 1 and 3 are affected by anisotropy, the in-situ conditions are well represented using Archie's Law.

Conclusions

We present the in-situ hydrate saturation and salinity at four hydrate-bearing sites, calculated using an iterative application of Archie's Law and a salinity correction. We calculate the salinity required for three-phase equilibrium at the in-situ pressure and temperature using a thermodynamic model. We compare the in-situ salinity to the three-phase salinity at each site to determine the thermodynamic state throughout the GHSZ. We conclude that:

- ODP Site 1249A and NGHP Site 01-10A both contain thick regions within the GHSZ where the in-situ pressure, temperature, and salinity conditions suggests that the system is at three-phase equilibrium.
- Mallik Site 5L-38 has a small region near the base of the GHSZ where the in-situ conditions may result in three-phase equilibrium.
- IODP Site U1328A has elevated in-situ salinities near the top of the GHSZ, but the values are not greater enough to reach the three-phase boundary, indicating that this site is not at three-phase equilibrium. This concentration of hydrate near the seafloor is likely a result of the sedimentation and dissolved methane advection rates (Malinverno et al., 2008).

- At ODP Site 1249A, the interpreted three-phase region from 15 – 50 mbsf is associated with hydrate-filled fractures. Between 24-50 mbsf, however, there is little difference between the resistivity of the fractures and matrix, which reduces the effect of anisotropy on the resistivity measurement.
- At NGHP Site 01-10A, the propagation resistivity curve indicates that Zone 2, interpreted to be at three-phase equilibrium, is not associated with resistivity anisotropy, suggesting that the use of Archie's Law here accurately calculates water saturation. We believe that this is due to both a lower occurrence of hydrate-filled fractures, as well as a lower discrepancy between the fracture and matrix resistivities within this region.
- Within Zones 3 and 4, at NGHP Site 01-10A, the presence of carbonate cement could be limiting the formation of hydrate and, therefore, the development of elevated in-situ salinities.
- At NGHP Site 01-10A, although there are fractures present, our saturations correlate well with those from pressure cores and forward fracture models, indicating that the Archie parameters used are attributing for some anisotropic effects.

2.4. Task 4 - Laboratory Evaluation of Hydrate Dissociation (Complete)

Milestone 1.E Demonstrate ability to create and dissociate methane hydrate within sediment columns under conditions analogous to natural systems.

A. Goal:

The Recipient shall observe dissociation behavior in high-hydrate-saturation deposits like those resulting from cooling of Arctic gas reservoirs. To create the hydrate, the Recipient shall use the technique developed at Lawrence Berkeley National Lab by the PIs for moving the base of gas hydrate stability down through a sediment-packed column containing gas and brine. The temperature control scheme shall be adapted to cause the hydrate to start dissociating either at the top or the bottom of the column, which will result in different behavior of the system because of different gas transport pathways relative to the hydrate stability zone.

Subtask 4.1 - Freezing to 3 phase stability conditions, followed by melting from above

The Recipient shall fill the experimental vessel with coarse sand, or with alternating layers of coarse and very fine sand to provide capillarity and permeability contrast, and then X-ray CT scan the vessel. The vessel shall then be saturated with seawater and re-scanned. Temperature control for gas-brine stability (no hydrate) shall be established. Gas shall be introduced into the top of the vessel through a mass flow controller. Seawater shall be slowly withdrawn out the bottom using a high-pressure syringe pump. A scan of P-wave velocity along the column combined with an overall mass balance on each phase permits estimating the initial saturation profile in the column. The temperature control, through a set of individual cooling jackets distributed along the outside of the column shall then be activated so that successive sections of the column become "cool", starting from the top section. In this fashion the base

of gas hydrate stability is caused to move at a prescribed rate (ca. 10 to 100 cm/day) down the column. Hydrate formation will increase salinity such that three-phase equilibrium occurs throughout the column, with the "cool" temperature selected to insure that concentrated (approximately 2x) brine remains. Temperatures, pressures, and resistances shall be recorded frequently (~ every 30 sec) and ultrasonic (P wave) velocities shall be collected by hand regularly (~daily). The column shall remain connected to an external reservoir of brine and gas that allows gas to leave the column (in response to pressure elevation) and brine to enter the column (to replace fluid phase volumes consumed by hydrate). The mass of fluid in the external reservoir shall be recorded continuously. This data combined with pressure and temperature measurement enable quantification of all fluid movement into/out of the column. The resistances shall be interpreted for the salinity distribution; the P wave velocities shall be interpreted to help understand three–phase saturations; the temperature and pressure shall be interpreted for the locus of three-phase equilibrium in the column and for fluid phase transport. The variation in salinity distribution over time in all the cooled sections shall be closely monitored to assess whether diffusive transport is significant.

Once the entire column is equilibrated at the three-phase stability condition, the vessel shall be rescanned using CT. The temperature control shall then be programmed to raise the temperature at the top of the column slightly above the three-phase stability threshold. When dissociation is underway, as indicated by pressure and temperature changes, the temperature shall be increased in the next uppermost section of the sand column. This process shall be repeated until dissociation is complete. Gas mass flow, temperatures, pressures and P-wave velocities shall be recorded over the dissociation and analyzed to infer hydrate location and phase saturations.

Subtask 4.2 - Freezing to L+H condition, warming from above

The Recipient shall perform an experiment analogous to that in Task 4.1 to examine the case where gas hydrate is more stable above the base of the gas hydrate stability zone (BGHSZ), with additional cooling applied in the central region of the vessel to increase stability there. Warming from above (akin to a downward moving thermal pulse), shall be performed and results compared with the results from subtask 4.1 using models developed in Task 2.

Subtask 4.3 - Freezing to L+H condition, warming from below

Similar to Subtask 4.2, the Recipient shall form hydrate in their apparatus to the liquid-brine region (L+H) in the central region. Dissociation shall be induced by warming from below simulating dissociation at the BGHSZ from a slowly downward moving or wide thermal pulse. Results from this task shall be compared to results from Subtasks 4.1 and 4.2 using the models developed in Task 2.

B. Activities Phase 1:

We successfully simulated the formation and dissociation of methane hydrate including the effect of salinity. We successfully demonstrated our ability to experimentally simulate 3-phase equilibrium and we showed how cooling impacted the amount of hydrate that could be formed. Our laboratory results are well-matched by our simulation results. We extended this study to form methane hydrates in a meter-long cell and then have this cell undergo warming both from above and from below.

Experimental setup

The experimental chamber consisted of three primary components: sample holder, temperature control, and plumbing and sensing. The sample holder (Figure 29) consists of an aluminum X-ray transparent pressure vessel, two stainless steel end plugs with multiple high-pressure feed-throughs, and an EPDM sleeve attached to two PVC endcaps.

Methane gas (99+%, Praxair) was fed to the sample and pressure was maintained using a Teledyne-Isco (Lincoln, NE) 500D syringe pump running in the constant pressure mode (Figure 29). The volume of gas in the pump was recorded manually. A second Teledyne Isco 500D syringe pump was connected by way of a valve to the downstream end of the sample (Figure 29). This valve was maintained in closed position throughout the test except for one time when a gas connectivity test was performed. Plumbed into the upstream pore fluid line was a 1 L steel sampling bottle containing additional methane gas (Figure 29). This additional methane gas was present for pump refilling if necessary. Pressure was monitored using outputs on the pumps, as well as a Wika S-10 pressure transducer calibrated to an Omega Engineering PCL342 pressure calibrator.

Temperature was measured at a number of locations using thermocouples (Omega Engineering, Stamford, CT). A type J thermocouple was inserted into the sample (T_{in}), and a type T thermocouple was attached to the outside of the sleeve containing the sample (T_{out}), both of which were at the same distance from the downstream end of the sample (Figure 29). A type T thermocouple was used to monitor the tubing temperature, and another was attached to a steel sampling bottle near the syringe pumps to provide an accurate estimate of the gas temperature inside the syringe pumps. Temperature and pressure were recorded every 20 seconds throughout the test using a Keithley 2701 digital multimeter and recorded to a computer. All thermocouples were compared to melting ice, and the temperature indications are corrected using the difference between the indicated temperature and 0 ^{o}C.

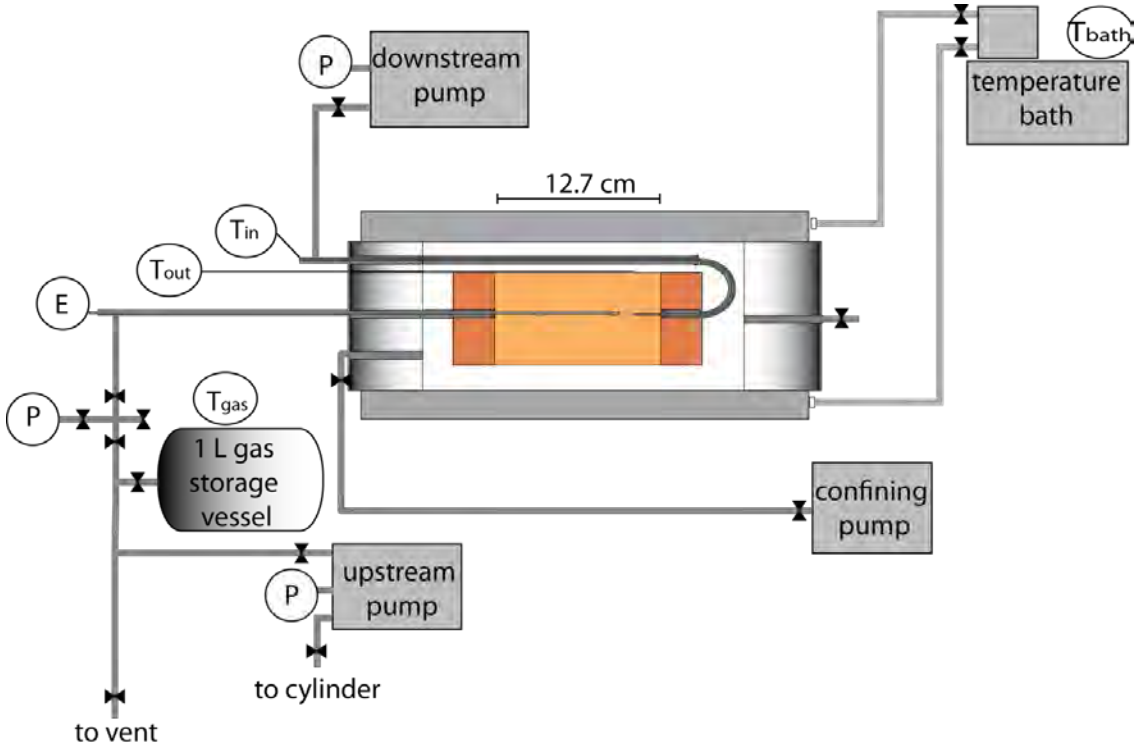

Figure 29: Sketch of experimental setup. P refers to pressure transducer. T_{in}, T_{out} and T_{gas} are thermocouples. T_{out} is placed on the EPDM sleeve, which measures the temperature on the outer radius of the nearly cylindrical sample. T_{in} is placed in the center of the sample. T_{in} and T_{out} are at the same distance from the downstream side of the sample. T_{gas} measures the temperature of the gas in the pumps. E refers to two electrodes measuring the bulk resistivity of the sample.

(a)

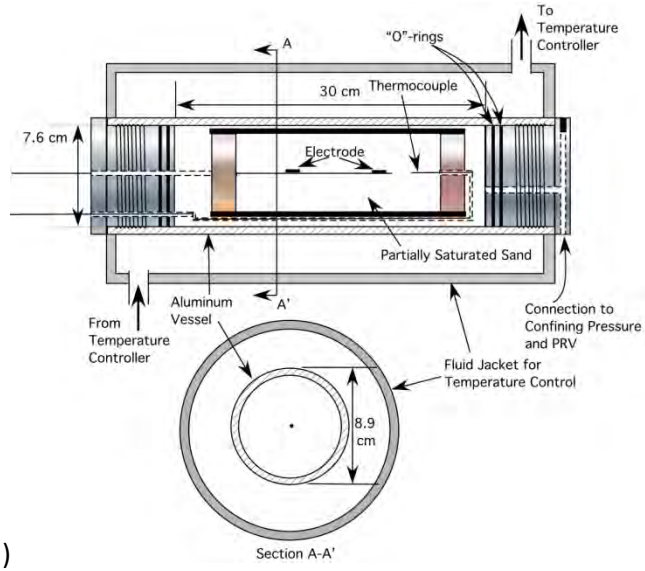

(b)

(c)

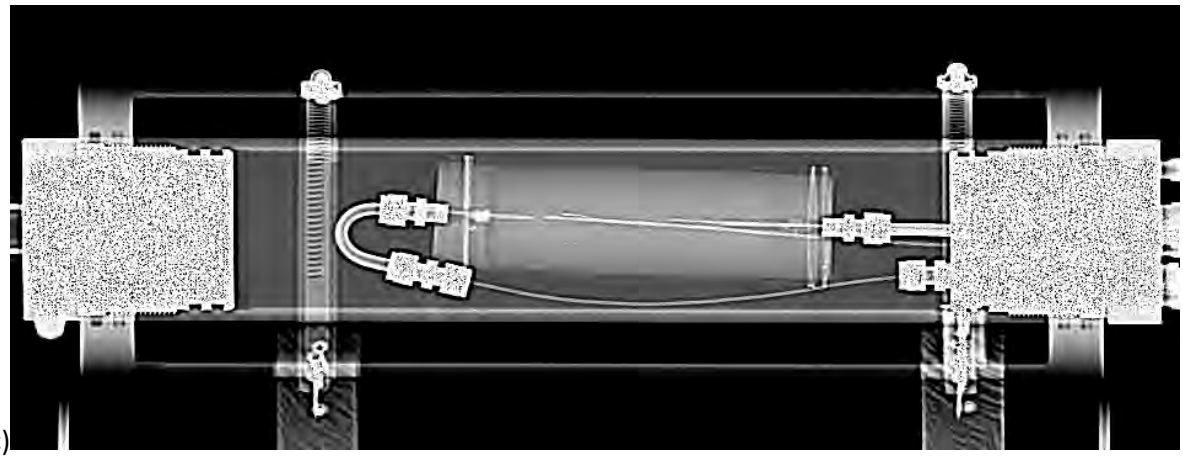

Figure 30: The detailed sketch (a), photograph (b) and X-ray image (c) of the core. The nearly cylindrical sample has a length of 12.7 cm and diameter of 5.1 cm. The two electrodes are about 3.8 cm from the upstream and downstream ends of the core, respectively. In the X-ray image lighter shade means higher density while darker shade means lower density.

The electrical resistivity probes consisted of two 0.8 mm in diameter (o.d.), 0.8 cm long silver-silver chloride electrodes (In Vivo Metrics, Healdsburg, CA) separated by 5 cm (Figure 30). The silver-silver chloride electrodes were attached to an electrically resistive garolite rod using adhesive-lined heat-shrink tubing (Figure 30). Each electrode was connected to a 0.2 mm enamel-coated copper wire, which was potted in epoxy inside a 1.6 mm diameter stainless steel tube. Prior to packing the sample, we calibrated the electrodes (resistivity array) in a series of potassium chloride solutions (Hodgman, 1960). Impedance between the electrodes was measured using a QuadTech 7400B Precision LCR meter. Both impedance and phase angle were recorded when desired over the frequency range from10 Hz to 100 kHz.

CT scanning was performed using a modified General Electric Lightspeed 16 medical CT scanner. Scans were performed at critical junctures during the experiment, and intermittently for monitoring. Scanning was performed at 120kV and 160 mA, with 0.195 x 0.195 x 0.625 voxel size. Data was analyzed using modified relations from Seol and Kneafsey (2011).

Sample preparation

The sediment used in this experiment was composed of F-110 sand, 99.99% silica sand from U.S. Silica. This silica sand consisted of rounded to subangular grains with a D_{50} of about 110 microns. Prior to the experiment the sand was rinsed with deionized water and allowed to dry under blowing air for 48 hours. We then weighed the sand and placed it in a sealed bag. With the sand grain density of 2.65 g mL^{-1} and target porosity of 36%, we calculated the mass of water needed to achieve a saturation of 55%. Prior to adding the water, we added reagent grade NaCl to the water to achieve a 3.5 wt. % brine solution. We added the brine solution to the sand stepwise, sealed the bag, and kneaded the sand to thoroughly mix the constituents. We allowed the sand to rest overnight to ensure equal distribution of the brine solution.

To pack the sample, a sleeve was attached to the bottom PVC endcap using a double-wrap of wire. A hollow 6 mm o.d. tube was placed over the resistivity probe to protect it. This tube was sequentially raised as the sand was packed. Sand packing was performed by measuring the mass of sand-brine mixture, adding the mixture two teaspoons at a time, and tamping each layer (~ 0.5 cm) approximately 100 times using a 1.2 cm o.d. aluminum rod, rotating the sample frequently to avoid overpacking one side. When the sample was packed to the desired level, the mass of sand and brine in the bag was again weighed, the opposing PVC endcap (the downstream side) containing a Type J thermocouple (T22) was inserted into the sample, and attached using a double wrap of wire. A CT cross section of the sample is shown in Figure 30.

Experimental procedures

At room temperature, we pressurized the confining fluid (a mixture of propylene glycol and water) to 8.27 MPa and the pore pressure to 6.94 MPa and then held the sample under these conditions for 60

hours. This allowed ample time for methane to dissolve into the brine to equilibrium solubility. During this time, we also collected baseline measurements of resistivity and CT images.

During the experiment we cooled the vessel slowly and step-wise to form hydrate and then warmed the vessel similarly to disassociate any hydrate present (red line, Figure 2). Immediately prior to the onset of cooling we closed the valve to the downstream pump. We supplied methane to the sample through the upstream valve so that gas was free to flow into/out the sample at constant pressure in response to the volume changes associated with methane hydrate formation and dissociation in the sample. We successively decreased the temperature in the sample from room temperature (17 ^{o}C) to 12, 10, 8.0, 6.0, 4.0, 2.0 and 0.5 ^{o}C over a period of 15 days (Figure 2). After each temperature change, we waited from one to seven days for the system to reach equilibrium such that neither temperature, pressure, or gas consumption (after leak rate correction) changed.

We equilibrated the sample for four days at the lowest temperature and on Day 19 of the experiment we began to increase the temperature. We successively increased the sample temperature from 0.5 ^{o}C back to 2, 4.0, 6.0, 8.0, 9, 10, 12 ^{o}C and to room temperature (Figure 2). After each temperature change, we found that it only took about 1 day for the system to reach equilibrium (no further change in pressure, temperature, or gas consumption).

In addition to hydrate formation and dissociation, volume change in the upstream pump can be caused by temperature fluctuation, pressure change, and leakage. Analysis of the volume change in the upstream pump allowed us to identify and remediate a leak early in the experiment, however another small leak persisted. The unexpected volume consumptions shown over the first 3 days of the test when the sample was outside the hydrate stability region result largely from laboratory temperature swings which were controlled over the remaining duration of the experiment. There were 16.27 mL less gas in the upstream pump at the end of the experiment (Day 28) than there was at Day 3 although the temperatures and pressure were the same. The average leakage rate was estimated by dividing 16.27 mL by the time elapsed (24.67 days) resulting in a value of 0.66 mL day^{-1}.

We collected several baseline CT images. At the end of the experiment, the sample was saturated with brine by flushing 20 pore volumes of brine with salinity of 3.5 wt.% and CT-scanned. It was then saturated with fresh water by flushing 20 pore volumes of tap water and CT-scanned. It was flushed with three pore volumes of methanol and several days of dry nitrogen gas to dry the sample and CT-scanned at the dry condition.

Experimental results

As the temperature decreased from room temperature to 10, 8, 6 and 4^{o}C (0-7 days, red circles, Figure 2), the measured methane gas consumption slightly increased (0-7 days, black boxes, Figure 2); the gas consumption was 0.2 g, which exactly equaled the gas mass decrease caused by the temperature decline in the sample and room temperature fluctuation (0.2 g) (green line). When the temperature was decreased from 4 to 2 ^{o}C, the accumulated methane gas consumption increased dramatically: 1.7 g of gas was consumed over 7 hours and then 2.1 g of gas was consumed over the next 16 hours. Then over a period of 6 days, more methane was gradually consumed by the system (0.8 g). The final temperature decrease, from 2 to 0.5 ^{o}C resulted in an immediate increase in methane gas consumption to 5.0 g. No further change is observed over 4.5 days.

On Day 19, we began to increase the temperature from 0.5 to 2, 4, 6, 8, 9, 10 and 12°C over a period of 8 days. Methane gas was produced by the dissociating hydrate resulting in gas release (Figure 2). Gas was produced rapidly with each temperature increase. It took about 4 hours for the temperature to increase from one value to the new temperature and the same amount of time for methane gas consumption to decrease. No further gas consumption decrease was detected over one day. Almost 50% of the methane hydrate dissociated when the temperature was increased from 6 to 8 °C on Day 22. The methane consumption (corrected) returned to the original value at the last temperature increase from 8 to 9°C.

The average bulk densities between 10 mm and 105 mm along the sample axis were 1.898, 2.028, 2.020 and1.750 g $cm^{-3}$from our collected baseline CT images at initial, brine-saturated, fresh water-saturated and dry conditions, respectively. We averaged the data only between 10 and 105mm for the following reasons. First, the packing was different at downstream end (left end) because inserting the end cap inevitably disturbed the sample there (0-10 mm, packing was conducted from upstream end to downstream end); second, sand flowed out of the sample during the brine and water floods at the end of the test, thus some parameters cannot be directly computed over this length at the upstream end (105-127 mm, right end). The grain density, density of brine with 3.5 wt.% salinity and water density are 2.65, 1.030 and 1.002 g cm^{-3} at pressure of 6.94 MPa and temperature of 17 °C, respectively. Gas density is assumed to be 0.0 g cm^{-3} compared with other density values (about 0.053 g cm^{-3} for methane at 6.94 Mpa and 17 °C). Using these data and an initial water saturation of 51%, we compute the estimated porosity to be 35%, 34%, 38% and 38% at initial, dry, brine-saturated and water-saturated conditions, respectively. These estimated porosities were all close to the actual porosity of 35%.

Figure 31(a) shows differential CT images (image at the initial condition subtracted from the image at later times) during methane hydrate formation and dissociation. Information about these images is listed in Table 2. The downstream end of the sample (left side) was closed during the experiment, and the coolant entered the cooling jacket from the downstream side (left side, Figure 31). As the sample was cooled to about 2 °C, the CT images recorded a density increase (red) in the left half of the sample and a density decrease (blue) in the right half (Figure 31). In addition, there was a gradual shift of the area of the density increase, which became more focused on the left side and along the central axis of the sample (images 3-7, Figure 31 (a)). As temperature was increased, the zone of increased density (left) decreased in density, and there was a small increase in density in the low density zone on the right (images 8-10, Figure 31 (a)).

The average density change from the initial condition of each of the 204 slices (0.625 mm in thickness) for a single scan is plotted in Figure 31 (b). As methane hydrate started to form after Day 7.4, the bulk density on the left side increased while that on the right side decreased. The zone with increased density gradually condensed toward the middle of the left half sample with greater density increase from Day 8.7 to Day 15.4, and also towards the sample axis (Figure 31 (b)). From Day 19.4 to Day 25.4, the temperature was stepwise increased and the bulk density change gradually returned to about zero across the sample.

Using the method described in Seol and Kneafsey (2011), we calculated an initial water saturation of 53%. This is close to saturation that was experimentally prepared (51%).We used this approach to calculate the saturations from the CT data (Figure 32). On Day 5.5 and 7.4, the hydrate saturation was zero, and the water and gas saturations were relatively uniform across the sample. As hydrate formed, its saturation increased to more than 50% on the left side whereas it increased to only about 40% on the right side (Day 8.7 to 19.4 in Figure 32 (a)). The water saturation decreased across the sample; however, the decrease was greater in the right half than the left half (Figure 32 (b)). The gas saturation decreased

to almost half of the initial value in the left half sample, while it slightly increased in the right side (Figure 32 (c)).

The saturation diagrams illustrate that the bulk density increased in the left half of the sample (Figure 31) because hydrate formed in some fraction of the pore space that was originally gas filled (Figure 32). In contrast, the density on the right side decreased (Figure 31) because as hydrate formed, brine migrated to the left side.As the sample temperature was increased, the phase saturations gradually returned to the initial distributions (Figure 31).

Electrical resistivity data are presented in Figure 33. Bulk resistivity measured with different AC frequencies had the similar trends. When frequencies were greater than 120 Hz, bulk resistivity increased with frequency. Bulk resistivity measured with frequencies no larger than 120 Hz were similar to each other (Figure 33). We divided the experiment to four periods - Period 1 (Day 0 to Day 7.4), 2 (Day 7.4 to Day 14.4), 3 (Day 14.4 to Day 19.4) and 4 (Day 19.4 to Day 27.4), respectively (Figure 33). Bulk resistivity measured with 10 Hz started with a value of 2.8 Ωm and slightly increased with time in Period 1 (red line). As methane gas consumption dramatically increased from Day 7.4 (Period 2), resistivity immediately increased to the first peak value of 35 Ωm on Day 9.4 (red line). Resistivity then gradually declined to about 13.4 Ωm on Day 14.4 (red line), although the gas consumption kept increasing during this time. In Period 3, as temperature was further decreased to 0.5 ^{o}C and more gas was consumed in the sample, resistivity immediately increased to the second peak value of 16.4 Ωm within 3 hours on Day 14 (red line). Resistivity then slowly decreased again at 0.5 ^{o}C. Resistivity gradually decreased as temperature was increased and methane gas consumption decreased stepwise in Period 4. Resistivity quickly increased to a short-lived peak value on Day 22.4 when hydrate was melting. Resistivity did not return to the initial values, but remained slightly higher at the end of the experiment.

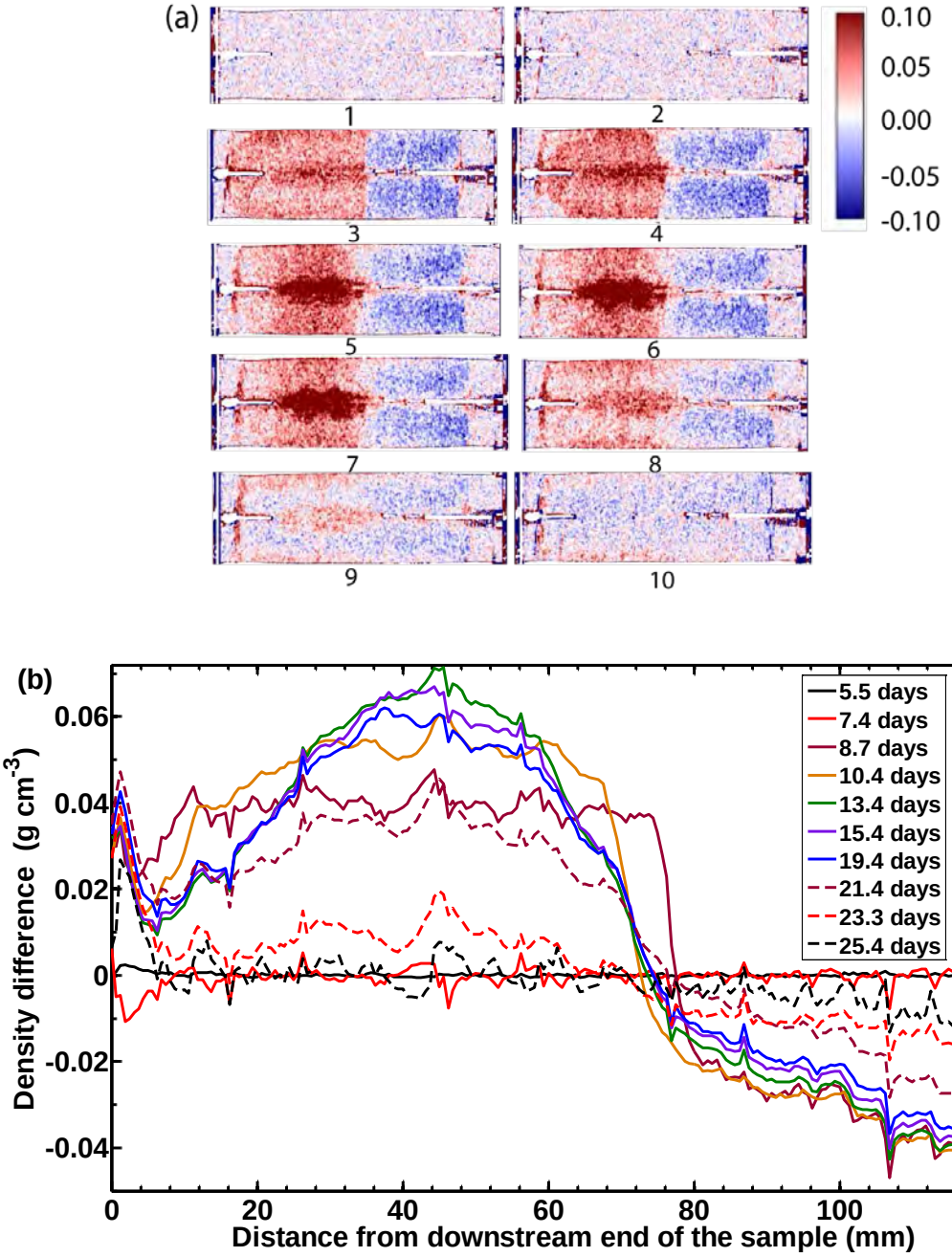

Figure 31: (a) Calibrated difference (image at time = 0 subtracted from image at later times) CT images of the sample at different times. The red color means density increases from the initial condition, while the blue color means density decreases from the initial condition. The unit for the scale is g cm-3. The left hand side of each image is the downstream side of the sample, which is closed during the experiment. The right hand side of each image is the upstream side. Table 2 shows the measurement time, sample temperatures and the accumulated methane gas consumptions for each image. (b) Bulk density change from the initial condition across the sample during methane hydrate formation and dissociation. Bulk density and density change are the average values of all the pixels in one 0.625 mm thick slice from each cross section perpendicular to the longitudinal axis of the sample.

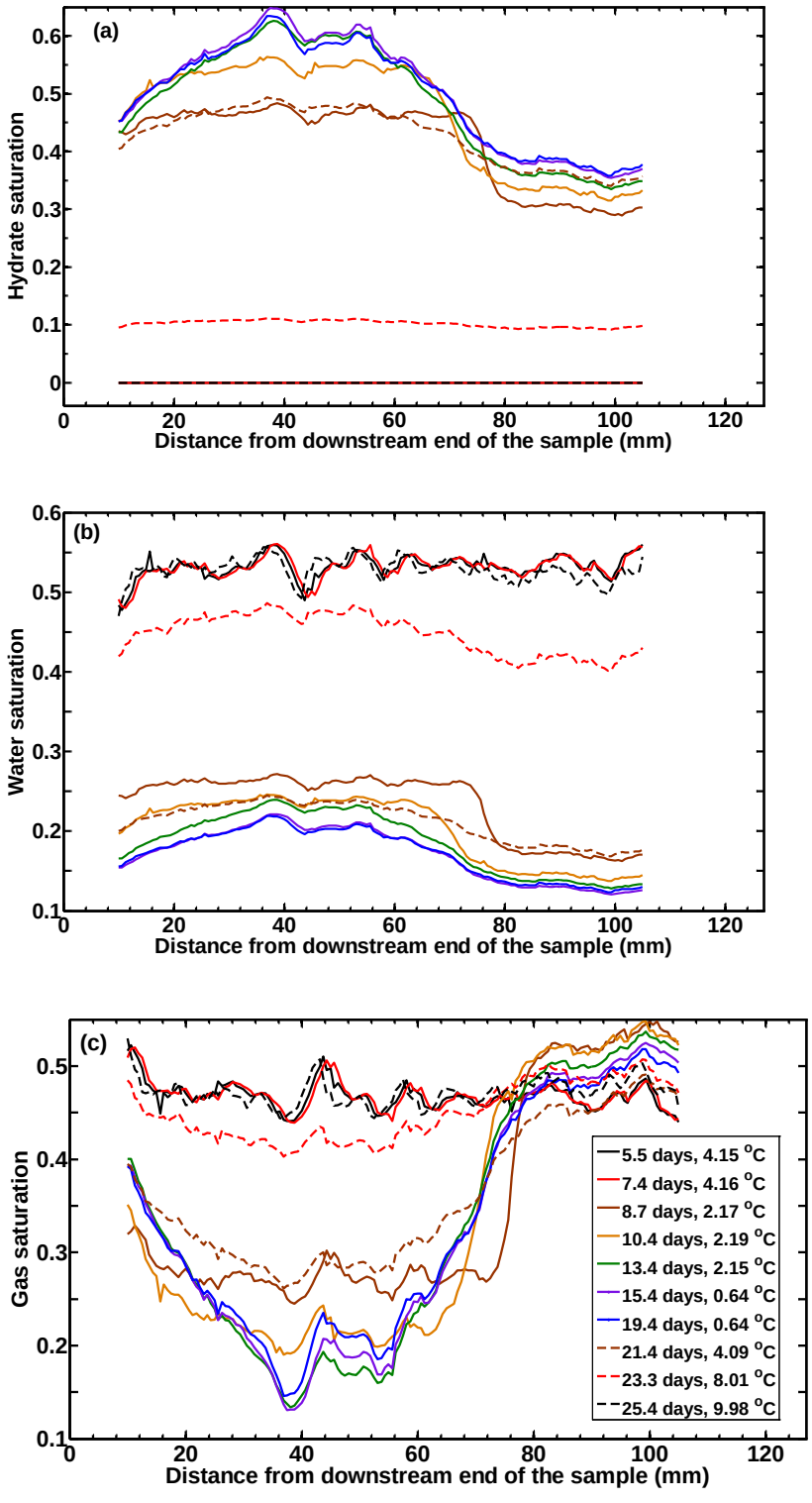

Figure 32: Calculated (a) hydrate, (b) water and (c) gas saturation distributions in the sample at different time using the CT data in Figs. 6 and 7(b). The saturations between 0 and 10 mm, and between 105 and 127 mm are

not included here. In Figure 32(a), the solid black, solid red and dashed black lines overlay each other with value of zero.

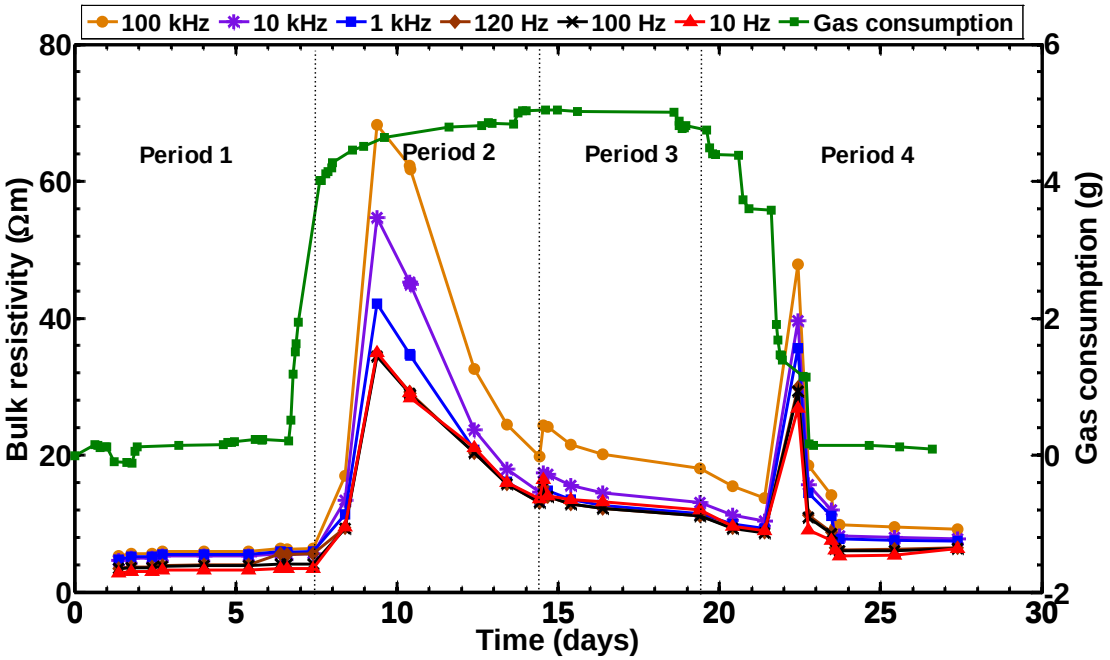

Figure 33: Bulk resistivity (red line) changes during methane hydrate formation and dissociation. The bulk resistivity are measured by two electrodes which are separated by 5.1 cm and are 3.8 cm from the upstream and downstream ends of the sample, respectively.

Number on Montage	Time (days)	Sample temperature T2 (°C)	Accumulated methane gas consumption (g)
1	6.4	4.13	0.2
2	7.4	4.16	0.2
3	8.7	2.17	4.3
4	10.4	2.19	4.6
5	13.4	2.15	4.8
6	15.4	0.64	5.0
7	19.4	0.64	5.0
8	21.4	4.09	4.4
9	23.3	8.01	1.2
10	25.4	9.98	0.1

Table 2: Measurement time, sample temperatures and accumulated methane gas consumptions for CT images in Figure 31(a).

Discussions of experimental results

Three-phase equilibrium behavior of hydrate system

The average pressure during this experiment was 6.94 MPa. As discussed before, methane hydrate is predicted to form at 8.4 ^{o}C at 6.94 MPa and salinity of 3.5 wt.%. However, as the temperature is decreased to 8, 6 and 4 ^{o}C in our experiment, the accumulated methane gas consumption only slightly increased due to room temperature fluctuations and temperature decrease in the sample. Methane hydrate started to form when the temperature was decreased to about 2 ^{o}C when the subcooling was 6.4 ^{o}C (Figure 2). The same subcooling effect has been observed in many previous experiments, e.g. Rees et al. (2011a), Seol and Kneafsey (2009), and Spangenberg et al. (2005). As discussed by Lederhos et al. (1996), when the temperature and pressure is within the hydrate forming region, water molecules will organize themselves around each methane molecule to form labile clusters upon the dissolution of methane in water. These labile clusters may either dissipate or combine to form unit cells. The unit cells may either grow or shrink stochastically. Catastrophic methane hydrate growth begins only after a critical radius is reached by the stochastic growth of unit cells. In an isobaric system, subcooling is the driving force for hydrate nucleation (Sloan, 1998). Hydrate nucleation is stochastic at low driving force. However, the system is less stochastic or more predictable at higher driving force (Sloan, 1998). The time from the moment when temperature is decreased to the hydrate stability zone to the initiation of hydrate nucleation is called induction time. The data of Yousif (1994) showed that induction time increased dramatically with the decrease of subcooling (e.g. induction time increased from about 20 minutes at the subcooling of 10 ^{o}C to more than 1000 minutes at the subcooling of 5 ^{o}C). From the entropy point of view, when methane hydrate forms, the disorderly associated gas and liquid phases transform to orderly hydrate crystals, while when methane hydrate dissociates, the orderly hydrate crystals change to disorderly gas and liquid. Entropy favors disorder over order. Therefore, during hydrate formation, there is a long, metastable period for re-arranging the disorderly gas and liquid into orderly hydrate crystals (Sloan, 1998) (Figure 2). However, methane hydrate melting usually happens rapidly once the system temperature and pressure is out of the hydrates stability zone (Sloan, 1998) (Figure 2). The kinetics of hydrate dissociation have been investigated by Moridis et al. (2005).

As methane hydrate started to form at 2 ^{o}C, the gas consumption or hydrate formation was very fast initially (3.8 g methane gas was consumed in 23 hours) and then became slow (0.8 g methane gas was consumed in 6 days, Figure 2). That is because as hydrate forms and salinity increases, the driving force (the difference between the current salinity and the equilibrium salinity at the current pressure and temperature) for further hydrate growth decreases (Sloan, 1998). Additionally, hydrate tends to form at the gas-water interface, thus pockets of water may be partially occluded from the gas. Hydrate ripening will likely change the occlusion over time, allowing more hydrate formation.

The predicted methane gas consumption at three-phase equilibrium is 4% higher than the measurements on Day 13.4 and 15.4 (Figure 2). The calculated hydrate saturations from the measured methane gas consumption (one volume of methane hydrate formation corresponds to about 2.13 volumes of methane gas consumption in this experiment, 47% on Day 13.4, and 49% on Day 15.4) are 2% less than the predicted ones at three-phase equilibrium on Day 13.4 and 15.4 (Figure 34). The most likely reason for the difference between the measured and predicted methane consumptions and hydrate saturations is that as methane hydrate forms, the pores of the sediment is blocked by methane hydrate, and brine with lower-than-equilibrium salinity is isolated from methane gas slowing or preventing further hydrate growth. The differences can also result from the uncertainty of the

thermodynamic model used in this study (e.g. the three-phase equilibrium temperatures predicted by Moridis (2008) are slightly lower than that predicted by the model used in this study) and differences between the assumed and unknown actual hydration number (e.g. hydration number is assumed to be 5.75 as used in Liu and Flemings (2007) and Seol and Kneafsey (2011). However, the measurement of Circone et al. (2005) gave an average hydrate stoichiometry of 5.99±0.07 along the three-phase equilibrium boundary). During hydrate dissociation, the difference between the measured and predicted methane gas consumptions decreases with increasing temperature (Figure 2).

The average hydrate saturation calculated from CT data on Day 13.4 and 15.4 are 48% and 50%, respectively (Figure 32(a)), which are very close to 47% and 49% calculated from measured methane gas consumption. The predicted gas saturations are slightly higher than the calculated values at those times, while the predicted water saturations are slightly lower than the calculated values at those times (Figure 4). The predicted bulk average salinity increases as hydrate forms and decreases as hydrate dissociates (Figure 4).

Our experiment was close to three-phase equilibrium at 2 and 0.5 ^{o}C during hydrate formation and entire hydrate dissociation. This conclusion is drawn from the following facts: first, the methane hydrate dissociated synchronously with temperature increase in our experiment (Figure 2); second, the predicted methane gas consumption and bulk hydrate saturation based on three-phase equilibrium were close the measurements or direct calculations from the measurements (Figures 2 and 4). Additionally, the presence of hydrate and gas, and forming additional hydrate from cooling beneath 2^{o}C confirms that all three phases were available at 2^{o}C. Previous studies have experimentally observed the effect of salinity in limiting hydrate formation (Husebø et al., 2009; Wright et al., 2005). However, the thermodynamic status of their hydrate systems was unexplored and not clear. To the best of our knowledge, this work is the first to clearly check the status of the hydrate system and demonstrate that the hydrate system is close to three-phase equilibrium constrained by pressure, temperature and salinity.

Mass transport during hydrate formation

As methane hydrate formed, the left half sample had higher hydrate saturation than the right half (Figure 32(a)). We attribute this to hydrate first nucleating there. This could have happened because coolant flowed from left to right resulting in a slight thermal gradient and slightly higher subcooling on the left side when temperature was decreased from 4 to 2 ^{o}C. This would induce two processes. First, salinity would increase in the left half relative to the right during hydrate growth due to earlier hydrate formation. Salt would tend to diffuse away from the left to the right promoting more hydrate formation in the left half sample at the early stage of hydrate formation. The effective salt diffusivity could be small due to hydrate formation; however, the salinity gradient could be great during earlier stage of hydrate growth. In addition, the system was kept at 2 and 0.5 ^{o}C for 7 and 5 days, respectively, to wait for equilibrium (and salt diffusion). Second, the pore size would be smaller in the left half sample than in the right due to the earlier hydrate growth in the left. Therefore, capillary pressure in the left side would be higher than the right side (gas pressure had the constant value of 6.94 MPa across the sample), which would draw in water with lower than equilibrium salinity from right side and provide more water for further hydrate formation in the left half. This core-scale migration of water induced by capillary pressure has also been observed by Kneafsey et al. (2007) and Rees et al. (2011a) in fresh water systems. Clennell et al. (1999) theoretically discussed the effect of salt diffusion and brine migration on hydrate formation.

Based on mass conservation of H_2O and NaCl and the calculated hydrate and water saturations (Figure 32), about 6.01 g H_2O and 0.50 g NaCl were estimated to migrate into the region 10-70 mm, and about 1.95 g H_2O was estimated to migrate out and 0.04 g NaCl migrate into the region 70-105 mm on Day 13.4 compared with the initial condition (Figure 32). In this calculation, we used a uniform salinity of 12.7 wt.% across the core (Three-phase equilibrium salinity on Day 13.4 should be 13.4 wt.%, and the calculated methane gas consumption is equal to the measured one if salinity is 12.7 wt.%. Since our experiment was close to three-phase equilibrium and pressure and temperature were the same across the core, the salinity should be relatively uniform across the core). The H_2O and NaCl mass change in the two regions 10-70 mm and 70-105 mm did not balance. That is because we did not calculate the H_2O and NaCl mass changes in regions of 0-10 mm and 105-127 mm (saturations were not calculated there as discussed in Section 3.4). Mass transport should happen and mass balance should be observed among these four regions (0-10 mm, 10-70 mm, 70-105 mm and 105-127 mm) instead of the two regions (10-70 mm and 70-105 mm). H_2O mass decrease and NaCl mass increase in the region of 70-105 mm indicated that during hydrate formation, two mechanisms of salt transport could happen: 1) salt advection with brine from 70-105 mm to 10-70 mm; 2) salt diffusion from 10-70 mm to 70-105 mm.

Bulk resistivity changes during hydrate formation and dissociation

The bulk resistivity in hydrate-bearing sediments is a complex function of water saturation, salinity, brine phase connectivity, hydrate morphology and temperature. In hydrate-bearing sediments, electric current transport is mainly conducted by free charge migration in brine (Na^+ and Cl^- here). As methane hydrate formed, the throats of pores are blocked, leading to poor brine connectivity and a fast increase in bulk resistivity (Figure 33). The resistivity gradually declined after the peak values in Period 2 and 3 (Figure 33). This behavior is different from previous studies, where the bulk resistivities of hydrate-bearing sediments reached nearly constant values after hydrate formation (Birkedal et al., 2011; Li et al., 2012; Li et al., 2010; Ren et al., 2010). This declining in bulk resistivity could be caused by the core-scale hydrate and salt redistribution. The methane hydrate saturation increased at the center of the left electrode side but slightly decreased in the surrounding area from image 4 to 5 in Figure 31(a), which were collected during resistivity declining period after the first peak value. This could also be caused by the pore-scale hydrate morphology change. The study by (Katsuki et al., 2007) showed that when methane hydrate formed at the subcooling of greater than 3.4 ^oC (subcooling was 6.4 ^oC in our experiment), the initial hydrate crystals had faceted ends and wavy surfaces. After some time, the wavy surfaces changed to smooth surfaces, and liquid water layers remained between the hydrate crystal and the silica surfaces of the channels. This morphology change led to better brine connectivity and would lead to declining bulk resistivity.

The bulk resistivity decreased with hydrate dissociation in Period 4 (Figure 33) because the brine connectivity became better. However, there was another peak in resistivity on Day 22 (Figure 33). This might be caused by the blockage of pores or poor contact between the electrodes and sediment because of the large amount of gas released from hydrate dissociation, which can be detected a significant decrease in accumulated methane gas consumption during the following day (Figure 33). The hydrate formation and dissociation could redistribute the salinity in the sample resulting in fresher water in the region of the electrodes and thus led to a slightly higher measured bulk resistivity on Day 28 when all the hydrate formed was dissociated (Figure 33).

2.5. Task 5: Gas Expulsion Modeling (Complete)

Milestone 2.A 1-D simulation of gas expulsion into hydrate stability zone.

Milestone 2.B Determination of conditions for which gas expulsion into hydrate-stability zone is self-limiting.

A. Goal:

The Recipient shall use the validated model of dynamics within a dissociating hydrate from Task 2 to drive a model of the transport of gas expelled upward from the hydrate - bearing sediment. The Recipient shall focus on a situation which is inevitable in several combinations of initial and boundary conditions: the gas rises into water - saturated sediment which is in the hydrate stability zone. The effect of latent heat of formation and of salinity shall be included in this model. The Recipient shall validate the models against laboratory experiments on methane migration at three phase stability, hydrate formation and hydrate dissociation.

The Recipient shall explore both the role of capillarity and the role of sediment fracturing in driving this migration. For example, under certain conditions the gas pressure shall exceed the least principle stress in the rock matrix and the flow will be driven along fractures. The Recipient shall explore the role of both these processes with a goal to bring all these considerations to bear on the question of gas migration during hydrate dissociation and gas migration.

B. Activities Phase 2:

B1. Subtask 5.1: Develop 1D model of gas expulsion into water-saturated hydrate-stability zone (Complete)

B1.1. Goal:

Based on results from Task 3.0, it is expected that under certain scenarios, gas pressures will elevate sufficiently enough to result in overcoming the capillary barrier of the overburden or to overcome the least principal stress and migrate by fractures. Therefore, the Recipient shall extend existing models of hydrate formation and gas propagation to account for the coupling between heat transport, salinity transport and gas phase pressure and shall include a mechanism to describe whether flow is through the matrix or via fractures. The extended model shall be applied to determine the conditions for which the gas expulsion is self-limiting, i.e. when growth of hydrate effectively creates a seal in the overlying sediment. The Recipient shall compute the conditions for which self-limiting gas expulsion is permanent, i.e. the temperature perturbation is insufficient to move the gas contained in the original accumulation all the way to seafloor or land surface. For other conditions, the delay in arrival of methane at the seafloor/atmosphere for conditions shall be computed.

B1.2. Activities Phase 2:

1D Numerical Expulsion Model

We have fully developed a 1D numerical model. We add a new phase, ice, into the model, which allows us to simulate the permafrost associated hydrate dynamics. To include the ice phase, we have to introduce a new model for the hydrate phase boundary, which is described as below.

The phase boundary for methane hydrate depends on water pressure (P_w), temperature (T) and salinity (X_l^s).In salt-free systems (Figure 34), it is described as (Moridis, 2008)

$$\ln(P_w) = a_1 + a_2 T + a_3 T^2 + a_4 T^3 + a_5 T^4 + a_6 T^5, \quad \text{Eq 29}$$

when temperature is greater than pure water freezing temperature (273.2 K or 0 °C). a_1, a_2, a_3, a_4, a_5 and a_6 are constants listed in Table 3. On this phase boundary, methane hydrate coexists with liquid water and methane gas (Figure 34). When temperature is lower than water freezing temperature, it is described as (Moridis, 2008)

$$\ln(P_w) = b_1 + b_2 T + b_3 T^2 + b_4 T^3 + b_5 T^4 + b_6 T^5. \quad \text{Eq 30}$$

b_1, b_2, b_3, b_4, b_5 and b_6 are constants listed in Table 3. On this phase boundary, methane hydrate coexists with ice and methane gas (Figure 34).

The phase boundary for water and ice depends on salinity (X^s_l) and temperature (T). The pressure effect is negligible under typical hydrate conditions (Sloan and Koh, 2007; Sun and Mohanty, 2006). In salt-free systems, the water freezing temperature or ice melting temperature is 273.2 K or 0 °C. Salinity shifts this phase boundary toward lower temperature (Figure 35). The water freezing temperature (T_w) in presence of sodium chloride (NaCl) is obtained from Lide (2004) as (Sun and Mohanty, 2006)

$$T_w = T_{w0} - X_l^s \left(164.49 X_l^s + 49.462\right), \quad \text{Eq 31}$$

T_{w0} is the pure water freezing temperature (273.2 K or 0 °C). X_l^s is the mass fraction of NaCl in liquid water phase. Eq. (31) is valid in the salinity range of 0 and 0.22 (mass fraction) (Sun and Mohanty, 2006).

Salinity also shifts the phase boundary of methane hydrate toward lower temperature (Figure 35). The depression of the hydration temperature (ΔT_h ,°C) in presence of salt is described as (Sloan and Koh, 2007; Sun and Mohanty, 2006)

$$\frac{\Delta T_h}{T_{h0}\left(T_{h0} - \Delta T_h\right)} = 0.6723 \frac{\Delta T_w}{T_{w0}\left(T_{w0} - \Delta T_w\right)}, \quad \text{Eq 32}$$

where T_{h0} is the hydration temperature in salt-free systems (°C) described in Eqs. (33) and (34). ΔT_w is the depression of water freezing temperature (°C) in presence of sodium chloride (NaCl), and (Sun and Mohanty, 2006)

$$\Delta T_w = X_l^s \left(164.49 X_l^s + 49.462\right). \quad \text{Eq 33}$$

In this model, we consider 11 equilibrium thermodynamic status in total (Table 4). If the sediment is initially filled with brine, the system thermodynamic status can never go to the left side of the ice-water

phase boundary (dashed lines in Figures 34 and 35). It is a reasonable assumption for typical permafrost and methane hydrate system, because solubility of NaCl is about 22 wt.% (Sun and Mohanty, 2006), which can shift the water freezing point to as low as -18.8 °C. If the sediment is initially filled with pure water or ice, the system can shift among the 11 thermodynamic status listed in Table 4 (Figure 34). Four independent primary variables are required for this three-component system (Liu and Flemings, 2007). Primary viables are switched according to the different thermodynamic status (Table 4).

Our work has led us to explore two additional models arguments: 1) An analytical approach to the 1D modeling and 2) A numerical approach to look at hydrate in fractures.

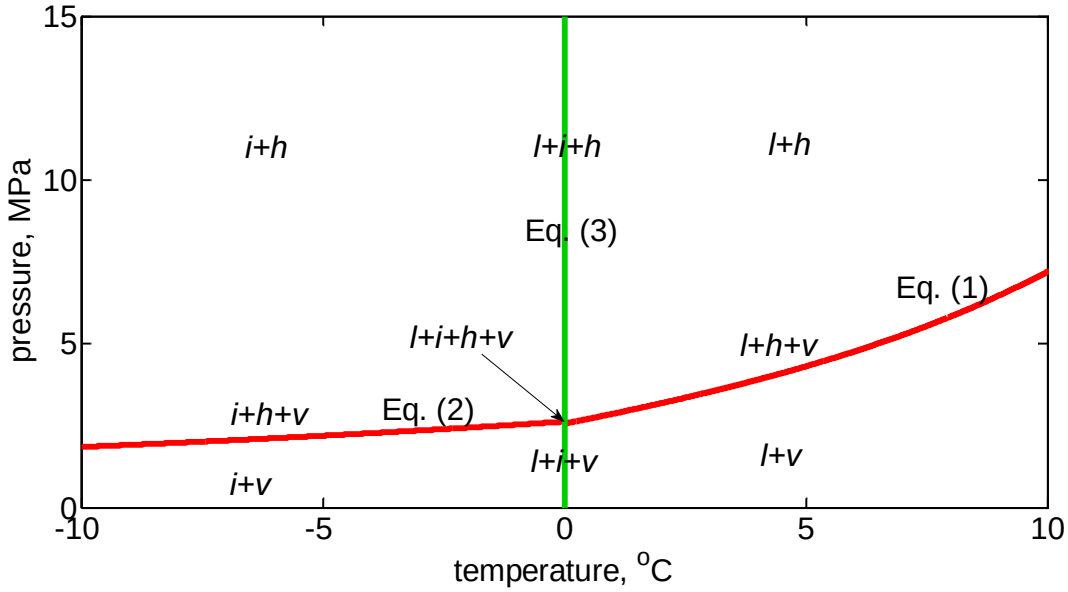

Figure 34: The pressure-temperature phase diagram of methane hydrate for salt-free systems. The red line is the phase boundary for methane hydrate and methane gas phases. The green line is the phase boundary for ice and liquid water phases. Three phases coexist on these phase boundaries. At the quadruple point, liquid water, ice, hydrate and gas phases coexist. h, i, l and v means hydrate, ice, liquid water and gas phases, respectively.

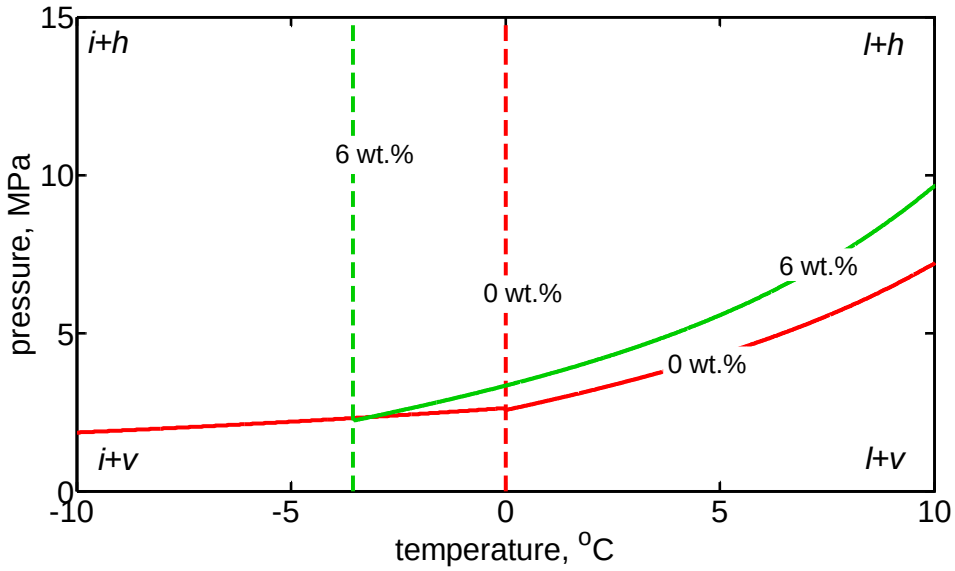

Figure 35: Shifts of phase boundaries with salinity. The solid lines are the phase boundaries for methane hydrate and methane gas phases. The dashed lines are the phase boundaries for ice and liquid water phases. The ice-hydrate-gas curve does not change with salinity.

Table 3: Constants used in Eqs. (29) and (30) [Moridis et al., 2008].

Constants	Values
a_1	-1.94138504464560e5
a_2	3.31018213397926e3
a_3	-2.25540264493806e1
a_4	7.67559117787059e-2
a_5	-1.30465829788791e-4
a_6	8.86065316687571e-8
b_1	-4.38921173434628e
b_2	7.76302133739303e-1
b_3	-7.27291427030502e-3
b_4	3.85413985900724e-5
b_5	-1.03669656828834e-7
b_6	1.09882180475307e-10

Table 4: Phase states, corresponding primary variables and additional constrains.

Phase state	Phase present	Primary variables	Supplementary constrains
1	l	$P_w,\ X_l^s,\ X_l^m,\ T$	S_l=1, S_i= S_v= S_h=0
2	l +v	$P_w,\ X_l^s,\ S_l,\ T$	S_v=1- S_l, S_i= S_h=0, $X_l^m = X_{l+v}^m$
3	l +h	$P_w,\ X_l^s,\ S_l,\ T$	S_h=1- S_l, S_i= S_v=0, $X_l^m = X_{l+h}^m$
4	i+ v	$P_w,\ X_l^s,\ S_i,\ T$	S_v=1- S_i, S_l= S_h=0, X_l^m =0
5	i + h	$P_w,\ X_l^s,\ S_i,\ T$	S_h=1- S_i, S_l= S_v=0, X_l^m =0
6	l + i	$P_w,\ X_l^m,\ S_l,\ T$	S_i=1- S_l, S_h= S_v=0, $X_l^s = X_{l+i}^s$
7	l + h + v	P_w, S_h, S_l, T	S_v=1- S_l- S_h, S_i =0, $X_l^m = X_{l+h+v}^m$, $X_l^s = X_{l+h+v}^s$
8	i + h + v	P_w, S_h, S_i, T	S_v=1- S_i- S_h, S_l =0, X_l^m =0, X_l^s =0
9	l + i + h	P_w, S_h, S_l, T	S_i=1- S_l- S_h, S_v =0, $X_l^m = X_{l+h}^m$, $X_l^s = X_{l+i}^s$
10	l + i + v	P_w, S_i, S_l, T	S_v=1- S_l- S_i, S_h =0, $X_l^m = X_{l+v}^m$, $X_l^s = X_{l+i}^s$
11	l + i + h + v	S_i, S_h, S_l, T	S_v=1- S_l- S_i - S_h, $X_l^m = X_{l+v+h}^m$, $X_l^s = X_{l+i}^s$, P_w=P_e

Note: in Table 4, $X_{\sum\beta}^{\kappa}$ is the mass fraction (or solubility) of component κ in liquid phase when phases $\sum\beta$ are in equilibrium (dimensionless). Pe is the quadruple point pressure (Pa).

1D Analytical Methods of Characteristics Expulsion Model

Mathematical models

We develop an analytical model using method of characteristics to describe the one-dimensional hydrate system development in this section. Figure 36 is a schematic diagram of the model. The sediment is initially fully saturated with brine of salinity cl_0. The sediment has a uniform temperature T_0 and a small pressure gradient with an average pressure of P_0. The initial system is in hydrate stability zone. Methane gas is injected with a fixed rate of q_{gi} and density of ρ_{gi} from the left end. Methane hydrate forms from the gas inlet and increases the local salinity to three-phase equilibrium value, when no more hydrate can form. Hydrate solidification front and gas front moves further into the sediment (rightward). We neglect the hydrate formation kinetics because hydrate formation is rapid as shown by

laboratory (Zatsepina and Buffett, 2003) and field (Rehder et al., 2002) studies. Therefore, gas saturation is zero at the downstream side of the hydrate solidification front (point *a* in Figure 36). It increases gradually from the hydrate solidification front to the gas inlet (Figure 36). We also neglect the diffusion transport.

This semi-infinite system contains three phases (subscript κ), gas (g), liquid water (l) and hydrate (h) phases, and three components (subscript β), brine with the three-phase equilibrium salinity (*B*), pure water (*W*) and methane (*M*).

The mass conservation equation for methane is

$$\frac{\partial G_M}{\partial \tau} + \frac{\partial H_M}{\partial \varepsilon} = 0, \qquad \text{Eq 34}$$

where τ is the dimensionless time; ε is the dimensionless distance from the gas inlet; G_M is the dimensionless overall concentration of methane; and H_M is the dimensionless overall flux of methane. These parameters are defined as

$$\tau = \frac{q_{gi} t}{L\phi}, \qquad \text{Eq 35}$$

$$\varepsilon = \frac{x}{L}, \qquad \text{Eq 36}$$

$$G_M = X_{M,l}\rho_{lD}S_l + X_{M,g}\rho_{gD}S_g + X_{M,h}\rho_{hD}S_h, \qquad \text{Eq 37}$$

$$H_M = v_D\left(X_{M,l}\rho_{lD}f_l + X_{M,g}\rho_{gD}f_g\right), \qquad \text{Eq 38}$$

where t is time (sec); L is characteristic length (m); ϕ is porosity of the sediment ($m^3\ m^{-3}$); $X_{M,l}$, $X_{M,g}$ and $X_{M,h}$ are the mass fraction of methane (dimensionless) in liquid water, gas and hydrate phases, respectively; ρ_{lD}, ρ_{gD} and ρ_{hD} are the dimensionless density of liquid water, gas and hydrate phases, respectively, and $\rho_{lD} = \frac{\rho_l}{\rho_{gi}}$, $\rho_{gD} = \frac{\rho_g}{\rho_{gi}}$, $\rho_{hD} = \frac{\rho_h}{\rho_{gi}}$; ρ_l, ρ_g and ρ_h are the density of liquid water, gas and hydrate phases (kg m^{-3}), respectively; S_l, S_g and S_h are the saturation of liquid water, gas and hydrate phases (dimensionless), respectively; v_D is the dimensionless total flux, and $v_D = v \big/ q_{gi}$; v is the total flux (m sec^{-1}) of the mobile phases; f_l and f_g are the fractional flow of liquid water and gas phases (dimensionless), respectively.

$$f_g = \frac{\lambda_g}{\lambda_g + \lambda_l}\left[1 + \frac{k\lambda_l}{v}\left(\frac{\partial P_c}{\partial x} + (\rho_l - \rho_g)g\sin\theta\right)\right], \quad \text{Eq 39}$$

$$f_l = 1 - f_g, \quad \text{Eq 40}$$

where λ_l and λ_g are the mobility ($Pa^{-1}\ sec^{-1}$) of gas and liquid water phases, respectively, and $\lambda_g = k_{rg}/\mu_g$, $\lambda_l = k_{rl}/\mu_l$; k_{rg} and k_{rl} are the gas and liquid water phase relative permeabilities (dimensionless), respectively; μ_g and μ_l are the gas and water dynamic viscosities (Pa sec), respectively; k is the intrinsic permeability of the sediment (m^2); g is the gravitational acceleration (m sec^{-2}); θ is the dip angle measured as the angle between the flow direction and a horizontal line (rad); P_c is the capillary pressure between the gas and liquid water phases (Pa). f_g can be broken into three components: a viscous component ($\frac{\lambda_g}{\lambda_g + \lambda_l}$), a capillary component ($\frac{\lambda_g}{\lambda_g + \lambda_l}\frac{k\lambda_l}{v}\frac{\partial P_c}{\partial S_g}\frac{\partial S_g}{\partial x}$) and a gravity component ($\frac{\lambda_g}{\lambda_g + \lambda_l}\frac{k\lambda_l}{v}(\rho_l - \rho_g)g\sin\theta$) (DiCarlo et al., 2012).

According to method of characteristics (Orr, 2007), the overall concentration of methane G_M does not change with time on the characteristic curve

$$\xi = \frac{\partial H_M}{\partial G_M}\tau + \varepsilon_0, \quad \text{Eq 41}$$

where ε_0 is the initial dimensionless position of the composition G_M. The same procedure can be applied to the component of pure water and brine with three-phase equilibrium salinity.

A leading shock develops at the hydrate solidification front where the system changes from three phases to one phase (Orr, 2007) (Figure 36). The shock wave velocity equals the composition wave velocity at *b* in Figure 36. Each component must have the same shock wave velocity. Therefore,

$$\Lambda_B^{ab} = \Lambda_W^{ab}, \quad \text{Eq 42}$$

$$\Lambda_B^{ab} = \Lambda_M^{ab}, \quad \text{Eq 43}$$

$$\Lambda_B^{ab} = \frac{\partial H_\beta}{\partial G_\beta}\Big|_b = v_D^b \frac{\partial f_g}{\partial S_g}\Big|_{S_g = S_g^b}, \quad \text{Eq 44}$$

where the superscripts *a* and *b* means the downstream and upstream side of the leading shock, respectively; Λ_β^{ab} is the dimensionless leading shock velocity calculated by the component β. It is also the dimensionless hydrate solidification front advancing velocity and is expressed as

$$\Lambda_\beta^{ab} = \frac{H_\beta^a - H_\beta^b}{G_\beta^a - G_\beta^b}, \quad \beta = B, W, M \,. \qquad \text{Eq 45}$$

If both the gravity and capillary components of the gas fractional flow f_g is neglected, we can obtain the hydrate (S_h), liquid water (S_l) and gas phase saturations (S_g) at *b* and the ratio of the flux between *a* and *b* (v_D^a / v_D^b) by solving the nonlinear equation group of Eqs. (34), (35) and (37)-(40). The trailing shock calculation provides the saturations at point *c* in Figure 36.

The total liquid water and gas phase flux between *c* and *b* is uniform and equals that at *c* or *b* because it is in the three-phase region and the phase compositions are fixed (Orr, 2007). Therefore, composition wave velocity between *c* and *b* can be calculated as (Orr, 2007)

$$\Lambda^e = v_D^c \frac{\partial f_g}{\partial S_g}\Big|_{S_g = S_g^e}, \qquad \text{Eq 46}$$

where S_g^e is an arbitrary gas saturation between *c* and *b* or between S_g^c and S_g^b; Λ^e is the dimensionless composition wave velocity for gas saturation of S_g^e. At the dimensionless time τ, the dimensionless distance between the place where gas saturation equals S_g^e and the gas inlet ξ^e is calculated as

$$\xi^e = \Lambda^e \tau \,. \qquad \text{Eq 47}$$

Hydrate saturation is homogeneous from *c* to *b* ($S_g^c = S_g^b$). That is because the system initial condition is nearly homogeneous and we neglect the salt diffusion. Hydrate and liquid water phase saturation at ξ^e (S_l^e) are

$$S_h^e = S_h^b, \qquad \text{Eq 48}$$

$$S_l^e = 1 - S_g^e - S_h^e \,. \qquad \text{Eq 49}$$

Example calculations

Figure 37 shows the characteristics of an example calculation with the parameters listed in Table 3. The saturations of each phase does not change along the characteristics (Figure 37). The characteristics for the initial composition (100% liquid water) emanate from $\tau = 0$ and have the slope of 5.9 (red lines in Figure 37). The characteristics for the injection composition (100% gas) emanates from $\tau = 0$ and along the $\xi = 0$ line (Figure 37). There is a trailing shock from the injection composition to the gas saturation of 28.5%, but it has zero wave velocity. Therefore, the fan of characteristics for the discontinuity initially present at the gas inlet extends all the way from the gas saturation of 10.7% to $\xi = 0$. Leading shock happens where the characteristic of gas saturation 10.7% intersects the initial composition (red lines in Figure 37). Any line in the characteristics figure that is parallel to the line of $\tau = 0$ provides the

saturation distribution along the column at a certain time. Any line that is parallel to the line of $\xi = 0$ provides the system composition evolution with time at a certain distance from the gas inlet (Figure 38).

The hydrate solidification front advancing velocity or the leading shock wave velocity is 0.63 cm hour^{-1}. The hydrate saturation is 68.4% behind the hydrate solidification front (Figure 38). The gas saturation continuously decreases from 28.5% (point *c*) to 10.7% (point *b*), and water saturation continuously increases from 3.1% (point *c*) to 20.9% (point *b*) (Figure 38). Hydrate formation at the hydrate solidification front causes total volume loss and decreases the total flux from 10^{-6} m sec^{-1} (point *b*, *c* and *d*) to 1.71×10^{-7} m sec^{-1} (point *a*).

Comparison with numerical models

Liu and Flemings (2007) developed a fully coupled multiphase multicomponent fluid flow and mass transport numerical model to simulate the methane hydrate formation and dissociation dynamics. We did two simulations to investigate the hydrate system development using this model with the same parameters listed in Table 3. The first one considers the capillary pressure (dashed lines in Figure 38), and the second one neglects the capillary pressure (dotted lines in Figure 38). Compared with these two numerical simulations, the hydrate saturation calculated by the analytical solution are lower while the gas saturation are higher (Figure 38). Hydrate solidification front calculated by the analytical solution moves a little faster than the numerical simulations (Figure 38). The analytical solution matches much better with the numerical simulation neglecting the capillary pressure effect (solid lines are more close to the dotted lines than to the dashed lines), because we did not include the capillary component in the fractional flow curve in this analytical simulation. The difference between the analytical and numerical results neglecting the capillary pressure close to the gas inlet is caused by the boundary effect in the numerical simulation. Their difference at the leading shock is caused by the fact that the numerical solution inevitably has numerical diffusion causing smearing of shocks.

Gravity effects

In the above discussions, we only consider viscous component of the fractional flow. The viscous component describes the gas flow induced by the gradient of water pressure deviation from the hydrostatic pressure (overpressure gradient). The gravity component describes the gas flow induced by the density difference between the gas and liquid phases (buoyancy). As gravity component is also included, we define the ratio of the vertically upward gas flow under buoyancy to that under overpressure gradient in absence of hydrate as gravity number (R_g , dimensionless) (Lake, 1989)

$$R_g = \frac{k_0 k_{rl}^*}{q_{tot}\mu_l}\left(\rho_l - \rho_g\right)g\,, \qquad \text{Eq 50}$$

where k_{rl}^* is the relative liquid permeability when the effective gas saturation reaches the residual value (S_{gr}).

Overpressure gradient dominates gas flow when gravity number R_g is much less than one:

$$R_g = \frac{k_0 k_{rl}^*}{v\mu_l}\left(\rho_l - \rho_g\right)g << 1. \quad \text{Eq 51}$$

This case is the similar with and the solution construction is the same with the case presented above where only the viscous component of the gas flow is included.

Buoyancy dominates upward gas flow when R_g is much greater than one:

$$R_g = \frac{k_0 k_{rl}^*}{q_{tot}\mu_l}\left(\rho_l - \rho_g\right)g >> 1. \quad \text{Eq 52}$$

The leading shock is no longer a semi-shock (Orr, 2007), as the semi-shock condition would lead to a landing point with a gas fractional flow greater than unity. Instead, the shock is directly to a gas fractional flow of unity. The hydrate saturation from point 'b' to 'c', the gas and liquid saturation at point 'b', and the ratio of the total flux between point 'a' and 'b' are obtained by solving the nonlinear equations ((37), (38), (40) and (48) (DiCarlo et al., 2012).

$$f_g\left(S_{gf}, S_h\right) = 1,\ k_{rw} \neq 0. \quad \text{Eq 53}$$

There is no longer a rare-faction between point 'b' and 'c'. Hydrate, gas and liquid saturations are all constant behind the shock. The gas volumetric flux is constant and equals gas injection rate, and the liquid volumetric flux is zero from point 'b' to 'c'. The water pressure equals the hydrostatic water pressure, overpressure equals zero, and gas migration is driven solely by buoyancy (England et al., 1987; Hubbert, 1953).

The dimensionless and dimensional advancing velocity of hydrate solidification front is calculated by Eq. (49a) and (49b), respectively.

$$v_{reaction}^D = \frac{H_\beta^b - H_\beta^a}{G_\beta^b - G_\beta^a}, \quad \beta = B, W, M, \quad \text{Eq 54}$$

$$v_{reaction} = \frac{q_{gi}}{\phi}\frac{H_\beta^b - H_\beta^a}{G_\beta^b - G_\beta^a}, \quad \beta = B, W, M. \quad \text{Eq 55}$$

Buoyancy dominates downward gas flow when Eq. (47) is true. The gas fractional flow f_g versus the saturation for downward flow decreases with gas saturation from zero, reaches a trough value less than zero, and then increases with gas saturation and gradually converges to one at high gas saturation. The solution is similar with and the solution construction is the same as the case when overpressure gradient dominates the gas flow. The only difference is that the fractional flow curve goes negative for certain saturations – these saturations are not observed in the solution because of the discontinuous changes in saturations at the shock.

For this discussion, we will concentrate on the results for a flow velocity of 10^{-9} $m^3\ m^{-2}\ s^{-1}$, combined with the other parameters listed in Table 3 results in a gravity number of R_g=464. We begin the discussion with the gas saturation behind the hydrate solidification front. Gas saturations are quite different for horizontal, downward, and upward flows (Figure 39a). Gas saturation continuously

decreases from the gas inlet to the hydrate solidification front for horizontal and downward flow, whereas gas saturation is homogeneous behind the hydrate solidification front for upward flow (Figure 39a). Gas saturation is over 42.9% for downward flow at this rate, is over 10.7% for horizontal flow, and is at 2.6%, close to the residual value for upward flow ($S_{gr} = 2.0\%$).

These differences are caused by the effect of gravity and can be understood as follows. According to Darcy's law of gas volumetric flux, the gravity or the buoyancy contributes to upward flow, is zero for horizontal flow, and inhibits downward flow. Therefore, for the same overpressure gradients, the magnitude of the impelling force (overpressure gradient plus buoyancy) for a gas element is smallest for the downward flow, and largest for the upward flow. The gas relative permeability adjusts itself to allow flow at the rate it is supplied, and gas permeability depends monotonically on the gas saturation. Thus the gas saturation is higher for downward flow in order to overcome gas buoyancy (lower driving force), and it is lower in upward flow where buoyancy works with the flow. These differences disappear at high gas supply rates, when the overpressure gradients dominate the flow.

In contrast to the gas saturation, the liquid saturation behind the front is highest for upward flow and lowest for downward flow (Figure 39b). It is over 20% for upward flow, and less than 15% for the downward flow (Figure 39b). These differences are caused by the gas saturation differences at the hydrate solidification front. When there is a low gas saturation behind the front, as seen for upward flow, there is necessarily more water behind the front. When there is a high gas saturation behind the front, as seen in downward flow, there is necessarily less water behind the front. In all cases, the water behind the front is converted to hydrate until the remaining water reaches the three-phase salinity. More water initially left behind the front results in a higher liquid saturation after hydrate formation (upward flow).

In addition, more water initially left behind the front means more fresh water available to form hydrate. Since gas is being continuously supplied, the limiting factor for hydrate formation is the amount of fresh water available. Simply, more water initially left behind the front results in a higher hydrate saturation. Therefore, the hydrate saturation follows the liquid saturation. It is highest for upward flow and lowest for downward flow. It is 76.7% for upward flow, 68.4% for horizontal flow, and 43.4% for downward flow (Figure 39c).

In all these cases gas is supplied at the same rates, but the velocities of the fronts change with these changes in saturations due to the volume change on mixing. Because the density of methane in the hydrate phase is much greater than in the gas phase for the parameters listed in Table 3, flow with the highest hydrate saturation (upward) yields the lowest front velocity, and the lowest hydrate saturation (downward) yields the highest front velocity. In addition to changing the front velocity, the different hydrate saturations also change the exiting volumetric flux. Higher hydrate saturations consume more methane with the result being the exiting volumetric flux is highest for downward flow and lowest for upward flow (Figure 39d).

In addition to the flow direction, the saturations depend on the flow rate. We will focus the discussion on hydrate saturation here. For horizontal flow, hydrate saturation is independent on the gas injection rate (Figure 40: the red line is flat). That is because there is no gravity or buoyancy, and the impelling force only includes the overpressure gradient. Overpressure gradient increases with the flow rate, and a same gas or hydrate saturation can be obtained for different flow rates.

For upward flow, hydrate saturation increases with decreasing gas injection rate when it is between 10^{-11} and 10^{-6} m^3 m^{-2} s^{-1} (Figure 40: green line). Buoyancy decreases the gas saturation and increases the

hydrate saturation for upward flow. The relative importance of buoyancy increases as the overpressure gradient decreases with the flow rate, which results in a higher hydrate saturation at a lower flow rate. The hydrate saturation versus gas injection rate flattens out at very low ($<10^{-11}$ m^3 m^{-2} s^{-1}) gas injection rate, where buoyancy dominates the flow, and gas saturation is very close to the residual value. It also flattens out at very high ($>10^{-6}$ m^3 m^{-2} s^{-1}) gas injection rates, where the overpressure gradient dominates the upward flow.

For downward flow, hydrate saturation decreases with the gas injection rate when it is less than 10^{-6} m^3 m^{-2} s^{-1}(Figure 40: blue line). Buoyancy increases the gas saturation and decreases the hydrate saturation for upward flow. Therefore, a lower flow rate results in a lower hydrate saturation. The hydrate saturation versus gas injection rate flattens out at very high ($>10^{-6}$ m^3 m^{-2} s^{-1}) gas injection rates, where the overpressure gradient dominates the downward flow.

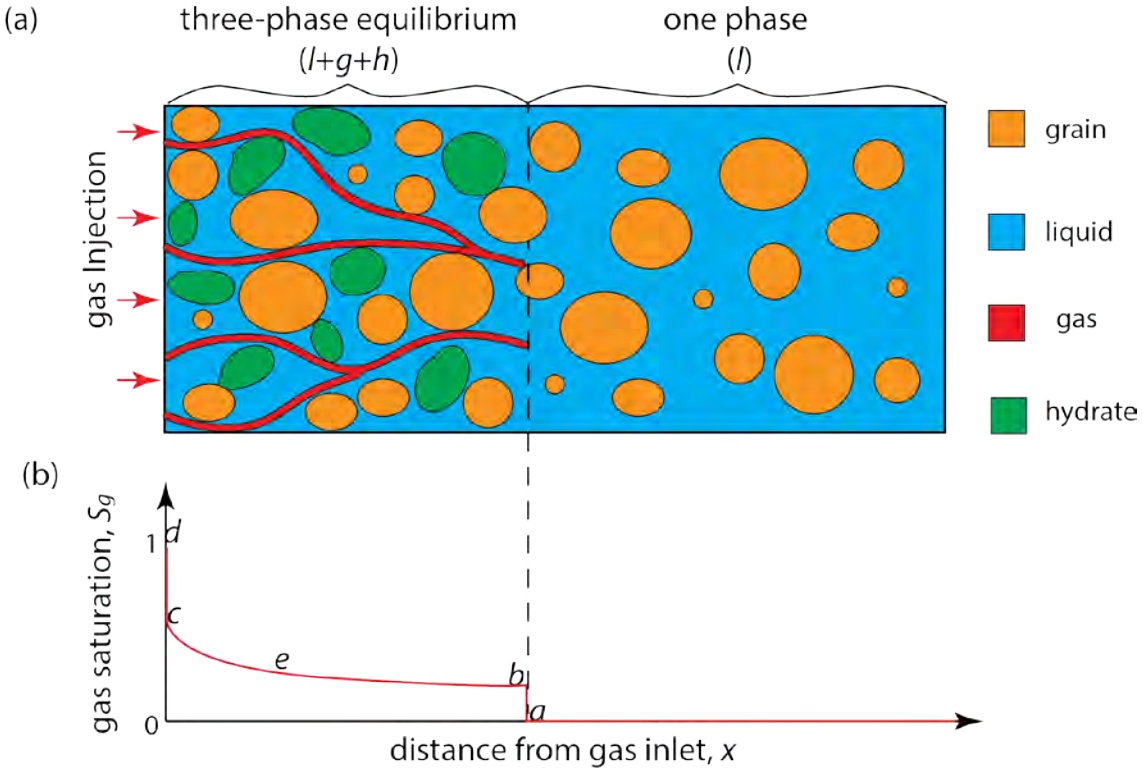

Figure 36: (a) Schematic diagram of methane gas injection into a brine-saturated sediment within the methane hydrate stability zone. (b) The corresponding gas saturation distribution. The system reaches three-phase equilibrium behind the hydrate solidification front (to the left of point b): in this region brine at an elevated salinity coexists with methane gas and hydrate. Gas saturation decreases from 100% at the upstream side of the gas inlet (point d) to 0% at the downstream side of hydrate solidification front (point a). l, g and h means liquid, gas and hydrate phases, respectively. Points a and b delineate the downstream and upstream sides of the leading shock, respectively. Points c and d delineate the downstream and upstream sides of the trailing shock, respectively. Point e is any position between point b and c.

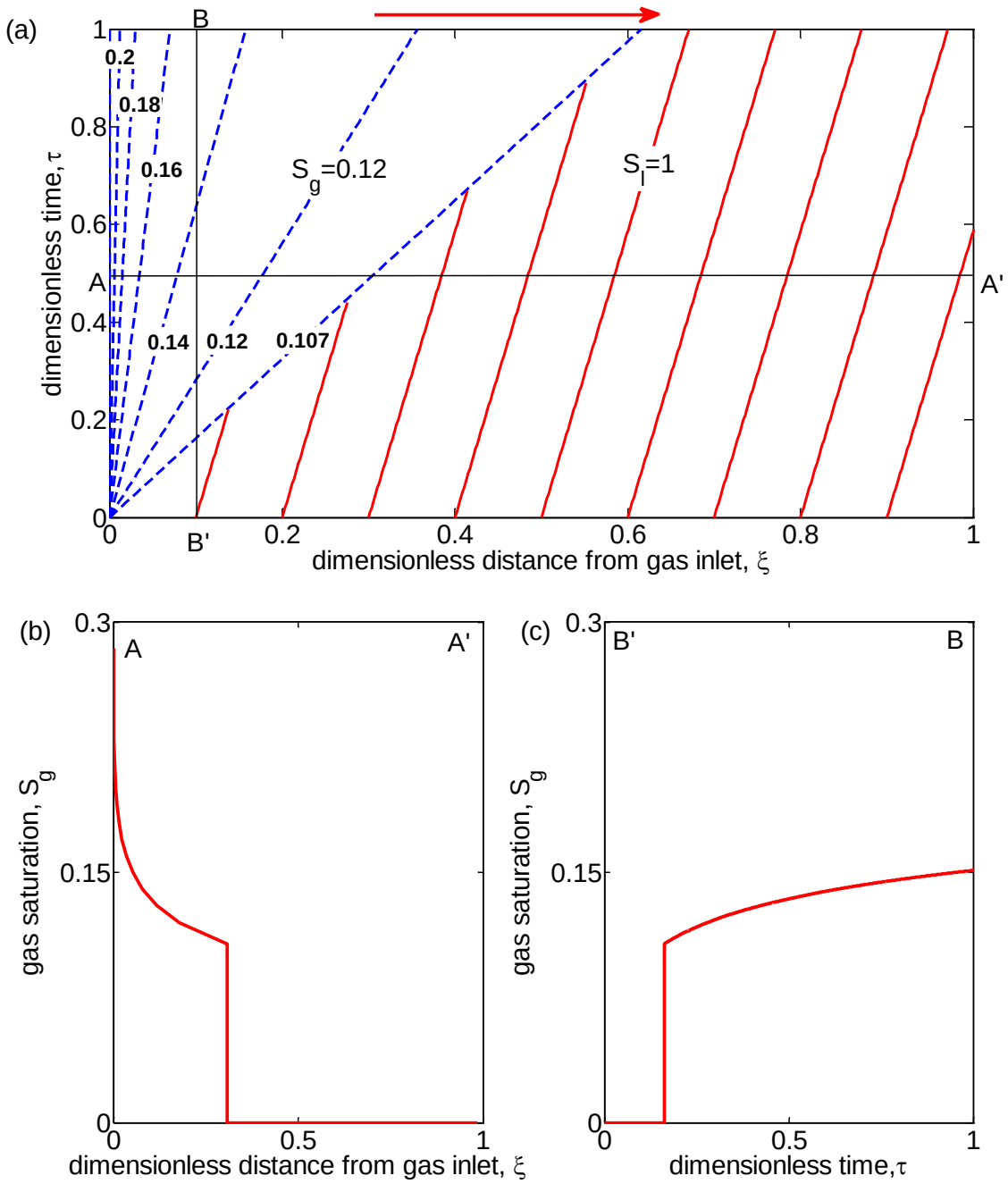

Figure 37: (a) Characteristics for methane gas injection into a brine-saturated sediment with the pressure of 6.89 MPa, temperature of 4 °C, initial salinity of 3 wt.% and gas injection rate of 10^{-6} m sec-1. The hydrate saturation is 0.684 behind the hydrate solidification front. The dashed blue lines are the characteristics for the discontinuity initially present at the gas inlet. Numbers on the blue lines are gas saturations. The red lines are the characteristics for the initial composition (S_I=1) in the sediment. The line $\tau = 0$ is the characteristics for the injection composition. (b) Change of gas saturation along line A-A' ($\tau = 0.5$). (c) Change of gas saturation along line B-B' ($\varepsilon = 0.1$). The red arrow on the top of shows the flow direction.

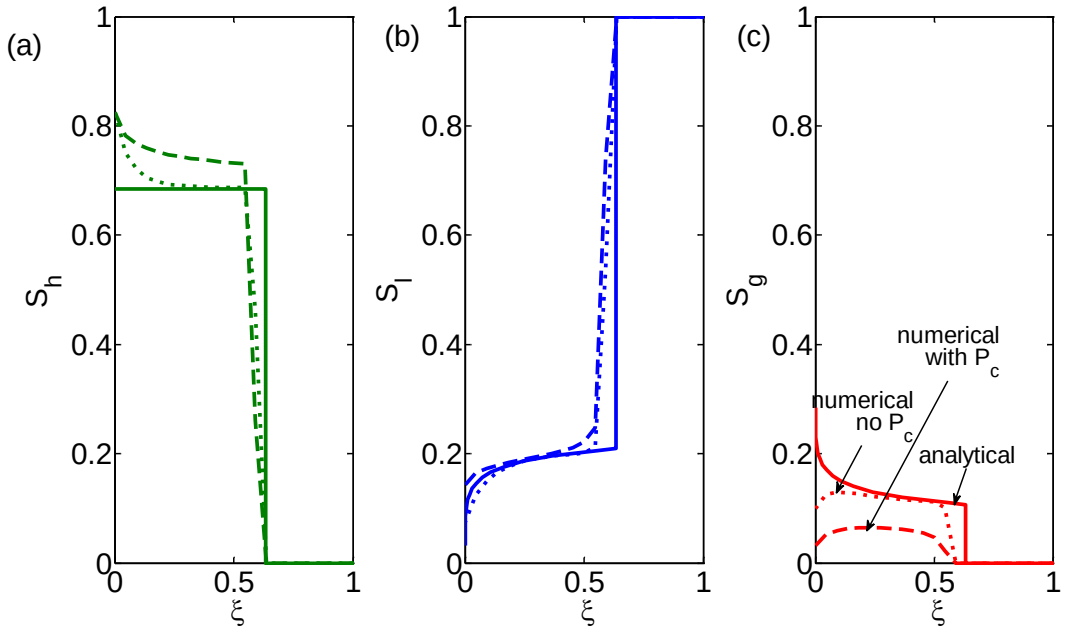

Figure 38: a) Hydrate (S_h , green lines), b) water (S_w , blue lines) and c) gas (S_g , red lines) saturation distributions in the sediment at dimensionless time 1.0 calculated by the analytical solution (solid lines), the numerical solution developed in Liu and Flemings (2007) with capillary pressure (dashed lines) and the numerical solution without capillary pressure (dotted lines).

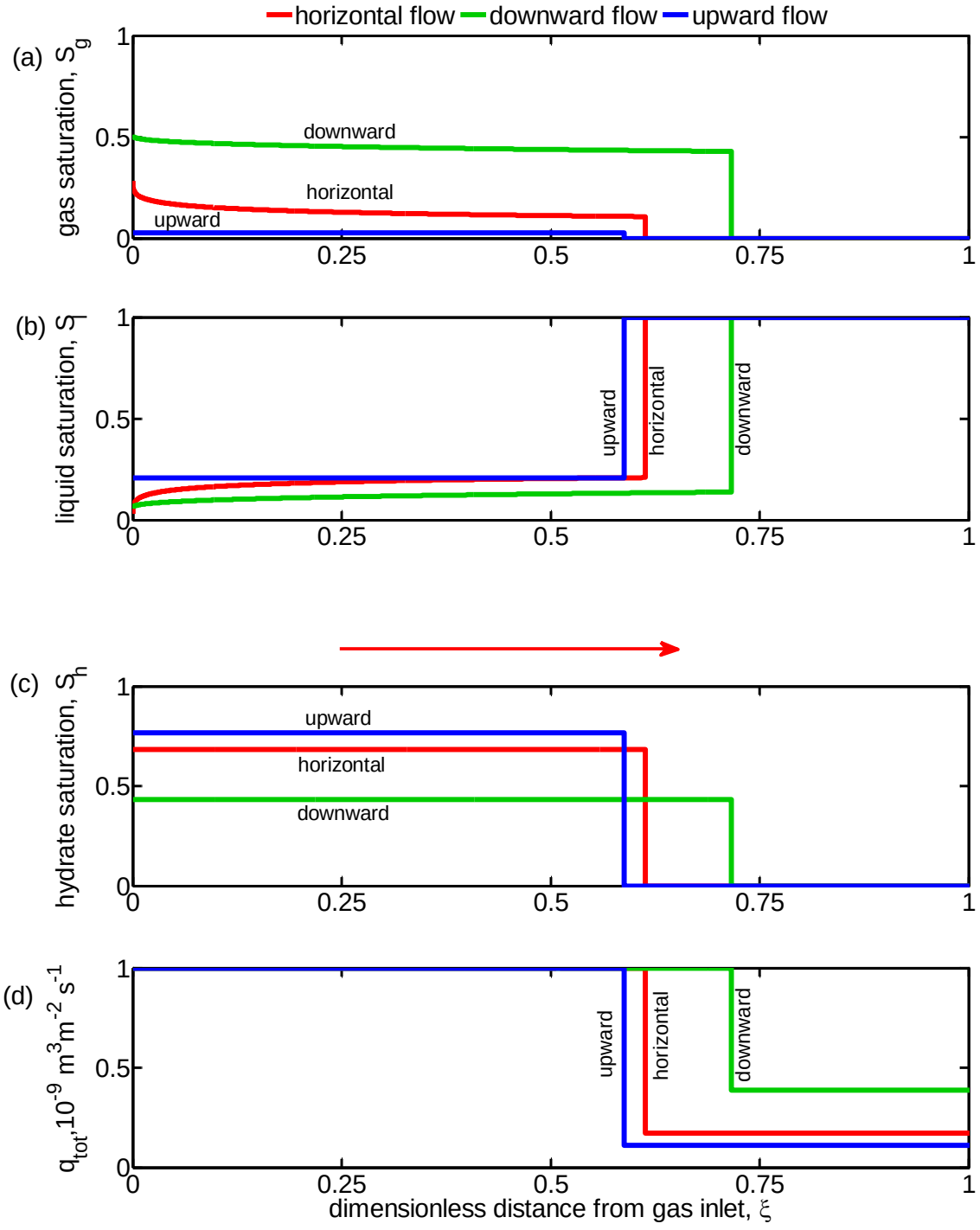

Figure 39: Comparison of (a) gas (S_g), (b) liquid (S_l), (c) hydrate saturation (S_h), and (d) total volumetric flux (q_{tot}) distribution at $\tau = 1$ for horizontal (red lines), downward (blue lines) and upward (green lines) flow at the gas injection rate of 10^{-9} m3 m-2 s-1. The red arrow indicates the flow direction. The thermodynamic and flow parameters are listed in Table 5.

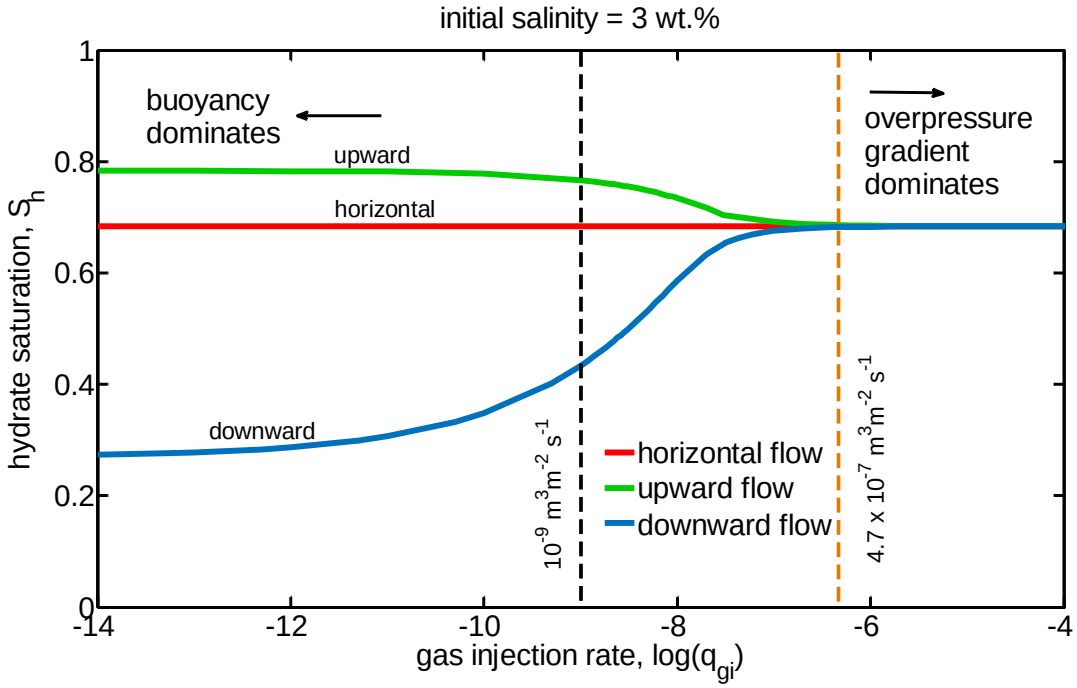

Figure 40: Change of hydrate saturation with gas injection rate for horizontal (red line), upward (green line), and downward flow into a hydrate stability zone at the pressure of 6.89 MPa, temperature of 4 oC and initial salinity of 3 wt.%. The flow parameters are listed in Table 5. The dashed orange line shows the critical flow rate of 4.7×10-7 m3 m-2 s-1. The dashed black line shows the flow rate of 10-9 m3 m-2 s-1. Gravity forces dominate the flow, and hydrate saturation depends on the flow direction when the flow rate is much less than 4.7×10-7 m3 m-2 s-1. Viscous forces dominate the flow, and hydrate saturation does not depend on the flow direction when the flow rate is much greater than 4.7×10-7 m3 m-2 s-1.

Table 5: Parameters used in the example calculation.

Variables	Physical meanings	Values
P_0	Pressure (MPa)	6.89
T_0	Temperature (°C)	4
cl_0	Initial salinity (wt.%)	3
cl_e	Three-phase equilibrium salinity (wt.%)	10.96
L	Column length (m)	0.11
q_{gi}	Methane gas injection rate (m sec^{-1})	10^{-6}
ρ_{gi}	Density of gas injected (kg m^{-3})	56
ϕ	Porosity in absence of hydrate	0.35
ρ_h	Hydrate density (kg m^{-3})	912

k_0	Sediment intrinsic permeability without hydrate (m^2)	10^{-13}
θ	Dip angle of the system (rad)	0
S_{gr}	Residual gas saturation	0.02
S_{wr}	Residual water saturation	0.1
μ_g	Gas dynamic viscosity (Pa sec)	2×10^{-5}
μ_l	Liquid water phase dynamic viscosity (Pa sec)	1.31×10^{-3}
$X_{M,h}$	Mass fraction of methane in hydrate (wt.%)	13.4
$X_{W,h}$	Mass fraction of water in hydrate (wt.%)	86.6

1D Numerical Fracture Growth Model

Introduction

We have been investigating the hypothesis that narrow, hydrate-filled fracture networks act as conduits for vertical gas migration through the hydrate stability zone. Our previous petrophysical analysis of various hydrate-bearing sites (Phase 1 report (Flemings, 2014b)), supported by additional published studies, has revealed that, in fine-grained material, hydrate frequently forms in high-angle fractures (Daigle et al., 2011; NGHP Expedition 01 Scientists, 2007; Rees et al., 2011b; Riedel et al., 2010; Ryu et al., 2013). It is commonly hypothesized that these fractures form from the development of a gas reservoir beneath the GHSZ with a pore pressure that overcomes the least principle stress and creates hydraulic fractures in the overlying sediment (Daigle and Dugan, 2011; NGHP Expedition 01 Scientists, 2007; Rees et al., 2011b; Riedel et al., 2010; Ryu et al., 2013). It is commonly hypothesized that these fractures form from the development of a gas reservoir beneath the GHSZ with a pore pressure that overcomes the least principle stress and creates hydraulic fractures in the overlying sediment (Daigle et al., 2011; Daigle and Dugan, 2011). Seafloor methane gas vents are also frequently observed above hydrate-filled fracture networks (Bangs et al., 2011; Haeckel et al., 2004; Torres et al., 2011), which suggests that these fracture networks also act as conduits for gas migration (Daigle and Dugan, 2011; Haacke et al., 2009; Mazumdar et al., 2009).

This observation has led researchers to question the mechanism that allows the vertical migration of gas in these fractures through the hydrate stability zone. Three primary hypotheses have been proposed (Figure 41). First, the kinetics of hydrate formation limit hydrate precipitation such that gas can migrate through the fractures without forming hydrate (Haeckel et al., 2004; Torres et al., 2004). Second, hydrate formation is limited by the amount of water available in the fracture such that, after some initial hydrate formation and gas consumption, hydrate ceases to precipitate and gas can migrate vertically (Clennell et al., 1999; Ginsburg and Soloviev, 1997). Finally, hydrate formation elevates the salinity in the pore water, producing three-phase equilibrium conditions and limiting the formation of additional hydrate, which allows the gas to pass through the remaining pore space (Liu, 2006; Meyer and Flemings, 2014; Milkov et al., 2004).(Liu, 2006; Meyer and Flemings, 2014; Milkov et al., 2004). As we have moved forward in our research concerning the formation of hydrate in fractures, we focused on this final

hypothesis as the primary mechanism for vertical gas migration, assuming that formation kinetics are negligible and that there is always water available to form hydrate.

Model Development

To gain some initial understanding of the physics controlling this process, we have developed a numerical model describing the movement of water and salt associated with the formation of hydrate in fractures. We are specifically interested in osmotic pressure as a potential driving force for fluid flow. The intrinsic osmotic pressure of a fluid is calculated with Equation 56 (Malusis et al., 2003):

$$u_{os} = -\omega \cdot \nu \cdot R \cdot T \cdot C \qquad \text{Eq 56}$$

where ω, ν, R, T, and C are the chemico-osmotic efficiency coefficient, ion reaction constant, gas constant (8.314 J/mol-K), temperature (K), and salt concentration, respectively. The ω-value describes how ideally semi-permeable a membrane acts. A value of $\omega = 1$ indicates an ideally semi-permeable membrane, while $\omega = 0$ indicates a fully permeable membrane. A membrane with a $\omega > 0$ separating two fluids of different salinities, will produce an osmotic pressure gradient that can result in fluid flow (Bader and Kooi, 2005). In our model, we assume a matrix of fine-grained material, which has been shown to act as a non-ideal, semi-permeable membrane. Although the ω-value is dependent on the porosity of the material and salt concentration of the fluid, it is typically non-zero (Barbour and Fredlund, 1989).

The model domain extends from the fracture wall to the half-fracture spacing and the model keeps track of the fluid overpressures (total, water, and osmotic), salinity, and porosity within the domain over time (Figure 42). External to the domain, within the fracture, the formation of hydrate increases the salinity of the water proximal to the fracture wall, increasing the osmotic pressure and decreasing the total pressure relative to hydrostatic pressure within the domain. This pressure gradient produces a driving force for the advection of water and salt from the matrix into the fracture, which supports the continual hydrate formation and salinity elevation. The model holds the following assumptions:

a. One-dimensional model (homogeneous material)
b. Constant water density
c. Darcy's Law applied for water flow
d. No salt diffusion
e. Matrix acts a non-ideal semi-permeable membrane ($\omega = 0.01$)
f. All the water that enters the fracture forms hydrate
g. Hydrate formation kinetics are negligible

Using water and salt mass balance and Darcy's Law (Eq. 59), we derived the follow water (Eq. 57) and salt (Eq. 58) advection equations and half-fracture thickness (Eq. 60) calculation:

$$\frac{du_w}{dt} = \left[\frac{k \cdot (1+e)^2 \cdot \sigma' \cdot \ln(10)}{C_c \cdot \mu}\right] \cdot \frac{du_{tot}}{dx} \quad \text{Eq 57}$$

$$\frac{d(\phi C)}{dt} = -\frac{d(q_w C)}{dx} \quad \text{Eq 58}$$

$$q_w = -\frac{k}{\mu}\frac{\partial(u_w - u_{os})}{\partial x} \quad \text{Eq 59}$$

$$L_{frac} = \left[\frac{\rho_w}{\left(\rho_h \cdot \left(\frac{M_w}{M_H} \cdot n\right)\right)}\right] \cdot \int_0^t q_w(x=0)_t \cdot dt \quad \text{Eq 60}$$

We then discretized equations B and C and solved them using an explicit, numerical method. The values for permeability (k) and compression index (C_c) were estimated from geotechnical tests previously performed on Resedimented Boston Blue Clay (RBBC) material (Schneider, 2011).

Results

The model was run on a domain 2 meters wide over a period of 1 year in order to achieve pressure equilibrium. The model results (Figures 43) express the following initial and boundary conditions as the solid lines:

a. Constant hydrostatic pressure and three-phase salinity at fracture boundary
b. No flow boundary at the half-fracture spacing
c. Initially seawater salinity and hydrostatic pressure throughout the domain

Once the model starts, water flows down the pressure gradient toward the fracture, decreasing the water and total pressure in unison (Figure 43a). The reduction in water pressure results in a decrease in effective stress and a 0.33 percent decrease in porosity due to consolidation (Figure 43b). Additionally, the consolidation resulted in a 0.33 percent increase in salinity (Figure 43c). After a year, the total pressure reaches equilibrium across the domain and water ceases to flow into the fracture (Figure 43d). At this point, the amount of water that entered the fracture would make a hydrate-filled fracture approximately 1.6cm thick (Figure 43e).

Conclusions

This model is a relatively simplistic look at the physics controlling hydrate formation in fractures; however the results provide some interesting initial understanding into this problem. The model uses well supported fluid flow physics with constrained sediment characteristics and produced a fracture thickness that is reasonable compared to those found in nature. This suggests that osmotic pressure gradients across fracture boundaries could be a reasonable driving force for water flow into a fracture and continual hydrate formation. From this point, we will be continuing our research in this area with additional model advancements, including salt diffusion, capillary-induced flow, and cryogenic suction effects.

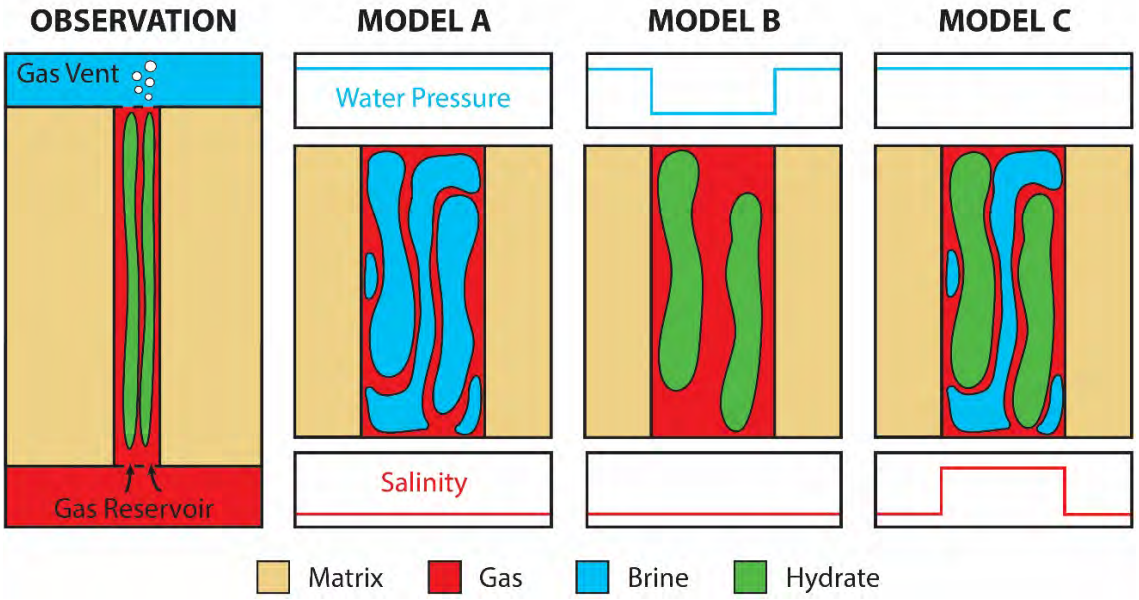

Figure 41: Cartoon describing the three major hypotheses presented to explain the observed methane gas vents associated with hydrate-filled fractures. Model A indicates that hydrate formation is limited by kinetics. Model B states that the hydrate consumes the readily available water and becomes water limited. Model C suggests that hydrate formation can locally elevate salinity and restrict hydrate formation.

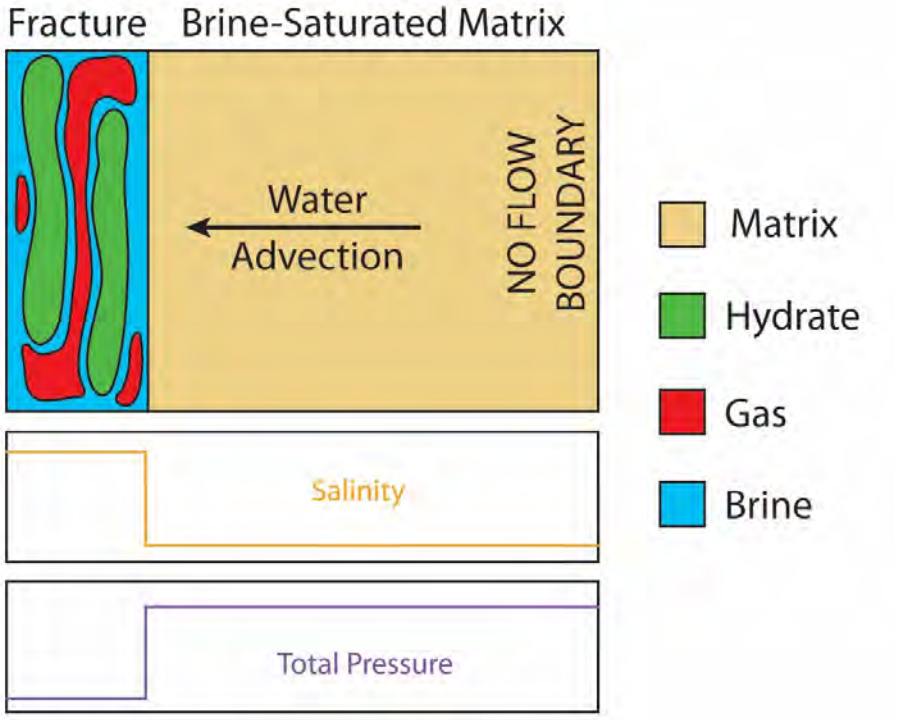

Figure 42: General conceptual model of osmotic pressure as a potential mechanism for water flow toward a fracture to support hydrate formation. Elevated salinity in the fracture, due to hydrate formation, reduces the

total pressure in the fracture. This produces a pressure gradient that induces water advection toward the fracture.

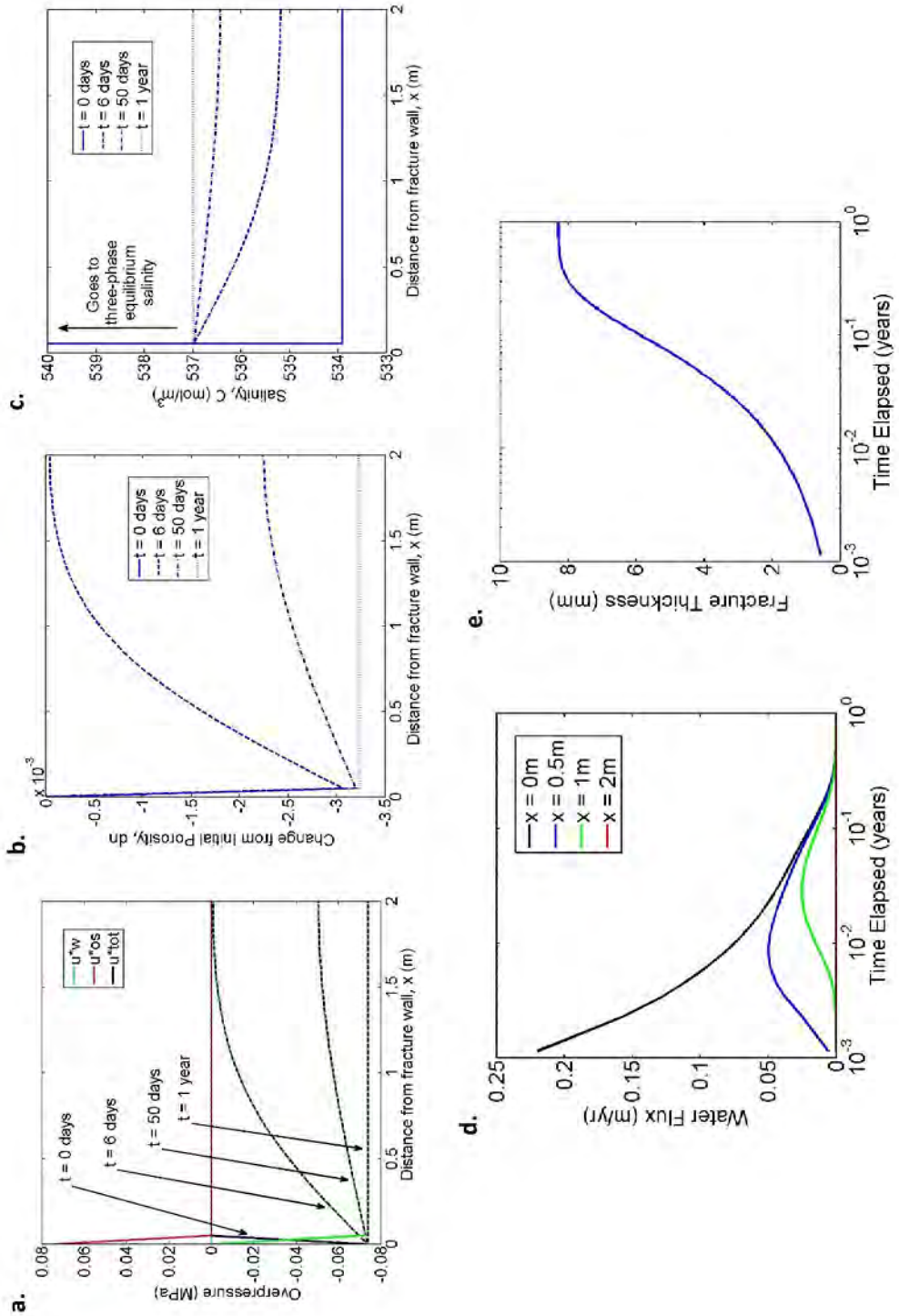

Figure 43: Compilation of the 1-year advection model results. A) Total (u*tot), water (u*w), and osmotic (u*os) overpressure profiles throughout time. B) Porosity profile across the domain during the model. C) Salt concentration within the matrix throughout time. D) Water flux over time at various points within the matrix. E) Fracture half-thickness as a function of time. Over the course of the model, water flows out of the matrix and

into the fracture, reducing overpressures, porosity, and water flux and increasing salinity and fracture half-thickness.

B2. Subtask 5.2 - Apply 1D expulsion to laboratory experiments (Complete)

B2.1. Goal:

The Recipient shall validate the conceptual and physical basis of the gas expulsion model against experiments conducted in Task 6.

B2.2. Activities Phase 2:

In this section, we discuss the numerical simulation of experiment HVT0008 where methane gas invades into a vertically-placed hydrate stability zone from the top. The sediment has a length of 13 cm and diameter of 5.08 cm. Initially, the sediment is saturated with brine (NaBr) of salinity 7 wt.%, at the pressure of 12.24 MPa and temperature of 1 ^{o}C (Figure 44). We keep a constant gas pressure of 12.24 MPa at the top to simulate the gas pump that is connected at the top of the sediment. We set a fixed water flow rate of 0.001 ml/min at the bottom to simulate the brine pump that is connected at the bottom of the sediment. We keep a constant sediment temperature of 1 ^{o}C through the simulation.

When brine is pulled out from the bottom, the pressure in the sediment decreases. Methane gas flows in from the top and forms methane hydrate from the top of the sediment (Figure 45). Hydrate formation excludes salt, and increases the local salinity until three-phase equilibrium value (31 wt.%). The gas and hydrate fronts move further down the sediment with a velocity of 0.035 cm/hour. There are three phases, gas, hydrate and liquid, from the gas inlet to the hydrate solidification front, and salinity equals 31 wt.%. There is one phase, liquid, from the hydrate solidification front to the bottom of the sediment. And the salinity is slightly increased close to the front because of the salt advection and diffusion from the front. Gas breakthroughs at about 375 hours, when the entire sediment reaches three-phase equilibrium. Hydrate saturation decreases from 88% at the top to about 79% at the bottom, with a bulk saturation of 82% in the sediment. The measured gas consumption is much less than the numerical prediction (Figure 46: the orange line is much lower than the red line), but it is greater than the measurement brine consumption. This means there was hydrate formation in the experiment, but hydrate saturation was much lower than the three-phase value and the bulk system did not reach three-phase equilibrium.

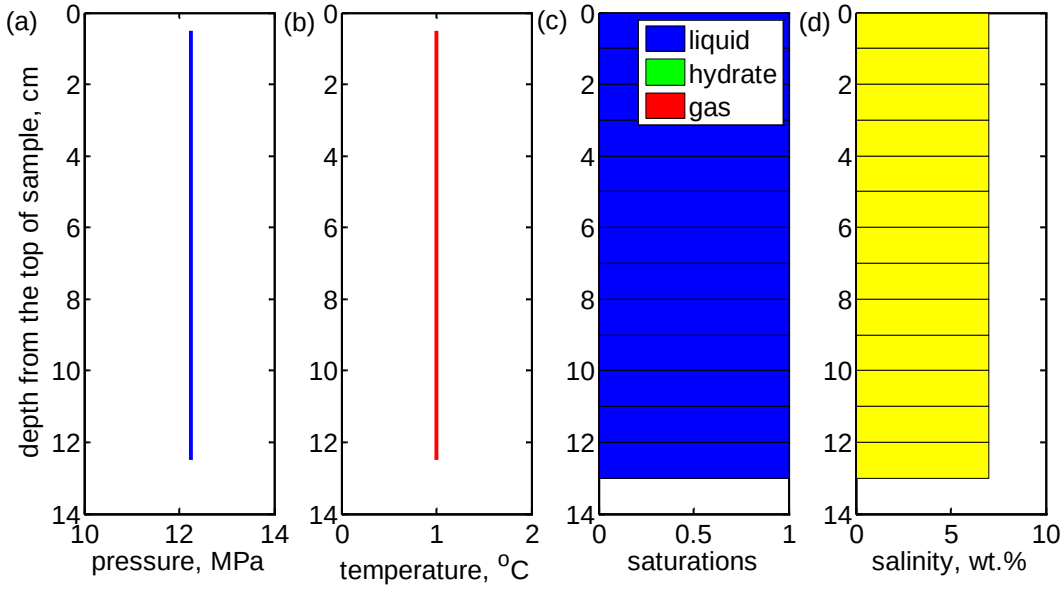

Figure 44: (a) the initial pressure, (b) temperature, (c) liquid (blue), hydrate (green) and gas (red) saturation, (d) salinity distribution in the sediment.

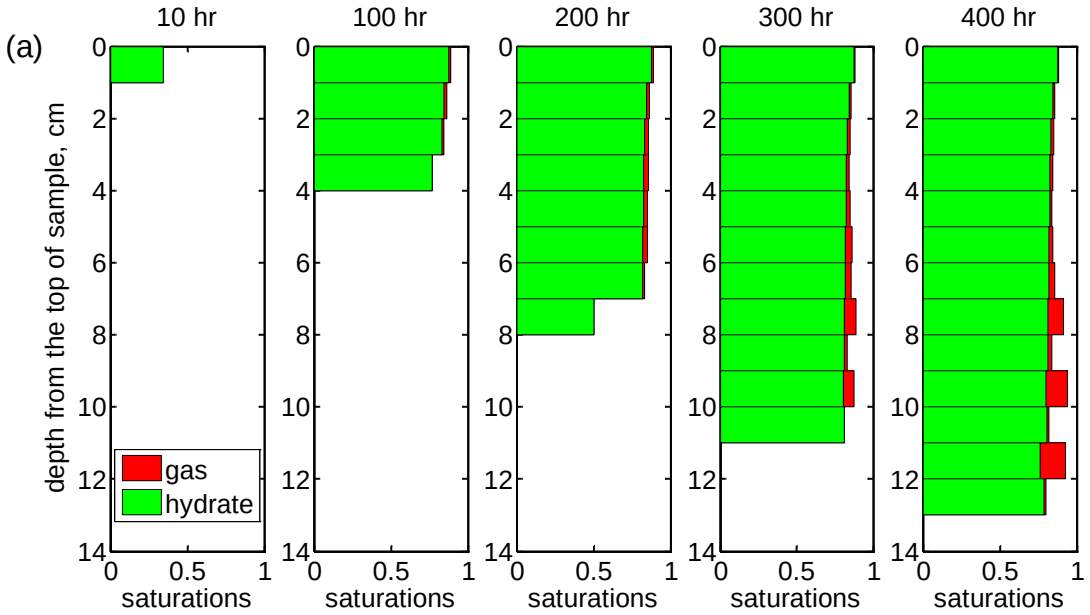

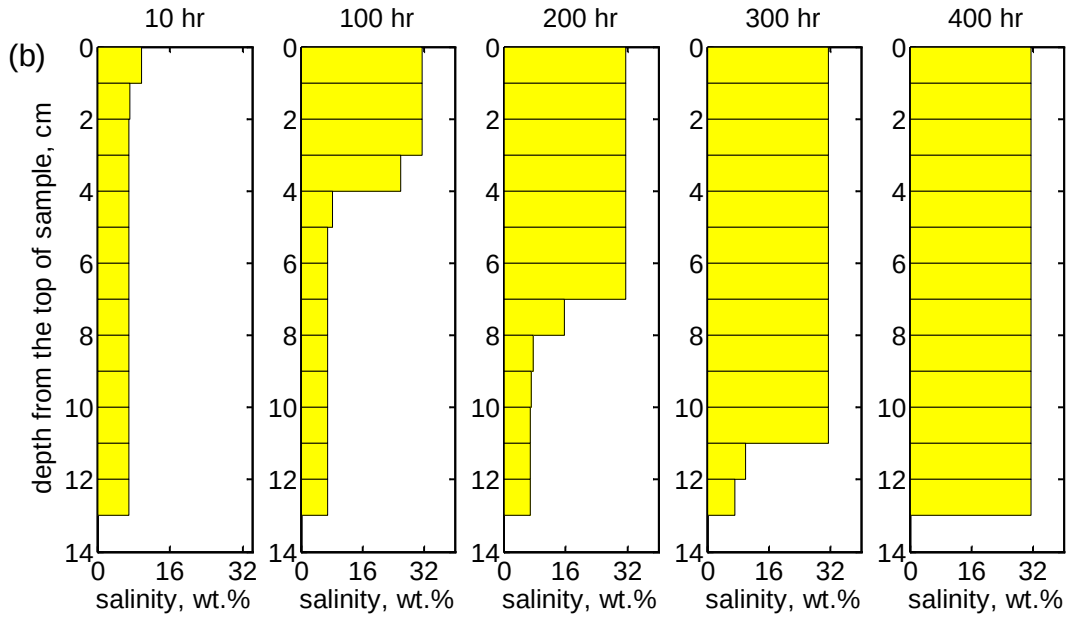

Figure 45: (a) hydrate (green) and gas (red) saturations, and (b) salinity (yellow) distribution in the sediment at 10, 100, 200, 300 and 400 hours after the start of brine withdraw.

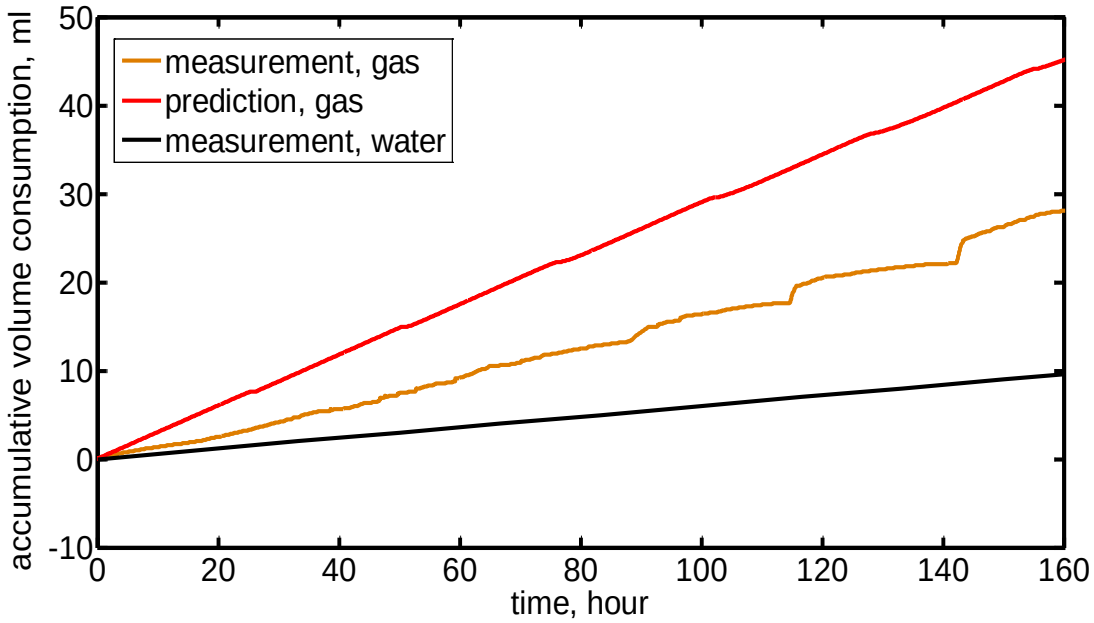

Figure 46: Comparison of the measured and numerically predicted accumulative gas consumption in the experiment HVT0008 .

Besides, we analyzed our laboratory experiments of gas invasion and hydrate front advancing using the MOC analytical model, which are discussed in subtask 6.1.

Subtask 5.3 - Apply 1D model of natural hydrate accumulations (Complete)

B2.3. Goal:

The Recipient shall simulate the migration of gas out of the hydrate‐bearing sediment, and shall determine conditions under which migration continues to the seafloor or atmosphere. Specifically, the latent heat of hydrate formation, the effect of salinity, and the effect of flow via fractures or matrix shall be included. The Recipient shall model the time evolution of the gas flow and predict under what conditions and at what rate gas will be vented. Initial conditions that are both within the liquid‐hydrate (L+H) stability region and within the three‐phase equilibrium (L+H+G) region shall be considered.

B2.4. Activities Phase 2:

The model has been developed and presented in the June 2014 quarterly report.

The model is currently being applied to the permafrost zone such as in Alaska (Figures 44-47) and to the deepwater continental margins (Figure 48).

Permafrost Zones:

The purpose of this section is to investigate the interrelated ice and hydrate melting during global warming. We use the Mallik gas hydrate field as an example. The same study can be extended to other hydrate fields. Mallik gas hydrate field is located in Mackenzie delta on the coast of Beaufort Sea, in the northwest territories of Canada (Haberer et al., 2005). It was shown to be one of the most concentrated gas hydrate deposits in the world (Dallimore and Collett, 2005). Relatively thick sections of high-saturation methane hydrate (often over 80%) lie between 897 and 1110 m (Taylor et al., 2005). Ice-bearing permafrost extends from ground surface to the depth of about 600m.

In our simulation, the initial water pressure increases hydrostatically with depth (Figure 47a). Present average ground surface temperature is -6 ^{o}C (Majorowicz et al., 2012) (Figure 47b). We set the initial temperature at the base of permafrost (600 m) at -1 ^{o}C (Henninges et al., 2005) (Figure 47b). Below the base of permafrost temperature increases linearly with the gradient of 26 ^{o}C km^{-1} (Figure 47b). A fixed geothermal flux of 56 mW m^{-2} is applied at the bottom (1400 m), providing an equilibrium initial temperature distribution. Sediments in the shallow depth of the Beaufort-Mackenzie Basin is largely terrestrial, and low salinities below 0.1-0.5 wt.% can be expected (Dallimore and Collett, 2005). We assume the salinity from ground surface to 600 m to be 0.5 wt.% in absence of ice. We also assumes there is no salt transport during ice freezing. The initial ice saturation S_{i0} can be calculated from the salinity $X^s_{l0} = 0.5wt.\%$ and the salinity when ice equilibrates liquid phases X^s_{l+i} (calculated from the initial temperature and ice-liquid phase boundary) as $S_{i0} = 1 - \frac{X^s_{l0}}{X^s_{l+i}}$ (Figure 47c). The BHSZ is at 1100 m.

Two hydrate layers with variable saturations are present from 900 to 1000 m, and from 1080 to 1100 m (Figure 47c). The initial hydrate saturations are obtained by averaging the nuclear magnetic resonance-derived gas hydrate saturation for Mallik 5L-38 well (Dallimore and Collett, 2005). The initial salinity decreases with depth in the permafrost, and is uniformly 3 wt.% beneath the base of permafrost (Figure 47d). The porosity is uniformly 35%, and the permeability of the hydrate and ice-free sediments is 10^{-13} m^2 (Dallimore and Collett, 2005).

At 0 k.y. we increase the ground surface temperature linearly from -6 to 0 ^{o}C for 300 years and then keep the surface temperature at 0 ^{o}C to reflect future climate warming caused by doubling of CO_2 (Majorowicz et al., 2012). Ice melts from ground surface immediately because the local thermal condition is initially on ice-liquid phase boundary (Figure 48). Ice also melts from the base of permafrost (Figure 48c), which is caused by the geothermal flux (Archer, 2015). Ice front retreats faster from the base of permafrost (Figure 48c). There are two reasons for this: first, the initial ice saturation decreases with depth and reaches minimum at the base of permafrost; second, there is a large initial salinity gradient toward the base of permafrost (Figure 48d), and salt diffuses into the base of permafrost and promotes ice melting there. At 18 k.y. the ice has shrunk to the depth between 40 and 420 m with an average saturation of 40% (Figure 48c). The entire ice layer disappears at 33 k.y. from 60 m in depth.

Hydrate starts to dissociate at 16 k.y. from the BHSZ, where the initial thermal state is most close to the hydrate phase boundary. Hydrate dissociation provides methane to the shallower hydrate layer, and secondary hydrate forms there (Figure 48c). Hydrate melting decrease the local salinity, and secondary hydrate formation increases the local salinity. Both effects bring the local system to three-phase (hydrate, liquid and gas) equilibrium and creates a gas pathway in the hydrate deposit (Figure 48c). The entire hydrate deposit and the gas front move upward with old hydrate melting and secondary hydrate formation (Figure 48c). Methane gas reaches ground surface and starts venting to atmosphere at 38 k.y., when hydrate deposit rises to the depth between 540 to 920 m. Hydrate deposit continues rising with methane gas venting at ground surface. Hydrate disappears at 55 k.y.. At 68 k.y. residual gas saturation (2%) remains in the sediment. Temperature is still increasing in the domain (Figure 48a). Ice and hydrate melting redistributes salinity in the sediment (Figure 48b). Salinity in the initial ice layer is much lower than the initial value (Figure 48b). Salinity in the initial hydrate layer reduces to two third to three fourth of the initial value (Figure 48b). We call this melting scenario as melting-1. During melting methane gas front is always far below the base of permafrost before ice disappears. For example, gas front is at 760 m when the remaining ice layer is at 60 m. Therefore, ice cannot prevent methane venting to atmosphere by decreasing the sediment intrinsic permeability.

When the initial ice saturation in each depth is reduced to one half (melting-2) and to zero (melting-3), methane gas starts venting at ground surface at 30 k.y. and 21 k.y., respectively, which was advanced by 8 k.y. and 17 k.y. respectively (Figure 49). There are two stages of gas venting at ground surface. The first stage lasts about 6 k.y. with an average gas flux of about 170 g m^{-2} yr^{-1} (Figure 49). The second stage lasts around 10 k.y. with an average gas flux of about 100 g m^{-2} yr^{-1} (Figure 49)

We then move the base of permafrost to 300 m. This yields a HSZ between 260 and 580 m. We move the entire hydrate deposit to the depth between 380 and 580 m, and do the same melting simulation as in melting-1. We call this simulation as melting-4. Methane gas starts venting at ground surface at 8.5 k.y. and lasts until about 18.5 k.y., when the entire hydrate deposit disappears and residual gas saturation remains in the domain (Figure 50). Different from melting-1, -2 and -3, gas venting at ground surface in this case lasts for shorter time but with a much higher average flux, about 200 g m^{-2} yr^{-1}.

We then investigate the effect of sea level rise. We set the initial water depth at ground surface to be zero. We increase the water depth with a rate of 3 mm yr^{-1} for 1 k.y. We then keep the water depth at 3 m for the remaining time. We immediately increase the ground surface temperature from -6 to 0 ^{o}C at 0 k.y. to simulate seawater flooding. We call this case melting-5. We have two drives for ice and hydrate dynamics in melting-5: the first is water pressure, and increasing water pressure stabilizes both ice and hydrate in the sediments; the second is temperature, and increasing temperature destabilizes both ice and hydrate. Very similar melting behavior is obtained with melting-1, except that the increasing water depth delays the time when gas starts venting at ground surface by 1 yr (Figure 50).

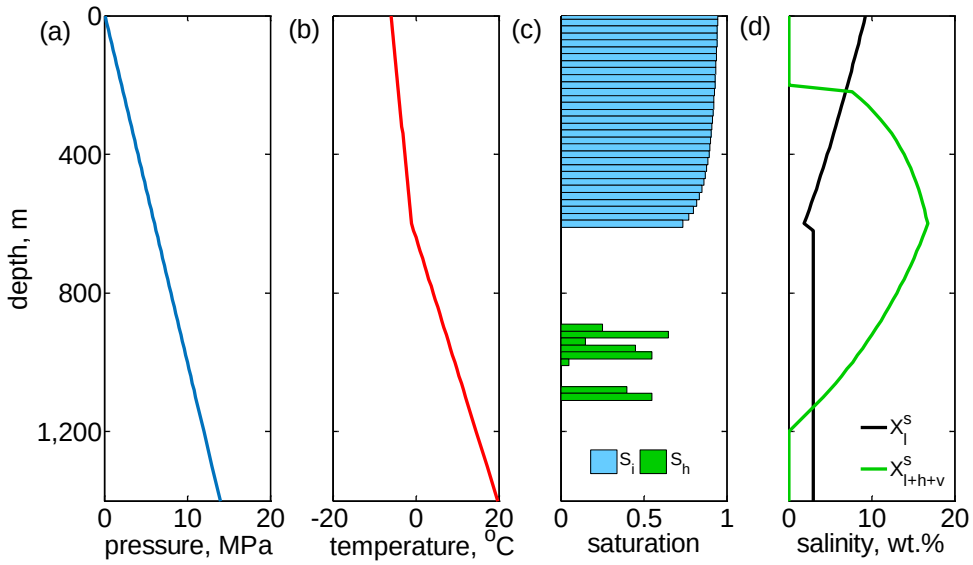

Figure 47: Initial (a) pressure, (b) temperature, (c) saturation and (d) salinity distributions for Mallik site hydrate melting simulation. Si is ice saturation, Sh is hydrate saturation, Xsl is initial input salinity, and Xsl+h+v is three-phase equilibrium salinity for liquid, gas and hydrate phases.

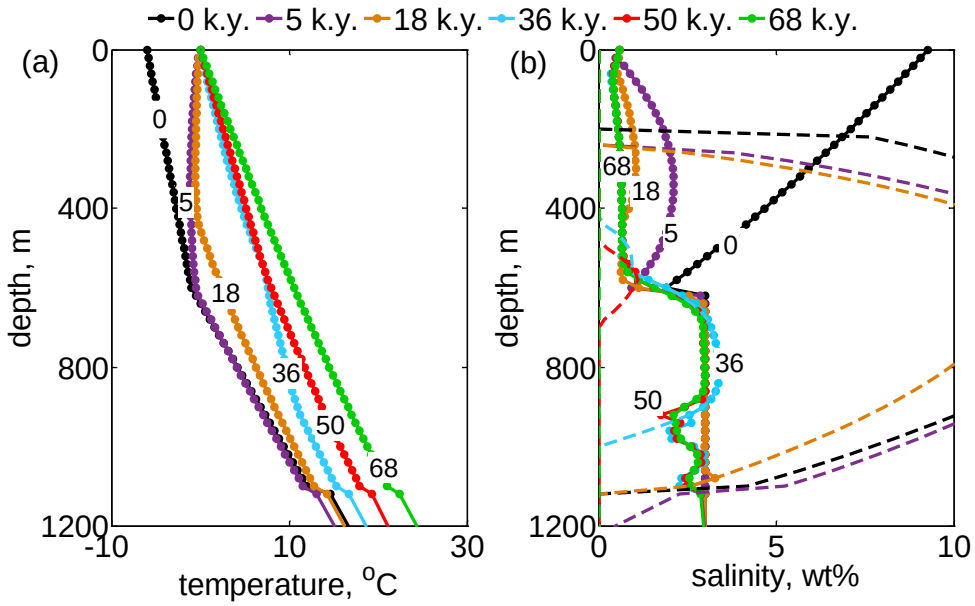

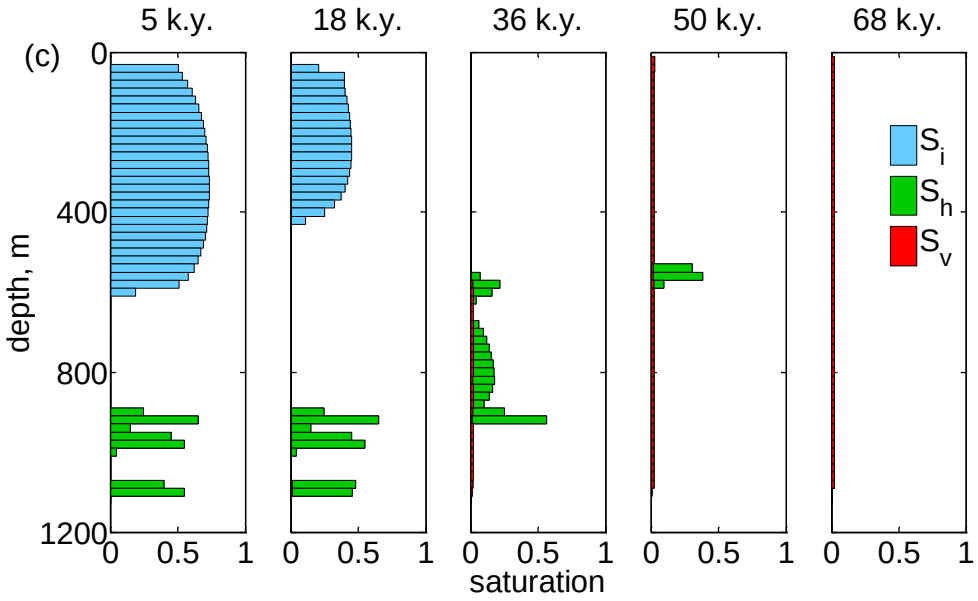

Figure 48: Hydrate and ice melting at Mallik site with average ice saturation 90%. (a) temperature, (b) in-situ salinity (solid lines with dots) and three-phase equilibrium salinity (dashed lines), and (c) ice (blue), hydrate (green) and gas (red) saturation distributions at 0 (black), 5 (purple), 18 (brown), 36 (blue), 50 (red) and 68 (green) k.y., respectively.

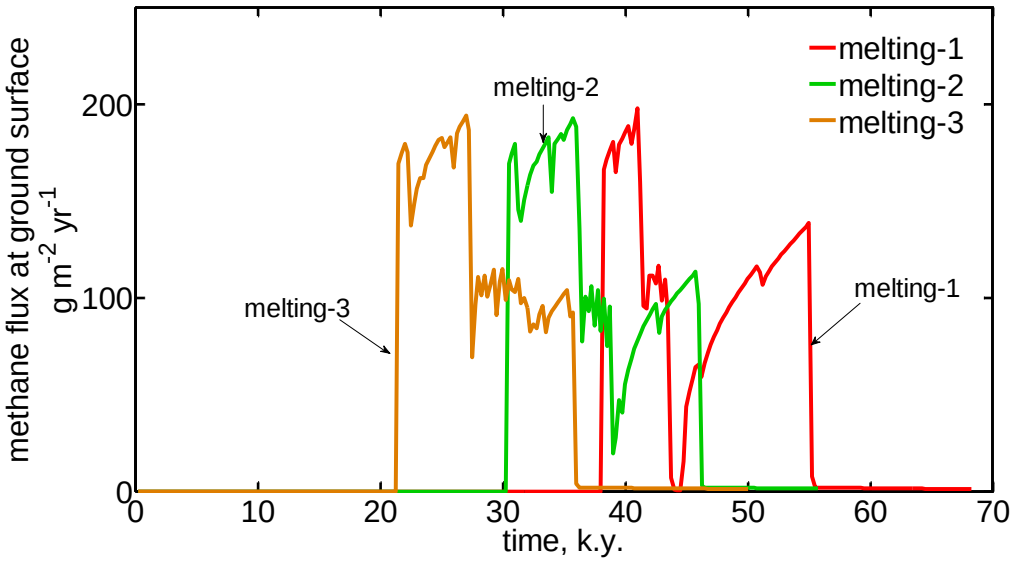

Figure 49: Evolution of methane gas flux at ground surface in response to future global warming when the base of permafrost is at 600 m, and the average ice saturation is 90% (melting-1), 45% (melting-2) and zero (melting-3).

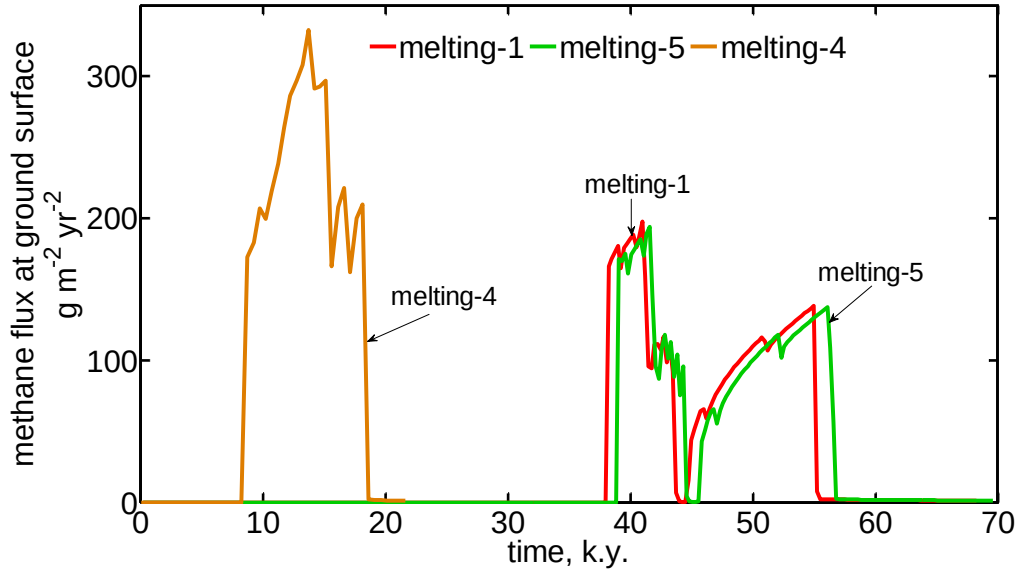

Figure 50: Evolution of methane gas flux at ground surface in response to future global warming when the base of permafrost is at 600 m (melting-1) and 300 m (melting-4), and in response to sea water transgression when the base of permafrost is at 600 m (melting-5).

Continental Margins:

On continental margins, we have extended our numerical results to describe the general behavior of venting in hydrate systems. Our results constrain when gas will vent due to a thermal perturbation and when it will not (Milestone 2.B). An analytical model captures the general behavior.

In the analytical model, we compare the mass of gas liberated by warming against the mass of gas that the warmed and shortened gas hydrate stability zone (GHSZ) can actually convert to hydrate. The liberated hydrate amount determined by the initial conditions, while the allowable hydrate amount in the warmed and shortened GHSZ is set by the three-phase equilibrium conditions. If more gas is available due to warming than is allowable by the system, venting temporarily occurs.

We calculate the depth of the BHSZ after complete warming, B_f. We assume that all hydrate beneath B_f dissociates, that no hydrate is initially above B_f, and that any salt transport is negligible[1]. We estimate the mass of gas supplied by dissociation, α, as

$$\alpha = A\theta_g \int_{B_f}^{B^i} S^i{}_h(z)dz, \qquad \text{Eq 61}$$

where S_h^i is initial hydrate saturation, ρ_h is hydrate density and A is the nominal area (1 m^2), θ_g is the fraction of methane contained in hydrate ($\theta_g = 0.14$ by assuming a hydration number of 6). We

[1] Multiple simulations showed that salt transport was negligible.

then calculate how much gas, γ, is necessary to establish a three-phase equilibrium chimney from B_f to the seafloor.

$$\gamma = A\theta_g \int_0^{Bf} S^{eq}{}_h(z)dz = A\theta_g \int_0^{Bf} (1 - {}^{c_0}/_{c_{eq}(z)})dz \quad \text{Eq 62}$$

where S_h^{eq} is the hydrate saturation corresponding to three-phase equilibrium salinity, c_0 is the initial salinity (3.5 w.t. %), and c_{eq} is the three-phase equilibrium salinity after complete warming. Then, Λ is the ratio of gas supplied (α) to the amount of hydrate needed to form a vent (γ):

$$\Lambda = \alpha\gamma^{-1}. \quad \text{Eq 63}$$

Transient venting occurs when $\Lambda > 1$ and when a GHSZ remains after warming ($B_f > 0$). *Complete venting* occurs when the GHSZ vanishes after warming ($B_f \leq 0$), and *no venting* occurs under all other scenarios. This analytical approach predicts similar behavior to the multiphase flow model. These simulations produce *transient venting* within the expected *transient venting* temperature range of the analytical model (filled circles, Figure 51b).

We use equation (32) to analyze venting for an idealized continental margin (Figures 46a and 46b) that has the same initial seafloor temperature and geothermal gradient as our previous simulations. A bottom water temperature increase of 2.5◦C shoals the base of the hydrate stability zone upward approximately 80m (dashed lines, Figure 51a). *Complete venting* occurs over a lateral distance of 400m, where the GHSZ vanishes ($B_f \leq 0$). *Transient venting* occurs over a finite distance downdip of the GHSZ pinch-out. According to the linear relationship between S_h^i and Λ in equations (30)–(32), the width of the *transient venting* zone is dependent on the concentration of hydrate within the dissociated layer (thick lines, Figure 51b). For instance, a few percent hydrate saturation causes venting for only tens of meters seaward of the GHSZ pinch-out, while nearly 100% hydrate saturation would be necessary to cause venting several kilometers seaward of the pinch-out (between vertical white lines, Figures 51a and 51b). If we assume 5% hydrate saturation, then the *transient venting* region spans approximately 200m downdip of the apparent pinch-out of the GHSZ (between vertical white lines, Figures 51a and 51b).

We evaluate the sensitivity of the analytical model (Figure 52) by perturbing the model from a base state. For this sensitivity, we perturb the water depth, seafloor temperature, magnitude of warming, geothermal gradient, and initial hydrate saturation. We include one base state that matches the conditions present in the example of transient venting (Figure 52a) and a second base state that does not produce venting (Figure 52b). Water depth and seafloor temperature (combined temperature from T_{sf} and ΔT) have the most dramatic effect on the results (Figure 52), since they control the locations of the BHSZ before and after warming. In addition, the initial hydrate saturation has a significant effect on the results where greater initial hydrate increases the potential for venting (Figure 52). These basic

relationships are corroborated in the multiphase model (Figure 53). We provide a code at https://github.com/kdarnell/TransientVenting that calculates Λ for a given set of input parameters.

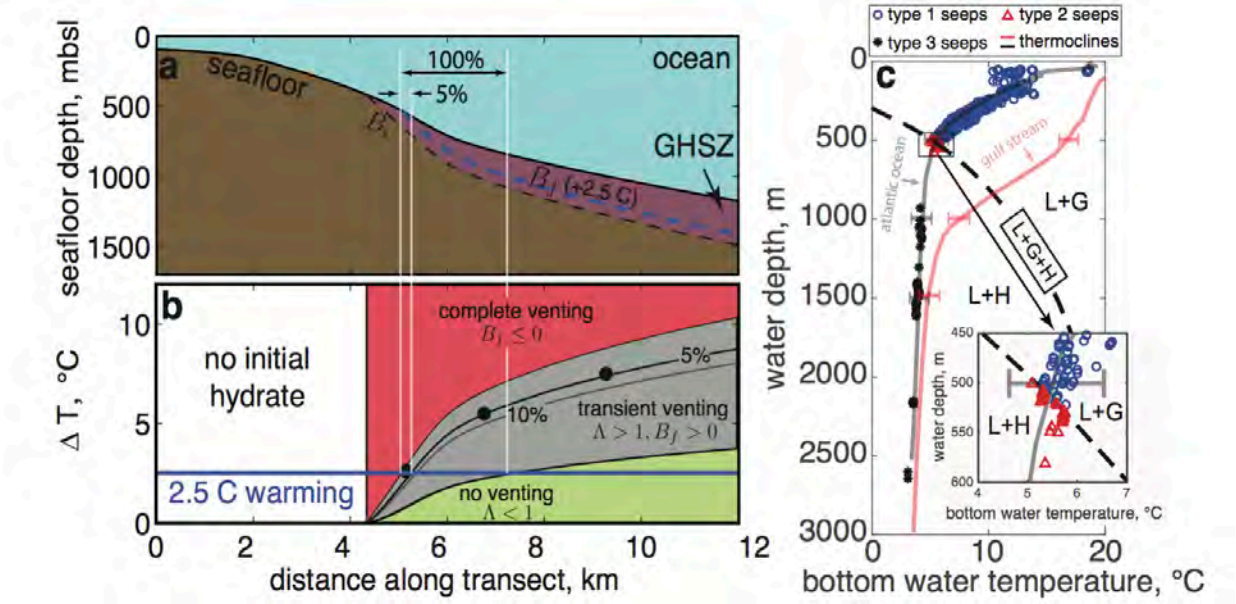

Figure 51: (From Darnell and Flemings (2015)) Venting predictions for an idealized continental margin using simple analytical model (equations (29)–(31)) and venting observations from a seep database. (a) Dip section of continental margin taken from eastern Atlantic. Black dashed line denotes initial BHSZ (Bi), and blue dashed line denotes warmed BHSZ (Bf). (b) Modeled warming response for initial 3°C seafloor temperature with 40°C/km thermal gradient and initial salinity of 3.5 wt %: complete venting (red region) for a large warming, no venting (green region) for a small warming, and transient venting (gray region) for warming in between end-member responses. Transient venting at a given temperature change occurs at hydrate saturation greater than saturation curve. Black, filled circles denote multiphase simulation results that record transient venting at 10% hydrate saturation. Vertical white lines denote region where transient venting is expected at warming of 2.5∘C for 5% and 100% hydrate saturation. (c) Hydrate phase diagram of calculated bottom water temperature using conductivity- temperature-depth (CTD) from World Ocean Database (Levitus et al., 1998) versus reported water depth for the 577 seeps observed by Skarke et al. (2014). Faint black and red lines denote the Atlantic Ocean and Gulf Stream thermoclines identified by Phrampus and Hornbach (2012).. Dashed line denotes the three-phase equilibrium (L + G + H) boundary for a salinity of 3.5 wt % and a density of 1030 kg m−3. Hydrate stability (L + H) occurs below L + G + H boundary. Twenty-nine Type 2 seeps (red triangles) are estimated to lie within the present-day hydrate stability zone but less than 2°C from destabilization.

We compare our venting predictions with a database of seeps identified by Skarke et al. (2014) (Figure 51c). We use their published water depths and geographical coordinates to calculate bottom water temperature using CTD data from the World Ocean Database (Levitus et al., 1998). These temperatures compare well with the Atlantic Ocean thermocline (Figure 51c) identified by Phrampus and Hornbach (2012).

We plot the seeps in a temperature versus water depth hydrate phase diagram (Figure 51c) assuming seawater salinity (3.5 wt %) and converting water depth to a hydrostatic pressure (with ρ = 1030 kg m^{-3}). We identify three types of seeps (Figure 51c). Type 1 seeps (blue circles, Figure 51c) are located

outside of the hydrate stability zone. Type 2 seeps (red triangles, Figure 51c) are located within the hydrate stability zone but would require warming of less than 2°C to destabilize hydrate. Type 3 seeps (black asterisks, Figure 51c) are well within the hydrate stability zone.

We interpret that the Type 2 seeps (29 of 577 seeps) could be transient vents, but additional field data are needed for confirmation. We base our interpretation on the fact that these Type 2 seeps are located where gas should not be stable (red triangles, Figure 51c) for the calculated seafloor temperature and assumed seawater salinity. Therefore, temperature or salinity at these seeps must be locally increased to explain their presence if thermodynamic equilibrium is assumed. The seeps may even be at three-phase equilibrium as has been shown for seeps in the Gulf of Mexico (Smith et al., 2014). If only salinity is elevated, we calculate the elevated salinity required for local three-phase equilibrium ranges from 3.55 wt % to 6.1 wt % depending on the temperature and water depth of each seep. Thus, transient venting induced by past warming, as might have occurred since the Last Glacial Maximum, could produce three-phase conditions and explain the present-day gas venting at these seeps. Precise bottom water temperature, seafloor salinity, and gas composition will test this interpretation.

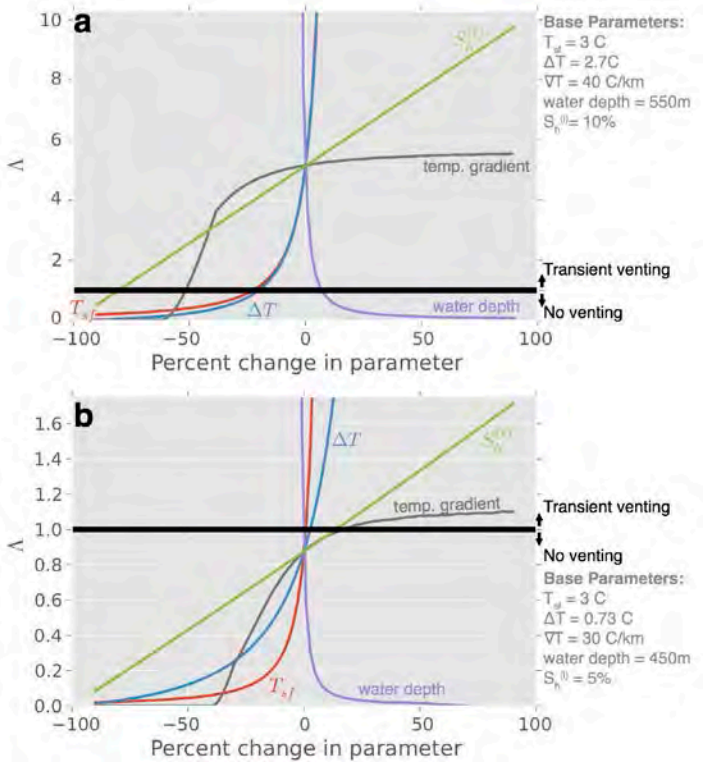

Figure 52: (From Darnell and Flemings (2015)) Sensitivity analysis of analytical model with variations to the seafloor temperature (Tsf), seafloor warming (ΔT), seafloor temperature gradient (∇T), water depth, and initial hydrate saturation ($S_h^{(i)}$). Each parameter is adjusted in isolation as a percentage change of its base value while all other parameters remain fixed. The resulting Λ value calculated from equation (32) is used to determine whether or not transient venting occurs. (a) The base parameters are the same as those used in the example of

the main text, which produced transient venting. (b) Arbitrary base parameters that are different parameters from Figure 39a and where the base parameters produce no venting.

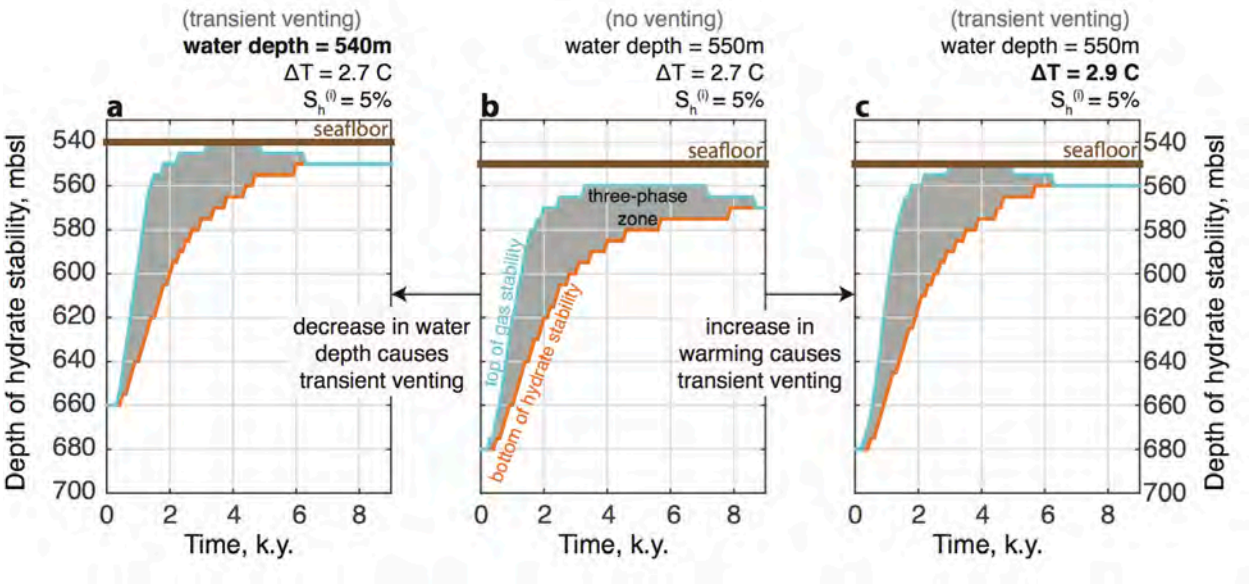

Figure 53: (From Darnell and Flemings (2015)) Comparison of multiphase dynamic simulation for initial hydrate saturation of $S_h^{(i)}$ = 5% with small variations in model parameters. For all three panels, the temperature gradient (40 °C/km) and initial seafloor temperature (3 °C) are held constant. Middle panel (b) is the base case. (a) Trajectory of hydrate/gas stability as a function of time where the water depth has been decreased by 10 meters from (b). (b) Trajectory of hydrate/gas as function of time where all parameters are equal to an example that produces transient venting, except $S_h^{(i)}$ has been decreased from 10% of pore volume to 5%. The gray area is the three-phase zone, which is located between the top of gas stability (cyan line) and bottom of hydrate stability (orange line) (c) Trajectory of hydrate/gas stability as a function of time where the temperature has been increased 0.2 °C from (b).

2.6. Task 6: Gas expulsion experiments (Complete)

Milestone 2.C Demonstration of reaction transport experiment where gas invades hydrate stability zone and creates three phase stability.

A. Goal:

The Recipient shall provide data to validate the gas expulsion model developed in Task 5, and to provide insight into whether this process of hydrate formation is self‐limiting. The hydrate saturation profile formed as gas invades the hydrate stability zone shall be representative of hydrate‐bearing sediments along continental margins. Thus the dissociation portion of the experiment also provides insight into possible differences in behavior between Arctic and oceanic systems.

B. Activities Phase 2:

B1. Subtask 6.1 - Gas invasion into water-saturated hydrate saturated zone

B1.1. Goal:

The Recipient shall perform a test to determine gas invasion into a water-saturated hydrate saturated zone. In this test, the vessel shall be filled with coarse sand and then X-ray CT scanned. The sand shall then be saturated with seawater and re-scanned. Temperature shall be held constant everywhere so that the entire column is within the hydrate stability zone. Methane gas shall be introduced into the top of the vessel through a mass flow controller operating at a prescribed (slow) rate. Seawater shall be allowed to leave from the bottom of the column using a high-pressure syringe pump operating at constant pressure mode. Although this geometry is inverted compared to natural systems, it results in a better-controlled gas front which is very important for the measurements to be made. Temperatures, pressures, resistances shall be recorded frequently (~ every 30 sec) and ultrasonic (P wave) data shall be collected by hand regularly (~daily). At the conclusion of the test (salt front breakthrough significantly advanced through the column), the vessel shall be rescanned and hydrate dissociated while observing using CT. Gas mass flow, temperatures, and pressures shall be recorded over the dissociation to determine hydrate location, saturation, and to characterize the advancement of the reaction front.

B1.2. Activities Phase 2:

Summary

Over the course of Phase 2 of the project we have addressed Milestones 1.E and 2.D through the following activities related to Task 6. 1) The design and construction of an operational experimental setup for running hydrate formation experiments at the University of Texas at Austin (UT). 2) The execution of 5 successful hydrate formation front experiments and 2 hydrate dissociation experiments between UT and Lawrence Berkeley National Laboratory (LBNL). 3) The analysis of the data from these experiments to improve our understanding of the distribution and saturation of the brine, hydrate, and gas phases within the samples.

Due to the challenging nature of the hydrate formation experiments required to complete Task 6, we decided previously (Flemings, 2014a) that it would be prudent to assemble an additional hydrate formation vessel at UT to increase our productivity. The most recent iteration of the hydrate formation equipment setup at UT is discussed in detail below. This setup has been continuously revised as we have determined way to improve our experimental execution.

The parameters of the successful hydrate formation experiments are described in Table 5. The purpose of each of these experiments was to form hydrate to three-phase equilibrium conditions through the induction of a propagating gas front into a brine-saturated sample. From these experiments we determined that: A) the degree of subcooling is an important control on the induction time, B) hydrate formation is rate-limited, and C) lowering the gas flow rate reduces the rate-limitation on hydrate formation. Through these experiments we demonstrated a successful reaction transport front with hydrate formation near three-phase equilibrium.

UT Hydrate Lab Equipment

As it currently stands, the synthetic hydrate formation lab at UT consists of the following major components: the hydrate formation vessel and cooling jacket, the vertical hanger frame, the 3 Teledyne ISCO 500D syringe pumps, the circulating refrigeration unit (CRU), and data acquisition system (DAQ), and the temperature control box (TCB). The pumps and TCB were purchased and assembled over the course of Phase 2 as we determined they were required for experimentation. We also collaborated with Dr. David DiCarlo at the UT Petroleum and Geosystem Engineering Department (PGE) to perform one test (HVT0005) in the computer tomography (CT) lab and collect CT data during the experiment.

The hydrate formation vessel (Figure 54) is constructed with steel endcaps and a CT-transparent aluminum wall. It was designed to be similar to the vessel at LBNL, but rated to a maximum pressure of 2500psi (maximum working pressure of 2200psi). Aluminum sleeve is contained within a PVC cooling jacket that allows the CRU to maintain a constant confining temperature to ±0.1^{o}C. The vessel can be hanged vertically using a compression hanger collar (Figure 55) and the aluminum hanger frame (Figure 56).The three syringe pumps separately control the pressure and flow of the confining, brine, and methane fluids during the experiment to an accuracy of ±1psi and 0.001mL/min, respectively. The vessel, hanger, and pumps are all contained within the TCB, which maintains a constant temperature of up to 5.5 ± 0.1^{o}C above the surrounding room temperature (Figure 56 and 57). Temperature is measured at the top and bottom of the confining cell as well as inside and outside the TCB. Confining, inlet, and outlet pressures are dually measured by transducers attached to each pump as well as by separate transducers built into the fluid lines. The pressure and temperature data are recorded automatically at a set interval by the DAQ.

Each sample consisted of a homogeneously-packed fine sand in a cylindrical sleeve to a 2” diameter and approximately 5” length. The sleeve was made of fluid impermeable Viton to separate the pore and confining fluids while allowing for the confining stress to translate to the sample. The sample was confined on top and bottom with two Delrin endcaps, each of which had a fluid port (Figure 58).

HVT0001

Introduction

This experiment was done in LBNL to examine methane hydrate formation under three phase (gas/brine/hydrate) conditions, followed by thermal dissociation from the bottom. In this test, a vertically oriented cylindrical sand sample saturated with 7% NaCl brine was drained at 1014 psia and 4C, with the brine replaced by methane. These conditions are within the methane hydrate stability zone, and hydrate formation was expected. The test was monitored using multiple pressure and temperature sensors, and X-ray computed tomography (CT) was used to assess phase saturations. When drainage proceeded to the point where the methane gas approached the sample bottom, the connection to the gas was closed, and brine was allowed to imbibe into the sample under constant pressure. Upon completion of imbibition, the hydrate was dissociated by warming, using system designed to heat the sample from the bottom.

Methods

Sample Instrumentation

A lightweight 1/16" garolite rod was assembled with four Type T thermocouple probes (Omega Engineering, Stamford CT) and 2 silver/silver chloride electrodes. This rod was attached to a 1/8 inch stainless steel tube, and the thermocouple probes and wires from the electrodes were sealed with epoxy in the tube. The tube was run concentrically through a ¼ inch stainless steel tube that connects to the bottom 2-inch diameter endcap (Figure 59a). A 2-inch inner diameter EPDM sleeve was attached to the endcap with a double wrap of wire forming the base and sides of the cylindrical sample.

Sample

White quartz sand (Sigma Aldrich) (50 to 70 mesh ~ 212 – 300 micron grain size sand properties) was poured into the EPDM sleeve preassembled onto the PVC endcap partially filled with 7% NaCl brine. The sand was slowly poured to reduce air entrainment, and the assembly was vibrated constantly during the pour to minimize pore space. When the appropriate quantity of sand had been poured into the sleeve, the top endcap containing a Type T thermocouple (Omega Engineering, Stamford CT) was emplaced and a double wrap of wire was placed around the sleeve at the top endcap. The temperature outside the sleeve was monitored with another Type T thermocouple attached to the sleeve with electrical tape, shown schematically in Figure 59b, and an X-ray scan is presented in Figure 59c.

Sample Assembly

The sample assembly was installed into a pressure vessel containing a confining fluid of 50% propylene glycol 50% water separated from the sample by the EPDM jacket and the endcaps. The pressure vessel was contained in a thermal jacket through which temperature-controlled water/propylene glycol was flowed (Figure 60). The pressure vessel assembly was mounted to a frame that held it in the vertical orientation under normal operation, but allowed it to be rotated into the horizontal orientation for brief periods for X-ray CT scanning. The frame was mounted to the moving table of the X-ray CT scanner to minimize alignment errors on ongoing sets of CT scans.

The confining fluid region outside of the sample was connected to an Isco 500D syringe pump to allow constant confining pressure control. The fluid inlet and outlet to the sample were also connected to Isco 500D syringe pumps, with the downstream pump connected to the sample bottom (when oriented vertically) containing 7% NaCl brine, and the upstream pump connected to the sample top containing methane. The pumps were exposed to room temperature in a temperature-controlled laboratory. The tubing within the vessel was initially filled with brine.

Temperature measurements at 7 locations and pressure measurements at 4 locations were recorded every 20 seconds during the test (Figure 61a). Thirty-five multi-energy (80, 100, 120, and 140 kV) sets of

CT scans were collected (an example is as shown in Figure 65) to document the status of the sample. Each set of scans required adjusting the orientation of the custom-built sample holder, and each set of scans was performed at 80, 100, 120, and 140 kV energies.

Test Sequence

The test was performed in three stages: 1) brine drainage under hydrate-stable conditions (4°C and 1010 psi), 2) brine imbibition under hydrate-stable conditions (4°C and 1010 psi), and 3) hydrate dissociation by warming from the bottom. Each stage will be described separately. Temperatures, pressures, and fluid volumes, and sample mass computed from CT data for these stages are shown in Figure 61.

Drainage (0 – 92.4 hours)

The sample temperature was set nominally to 4°C. As shown in Figures 61a and 61b, a temperature gradient formed in the sample, with warmer temperatures at the top of the sample. The magnitude of the temperature difference between the sample top and bottom was about 0.3°C during the drainage and imbibition. This temperature gradient was largely unaltered when the sample orientation was changed for CT scanning. The sample was drained at a rate of 0.003 mL/min while methane gas was supplied to the top of the sample at 1010 psi. This drainage rate yields a Darcy velocity of 2.13 mm/day (0.089 mm/hr). This drainage rate was maintained for the first 92.4 hours, after which it was determined by X-ray CT scanning that the invading methane gas phase was approaching the sample bottom, however all still completely contained in the sample. At this time, the valve allowing the methane gas to enter the sample was closed, and the brine pump that was previously withdrawing the brine at the constant rate was set to run at a constant pressure equal to 1010 psi. Methane hydrate formation would consume gas from the gas phase, allowing brine to imbibe.

Hydrate formation is indicated by concomitant increase in temperature and consumption of gas. Figure 62 shows temperature differences between locations in the sample and system over this time period to make comparisons easier. These locations include thermocouple locations in the sample (compared to the lowest thermocouple location) and either the temperature indicated by the lowest elevation thermocouple, outside the sleeve, or the temperature bath to examine environmental influences on the system and thermal driving forces. Two periods of probable hydrate formation are indicated as periods 1 and 2 in Figure 62, where temperature increases at the upper thermocouples exceeded those at the lower thermocouples. Two periods where the temperatures at the upper thermocouples decline also occur following the temperature increases. The temperature of the lower thermocouple reflects the temperature at the bottom of the sample. Little change would be expected at that location because drainage was not significant there (no gas/brine contact to induce hydrate formation). Temperature data show only mild temperature signals for hydrate formation because the salinity was high and rate of drainage was so slow resulting in the rate of heat-generating hydrate formation being low relative to the ability of the system to transfer heat to the bath.

Imbibition (92.4 hours – 546 hours)

Imbibition was performed by allowing brine to imbibe into the sample bottom at constant pressure (1010 psi). Brine then could fill the pore space as methane was consumed by hydrate formation. Over one period of about 100 hours, the imbibition was halted by shutting the valve allowing brine to reenter the vessel, and sample (shut in from both gas and brine) was allowed to equilibrate. Over that period, the pressure in the sample dropped to about 860 psia. Upon reopening the valve, the pressure was restabilized to 1010 psi and imbibition continued.

Imbibition, indicating methane consumption, continued over the imbibition duration with an initial rapid rate that slowed to a near zero rate while the system was shut in (233-329 hours) and increased again when imbibition was restarted, and then tailed to a very low rate at about 550 hours (see green line in Figure 61c.) These differences in fluid volumes indicate that methane was being consumed by hydrate formation over this time. Temperatures remained fairly constant over the imbibition showing no obvious indication of hydrate formation (Figures 61a and 63), with the exception of the temperature spike of several tenths of a degree lasting about 1.5 hours when brine was allowed to flow into the sample following the shut in period. Approximately 5 mL of brine imbibed over that time.

Dissociation (546 hours to 750 hours)

Hydrate was dissociated over the final 250 hours of the test by stepwise increasing the temperature of a heating coil situated at the base of the sample. Over this time period, the brine pump remained shut in, allowing fluids (gas + water) produced by methane hydrate dissociation to flow into the gas pump, which was maintained at a constant pressure of 1010 psia. Heating the coil in the bottom of the pressure vessel was accomplished by flowing temperature-controlled water through the tube using a separate controller from that used for overall temperature control.

Temperature differences over the dissociation are shown in Figure 64, and gas production is shown as decreasing values on the black and green curves in Figure 61c over this time period. At about 660 hours, the thermal gradient in the sample was reversed from top-warm to neutral, and then to bottom-warm at about 690 hours. Hydrate dissociation and gas production were minimal until that point. This bottom warm condition remained until about 720 hours when the sample became top-warm again. The lion share of the hydrate had dissociated by this time as well, although some gas production continued past 750 hours.

CT Data

CT images presented in Figure 65 show changes in density from the starting condition and proceed over the course of the experiment. In these images, replacing the brine-saturated sand with either partially gas-saturated or hydrate-saturated sand will result in a decrease in density (shown in red). Increases in

density, perhaps from brine concentration or most likely indicating a slight misalignment when subtracting two data sets are indicated in blue. The "internal standard slice" is also present in these images about one third down, and can be ignored. In the top row, the decrease in density is shown by the increasing red color showing the drainage process including gas replacing brine and hydrate formation. In the middle row, the red color is mitigated by imbibition of brine. Towards the end of this phase, a large amount of the previously red volume has become mostly resaturated with brine and residual hydrate. Upon hydrate dissociation however, it is clear that hydrate was present low in the sample because gas evolved from hydrate dissociation again reduces the density (more red color).

Analysis

There should be leakage in the brine pump according to the brine pump volume data. The brine pump was closed between 233.0667 and 329.4 hours. During this time, the volume in the brine pump decreased by 0.74 ml. These data yielded a leakage rate of 0.0078 ml/hour. During the brine drainage and hydrate formation period, the volume in the brine pump increased from 250.8 ml at 1.4333 hour to 267.17 ml at 92.4 hour. This yielded a brine withdraw rate of 0.1800 ml/hour. The corrected brine withdraw rate should be 0.1878 ml/hour (=0.0078+0.1800 ml/hour) when the leakage rate was considered. The diameter of the sample is 2 inches or 5.08 cm. Therefore, the water flow rate at the downstream end of the sample is 2.57e-8 m/sec.

With the sample pressure of 6.96 MPa, temperature of 4 ^{o}C, initial salinity of 7 wt.% (NaCl), and brine withdraw rate of 2.57e-8 m/sec, we can predict the saturations, the hydrate solidification front velocity, and the gas consumption rate in Table 7. We compare the gas consumptions measured in the first period of the experiment with prediction from the MOC analytical solution (Figure 66). There is clearly a significant amount of induction time at the beginning when the measured gas consumption follows the 1:1 ratio of gas to brine volume (Figure 61: the blue line follows the red line for brine volume less than 6 ml). After that, the measured gas consumption increases with a greater rate. However, the measured gas consumption is still lower than the prediction from the MOC solution, which means the hydrate system does not reach three-phase equilibrium. This is consistent with the fact that the volume in the brine pump keeps decreasing in the imbibition period (red line in Figure 61c).

HVT0004

Experimental Setup

The sample was packed using slow pluvation, had a final length of 5.125", and was vacuum saturated with a 7 wt% NaBr brine. The porosity was gravimetrically calculated to be 0.393 (Table 6). The level of sample saturation was qualitatively assessed by increasing the confining fluid pressure and recording the pore pressure response. The b-value ($b = P_{pore} / P_{conf}$) was greater than 0.95, indicating a very well saturated sample. Once the system reached temperature and pressure equilibrium at experimental conditions, the methane pump was set to a constant pressure of 1775 psi and the brine pump was set to

a constant outflow of 0.003 mL/min (0.18 mL/hr). This experiment did not have a shut-in phase and it is likely that, after 57 hours, gas was flowing out of the sample, which rendered mass balance impossible. Therefore, we only analyze data from the first 57 hours here.

Data Collection

In this experiment, the volumes of gas and brine in the pumps was recorded by hand at 30-minute to 14-hour intervals and the confining, outlet, and inlet pressures and confining, coolant, and room temperatures were recorded at a 5-second interval by the DAQ.

Analysis

Gas Consumption Analysis

We compared the gas consumption during this and the following experiments to three end-member cases (Figure 67): 1) The gas consumption assuming no hydrate formation (dashed line), representing the minimum potential gas consumption, 2) The gas consumption assuming S_h = 1 behind the hydrate formation front (dot-dashed line), representing in the maximum potential gas consumption, and 3) The Methods of Characteristics (MOC)-predicted gas consumption (solid black line) at the experimental conditions (Flemings, 2015) representing the expected gas consumption for this experiment. Cases 1 and 2 calculate the gas consumption from equations 64 and 65, respectively:

$$V_g = V_b \quad \text{Eq 64}$$

$$V_g = \left[\frac{L_f}{L} \cdot V_{TOT} \cdot \phi\right] \cdot \left[\frac{\rho_h \cdot M_g}{M_h \cdot \rho_g}\right] \quad \text{Eq 65}$$

Where L is the length of the sample, L_f is the length of the hydrate formation zone (HFZ), V_{TOT} is the total sample volume, ρ_h and ρ_g are the densities of hydrate (0.912 g/cm^3) and methane gas (0.111 g/cm^3) phases, respectively, and M_h and M_g are the molecular masses of hydrate (119.655 g/mol) and methane gas (16.04 g/mol), respectively.

Figure 68 shows the gas consumption during HVT0004 experiment compared to three end member consumption models. Gas was consumed at a relatively constant rate of 0.32mL/hour, which is 49 percent of the consumption rate predict by the MOC solution. In total, 18mL of methane were consumed during the drainage phase, which was far below the MOC-predicted gas consumption. These results indicate that hydrate was not forming to three-phase equilibrium behind the front.

Bulk Phase Saturations from Mass Balance

We derived a set of mass balance equations (Appendix A), using the mass of water withdrawn and gas consumed (You et al., 2014), to calculate the bulk saturation of each phase (brine, hydrate, and

methane) behind the hydrate formation front throughout each experiment. We began with the following set of mass balance equations (Eqs. 66 – 68):

$$\Delta W = V_{TOT}\phi\rho_W \cdot \Delta S_W + \frac{V_{TOT}\phi\rho_H N M_W}{M_H} \cdot \Delta S_H \quad \text{Eq 66}$$

$$\Delta M = V_{TOT}\phi\rho_G \cdot \Delta S_G + \frac{V_{TOT}\phi\rho_H M_G}{M_H} \cdot \Delta S_H \quad \text{Eq 67}$$

$$0 = \Delta S_G + \Delta S_H + \Delta S_W \quad \text{Eq 68}$$

Where, ΔS_W, ΔS_H, and ΔS_G are the changes in saturation in the water, hydrate, and gas phases, respectively; ΔM and ΔW are the changes in methane and water masses in the pumps, respectively, ρ_g, ρ_h, and ρ_W are the density of the gas (0.111 g/cm^3), hydrate (0.912 g/cm^3), and brine (1.037 g/cm^3) phases, respectively, M_g, M_h, and M_W are the molecular masses of methane (16.04 g/mol), hydrate (119.655 g/mol), and water (18.02 g/mol), respectively, and N is the hydration number for Structure I methane hydrate (N = 5.75). Assuming that all the gas was either consumed by hydrate or was in the free gas phase, we derived Eqs. 69 – 71, from Eqs. 66 – 68:

$$\Delta S_G = \frac{\left[\left(\frac{V_{TOT}\phi\rho_H M_G}{M_H}\cdot\Delta W\right)+\left(\left(V_{TOT}\phi\rho_W - \frac{V_{TOT}\phi\rho_H N M_W}{M_H}\right)\cdot\Delta M\right)\right]}{\left[\left(V_{TOT}\phi\rho_W\cdot\left(V_{TOT}\phi\rho_G - \frac{V_{TOT}\phi\rho_H M_G}{M_H}\right)\right)-\left(\frac{V_{TOT}\phi\rho_H N M_W}{M_H}\cdot V_{TOT}\phi\rho_G\right)\right]} \quad \text{Eq 69}$$

$$\Delta S_W = \frac{\left[\left(\Delta S_G\cdot\left(V_{TOT}\phi\rho_G - \frac{V_{TOT}\phi\rho_H M_G}{M_H}\right)\right)-\Delta M\right]}{\frac{V_{TOT}\phi\rho_H M_G}{M_H}} \quad \text{Eq 70}$$

$$\Delta S_H = -(\Delta S_G + \Delta S_W) \quad \text{Eq 71}$$

Using these mass balance equations, we calculated the correct bulk hydrate, gas, and brine phase saturations behind the front during the drainage phase of HVT0004, compared to the predicted hydrate saturation required for three-phase equilibrium (Figure 69). The hydrate, brine, and gas saturations are approximately 0.18, 0.6, and 0.21, respectively. These results indicate that hydrate did not form at three-phase equilibrium as the front progresses through the sample.

Conclusions

The gas consumption data indicated that the hydrate formation rate was lower than the MOC-predicted rate. The mass balance-derived bulk hydrate saturation was lower than the predicted saturation from three-phase equilibrium. The results suggest that the hydrate in the sample is not at three-phase equilibrium and that hydrate formation is rate-limited.

HVT0005

Experiment Setup

The sample was packed using slow pluvation, had a final length of 5.125", and was vacuum saturated with a 7 wt% NaBr brine. The porosity was gravimetrically calculated to be 0.383 (Table 6). The level of sample saturation was qualitatively assessed by increasing the confining fluid pressure and recording the pore pressure response. The b-value was greater than 0.95, indicating a very well saturated sample. Once the system reached temperature and pressure equilibrium at experimental conditions, the methane pump was set to a constant pressure of 1775 psi and the brine pump was set to a constant outflow of 0.003 mL/min (0.18 mL/hr). After 57 hours, we stopped the brine pump, because gas was entering the outlet tube, which would cause errors in the mass balance, and let the sample sit for an additional 180 hours.

Data collection

In this experiment, the volumes of gas and brine in the pumps was recorded by hand at 30-minute to 14-hour intervals and the confining, outlet, and inlet pressures and confining, coolant, and room temperatures were recorded at a 5-second interval by the DAQ. Finally, while remaining in the vertical position, CT scans were taken at high (130 keV) and low (100 keV) energies throughout the experiment to quantitatively assess the distribution and saturation of the water, hydrate, and gas phases within the sample. Each CT scan consisted of 26 slices taken at 0.5cm spacing and a beam thickness of 1cm. Each slice consisted of a 512x512 matrix of attenuation values in Hounsfield units that included attenuation data from the material outside the sample. The slices were filtered to include only the pixel inside the sample, resulting in a 213x213 matrix where all cells external to the sample are occupied by zeros. From these processed slices, an average attenuation for the slice was calculated by summing all the attenuations in the slice and dividing it by the number of cells in the sample (approx. 35300 cells).

Analysis

Mass Balance

Figure 70 shows the gas consumption during the experiment compared to three end member consumption models. In total, 27 mL of methane were consumed during the experiment, which ended just above the gas consumption predicted by the MOC solution for hydrate formation. During the brine withdrawal phase (0 – 57 hours), gas was consumed at a relatively constant rate of 0.28mL/hour, which is 43 percent of the consumption rate predict by the MOC solution. After the brine pump was shut off, gas consumption continued, but at a greatly reduced average rate of 0.06 mL/hr. It also appears that, during this period (57 – 240 hours), the rate of gas consumption decreased over time as the total gas consumption approached the value predicted by the MOC model.

Using the previously derived mass balance equation (Appendix A), we calculated the correct bulk hydrate, gas, and brine phase saturations behind the front throughout the experiment, compared to the predicted hydrate saturation required for three-phase equilibrium (Figure 71). The hydrate, brine, and gas saturations are approximately 0.15, 0.6, and 0.25, respectively, during the drainage phase of the

experiment. After the brine pump is stopped, these values increase to 0.39, 0.48, and 0.13, respectively, by the end of the experiment. These results indicate that hydrate did not form at three-phase equilibrium as the front progresses through the sample.

CT-Derived Bulk Density

Figures 72 and 73 shows slice montages from the initial, brine-saturated core and of the sample at the end of the experiment, respectively. Darker regions are interpreted to be lower density, indicating the presence of hydrate and/or free gas in the core. These images show a low density region forming near the inlet of the sample. This region develops slowing over the course of the experiment and suggests the propagation of a hydrate formation front away from the inlet as the experiment progresses.

We calculate the bulk density profile of the sample using the CT data by assuming the CT-value to be directly proportional to the scanned bulk density. Since the solid mass is not changing (assuming no grain movement), then any change in bulk density is due to changes in the phases occupying the pore space. To perform this analysis, we initially collected calibration scans of a gas- and brine-saturated sample. The average attenuations for each slice in these scans were used as endpoint calibration values. The attenuations from the dry scan (CT_{dry}) were assumed to be the lowest expected attenuation, while those from the saturated scan (CT_{wet}) represented the highest expected attenuation. The attenuation values collected throughout the experiment (CT_{exp}) were then used, in combination with the endpoint values, to linearly interpolate (Eq. 72) between the dry (ρ_b^{dry}) and wet (ρ_b^{wet}) bulk density values to determine the experimental bulk density (ρ_b^{exp}).

$$\rho_b^{exp} = \left[\rho_b^{dry} + \left(\left(\rho_b^{wet} - \rho_b^{dry}\right) \cdot \left(\frac{(CT_{exp} - CT_{dry})}{(CT_{wet} - CT_{dry})}\right)\right)\right] \quad \text{Eq 72}$$

The CT attenuation values are averaged across the entire slice to reduce the chance of anomalies resulting in non-physical saturations. The dry and wet bulk density of the sample was calculated to be 2.03 g/cm^3 and 1.67 g/cm^3, respectively, using the standard density equation (Eqs. 73 and 74) and knowledge of the porosity of the sample and density of the sediment (ρ_s), brine, and gas:

$$\rho_b^{dry} = \left((1 - \phi) \cdot \rho_s\right) + \left(\phi \cdot \rho_g\right) \quad \text{Eq 73}$$

$$\rho_b^{wet} = \left((1 - \phi) \cdot \rho_s\right) + \left(\phi \cdot \rho_w\right) \quad \text{Eq 74}$$

Figure 74 shows a combined analysis of the CT images and CT-derived bulk density for HVT0005 at the end of the drainage phase (blue line) and shut-in phase (red line). At the end of the drainage phase, we interpret three zones to be present: 1) hydrate formation zone (HFZ) (0 – 5.5 cm); 2) gas invasion zone (5.5 – 9.5 cm) (GIZ); and 3) a water saturated zone (9.5 – 12 cm) (WSZ). The CT images show that there is a large decrease in density near the inlet (0 – 1.75cm). We attribute this to the presence of a high gas saturation in this region. The uniform drop in density in the rest of the HFZ suggests a relatively uniform gas and hydrate saturation in the hydrate formation zone. In the HFZ, the experimental hydrate saturation is interpreted as be approximately 0.2 according to the mass balance results. In the GIZ, the

density increases back to nearly initial values. In this region, there is likely some hydrate present, however the density gradient is likely due to a decrease in gas saturation further from the inlet. In the WSZ, densities are approximately equal to the initial value and this is interpreted to be brine-saturated with no free gas or hydrate present. At the end of the experiment, the bulk density within the HFZ and GIZ have increased, due to the additional formation of hydrate and consumption of gas.

CT-Derived Bulk Phase Saturations

We derived a set of equations to calculate the phase saturation profiles (Appendix B) throughout the experiment similar to those presented in Seol and Kneafsey, 2011 and You, K., et al., 2014. The derivation begins with Equation 75, which defines our experimental bulk density as a function of the porosity, grain and phase density, and phase saturations and Equation 76, which defines the fraction of the pore space that is occupied by each phase:

$$\rho_b^{exp} = \left((1 - \phi) \cdot \rho_s\right) + \left(S_W \cdot \phi \cdot \rho_W\right) + \left(S_G \cdot \phi \cdot \rho_G\right) + \left(S_H \cdot \phi \cdot \rho_H\right) \quad \text{Eq 75}$$

$$S_W + S_H + S_G = 1 \quad \text{Eq 76}$$

The saturation (S_g, S_H, and S_w) are unknown. To continue the derivation, we make the following critical assumptions: 1) Gas density is negligible, 2) brine density remains constant, C) the solid grains in the sample do not move, and 3) hydrate only forms within HFZ. With these assumptions, equations 77 – 79 are derived to solve for the phase saturations:

$$S_w = \frac{S_T}{\left(1 + \frac{Xf}{(1-X-Y)}\right)} \quad \text{Eq 77}$$

$$S_H = \left[\frac{S_T}{\left(1 + \frac{(1-X-Y)}{Xf}\right)}\right] \cdot \left[\frac{\rho_w}{\rho_h}\right] \quad \text{Eq 78}$$

$$S_G = 1 - S_w - S_H \quad \text{Eq 79}$$

Where S_T is the total saturation, *X* is the fraction of the initial water converted into hydrate, *Y* is the fraction of initial water removed from the sample, and *f* is the mass ratio of hydrate to water in hydrate, equal to 1.15. These values are defined by equations 80 – 82:

$$S_T = \left(\frac{\rho_b^{exp} - \rho_b^{dry}}{\rho_b^{wet} - \rho_b^{dry}}\right) \quad \text{Eq 80}$$

$$X = (\Delta V_m - \Delta V_w) \cdot \frac{M_w \cdot N \cdot \rho_H}{V_{pore} \cdot \rho_w \cdot (1-C) \cdot M_H} \cdot \frac{L_{HFZ}}{L} \quad \text{Eq 81}$$

$$Y = \frac{\Delta V_w \cdot \rho_w}{V_{pore} \cdot \rho_w} \cdot \frac{L_{HFZ}}{L} \quad \text{Eq 82}$$

Where ΔV_m and ΔV_w are the changes in volume in the methane and brine pumps, respectively, V_{pore} is the pore volume ($V_{pore} = V_{TOT} \cdot \phi$), C is the initial salinity in weight percent, L is the total sample length, and L_{HFZ} is the length of the HFZ. X and Y are corrected for the location of the hydrate formation using the ratio between L and L_{HFZ}.

The denominator of equations 77 and 78 weights the total saturation by the fraction of the total change in water mass in the sample that is due to hydrate formation. As more hydrate formed the denominator in equation 77 increases, reducing S_W while the denominator of equation 78 decreases, showing greater values for S_H. For slices taken beyond the extent of the HFZ, X and Y are assumed to equal zero, which forces $S_H = 0$, $S_W = S_T$, and $S_G = 1 - S_W$, such that any changes in density from the initial are due to gas invasion. For the analysis of this experiment, we assumed that there was no GIZ and that the HFZ extended from 0 – 8cm.

During the brine withdrawal phase (0 – 57 hours) in HVT0005, the CT-derived hydrate saturation profiles (Figure 75B) indicate that hydrate continuously forms throughout the HFZ, which was assumed to be between 0 – 8cm and was confirmed through CT scan images. The rate of hydrate formation increases later in the experiment, but the overall saturation within the HFZ is essentially uniform, ranging from 0.12 – 0.15. The CT-derived gas saturation profiles (Figure 75C) directly mirror the observed changes in density, showing regions with large density decreases as having a greater gas saturation. As the methane is the lowest density phase in the system, the gas saturation will logically be the greatest controlling factor on changes in density. The water saturation profiles (Figure 75D) show the largest decrease in water saturation near the inlet, where the gas saturation is the largest, a constant, uniform decrease in water saturation from 2 – 8cm, and very little drop in water saturation from 8 – 13cm.

After the brine pump was shut off and the outlet valve was closed in HVT0005 (57 – 172 hours), the bulk density profiles (Figure 76A) indicated the development of three distinct zones within the sample. Zone 1 extends from 0 – 3.75cm and the density continues to decrease over time, reaching a minimum density of 1.92 g/cm^3 near the inlet. Zone 2 extends from 3.75 – 8.25cm and is characterized by a rebound in bulk density back to near initial values, with a final range from 1.99 – 2.03 g/cm^3. Zone 3 extends from 8.75 – 13cm and is the only portion of the sample where the density increases above the initial value, reaching a max density of 2.045 g/cm^3.

The hydrate saturation profiles (Figure 76B) indicate that, after the brine pump was stopped, hydrate begins forming at a more rapid rate within Zone 2, relative to Zone 1, reaching a maximum saturation of

0.35. The overall rate of hydrate formation all appears to decrease over time, indicated by the change in saturation between time steps. The gas saturation profiles (Figure 76C) again mirrors the bulk density profiles, with a maximum gas saturation of 0.31 near the inlet and decreasing across the core. The water saturation profiles (Figure 76D) show an overall decrease in water saturation within in Zones 1 and 2, with a larger decrease in Zone 1.

The CT-derived saturations are lower than those calculated from the mass balance. This is likely due to the assumption that the HFZ extends from 0 – 8cm, which is 2.5 cm further down the core than predicted by the model. Regardless of this, however, these results suggest that hydrate front is not stable and does not form to three-phase equilibrium as the front progresses down the sample.

Conclusions

The mass balance results show that hydrate forms at a saturation far below the predicted three-phase saturation during the drainage phase and then continues to form after the brine pump is stopped. The CT-derived bulk density data indicates that there is a gas front that is moving ahead of the predicted hydrate formation front during the drainage phase and that hydrate continues to form in both the HFZ and GIZ during the shut-in phase. The CT-derived phase saturation data show uniform hydrate formation throughout the assumed HFZ during the drainage phase. Additional hydrate forms within the HFZ during the shut-in phase, with formation concentrated in Zone 1. These results suggest that hydrate formation is not homogeneous within the sample and that the hydrate is not forming to three-phase equilibrium within the HFZ.

HVT0007

Experimental Setup

The sample was packed using slow pluvation, had a final length of 5.125”, and was vacuum saturated with a 7 wt% NaBr brine. The porosity was gravimetrically calculated to be 0.393 (Table 6). The level of sample saturation was qualitatively assessed by increasing the confining fluid pressure and recording the pore pressure response. The b-value was greater than 0.95, indicating a very well saturated sample. Once the system reached temperature and pressure equilibrium at experimental conditions, the methane pump was set to a constant pressure of 1775 psi and the brine pump was set to a constant outflow of 0.003 mL/min (0.18 mL/hr). After 57 hours, we stopped the brine pump to match the execution of HVT0005.

Data Collection

In this experiment, the gas, brine, and confining volume and inlet, outlet, and confining pressure data, from both the pumps and inline transducers, were recorded at set intervals throughout the experiment by the DAQ system. Data was initially recorded every 10 seconds and was increased in several

increments to 2 minutes by the end of the experiment. Although the shorter interval was nice near the beginning of the experiment to confirm in real time that the experiment was running properly, we determined that it was recording an unnecessary amount of data after the first few hours.

Analysis

Figure 77 shows the gas consumption over the course of the experiment (pink line) compared to the three end member consumptions models. In total, 31 mL of methane were consumed during the experiment, which ended just above the gas consumption predicted by the MOC solution for hydrate formation. During the brine withdrawal phase (0 – 57 hours), gas was consumed at a relatively constant rate of 0.32mL/hour, which is 50 percent of the consumption rate predict by the MOC solution. After the brine pump was shut off, gas consumption continued, but at a greatly reduced average rate of 0.15 mL/hr. It also appears that, during this period (57 – 144 hours), the rate of gas consumption decreased over time as the total gas consumption approached the value predicted by the MOC model.

Figure 78 shows the bulk hydrate, water and gas phase saturations throughout the experiment calculated from mass balance equations dependent on the volumes of brine withdrawn and gas consumed. The bulk hydrate, water, and gas saturations reach final values of 0.24, 0.56, and 0.20, respectively. After the brine pump was stopped, these values continue to change to a final saturation of 0.62, 0.27, and 0.11, respectively. These results indicate that hydrate did not form at three-phase equilibrium as the front progresses through the sample.

Conclusions

The gas consumption data indicated a hydrate formation rate below the MOC-predicted rate and showed continued hydrate formation after the brine pump was shut-in. The bulk phase saturations showed a hydrate saturation far below the three-phase equilibrium saturation during the drainage phase that increased during the shut-in phase. These result suggest that hydrate formation is rate limited and that the hydrate in this experiment did not form at three-phase equilibrium.

HVT0008

Experimental Setup

The sample was packed using slow pluvation, had a final length of 4.875”, and was vacuum saturated with a 7 wt% NaBr brine. The porosity was gravimetrically calculated to be 0.377 (Table 6). The level of sample saturation was qualitatively assessed by increasing the confining fluid pressure and recording the pore pressure response. The b-value was greater than 0.95, indicating a very well saturated sample. Once the system reached temperature and pressure equilibrium at experimental conditions, the methane pump was set to a constant pressure of 1775 psi and the brine pump was set to a constant

outflow of 0.001 mL/min (0.06 mL/hr). After 57 hours, we stopped the brine pump to match the execution of HVT0005 and HVT0007.

Data Collection

Data collection for this experiment followed the same procedures as HVT0007.

Analysis

Figure 79 shows this data for HVT0008 during the drainage (0 – 171 hours) and shut-in (171 – 186 hours) phases. During the drainage phase of HVT0008, gas was consumed at 80 percent of MOC-predicted rate. During the shut-in phase, gas was continuously consumed, reaching 91 percent of the MOC-predicted gas consumption, indicating further hydrate formation and suggesting that the system was not at bulk thermodynamic equilibrium behind the formation front.

Figure 80 shows the mass balance-derived bulk water (blue line), gas (red line), and hydrate (green line) phase saturation behind the formation front during the first 17 hours of the experiment (Figure 80A) and over the entire experiment (Figure 80B). These phase saturations are compared to the predicted three-phase equilibrium hydrate saturation (S_h = 0.76) according the MOC solution and used to interpret three periods with distinct hydrate formation behavior. Period 1 (0 – 1 hours) shows little to no hydrate formation, followed by dramatic hydrate formation at the beginning of Period 2 (Figure 80A). We interpret this period to represent the induction time for the experiment.

In Period 2 (1 – 17 hours), following the rapid formation of hydrate to a saturation of approximately 0.65, the hydrate saturation drops to 0.21 at a decreasing rate (Figure 80A). We interpret that this is due to a hydrate formation rate that is lower than predicted due to a small number of nucleation sites behind the front. Over the course of Period 2, the number of nucleation sites grows, which increases the hydrate formation rate until, at 17 hours, the formation rate matches the predicted rate.

In Period 3 (17 – 186 hours), the bulk hydrate saturation increases steadily from 0.31 to 0.67 (Figure 80B), which is 87 percent of the predicted three-phase equilibrium saturation for these experimental conditions. We interpret that, during this period, the hydrate formation rate is greater than the predicted, because additional nucleation sites over time continue to increase the formation rate. This is also possible, because the system is not at bulk three-phase equilibrium and, therefore, hydrate formation is not limited by thermodynamics.

Conclusions

A detailed analysis of the phase saturation data indicates that this experiment had an induction time of only 1 hour and that over the course of the experiment the hydrate formation rate continued to increase. This is potentially due to an increase number of nucleation sites behind the front. The total

experimental gas consumption is lower than the predicted, the hydrate saturation during the drainage phase is always below the modeled three-phase saturation and increases during the shut-in phase. Therefore, despite the high hydrate formation rate, these results suggest that hydrate formation is rate-limited and that the hydrate in our sample did not form to three-phase equilibrium.

UT Experiment Comparison

Figure 81 shows the gas consumption data from the drainage phase of all four experiments we have run successfully at UT Austin: HVT0004 (blue line), HVT0005 (green line), HVT0007 (pink line), and HVT0008 (orange line) compared to the three end member solutions. Other than small variations in the sample porosity, the only variable parameter between these experiments is the flow rate (Table 6). The high flow rate experiments (HVT0004, HVT0005, and HVT0007) show a repeatable, rate-limited hydrate formation behavior where hydrate is forming at 46 percent of the MOC-predicted rate, indicating the system is not running at three-phase equilibrium. The low flow rate experiment (HVT0008) has a gas consumption rate that is 80 percent of the MOC-predicted value, indicating that the system is still not running at three-phase equilibrium, but is 1.7 times closer due to the lower flow rate. This indicates that lowering the flow rate reduces the rate-limitation on hydrate formation.

Figure 82 shows the gas consumption from the two experiments (HVT0005 and HVT0007) we've completed where the brine pump was shut off at 57 hours (black vertical line). Similar to Figure 61, the results are compared to the MOC solutions during a gas flooding and hydrate formation case, as well as the maximum potential gas consumption. After the brine pump was shut off, the gas consumption rate in HVT0005 and HVT0007 drops to 0.07 and 0.18 mL/hr, respectively. In both experiments, when the brine pump was stopped, that immediately reduced the gas consumption rate by 0.18 mL/hr, because brine withdrawal is no longer creating free space for gas. This accounts for 72% and 95% of the drop in average consumption rate in HVT0005 and HVT0007, respectively, but not the other 28 – 5% remaining. Additionally, the overall gas consumption rate decreases over time as both experiments near the MOC predicted gas consumption.

Test No.	Location	Brine Stopped	Temp Control Box	ϕ	P_{pore} (psi)	T_{conf} (degC)	Flow Rate (m/yr)	Salinity (wt%)	Salt
HVT0001	LBNL	Y	N	0.336	1000	4	0.78	0.07	NaCl
HVT0004	PRC	N	N	0.393	1775	1	0.78	0.07	NaBr
HVT0005	PGE	Y	N	0.383	1775	1	0.78	0.07	NaBr
HVT0007	PRC	Y	Y	0.393	1775	1	0.78	0.07	NaBr
HVT0008	PRC	Y	Y	0.377	1775	1	0.26	0.07	NaBr

Table 6: Experimental parameters for each of the successful hydrate formation experiments performed during Phase 2.

Hydrate saturation	0.275
Gas saturation at the gas inlet	0.303
Gas saturation at the front	0.652
Front moving velocity, mm/hour	0.62
Gas consumption rate, ml/hour	0.4139

Table 7: Predictions from the MOC analytical solution.

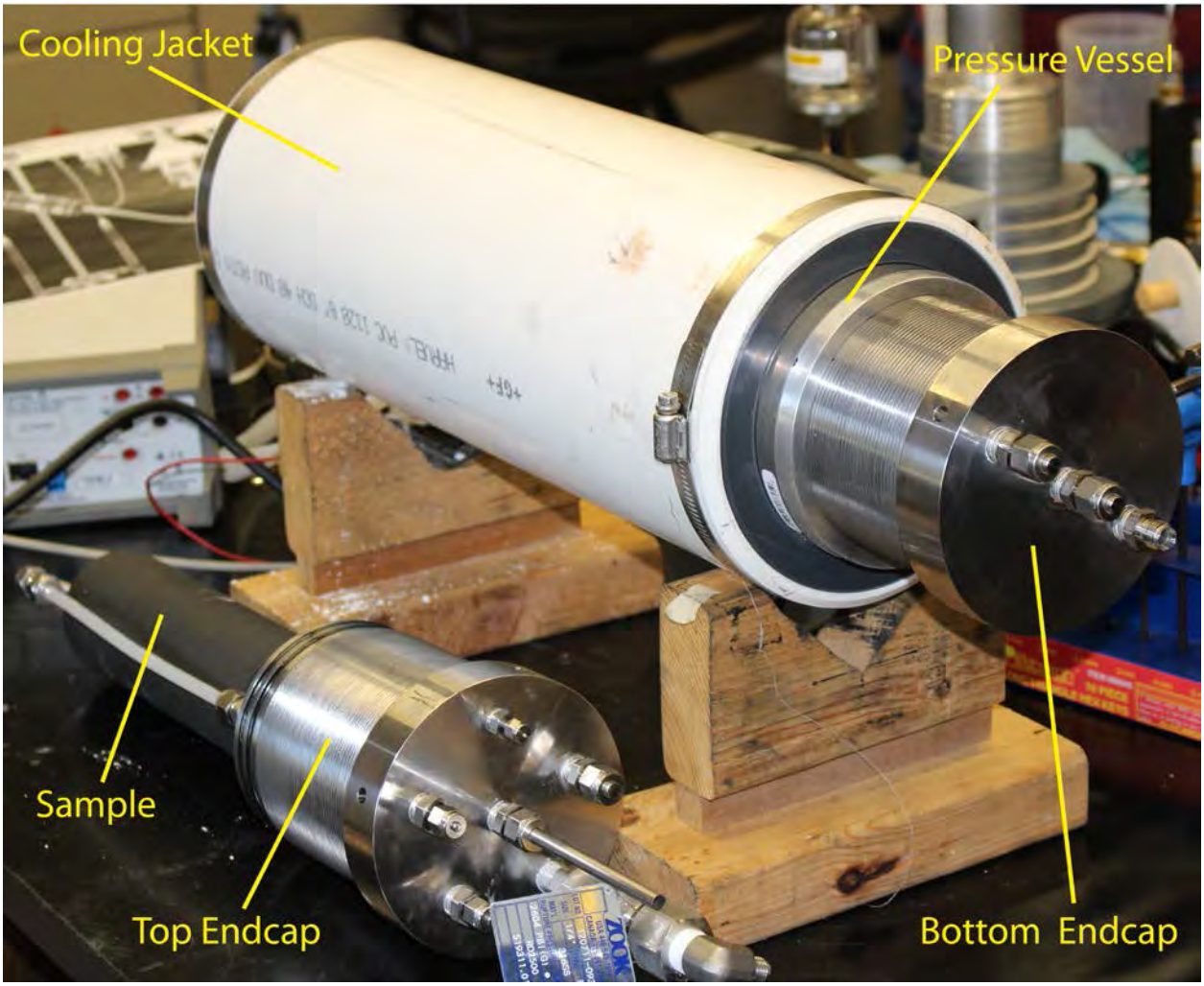

Figure 54. Disassembled hydrate formation vessel showing the top and bottom endcaps, the sample and fluid tubing, and the cooling jacket surrounding the aluminum sleeve.

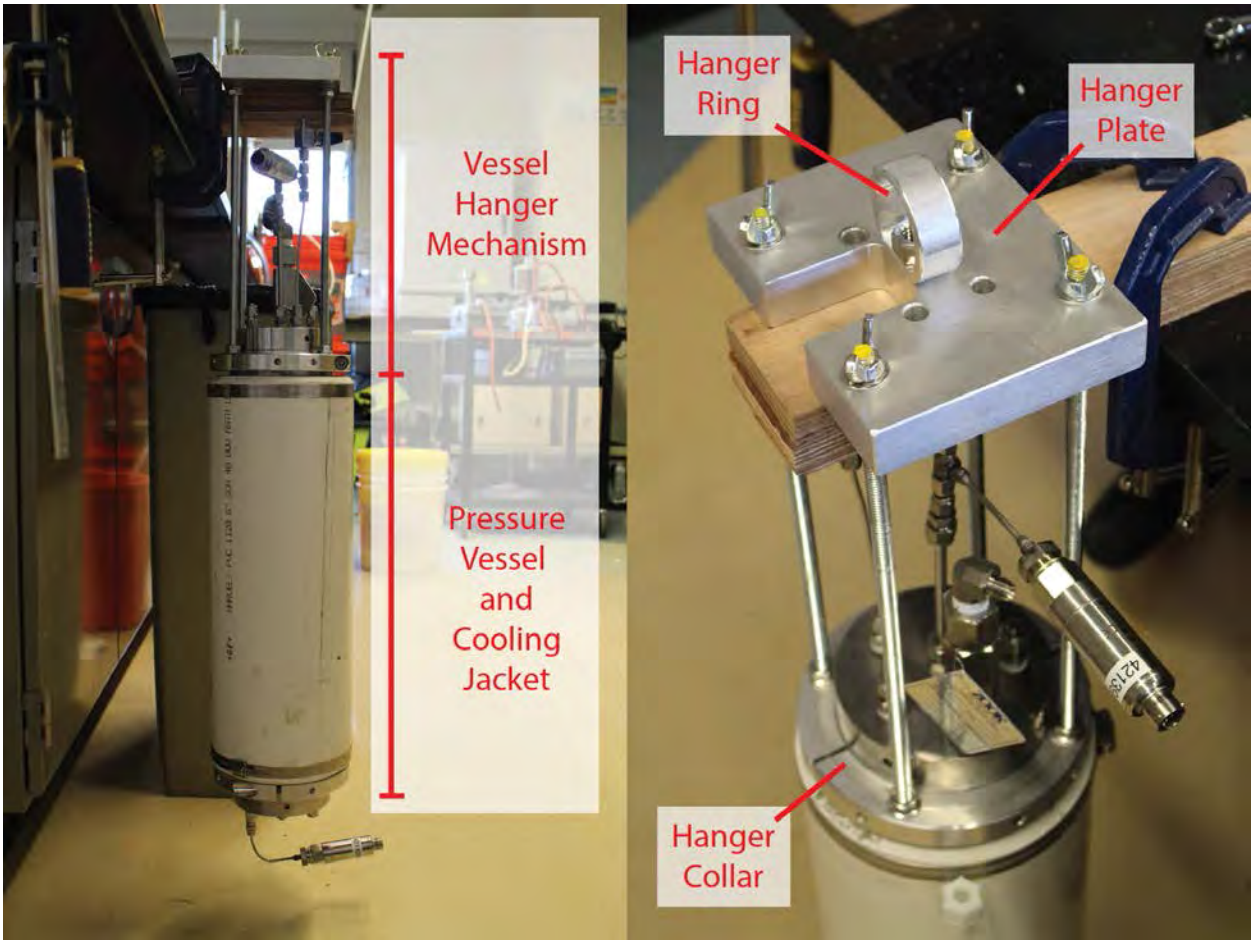

Figure 55: Image of hydrate formation vessel and hanger.

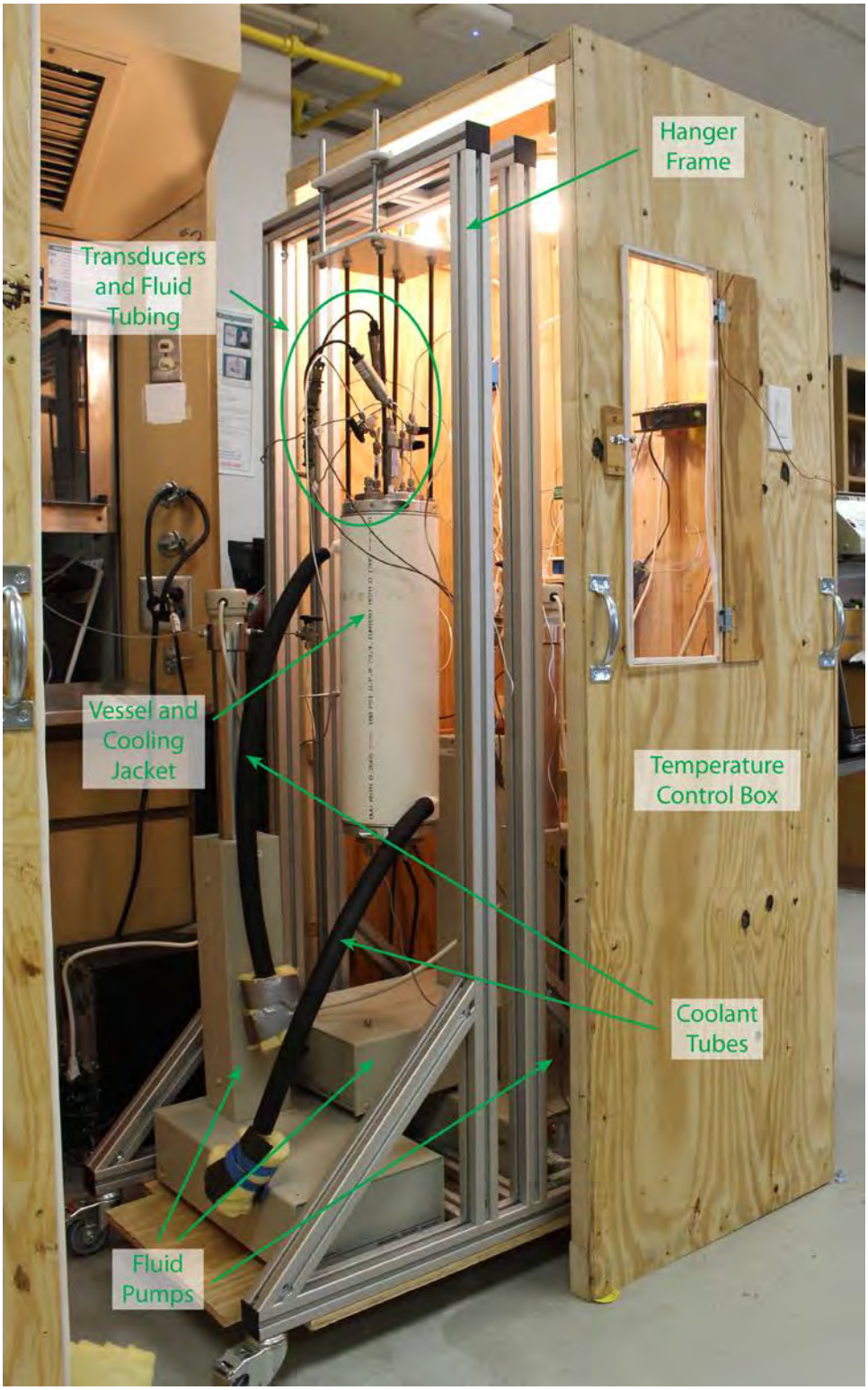

Figure 56: Hydrate formation vessel, aluminum hanger frame, and pore fluid pumps contained within the temperature control box. The two halves of the box close together to insulate the inside from the external room temperature. Four incandescent light bulbs act as heat sources to maintain a constant internal temperature.

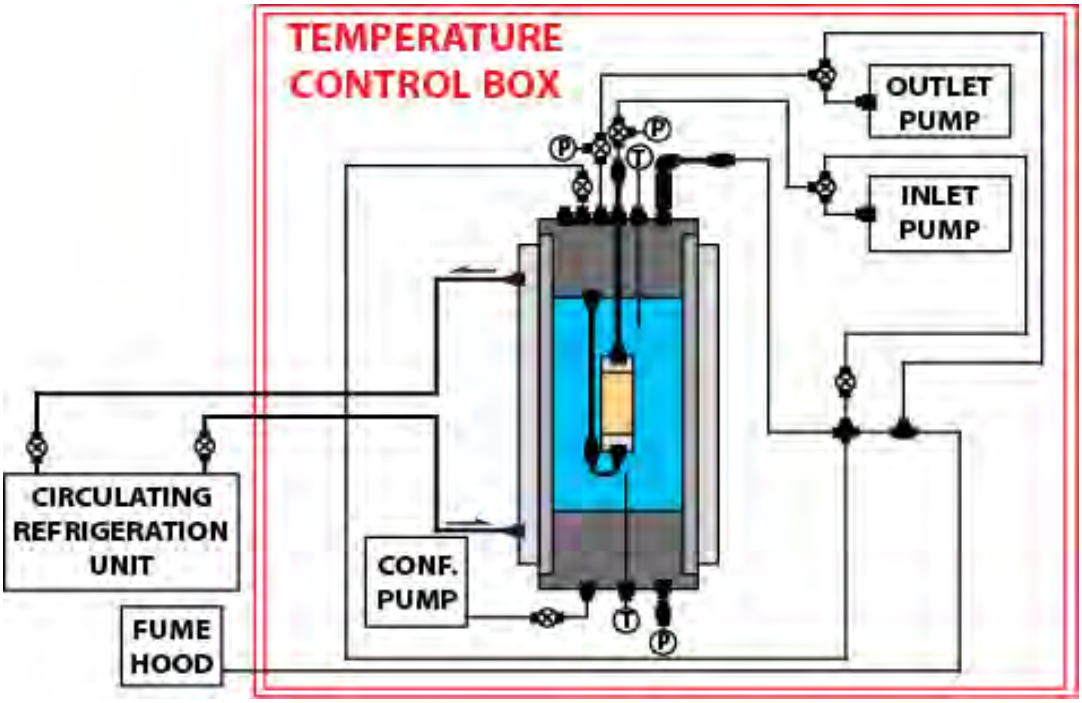

Figure 57: Schematic of the updated equipment setup for HVT0007 and associated plumbing and fittings. Inlet, outlet, and confining pumps were placed inside the temperature control box box to buffer them from diurnal temperature changes. P = pressure transducer; T = thermocouple.

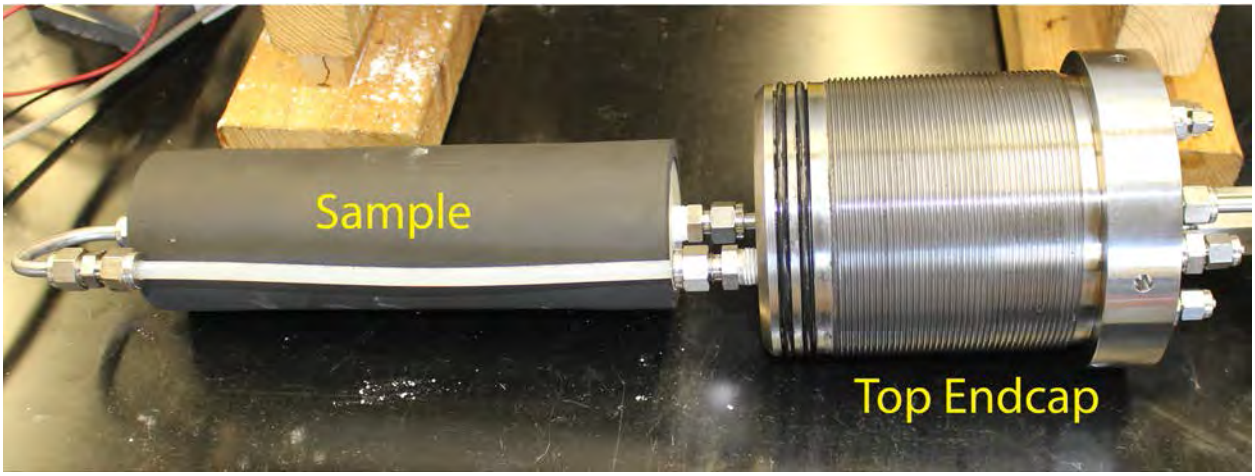

Figure 58: Image of sample connected to the top endcap by the inlet and outlet pore fluid tubing. Sample is encased in a 2" ID Viton sleeve.

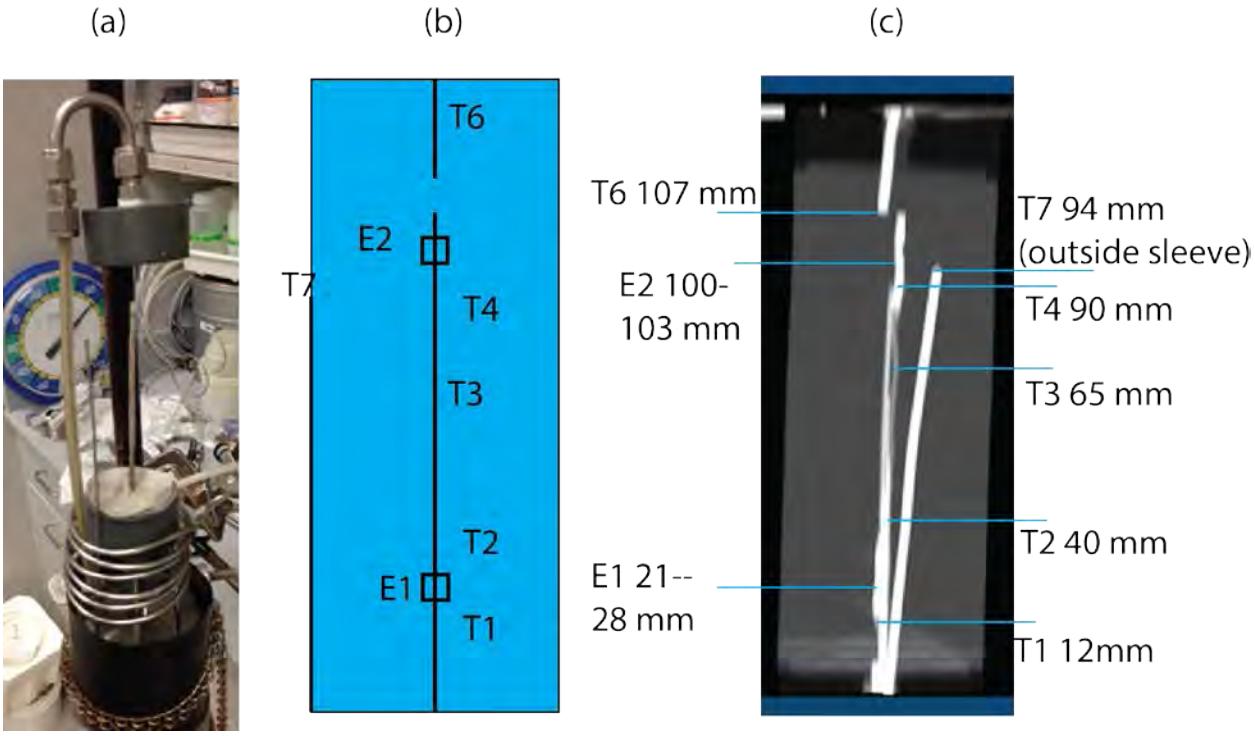

Figure 59: Instrument setup for thermocouples and electrodes in the sample and vessel. a. photo of assembly without EPDM sleeve or sample showing grey PVC endpieces, garolite rod with thermocouples and electrodes. b. schematic arrangement of instruments, c. X-ray image showing actual locations.

(a)

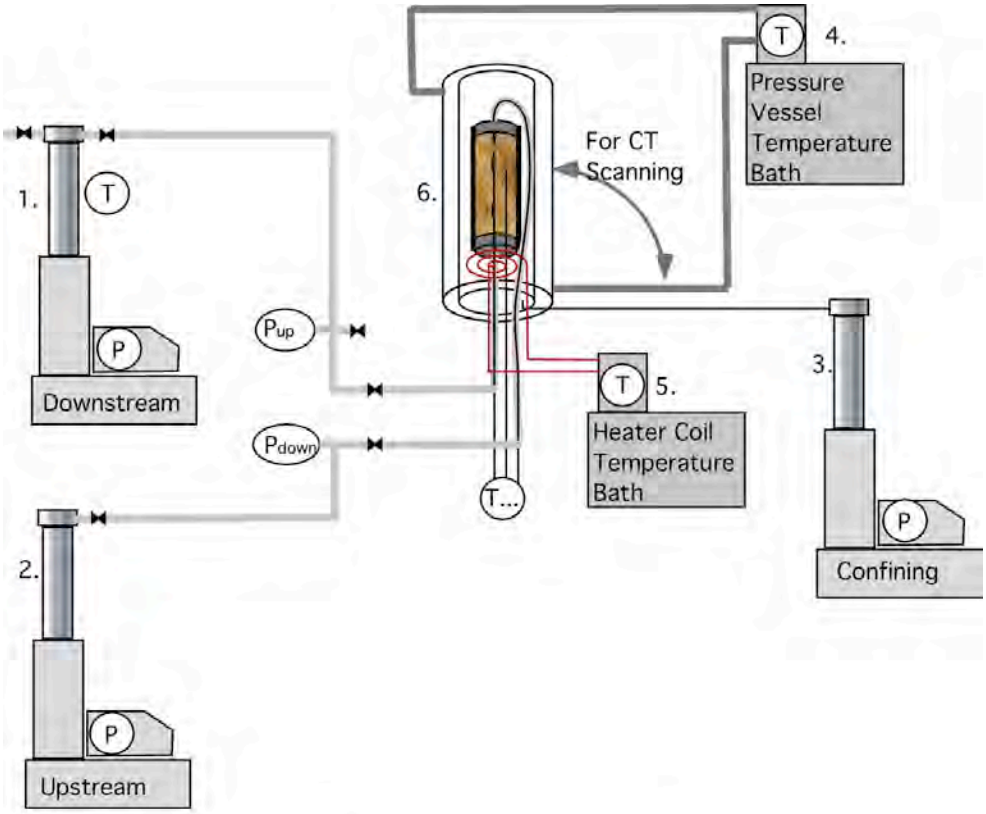

1 - 3. ISCO 500D High Pressure Syringe Pump
4-5. Temperature Controllers
6. Pressure Vessel w/ Sample

(b)

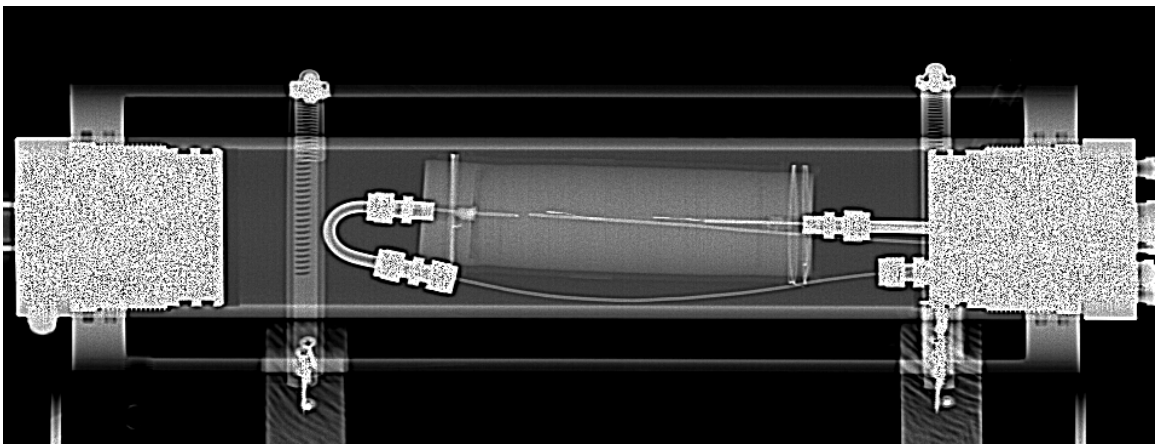

Figure 60: System setup. a. schematic showing sample configuration with respect to pumps controlling brine inlet to the sample bottom (downstream pump), gas inlet to the sample top (upstream pump), a pump to maintain confining pressure around the sample, and temperature control baths. b. X-ray scan showing sample, pressure vessel, and thermal jacket.

(a)

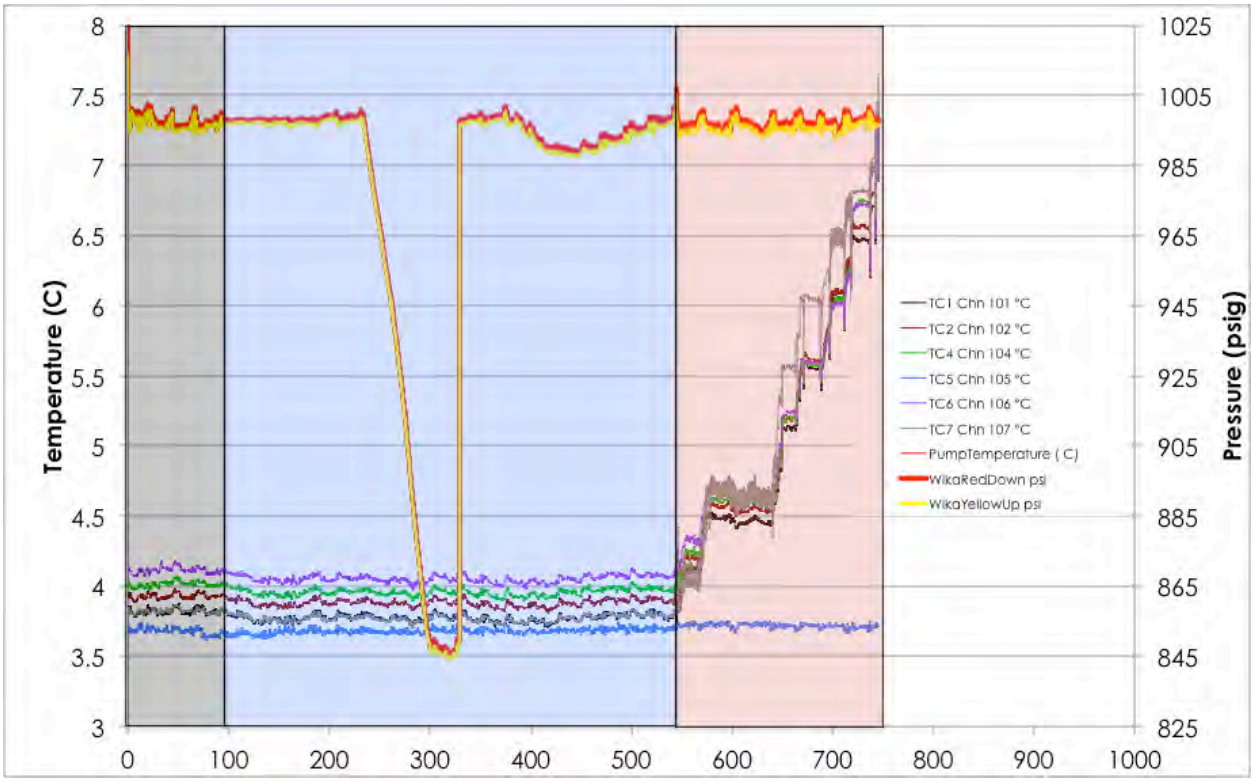
Temperature (C)
Pressure (psig)
8
7.5
7
6.5
6
5.5
5
4.5
4
3.5
3
1025
1005
985
965
945
925
905
885
865
845
825
0
100
200
300
400
500
600
700
800
900
1000
TC1 Chn 101 °C
TC2 Chn 102 °C
TC4 Chn 104 °C
TC5 Chn 105 °C
TC6 Chn 106 °C
TC7 Chn 107 °C
PumpTemperature (C)
WikaRedDown psi
WikaYellowUp psi

(b)

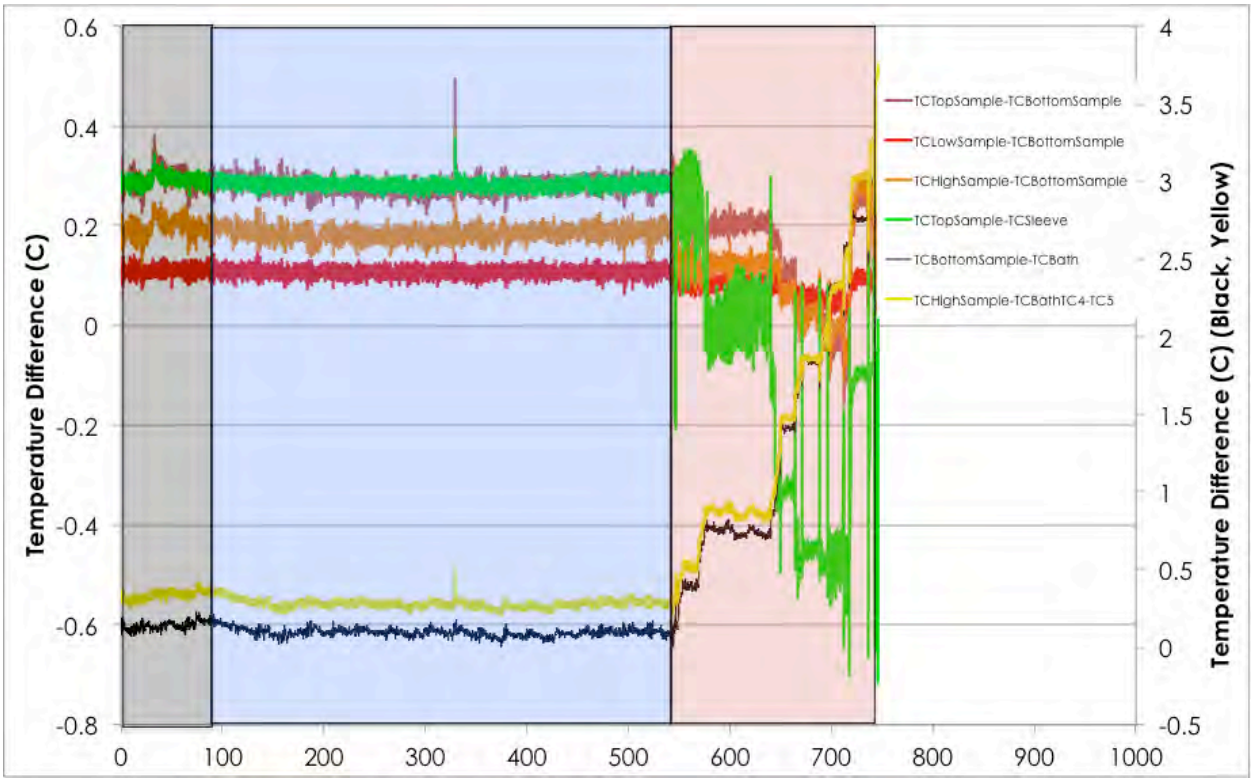
Temperature Difference (C)
Temperature Difference (C) (Black, Yellow)
TCTopSample-TCBottomSample
TCLowSample-TCBottomSample
TCHighSample-TCBottomSample
TCTopSample-TCSleeve
TCBottomSample-TCBath
TCHighSample-TCBathTC4-TC5
0.6
0.4
0.2
0
-0.2
-0.4
-0.6
-0.8
4
3.5
3
2.5
2
1.5
1
0.5
0
-0.5
0
100
200
300
400
500
600
700
800
900
1000

(c)

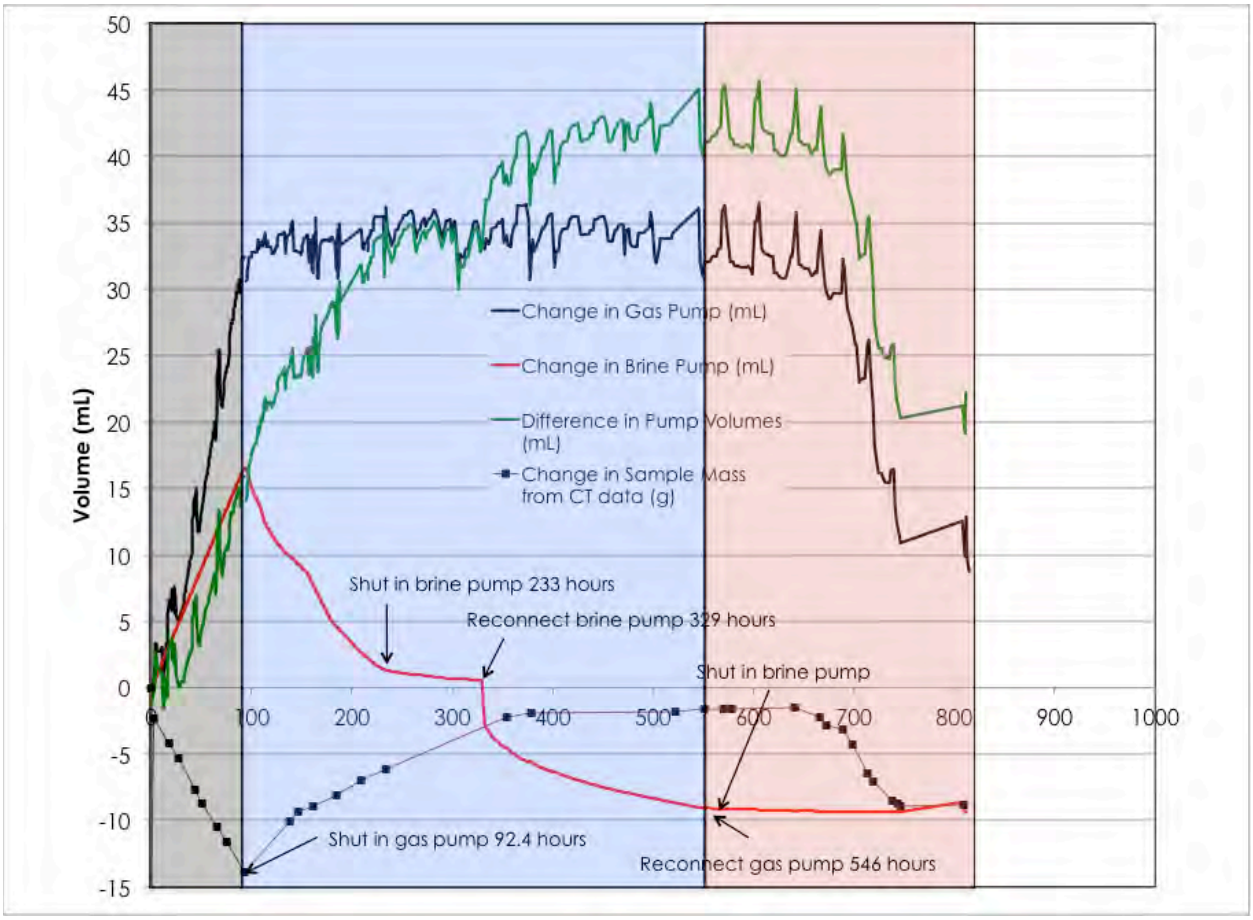

Figure 61: Test conditions. a. Temperatures and pressures over the test duration, b. temperature differences over the test duration, and c. fluid volumes from the syringe pumps, and sample mass computed from X-ray CT scans.

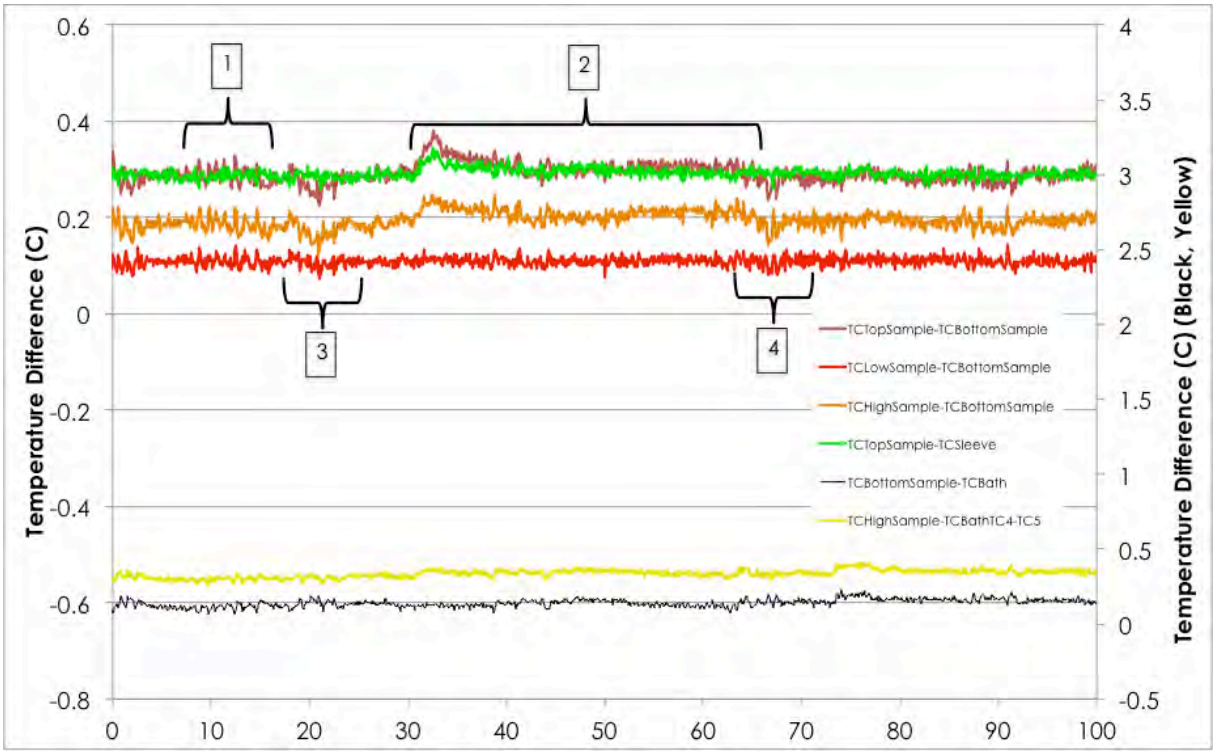

Figure 62: Temperature differences over the drainage test. Increases indicate hydrate formation.

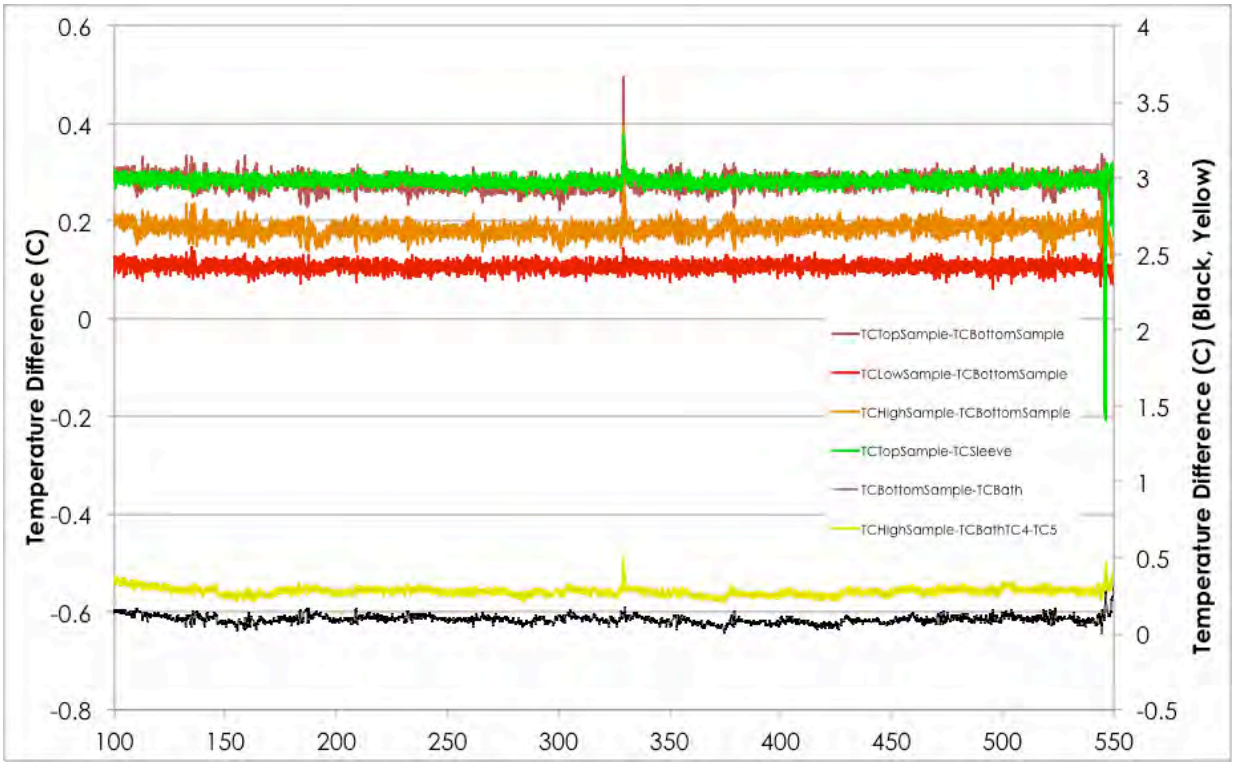

Figure 63: Temperature differences over the imbibition test. Increases indicate hydrate formation.

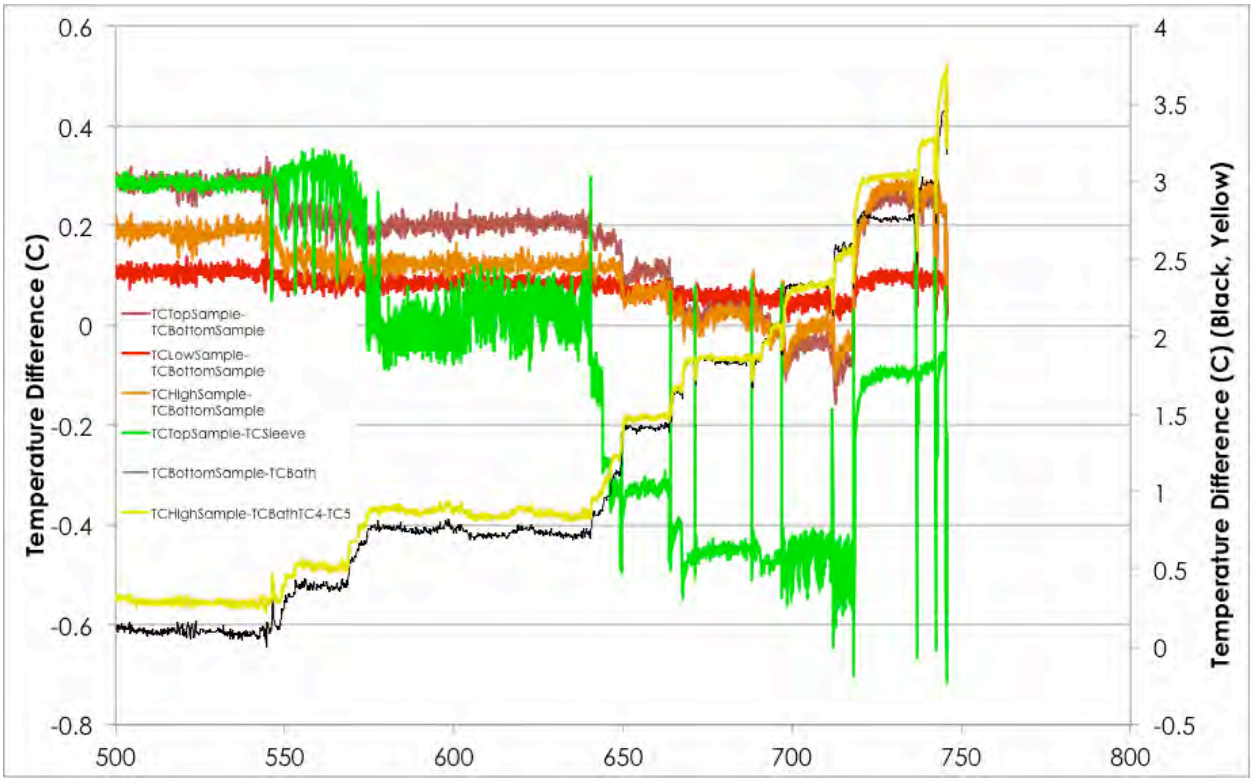

Figure 64: Temperature differences during dissociation. Temperature gradients neutralized and reversed over the 650 to 720 hour period when hydrate dissociation was dominant.

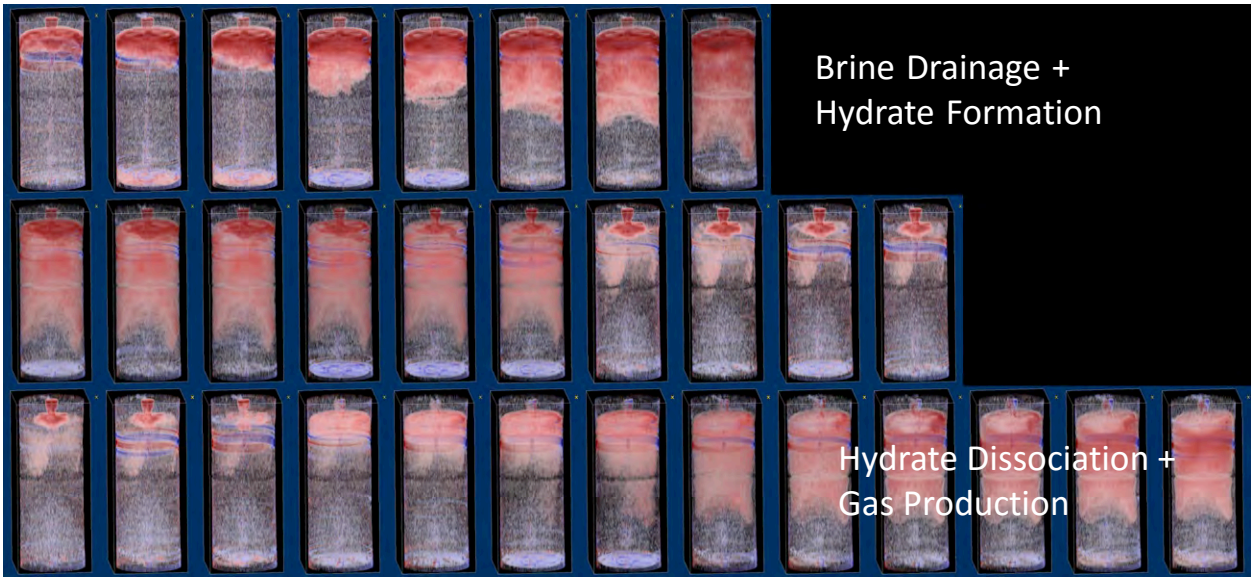

Figure 65: X-ray CT difference images showing density changes in the sample. Red indicates lower density than the initial condition (the highest density) and blue shows increases in density.

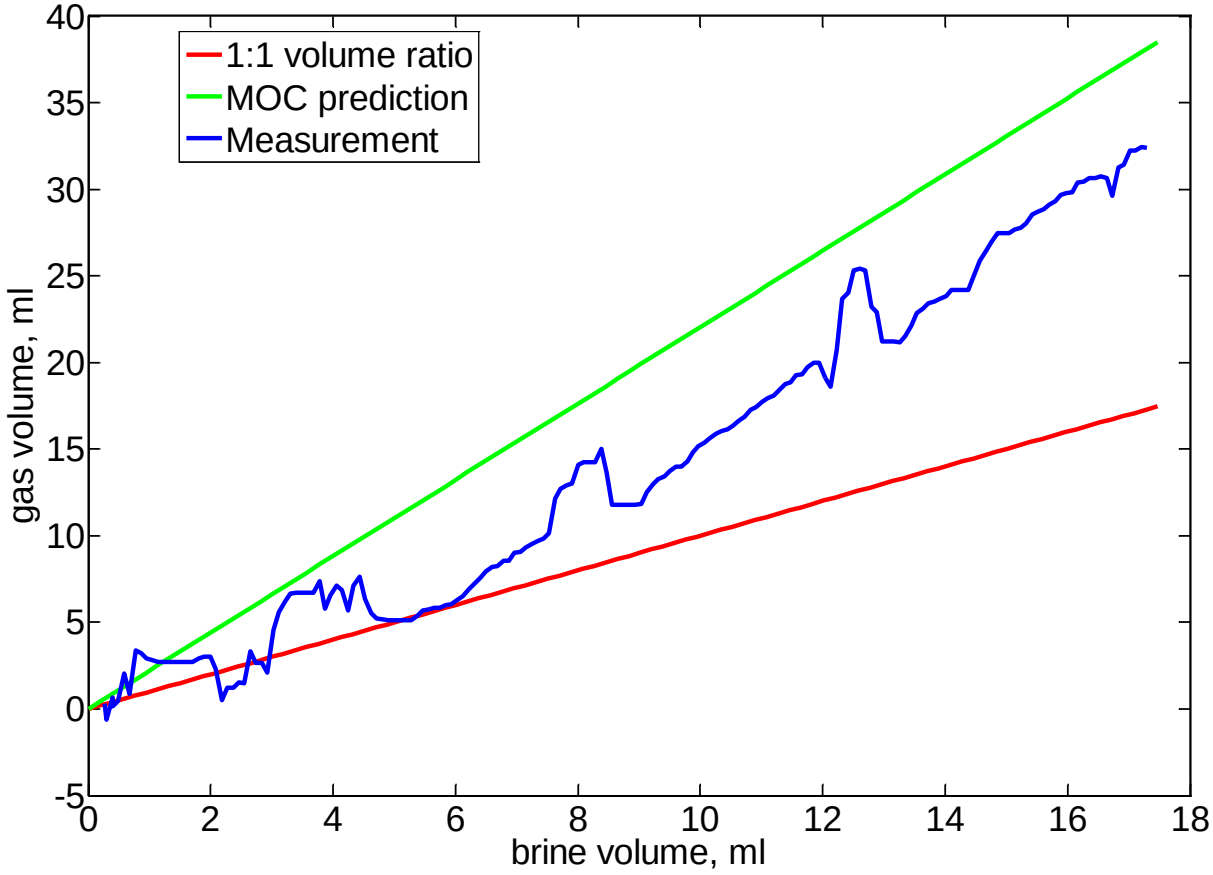

Figure 66: Comparison of gas consumption data for hydrate formation front experiment HVT0001 (blue line). Red line indicates the MOC solution for a gas flooding experiment and indicates the minimum gas consumption needed to maintain volume balance. Green line indicates the gas consumption predicted from the MOC solution for these experiments calculated at the experimental temperature and pressure conditions.

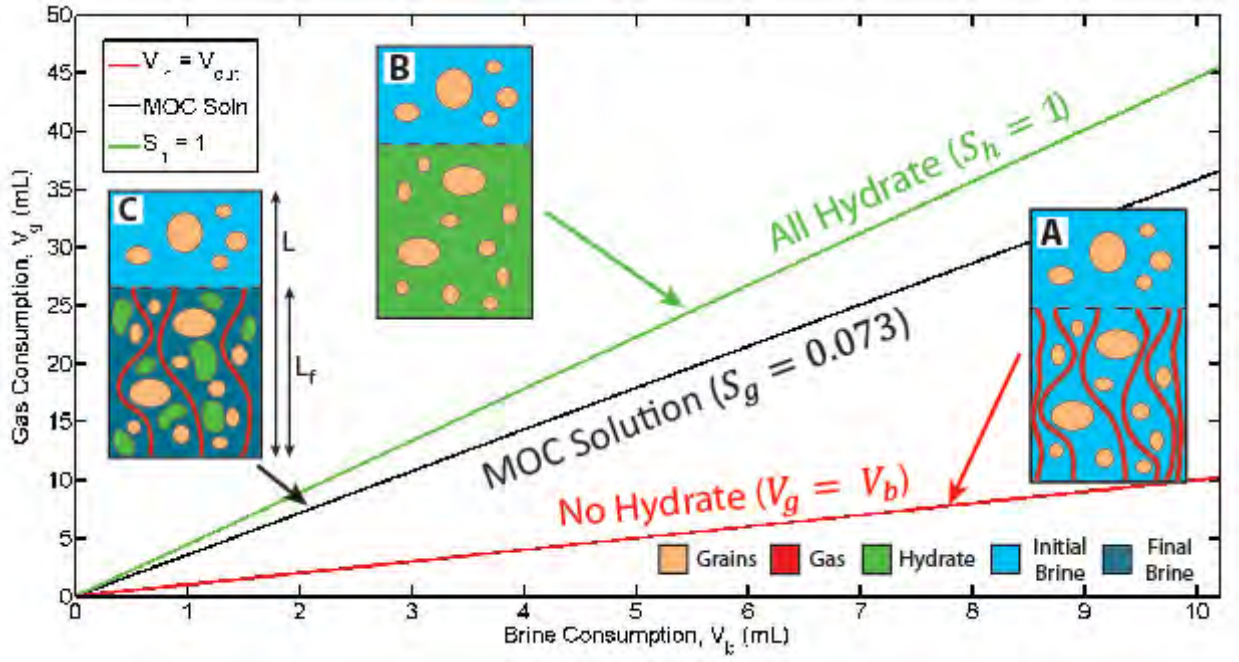

Figure 67: Description of the three gas consumption end member cases: A) no hydrate phase (red line); B) hydrate phase only (green line); C) the Methods of Characteristics (MOC) solution (black line). The no hydrate phase line assumes volume balance between the water withdrawn and the gas consumed. The hydrate phase only line assumes the hydrate saturation is equal to 1 behind the front and calculates the volume of gas required to form that hydrate. The MOC solution (You et al., 2015) is calculated at experimental P-T conditions and reflects the predicted gas consumption for the experiment. The inset figures (A, B, and C) show, graphically, the phases present ahead of and behind the front (dashed line) in each case.

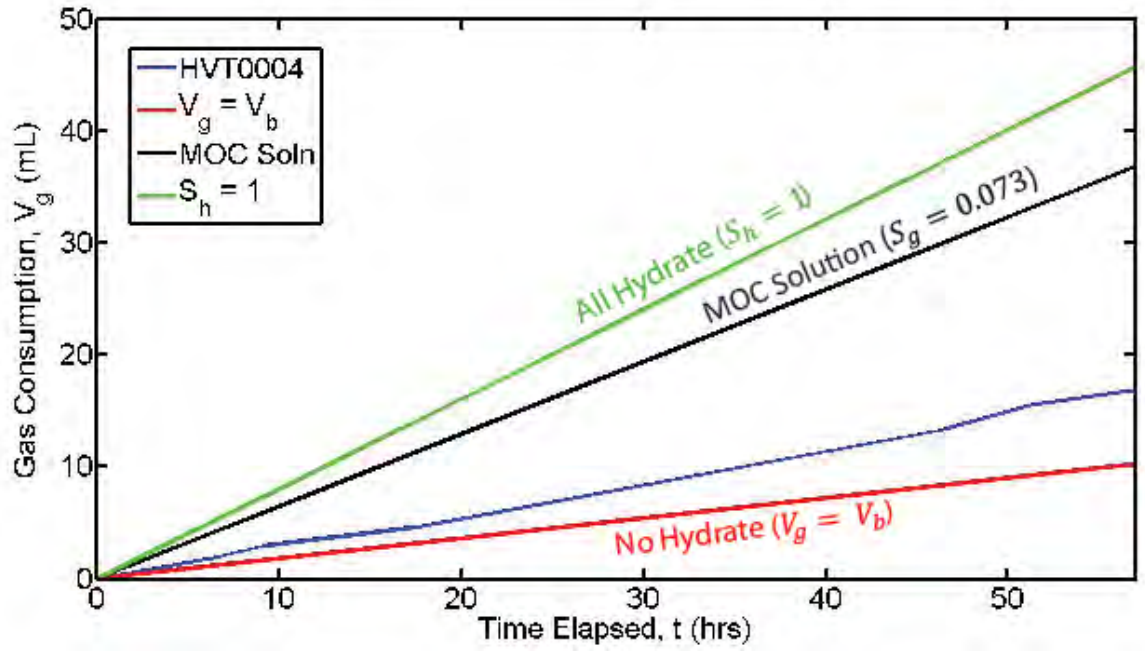

Figure 68: Comparison of gas consumption data for hydrate formation front experiment HVT0004 (blue line). Red line indicates the MOC solution for a gas flooding experiment and indicates the minimum gas consumption needed to maintain volume balance. Black line indicates the gas consumption predicted from the MOC solution for these experiments calculated at the experimental temperature and pressure conditions. Green line indicates the maximum potential gas consumption assuming that all the space made available through water withdrawal is occupied by hydrate.

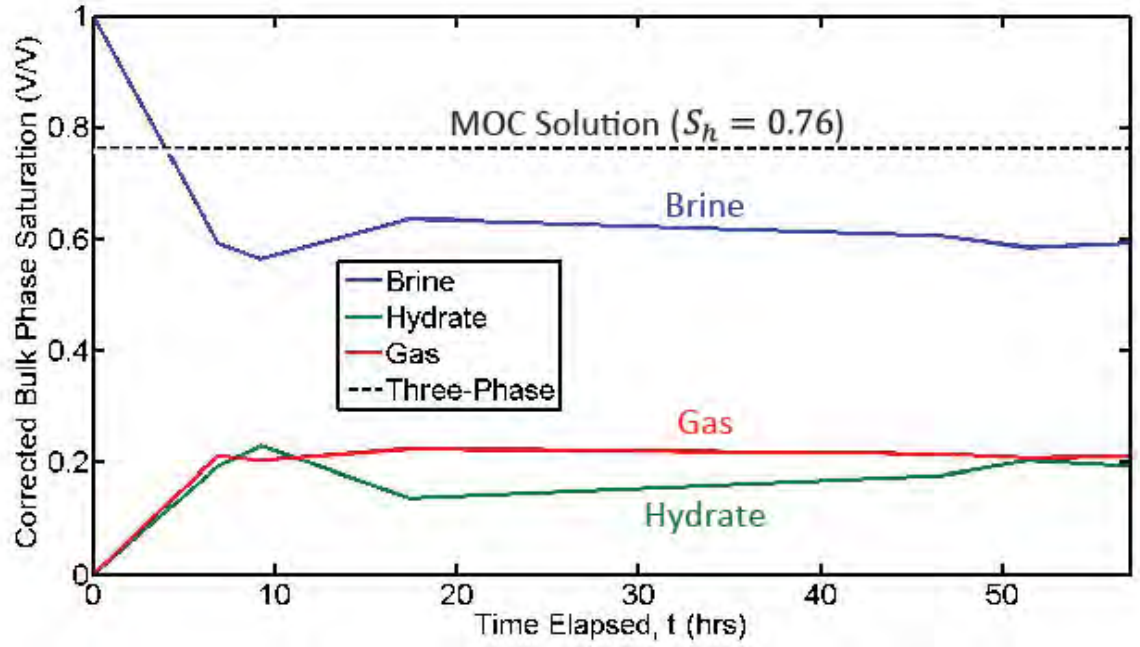

Figure 69: Brine (blue line), hydrate (green line), and gas (red line) bulk phase saturations from mass balance behind the hydrate formation front for experiment HVT0004. Black dashed line shows the predicted hydrate saturation required to elevate the in-situ salinity to three-phase equilibrium conditions.

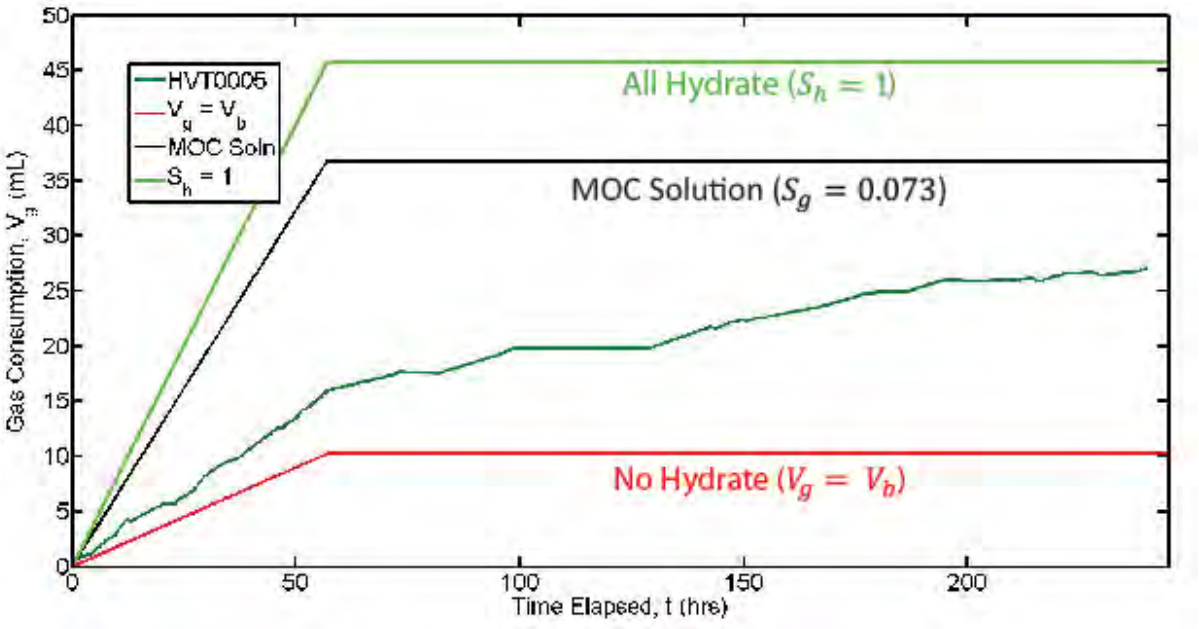

Figure 70: Comparison of gas consumption data for hydrate formation front experiment HVT0005 (dark green line). Red line indicates the MOC solution for a gas flooding experiment and indicates the minimum gas consumption needed to maintain volume balance. Black line indicates the gas consumption predicted from the MOC solution for these experiments calculated at the experimental temperature and pressure conditions. Green

line indicates the maximum potential gas consumption assuming that all the space made available through water withdrawal is occupied by hydrate.

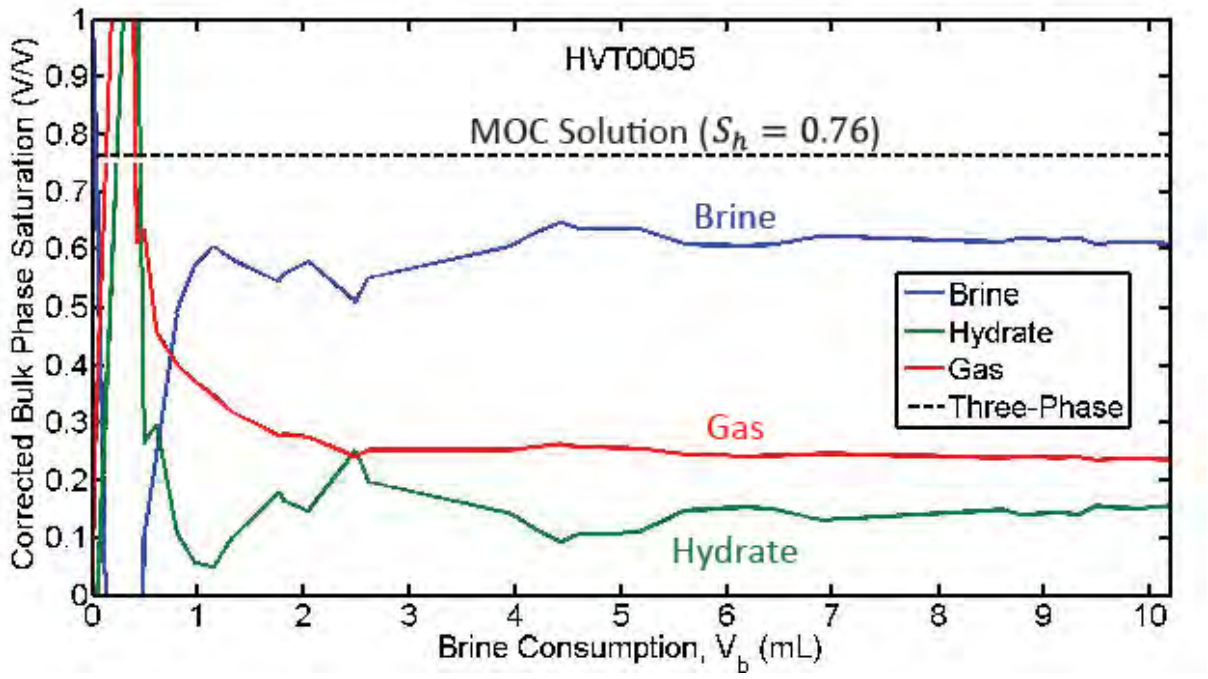

Figure 71: Brine (blue line), hydrate (green line), and gas (red line) bulk phase saturations from mass balance behind the hydrate formation front for experiment HVT0005. Black dashed line shows the predicted hydrate saturation required to elevate the in-situ salinity to three-phase equilibrium conditions.

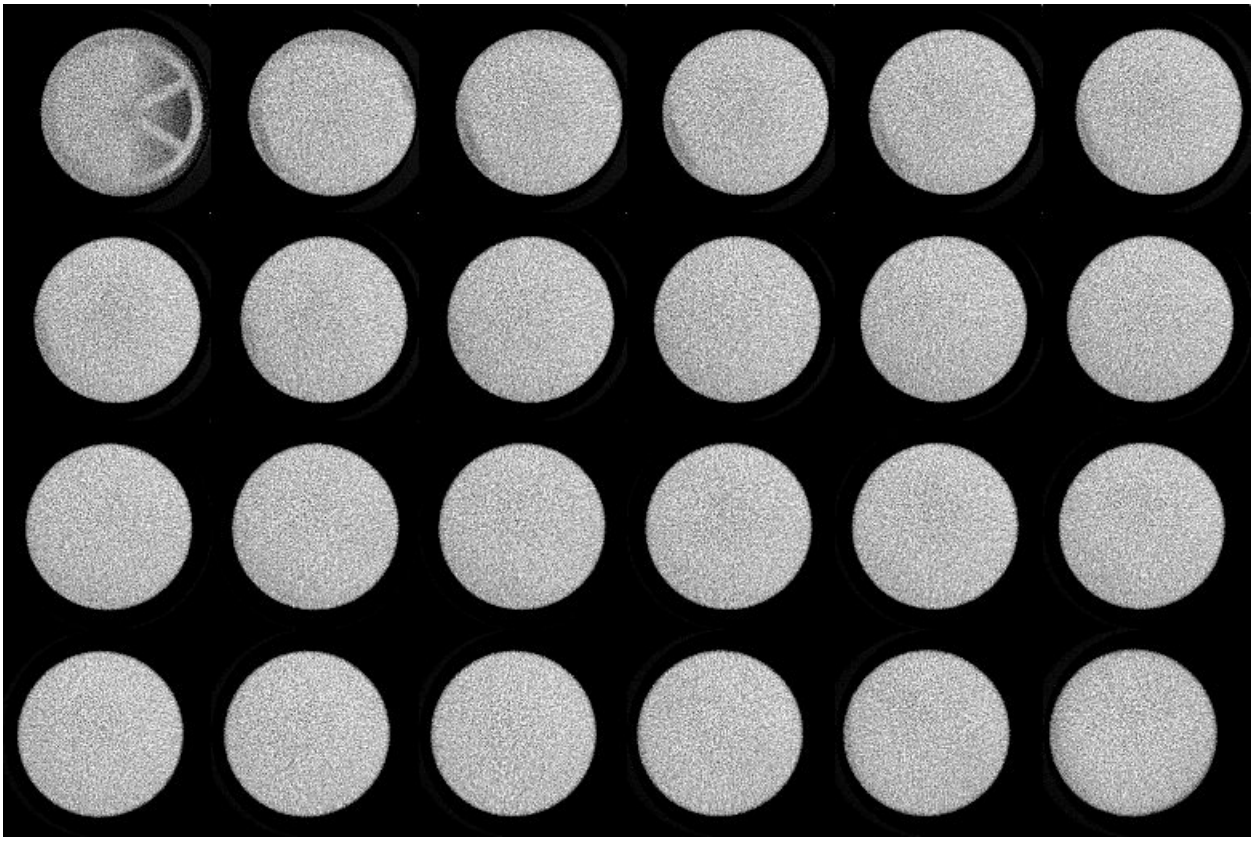

Figure 72: Montage of CT slices taken on the initial sample. Top left shows the endcap grooves at the sample outlet. Bottom right is the location of the inlet. Slices are spaced 0.5 cm apart within the sample. There is a low density region apparent in the bottom left portion of the slices in the lower 2.5 cm of the sample, which could be due to heterogeneous packing.

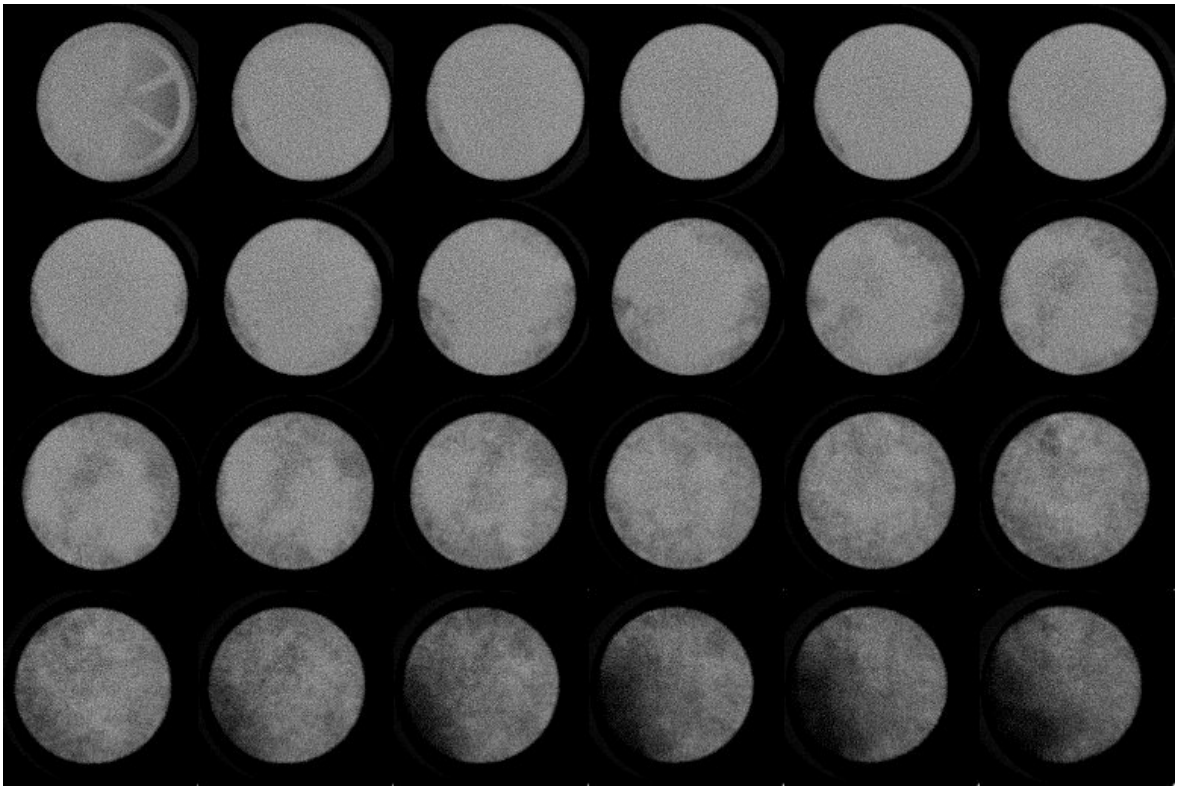

Figure 73: Montage of CT slices taken after 180 hours had elapsed. Top left shows the endcap grooves at the sample outlet. Bottom right is the location of the inlet. Slices are spaced 0.5 cm apart within the sample. The low density region in the lower 2.5 cm is still apparent. Low density regions in the upper 8cm of the sample are likely due to the presence of free gas and hydrate.

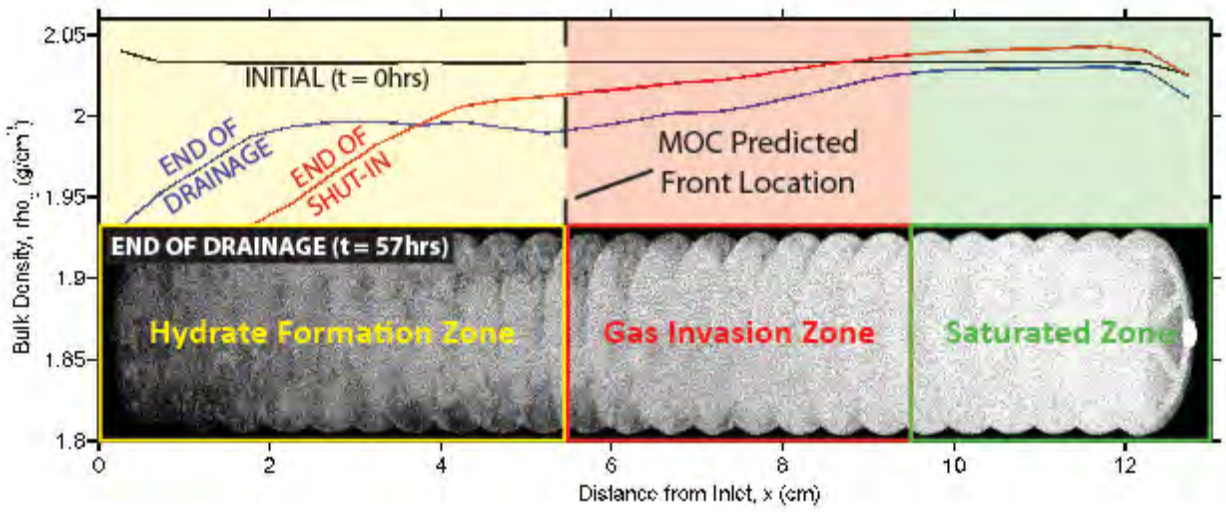

Figure 74: CT mass attenuation results for HVT0005 at the end of the drainage phase (57 hours). Slices were taken at 0.5cm spacing with a 1cm thickness. Lighter colors indicate high density. Darker colors indicate lower

density. The hydrate formation, gas invasion, and brine-saturated zones were determined using the MOC model, bulk density profiles, and the CT scans.

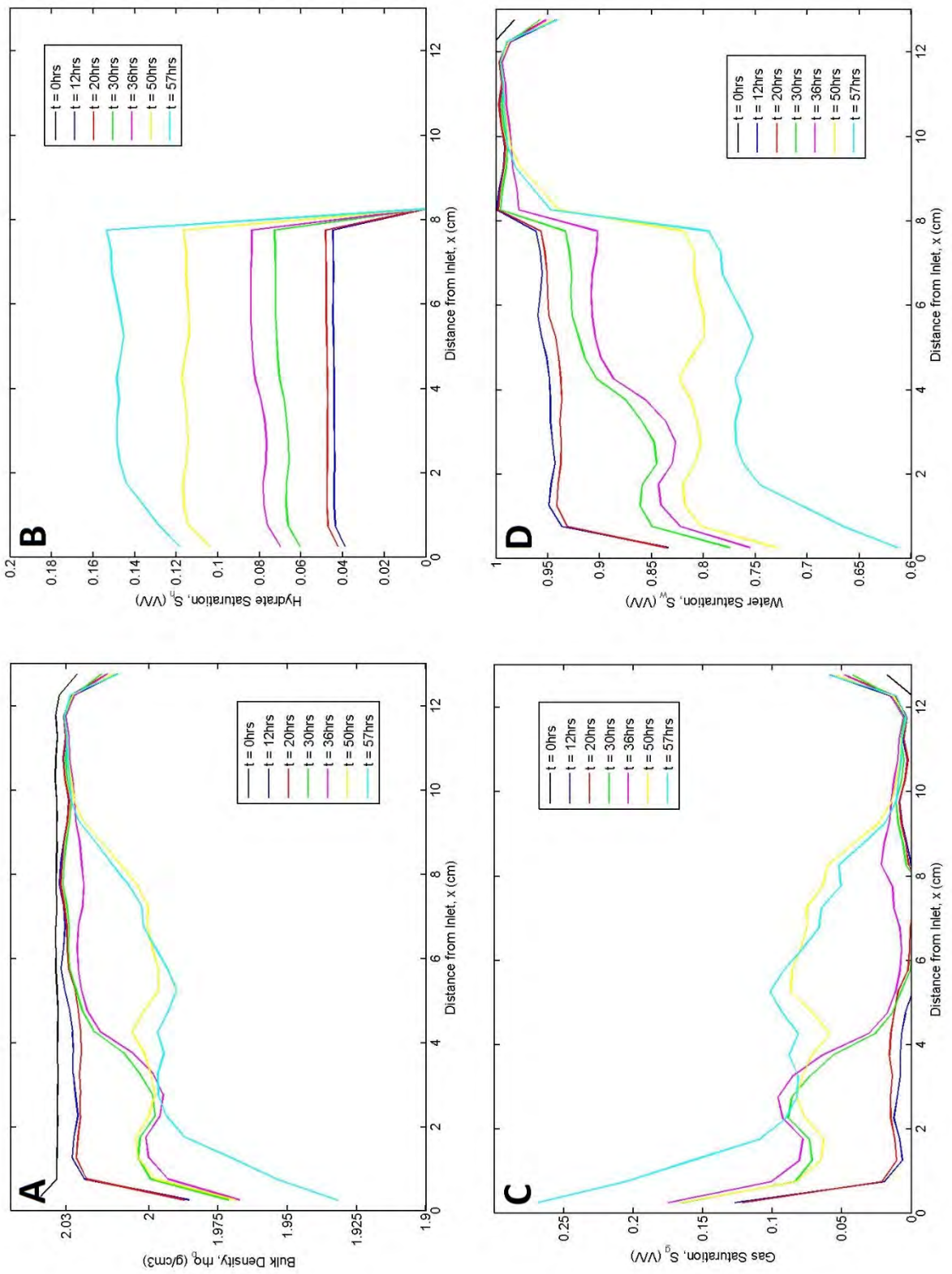
A
B
C
D
Bulk Density, rho$_B$ (g/cm3)
Hydrate Saturation, S_H (V/V)
Gas Saturation, S_g (V/V)
Water Saturation, S_W (V/V)
Distance from Inlet, x (cm)
t = 0hrs
t = 12hrs
t = 20hrs
t = 30hrs
t = 36hrs
t = 50hrs
t = 57hrs

Figure 75: CT-derived A) bulk density, B) hydrate saturation, C) gas saturation, and D) water saturation profiles during the brine withdrawal period (0 – 57 hours) of HVT0005.

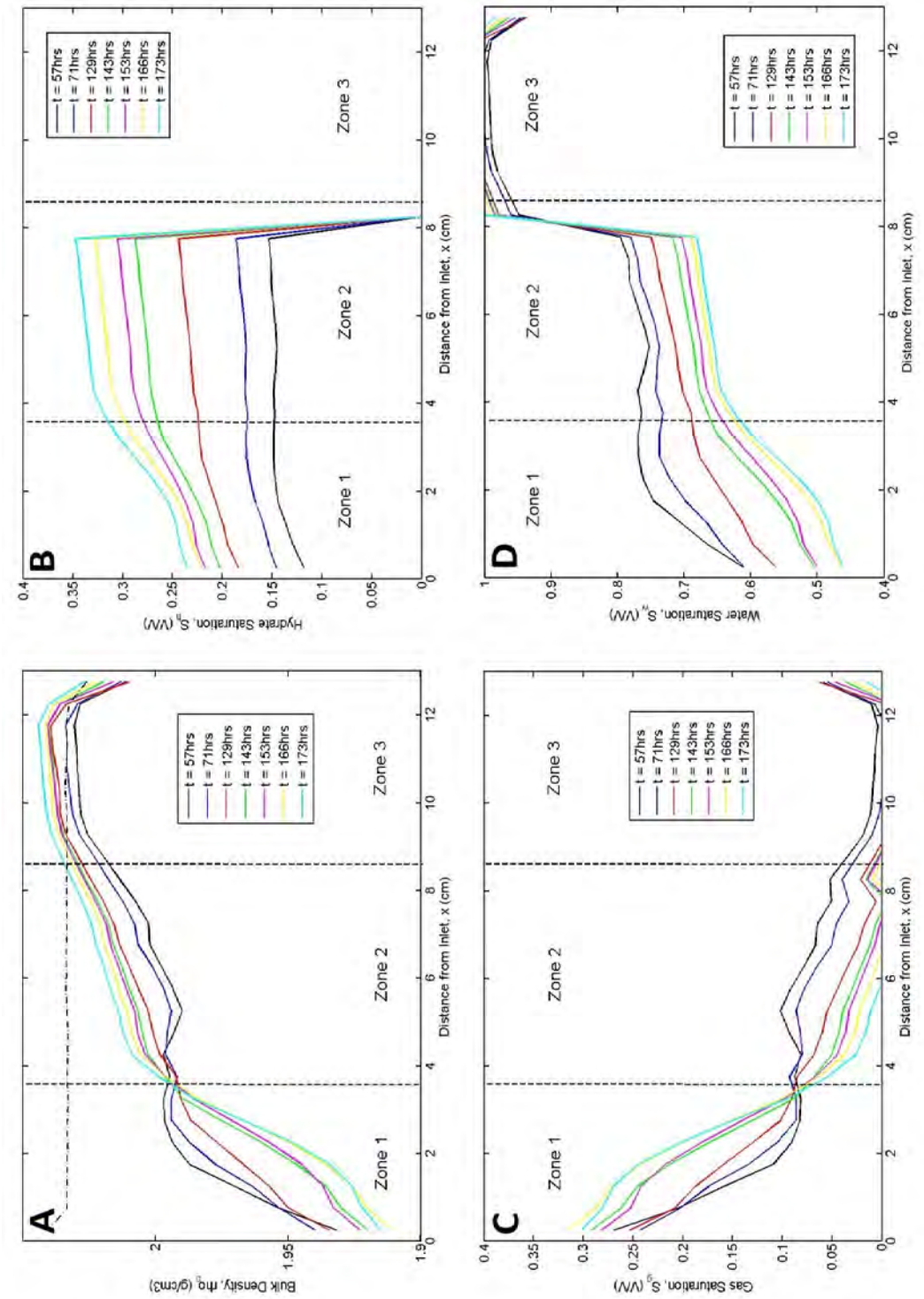

Figure 76: CT-derived A) bulk density, B) hydrate saturation, C) gas saturation, and D) water saturation profiles for HVT0005 after the brine pump was shut off and the outlet valve was closed (57 – 172 hours). Zones 1 – 3

were identified from bulk density trends after the brine was shut in. Zone shows continued density decrease, Zone 2 shows a density rebound to near initial values, and Zone 3 shows a density increase to greater than initial values.

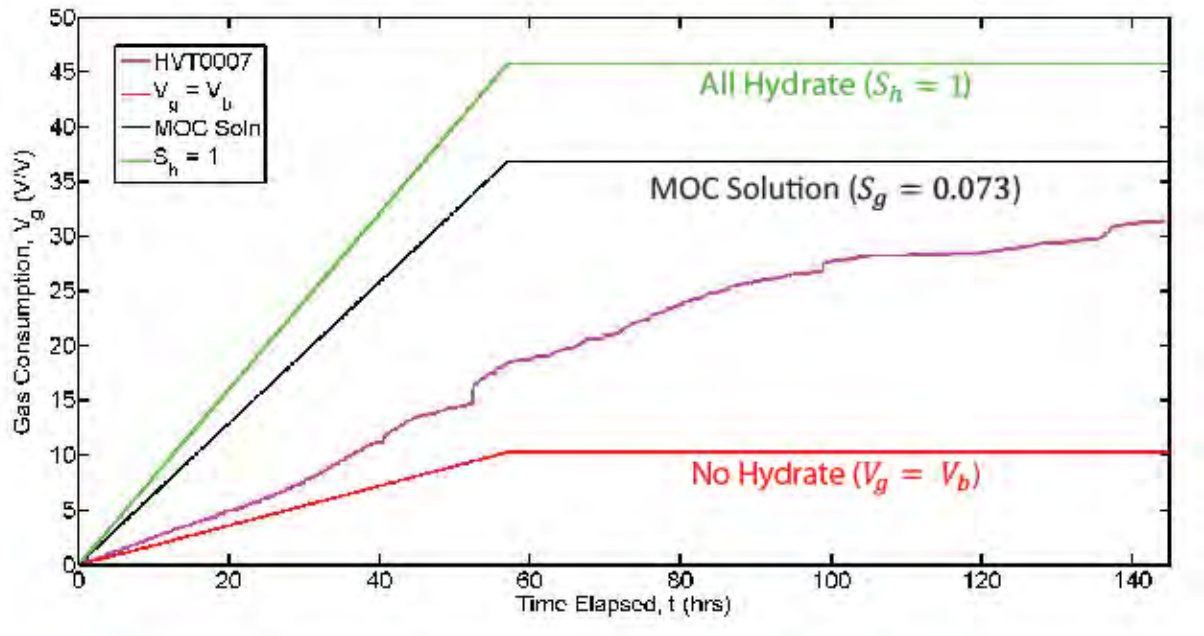

Figure 77: Comparison of gas consumption data for hydrate formation front experiment HVT0007 (pink line). Red line indicates the MOC solution for a gas flooding experiment and indicates the minimum gas consumption needed to maintain volume balance. Black line indicates the gas consumption predicted from the MOC solution for these experiments calculated at the experimental temperature and pressure conditions. Green line indicates the maximum potential gas consumption assuming that all the space made available through water withdrawal is occupied by hydrate.

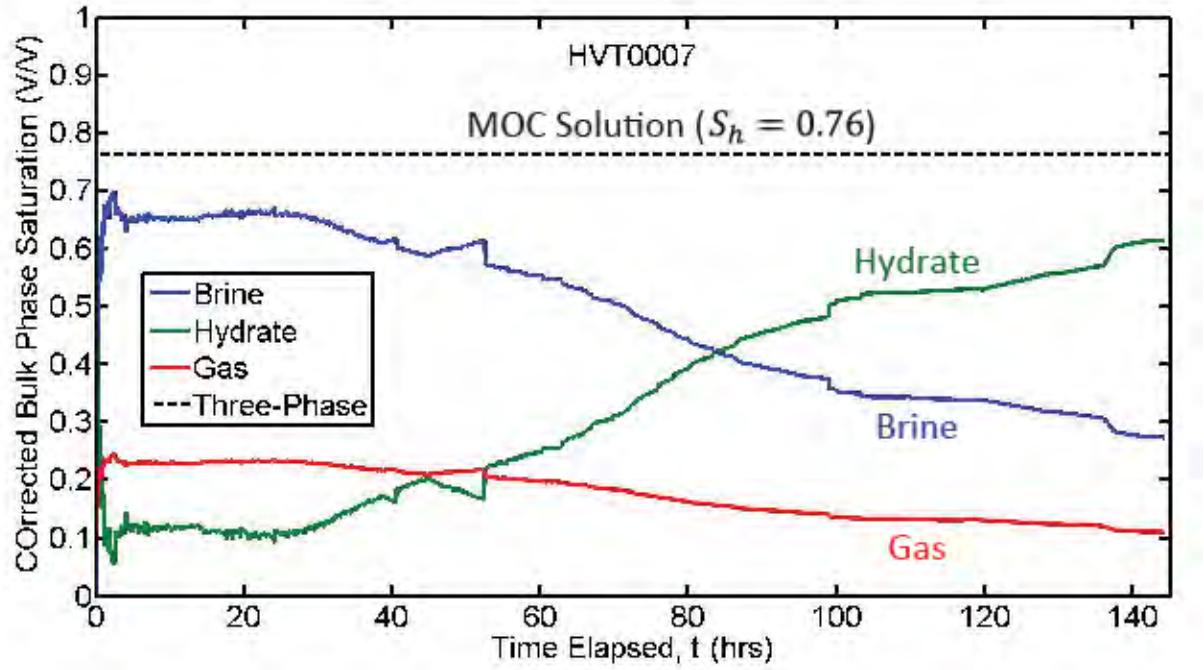

Figure 78: Brine (blue line), hydrate (green line), and gas (red line) bulk phase saturations from mass balance behind the hydrate formation front for experiment HVT0007. Black dashed line shows the predicted hydrate saturation required to elevate the in-situ salinity to three-phase equilibrium conditions.

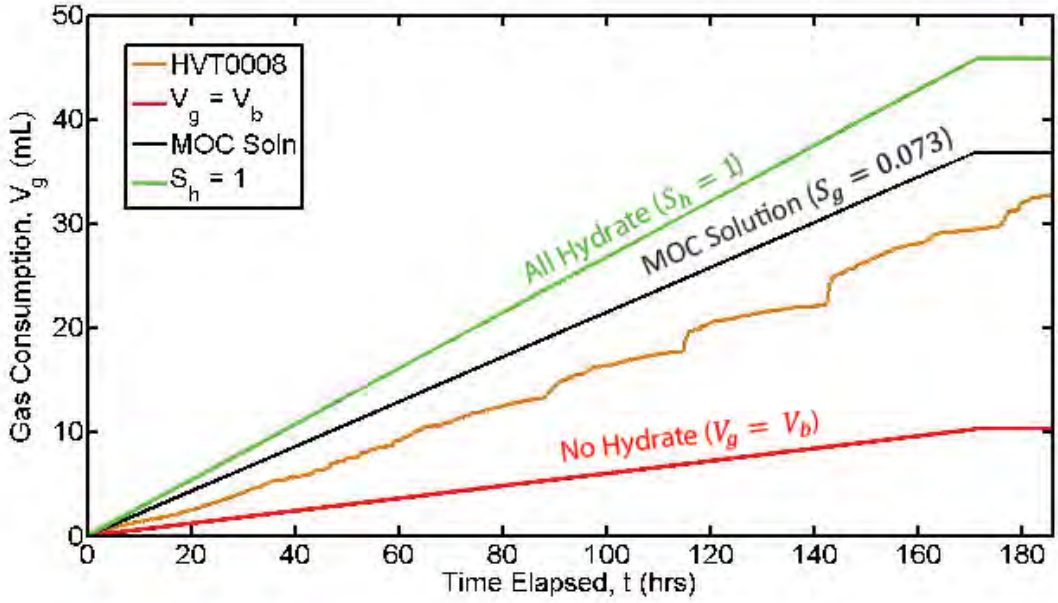

Figure 79: Comparison of gas consumption data for hydrate formation front experiment HVT0008 (orange line) Red line indicates the MOC solution for a gas flooding experiment and indicates the minimum gas consumption needed to maintain volume balance. Black line indicates the gas consumption predicted from the MOC solution for these experiments calculated at the experimental temperature and pressure conditions. Green line indicates

the maximum potential gas consumption assuming that all the space made available through water withdrawal is occupied by hydrate.

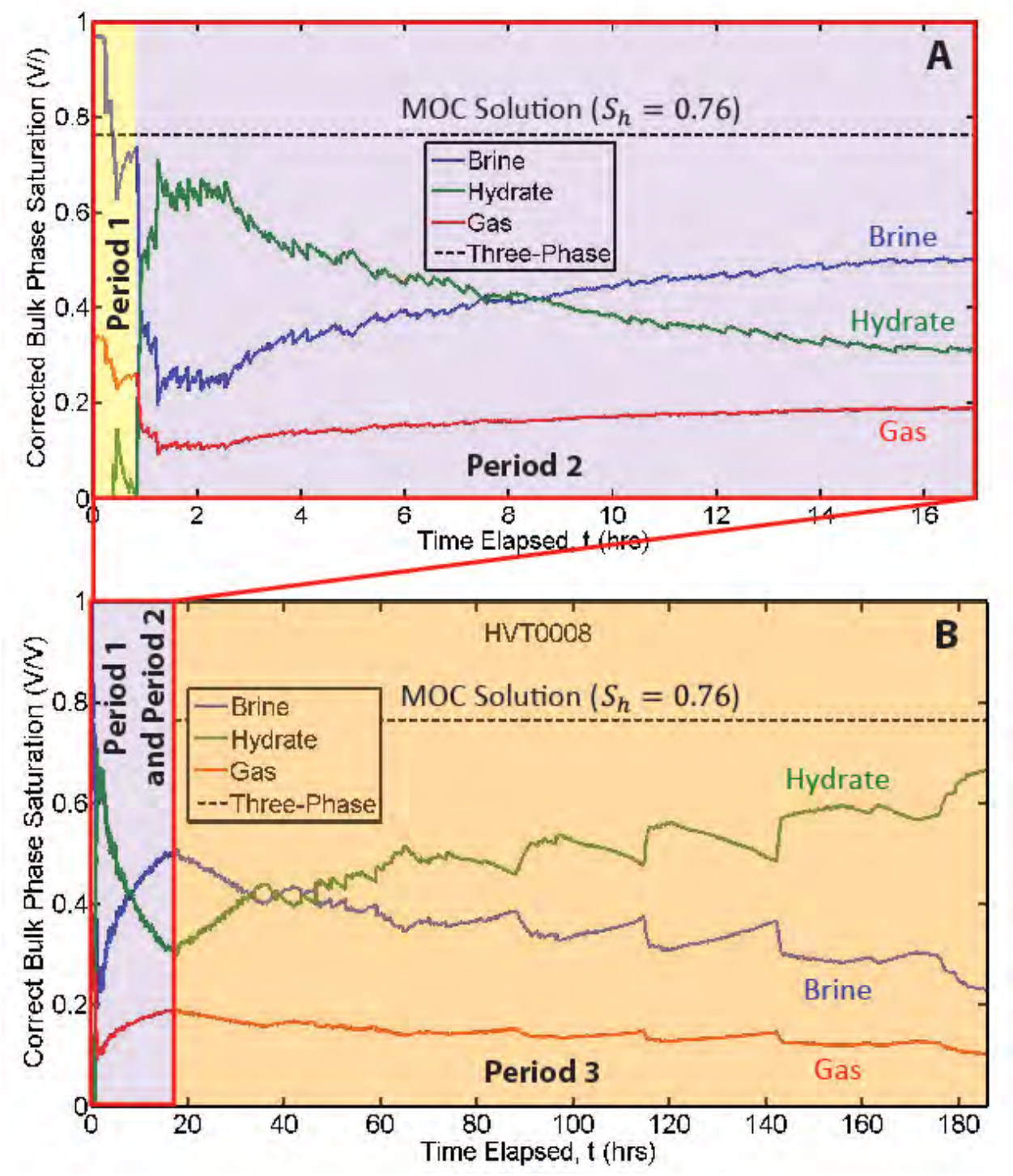

Figure 80: Brine (blue line), hydrate (green line), and gas (red line) bulk phase saturations from mass balance behind the hydrate formation front for the low flow rate experiment, HVT0008, from A) 0 – 17 hours and B) 0 –

186 hours. Black dashed line shows the predicted hydrate saturation required to elevate the in-situ salinity to three-phase equilibrium conditions.

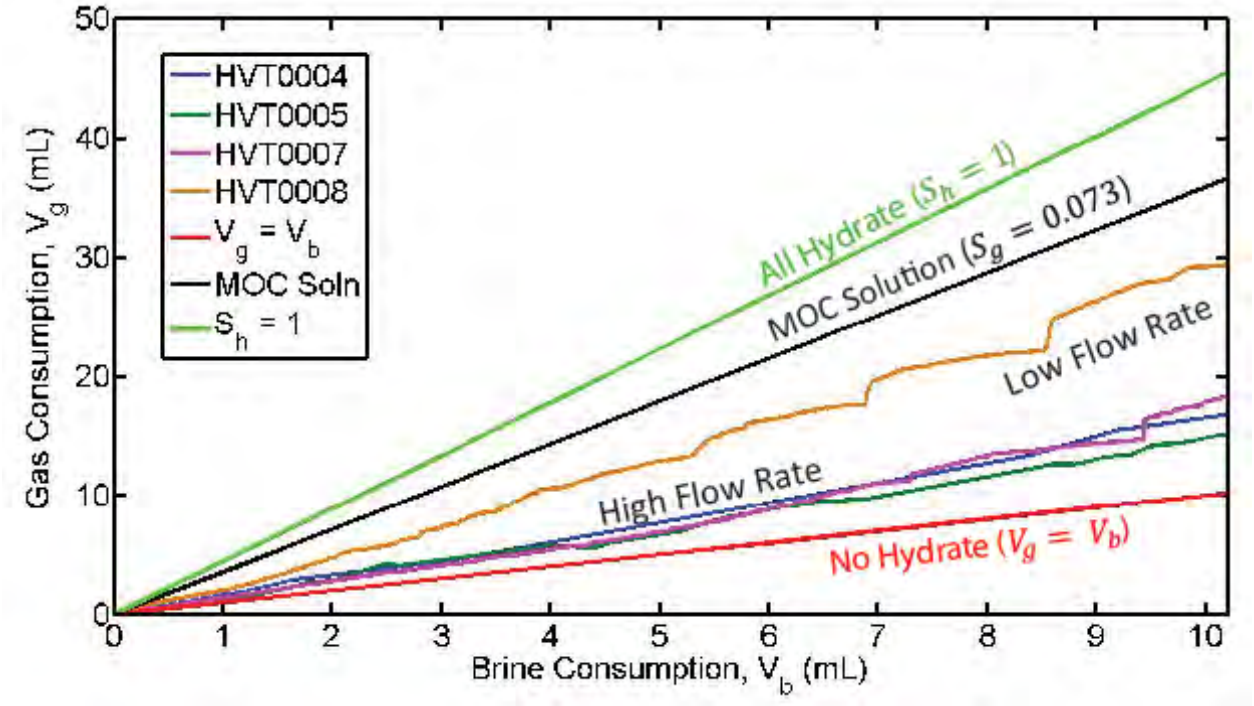

Figure 81: Comparison of gas consumptions from the high and low flow rate experiments during the drainage phase. Red line indicates the MOC solution for a gas flooding experiment and indicates the minimum gas consumption needed to maintain volume balance. Black line indicates the gas consumption predicted from the MOC solution for these experiments calculated at the experimental temperature and pressure conditions. Green line indicates the maximum potential gas consumption assuming that all the space made available through water withdrawal is occupied by hydrate.

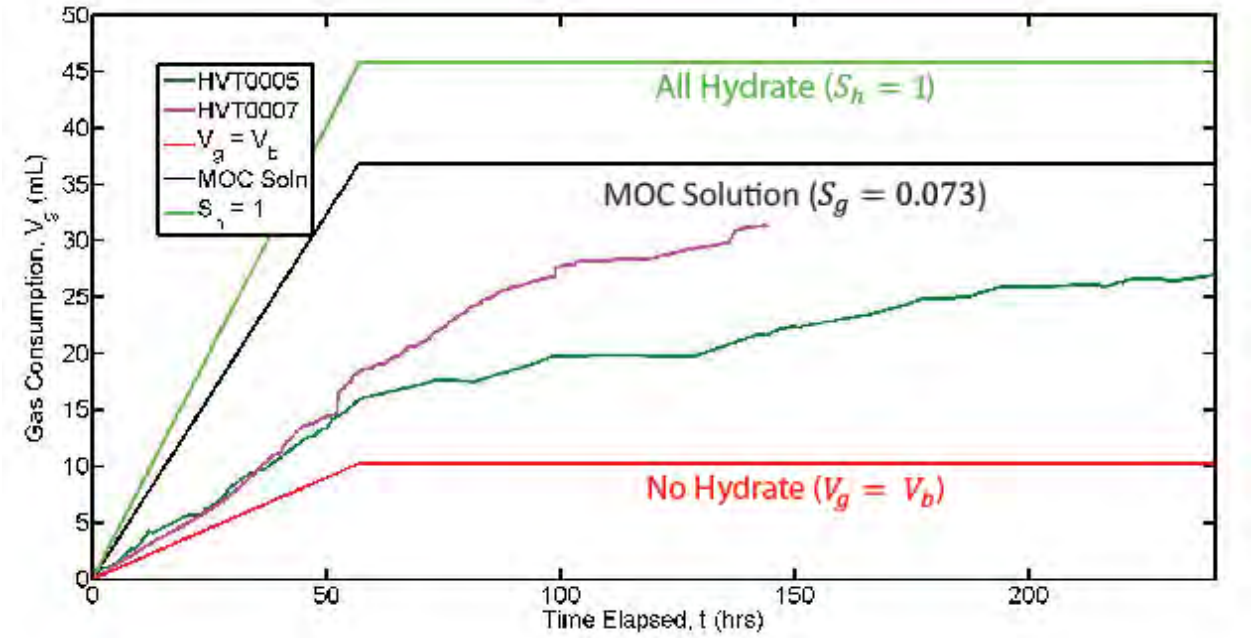

Figure 82: Comparison of gas consumption data for hydrate formation front experiments HVT0005 (dark green line) and HVT0007 (purple line). Red line indicates the MOC solution for a gas flooding experiment and indicates the minimum gas consumption needed to maintain volume balance. Black line indicates the gas consumption predicted from the MOC solution for these experiments calculated at the experimental temperature and pressure conditions. Green line indicates the maximum potential gas consumption assuming that all the space made available through water withdrawal is occupied by hydrate.

B2. Subtask 6.2 - Gas invasion from melting hydrate into water saturated HSZ

B2.1. Goal:

The Recipient shall perform an experiment analogous to Subtask 6.1 except that the gas source is not external, but rather from dissociated hydrate. The hydrate is established in the upper third of the column using methods of Task 4. Then the lower two thirds of the column are held within the hydrate stability zone while the upper third is warmed to dissociate the hydrate. Valves at the top of the column are closed so that gas from the dissociated hydrate moves downward into the hydrate stability zone. This shall enable observation of the feedback between pressure buildup and dissipation as hydrate dissociates in the top of the column and re-forms in the bottom of the column, and of the possibility that the all the hydrate re-forms lower in the column. As in Task 6.1, this geometry is inverted compared to natural systems but results in a better-controlled gas front. As time allows, the natural geometry may be attempted upon consideration of mineral grain size, capillary, dissociation rate, and gravitational forces to investigate differences.

B2.2. Activities Phase 2:

We performed dissociation experiments at the end of experiments HVT0007 and HVT0008 by depressurizing the experimental vessel containing methane hydrate. The goal of these experiments was to quantify the amount of methane in the sample, as well as characterize the dissociation behavior and

thermodynamic state of the methane hydrate. These experiments were performed by a stepwise depressurization of synthesized methane hydrate and releasing small volumes into an inverted graduated cylinder (Figure 83). A ball valve at the outlet of the experimental vessel was opened at each step to release gas to a needle valve, and then the ball valve was closed. The needle valve was then opened to release methane into the inverted cylinder. During the early stages of depressurization (high pressure) of HVT0007 some liquid was also produced in addition to gas. Before HVT0008 a secondary ball valve was added 7 cm above the outlet valve to allow for a smaller volume of gas to be produced (Figure 83). The modified setup in HVT0008 stopped the release of liquid and decreased the volume of gas in the first high pressure steps from over 200 mL to 20 mL. Once the pressure had decreased to less than 500 psi, the secondary ball valve was left open and gas was released from the experimental vessel to the needle valve, producing around 50 mL of gas with no liquid release.

The two dissociation experiments were performed over a period of 1-2 weeks with the temperature held constant at 1 deg C as in the hydration formation experiments. The cumulative methane recovery and pressure drop were recorded (Figure 84). Moles of methane recovered were calculated using the density and molecular weight of methane.

In plotting the cumulative gas recovery (in mL or mol) versus pressure (Fig. 51), we identified three regimes of methane release from the experimental vessel: (1) a high pressure release of free gas (2) dissociation of methane hydrate and (3) residual free gas after dissociation. Within the free gas regime there is a steady drop in pressure with each release of methane. In both HVT0007 and HVT0008 additional drops in pressure occurred overnight when the outlet valve was closed, suggesting possible formation of hydrate. During dissociation there is a recovery in pressure after each time the outlet valve is opened and methane released, indicating a continued dissociation and buildup of gas in the vessel.

Hydrate dissociation occurs between 3.3 and 2.8 Mpa, which corresponds to the 6 wt.% NaBr three-phase boundary and freshwater boundary. Because the starting brine is 7 wt.% NaBr, we interpret this dissociation path as due to possible localized freshening around dissociating hydrate.

There is good agreement when comparing the total moles of gas recovered during depressurization to the total moles consumed during hydrate formation (Fig. 52). When comparing the relative number of moles of methane as free gas or hydrate, the depressurization experiments underestimate the amount of hydrate and overestimate free gas relative to the synthesis experiment. These results suggest that this method of depressurization is accurate for determining the total amount of methane within a pressure core.

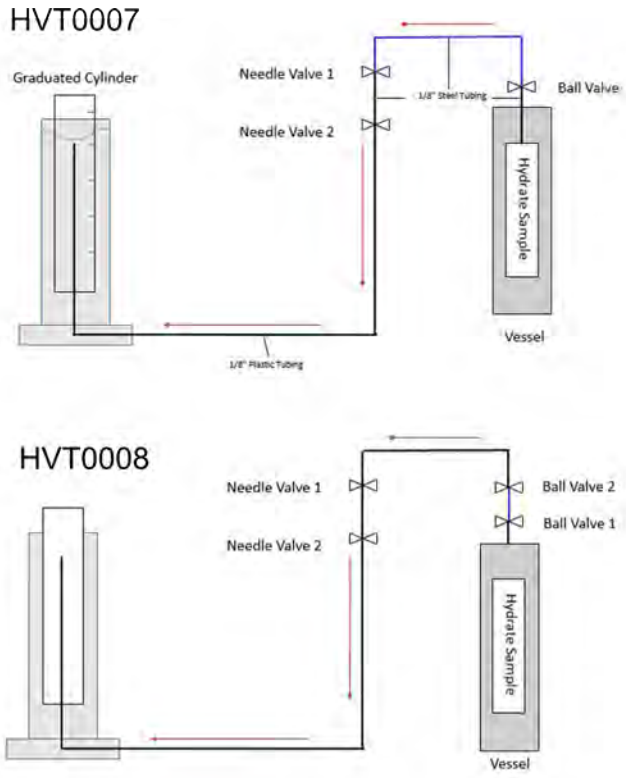

Figure 83: Experimental setup used during depressurization of HVT0007 (top) and HVT0008 (bottom).

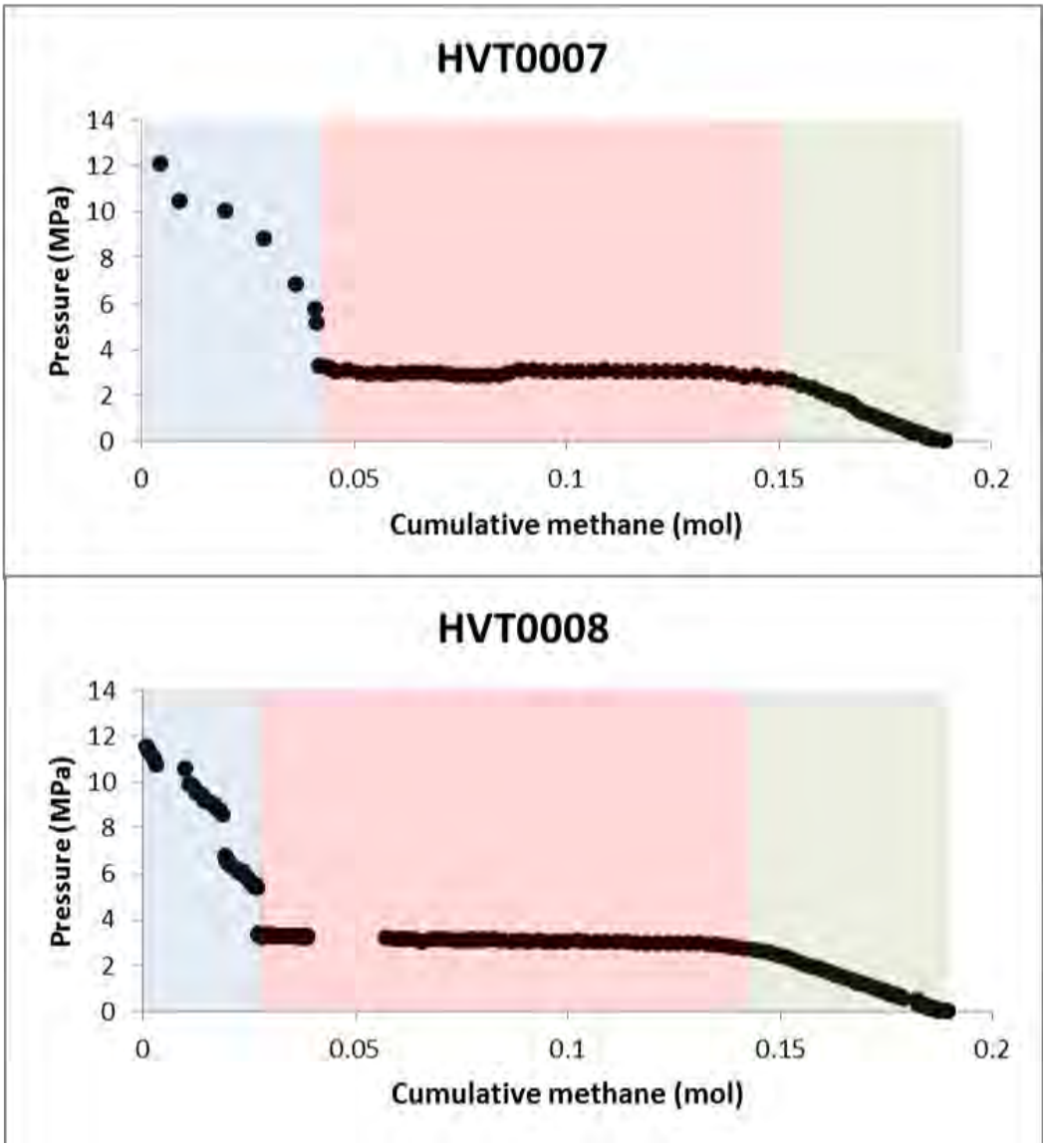

Figure 84: Outlet pressure versus cumulative volume and moles of methane released during depressurization of HVT0007 (top) and HVT0008 (bottom). Blue shaded area: high pressure free gas, red shaded area: hydrate dissociation, green shaded area: residual free gas.

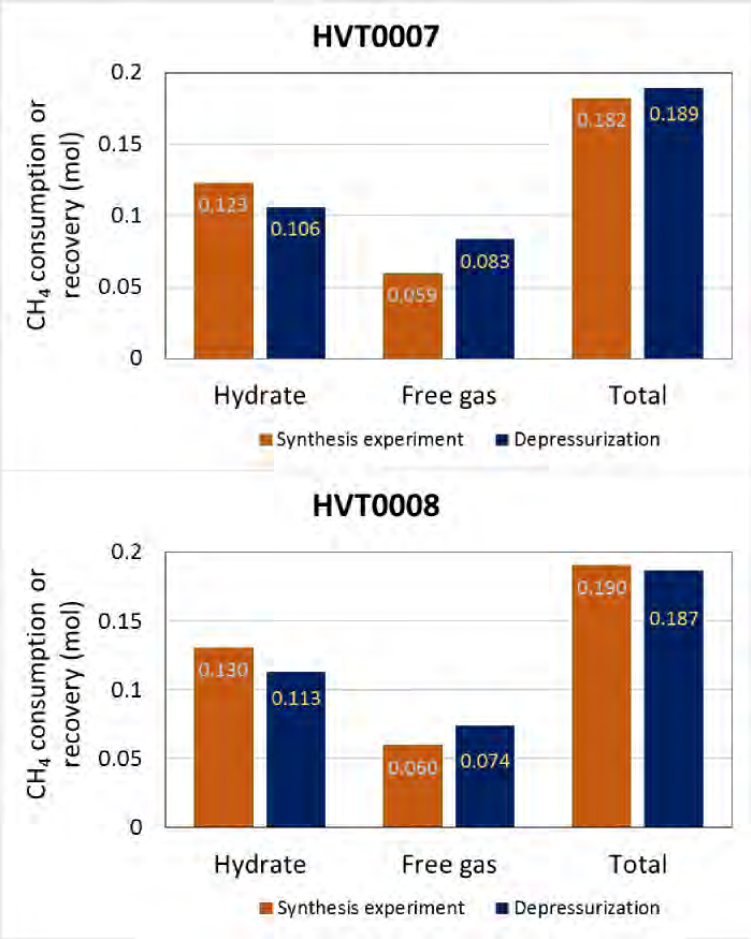

Figure 85: Comparison of total methane, hydrate and free gas between depressurization and synthesis experiments for HVT0007 (top) and HVT0008 (bottom).

2.7. Task 7: 2D model (Complete)

Milestone 2.D Demonstrate a 2D simulation of hydrate dissociation and gas expulsion.

A. Goal:

The Recipient shall extend the models developed in Tasks 2 and 5 to account for structure, primarily the effect of dip of the hydrate-bearing sediment layer and of the geometry of the hydrate accumulation. In addition the Recipient shall consider the effect of two-dimensional geometry on the local perturbation of the hydrate stability zone (e.g. the effects of lateral flow of salt and heat). The Recipient shall include the effect of heat of formation and fracture permeability.

B. Activities Phase 2:

We extended our 1D hydrate dissociation model to 2D, which takes into account both the lateral and vertical heat flow and mass transport. We set the lateral boundaries to be no flow. We introduced high permeability layers interbedded in low permeability matrix. These high permeability layers could be permeable sand layers or fractures. Hydrate preferentially forms in high permeability layers. In order to simulate the sloping seafloor and the corresponding sloping base of the hydrate stability zone, we introduced coordination transformation into the numerical model. We rotated the x axis clockwise from the horizontal direction to be parallel with the sloping seafloor, and the y axis from the vertical direction to be perpendicular with the sloping seafloor. Example simulations are given below.

B1. Subtask 7.1 - Hydrate dissociation in 2D systems

B1.1. Goal:

The Recipient shall extend the 1D dissociation model to allow for phase transport laterally as well as vertically. The boundary conditions shall be general. A constant heat flux shall be applied from below and initial distribution of hydrate gas saturation shall be assumed. A temperature perturbation shall be applied to the upper boundary.

B1.2. Activities Phase 2:

We have extended the 1D dissociation model to allow for phase transport both laterally and vertically, and both temperature and pressure perturbation can be applied to the upper boundary (See Subtask 7.3).

B2. Subtask 7.2 - Gas expulsion in 2D systems

B2.1. Goal:

The Recipient shall develop 2‐dimensional models of gas venting through the gas hydrate stability zone. A localized gas flux shall be applied from below. Gas shall propagate upwards forming a three‐phase stability zone. Heat and salt shall be generated as hydrate solidifies. These shall dissipate both laterally and vertically. The Recipient shall vary both gas and water flux and determine under what conditions the gas will solidify and not breakthrough the seafloor vs. under what conditions it will propagate to the seafloor.

B2.2. Activities Phase 2:

In this section, we present a two-dimensional numerical simulation of gas invasion and hydrate formation in a dipping layer with high-permeability interbedded with low-permeability matrix (Figure 86). This high-permeability layer could be either sand layer or fracture zone. This setting is typical in Northern Gulf of Mexico hydrate regions, where gas migration is regionally heterogeneous and focuses into discrete high-flux pathways (Boswell et al., 2012). The dip angle of the sand layer is 14^{o}. We set the permeability in the low permeability layer to be 1×10^{-18} m^2, and that in the high permeability layer to be 1×10^{-13} m^2.

We use the field parameters at Walker Ridge 313 to describe this system. The water depth is 2000 m (McConnell and Kendall, 2002). The initial pressure increases linearly downward from sea floor with hydrostatic pressure gradient (10 KPa/m) (Figure 87a). Temperature at seafloor is 4 ^{o}C, and increases downward with a geothermal gradient of 18 ^{o}C/km (Figure 87b) (McConnell and Kendall, 2002). There is 100% brine with salinity of 3 wt.% initially in the domain (Figure 87c, 87d). This makes the base of the hydrate stability zone to be between 900 and 950 mbsf (meter below seafloor) (McConnell and Kendall, 2002). We investigate the domain from 550 to 1000 mbsf, with a lateral distance of 900 m. We fix the pressure to be 25.77 MPa, temperature 13.9 °C, and salinity 3 wt.% at the top boundary (550 mbsf). We apply a fixed geothermal flux of 20.71 mW/m^2 at the bottom boundary (1000 mbsf). We supply methane gas from the bottom of the sand layer (Figure 86) with a high rate of 0.5 kg/(m^2 yr) (Liu and Flemings, 2007). We set the other boundaries to be no flow (Figure 86).

Hydrate forms from the base of the hydrate stability zone when gas enters there (Figure 88a). It increases the local salinity and bring the local system to three-phase equilibrium (Figure 88b, 88c), at which point no more hydrate can form. Hydrate formation releases heat and increases the local and surrounding temperature by heat conduction and advection (Figure 88d). This temperature increase melts the hydrate formed at the base of the hydrate stability zone (Figure 89), and moves the base of the hydrate stability zone to a shallower depth (Figure 90). Gas front and hydrate solidification front move together along the sand layer, horizontally from left to right and vertically toward seafloor (Figures 89, 90 and 91). At 100.122 k.y., the entire sand layer within the hydrate stability zone is at three-phase equilibrium, and hydrate coexists with methane gas and liquid brine with elevated salinities (Figure 91).

Hydrate saturation increases vertically toward seafloor (Figure 91). That is because as we move toward seafloor, the system initial thermal condition moves father away from the phase boundaries, and more hydrate is required to form to reach three-phase equilibrium. Hydrate saturation decreases horizontally from left to right (Figure 91). That is because salt advection and diffusion from hydrate solidification front increases the salinity on the right, and moves the local thermal condition toward phase boundaries. As time goes on, salt diffuses away from the sand layer, more hydrate is required to form to maintain three-phase equilibrium salinity, and hydrate saturation increases with time at a fixed spatial position (Figures 88, 89, 90 and 91). In a same horizontal sand layer, gas saturation is highest on the right (Figure 91). That is because hydrate saturation increases vertically toward seafloor, which decreases the intrinsic permeability and increases the capillary entry pressure.

Water flows horizontally from right to left and vertically downward in the sand layer (Figure 92a). Hydrate formation leads to volume expansion, increases the local pressure, and drives water to flow away from the hydrate solidification front (Figure 92a). Gas intrusion and hydrate formation in the sand

layer drives water to flow away from the sand layer (Figure 92a). Water velocity above the sand layer is greater than that below the sand layer. This can be explained by two reasons: first, pressure increase in the sand layer increases the pressure gradient above the sand layer while decreases the pressure gradient below the sand layer; second, we have an open boundary at the top and a closed boundary at the bottom. This leads to greater increase of salinity above the sand layer than that below the sand layer (Figure 90c and 91c). Gas flows horizontally from left to right and vertically toward seafloor (Figure 92b). Gas flow velocity is zero in the clay layer (Figure 92b).

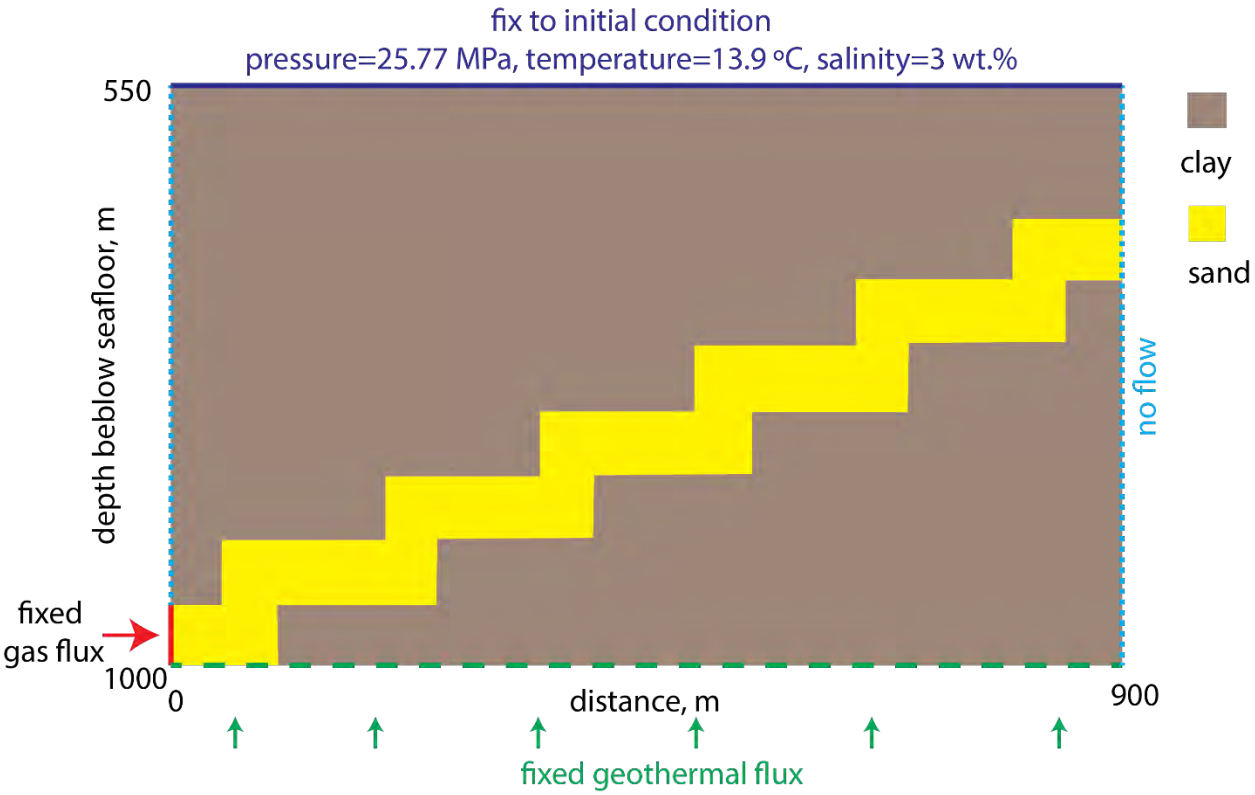

Figure 86: Schematic diagram of the simulated domain. A dipping sand layer (permeability of 1×10^{-13} m^2) is interbedded within a low permeability clay layer (permeability of 1×10^{-18} m^2). The dip angle of the sand layer is 14°. Hydrate stability zone extends from seafloor to between 900 and 950 meter below seafloor. Methane gas flows into the domain from the base of the sand layer with a fixed rate.

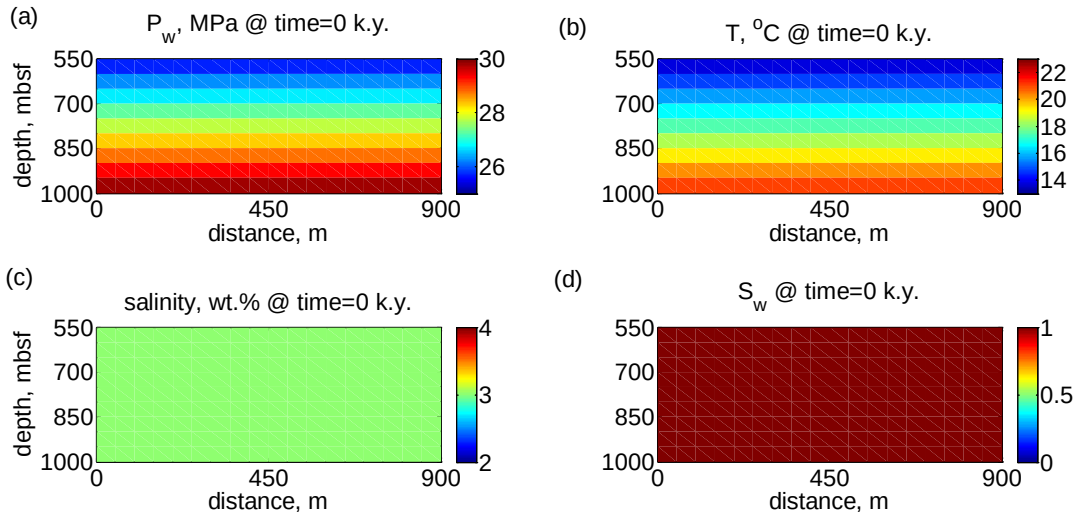

Figure 87: The initial (a) pressure, (b) temperature, (c) salinity and (d) water saturation in the domain.

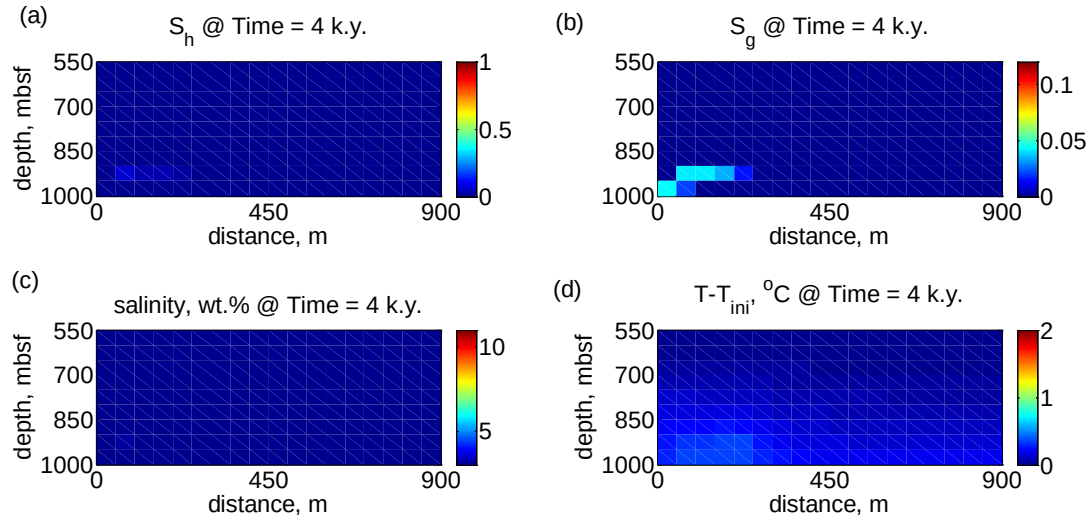

Figure 88: (a) hydrate saturation, (b) gas saturation, (c) salinity, and (d) temperature change from initial at 4 k.y..

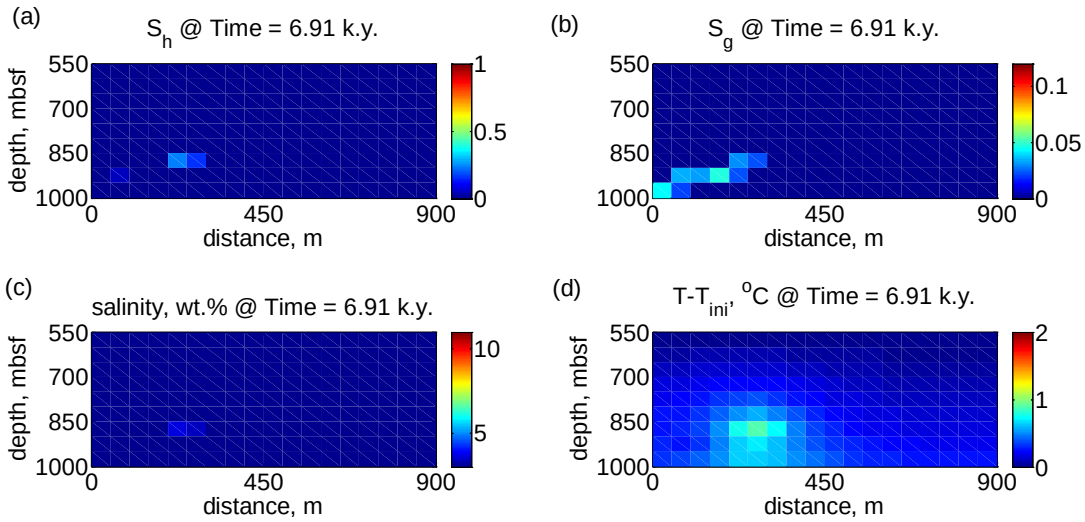

Figure 89: (a) hydrate saturation, (b) gas saturation, (c) salinity, and (d) temperature change from initial at 6.91 k.y..

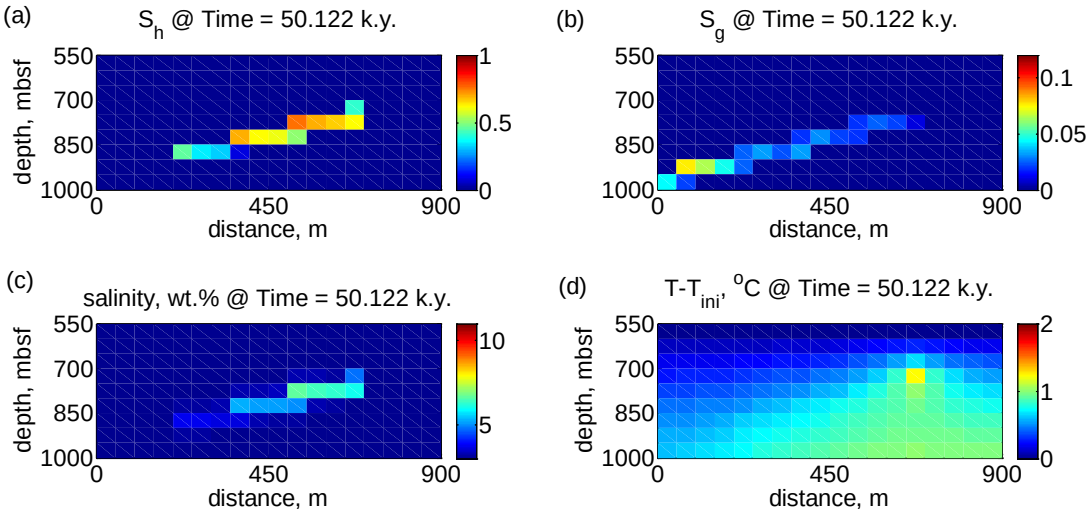

Figure 90: (a) hydrate saturation, (b) gas saturation, (c) salinity, and (d) temperature change from initial at 50.122 k.y..

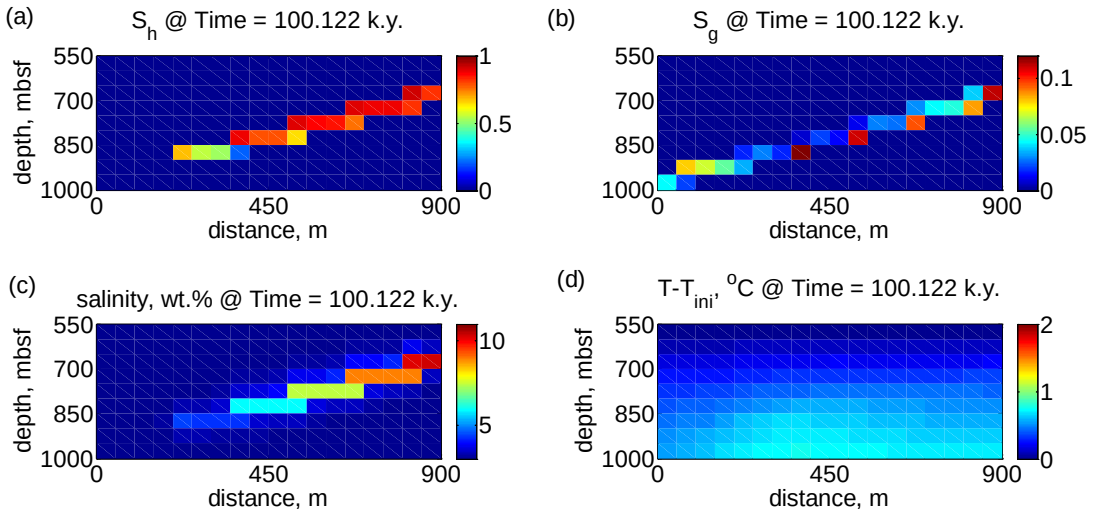

Figure 91: (a) hydrate saturation, (b) gas saturation, (c) salinity, and (d) temperature change from initial at 100.122 k.y..

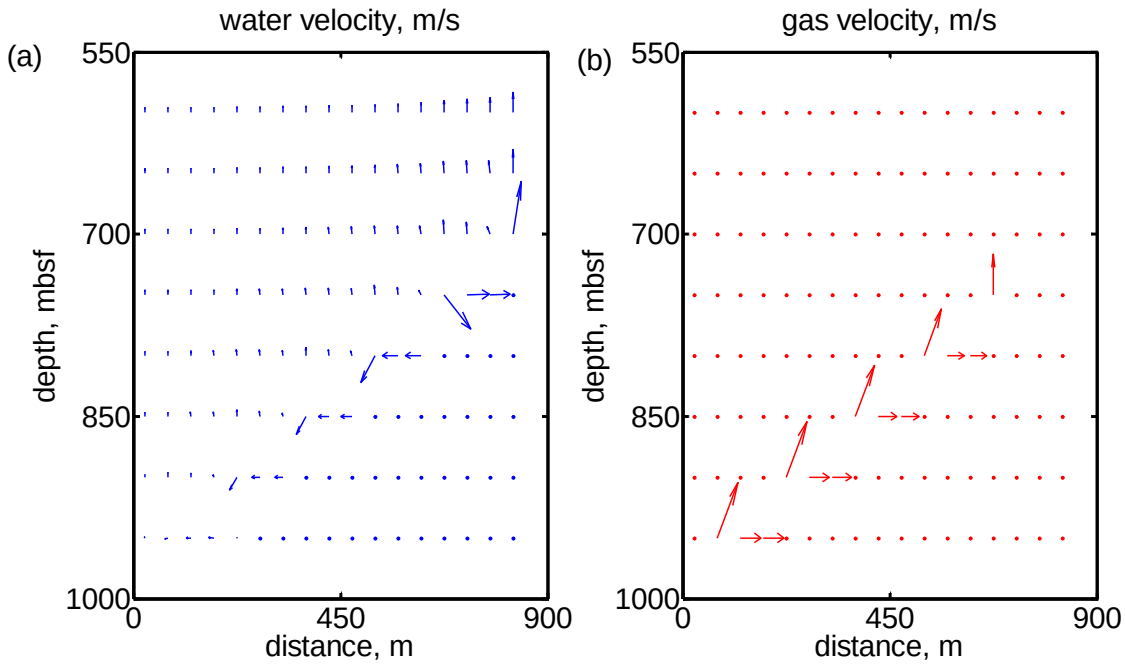

Figure 92: (a) water velocity, and (b) gas velocity field at 50.122 k.y..

B3. Subtask 7.3 - Apply 2D, gas expulsion model to natural examples

B4. Subtask 7.3.1 Pleistocene to Holocene Sea level rise

B4.1. Goal:

The Recipient shall simulate the impact of sea‐level rise during the Holocene sea level rise (e.g. 20,000 years ago). In this scenario 4 degree centigrade seawater abruptly floods a previously sub‐aerially exposed continental margin. The Recipient shall consider reservoirs both within the three phase stability zone and those that are within the two phase (L+H) region. The thermal and pressure effect of this response over the Holocene shall be simulated. A key question to be addressed is under what conditions will gas migrate through the hydrate stability zone vs. when will it just migrate laterally to be vented at the seaward limit of the stability zone.

B4.2. Activities Phase 2:

Arctic Ocean continental shelf (AOCS) are undergoing the most dramatic warming associated with the transgression of sea level since the end of the last ice age (Paull et al., 2011). The degradation of subsea permafrost and the consequent destabilization of methane hydrate can significantly increase the flux of methane to the atmosphere and accelerates global warming (Rachold et al., 2007).

We investigated how the carbon budget at the water depth of 110-120 m of North America Beaufort shelf responds to the dramatic changes on the AOCS. At 12 k.y. before present, pressure increased with a hydrostatic pressure gradient (11.03 KPa/m) from ground surface (Collett et al., 2011) (Figure 93a). The entire area between water depths of 110 and120 m was exposed to -13 °C Arctic air (Frederick and Buffett, 2014) (Figure 93b). Permafrost with a uniform ice saturation of 90% developed from ground surface to about 400 m below surface with a temperature gradient of 31.9 °C/km (Collett et al., 2011) (Figure 93b, c). Below the base of permafrost, temperature increased linearly with a gradient of 45 °C/km (Collett et al., 2011) (Figure 93b). We set the salinity below the permafrost to be homogeneously 0.9 wt.% (Collett et al., 2011), which rendered a hydrate stability zone from 250 to 600 m below ground surface (Figure 93d). We set two hydrate layers initially below the base of permafrost with a saturation of 80%: 450-500 m and 550-600 m, which were separated by a less permeable layer with an intrinsic permeability of 10-16 m2 (Figure 93c). The hydrate system at the lower layer (550-600 m) was very close to the hydrate phase boundary (Figure 93d).

At 12 k.y. before present, we imposed a sea level rise at the water depth of 120 m with a rate of 0.01 m/year (Frederick and Buffett, 2014). Sea water with bottom temperature of 0 °C would cover the entire simulated area, water depth of 110-120 m, within 1 k.y.. The ground surface temperature was immediately increased from -13 to 0 °C, and the ground surface salinity was immediately decreased to 3 wt.% when it was flooded by sea water. The pressure at ground surface increased linearly with sea level rising. We fixed the geothermal flux at the bottom of the domain (700 m) to be 55.9 mW/m2.

Temperature increases from ground surface, and from deeper to shallower water depth (Figure 94a). This induced ice melting from ground surface and from 120 m water depth (Figure 94c). The endothermic nature of ice thawing greatly buffered heat transfer to depth. Therefore, there was no temperature increase below the base of the permafrost until 9.6 k.y. before present (Figure 94a). At the same time, sea level rise increased the water pressure rapidly in the entire depth, with a greater magnitude at the depth below the base of permafrost (Figure 94b). This made the hydrate system more stable with time before 9.6 k.y. before present. Continuing warming from the top and geothermal flux from the bottom melted the ice from both the ground surface and the base of permafrost (Figure 94c). Temperature in the hydrate layers started to increase after 9.6 k.y. before present (Figure 94a). However, the rising sea level continuously increased the pressure in the hydrate layers (Figure 94b). Therefore, the distances of the hydrate layers toward the phase boundaries remained unchanged, and no methane gas was released until 1.1 k.y. before present. However, the volume of the ice has decreased by 73% (Figure 94c).

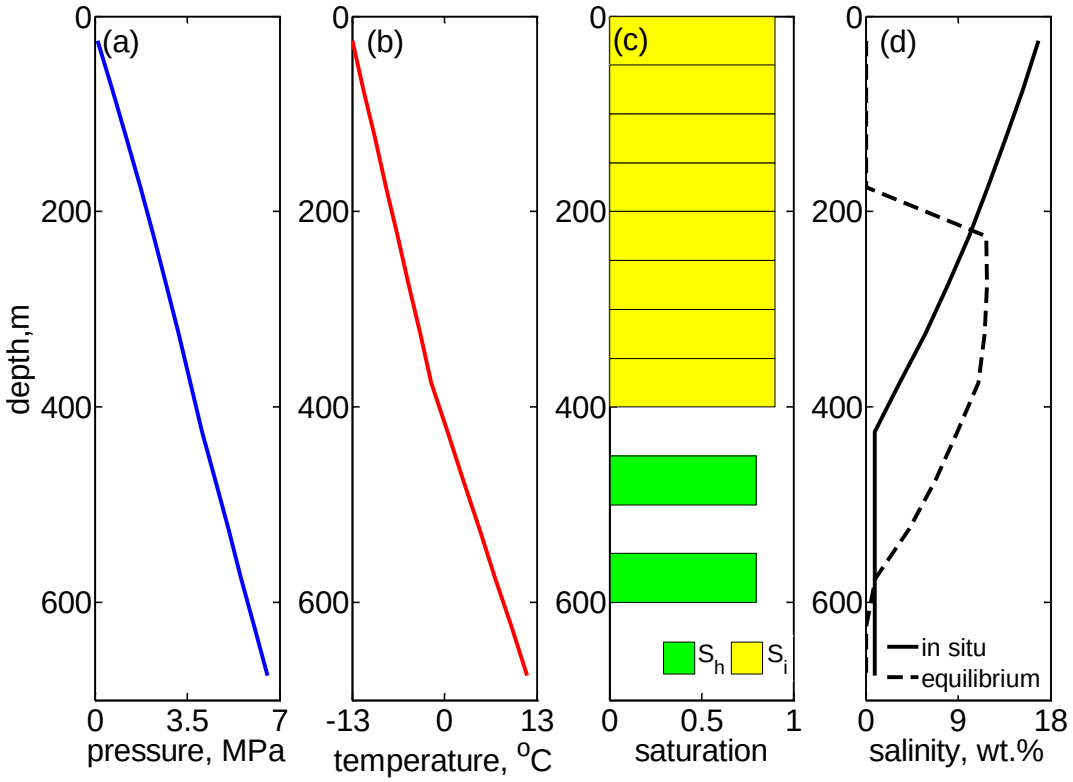

Figure 93: The (a) pressure, (b) temperature, (c) ice (yellow) and hydrate (green) saturations, and (d) in situ (solid line) and three-phase equilibrium (dashed line) salinity distribution at the water depth of 110-120 m on North America Beaufort shelf at 12 k.y. before present (Collett et al., 2011; Frederick and Buffett, 2014). We assumed lateral homogeneous condition.

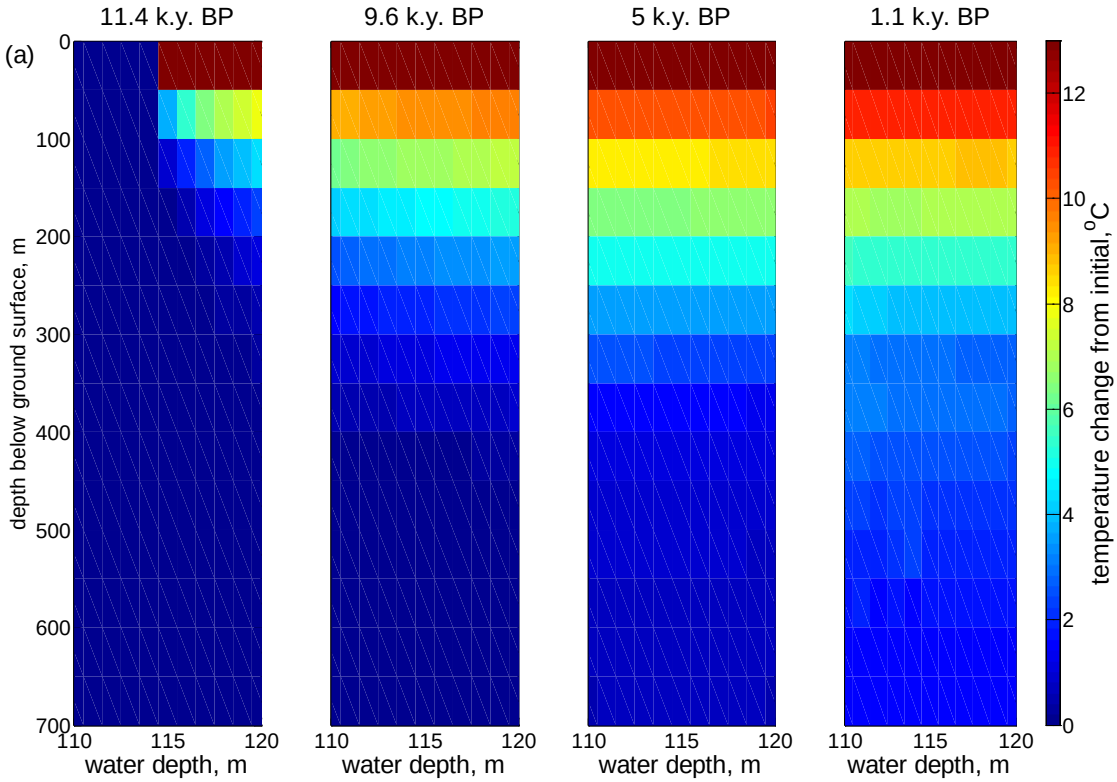
(a)
11.4 k.y. BP
9.6 k.y. BP
5 k.y. BP
1.1 k.y. BP
depth below ground surface, m
0
100
200
300
400
500
600
700
110
115
120
water depth, m
temperature change from initial, °C
0
2
4
6
8
10
12

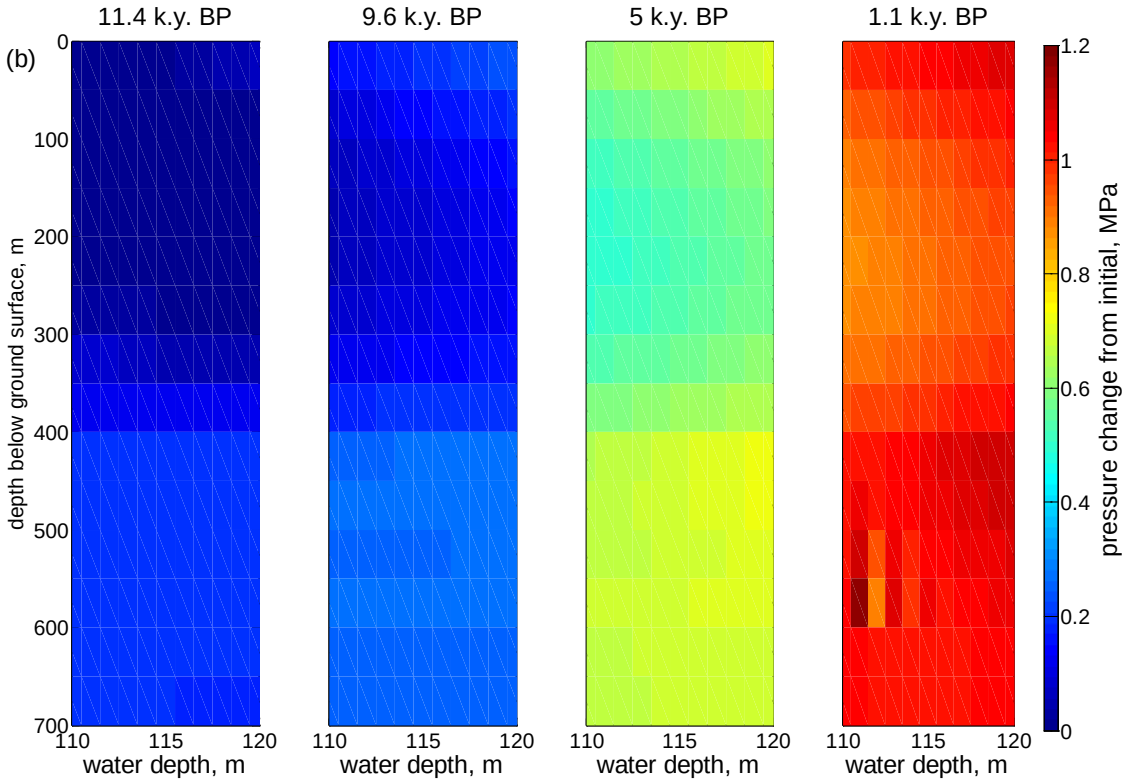
(b)
11.4 k.y. BP
9.6 k.y. BP
5 k.y. BP
1.1 k.y. BP
depth below ground surface, m
0
100
200
300
400
500
600
700
110
115
120
water depth, m
pressure change from initial, MPa
1.2
1
0.8
0.6
0.4
0.2
0

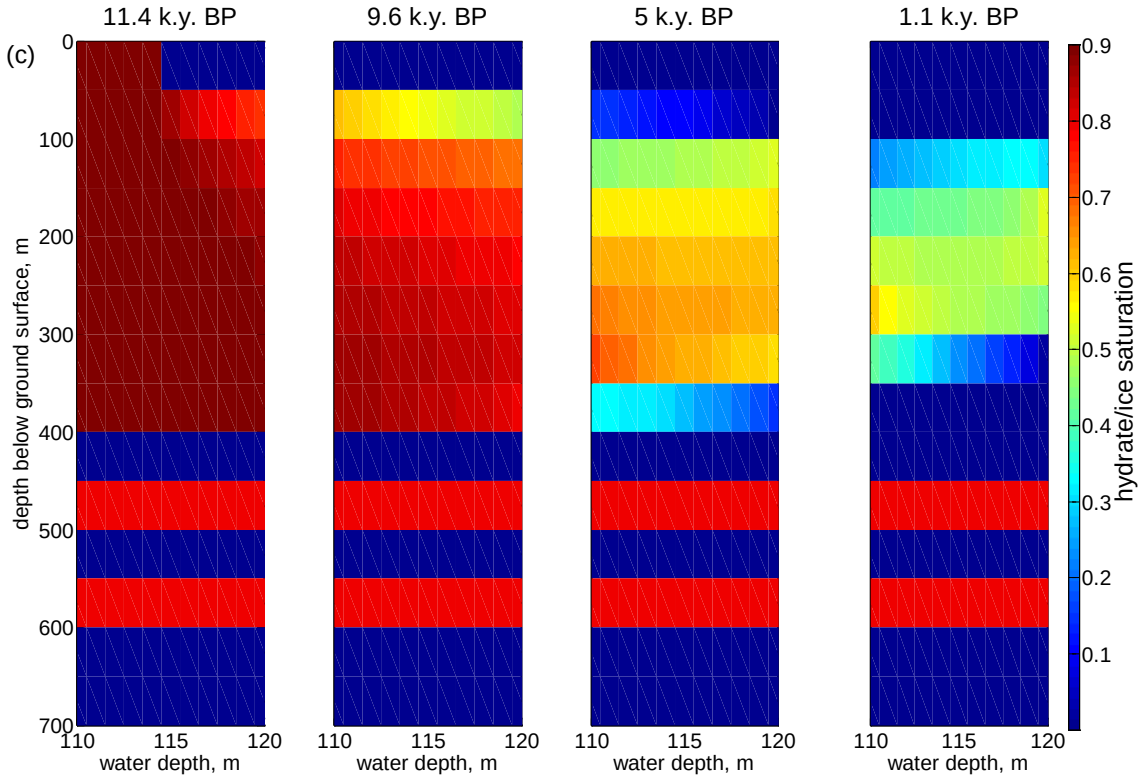

Figure 94: (a) Temperature change from initial, (b) pressure change from initial, and (c) ice (0-400 m) and hydrate (450-500 m, and 550-600 m) saturation at 11.4, 9.6, 5 and 1.1 k.y. before present.

B5. Subtask 7.3.2 - Recent warming

B5.1. Goal:

The Recipient shall simulate the impact of increasing bottom water temperature over the 100 year time scale. The effects of 1 degree per year and 3 degree per year shall be considered. The Recipient shall simulate the continental margin at the up-dip limit of the stability zone and shall consider reservoirs both within the three phase stability zone and those that are within the two phase (L+H) region.

B5.2. Activities Phase 2:

Under current climate conditions and a 1%/yr increase in atmospheric CO_2, the temperature at the seafloor would rise by 1 ^oC over the next 100 yr, and possibly by another 3 ^oC in the following century (Reagan and Moridis, 2009). We investigate the hydrate melting and gas expulsion during seafloor warming in an Arctic Ocean which extends from seafloor to 260 mbsf (meters below seafloor), and laterally from the water depth of 270 to 360 m (Reagan and Moridis, 2009). The seafloor has a slope of

30 degree. The upper boundary (seafloor) is an open boundary. The pressure at the upper boundary is variable with the water depth, but fixed with time. We fix the geothermal flux at the lower boundary to be 28.3 W/m^2. The initial salinity is uniformly 3 wt.% (Reagan and Moridis, 2009). The initial pressure in the sediment increases with depth with a hydrostatic pressure gradient. The initial temperature increases with depth with a geothermal gradient of 0.03 ^{o}C/m and seafloor temperature of 0 ^{o}C (Frederick and Buffett, 2014). These yield a hydrate stability zone in the sediment between the water depth of 290 and 360 m. Initially, there is a 10% hydrate saturation from the base of the hydrate stability zone (BHSZ) to 104 m above the BHSZ (Figure 95a).

We investigated the hydrate melting and gas expulsion in two scenarios of seafloor warming. In Case-1, we increase the seafloor temperature from 0 to 1 ^{o}C at time zero, and then keep this 1 ^{o}C seafloor temperature for the remaining time. Hydrate starts to melt from both the top and bottom of the hydrate deposits from the shallowest water depth with hydrate (Figure 95b). The gas released from the top of the hydrate deposit migrates both vertically upward toward the seafloor and laterally up the slope, and vents at the seafloor both directly above the melting hydrate and up the slope (Figure 96b). The gas released from the bottom of the hydrate deposits preferentially migrates up the slope where the sediment permeability is larger than that in the hydrate deposits and where the hydrate is unstable (Figure 96b). Secondary hydrate forms vertically above the base of the hydrate deposits, but with a less amount compared with the 1D model. That is because most of the gas released from the base of the hydrate deposits escaped up the slope, and vents at the seafloor. The gas venting area extends to the deeper water depth at the seafloor, as the hydrate there starts to melt from the base (Figures 95 and 96). Hydrate disappears from both the shallow water depth and the base of the entire deposits (Figure 95). At steady-state temperature (20 k. y.), the hydrate stability zone retreats to the water depth of 320 m (Fig. 62d). There are still a 17 to 50 m thick hydrate deposit at the base of the hydrate stability zone, which thins toward the shallower water depth (Figure 95d). Residual gas is present below the BHSZ and at water depth shallower than 320 m (Figure 96d).

In Case-2, we increase the seafloor temperature from 0 to 3 ^{o}C linearly in 300 years, and then keep this 3 ^{o}C seafloor temperature for the remaining time. The system behaves similarly as in Case-1, except that the hydrate melts and gas vents at much greater rates (Figure 97). The system reaches steady-state temperature at 12 k.y.., when the hydrate stability zone retreats to the water depth greater than 360 m, and the entire hydrate deposit disappears.

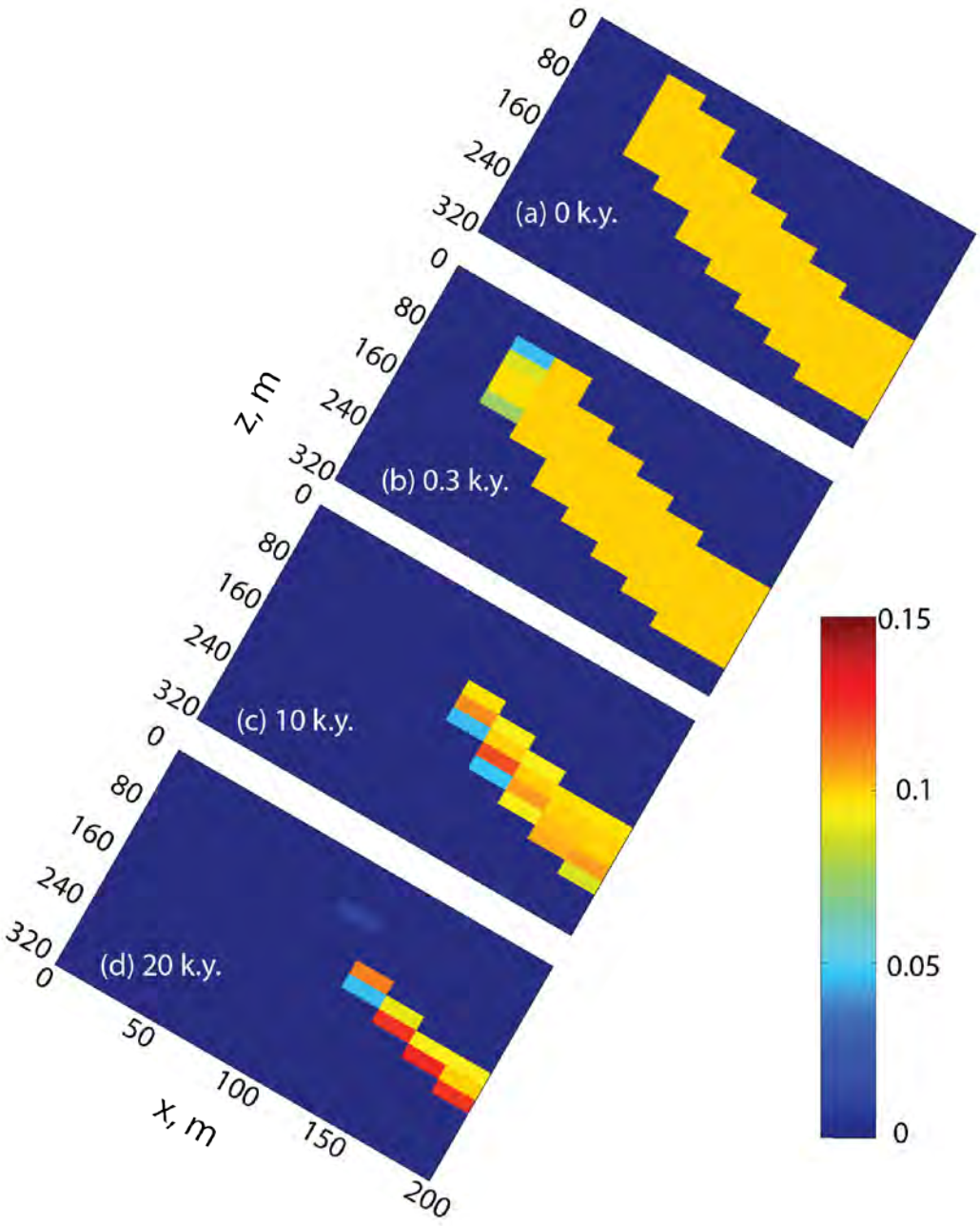

Figure 95: Case-1: hydrate saturation distribution at 0, 0.3, 10 and 20 k.y., respectively.

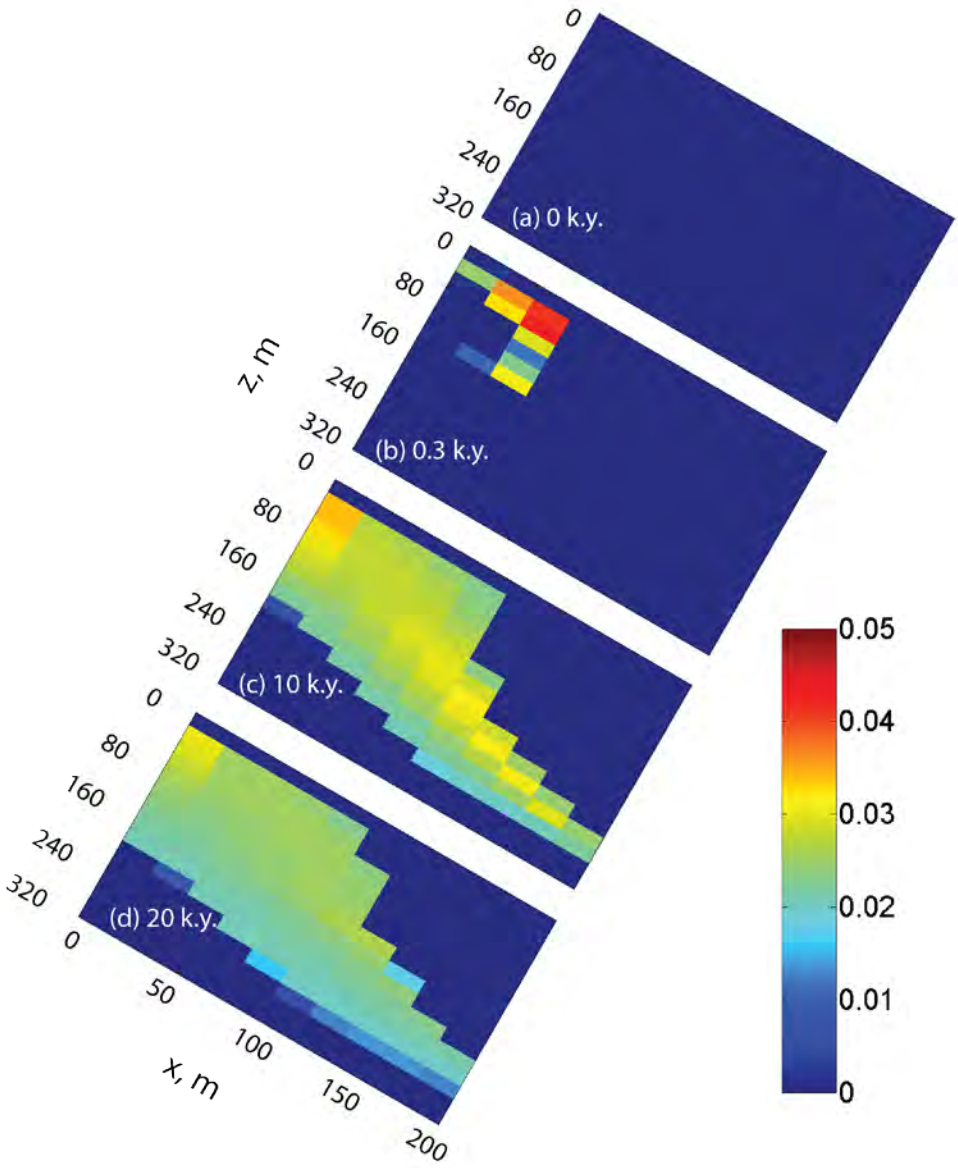

Figure 96: Case-1: gas saturation distribution at 0, 0.3, 10 and 20 k.y., respectively.

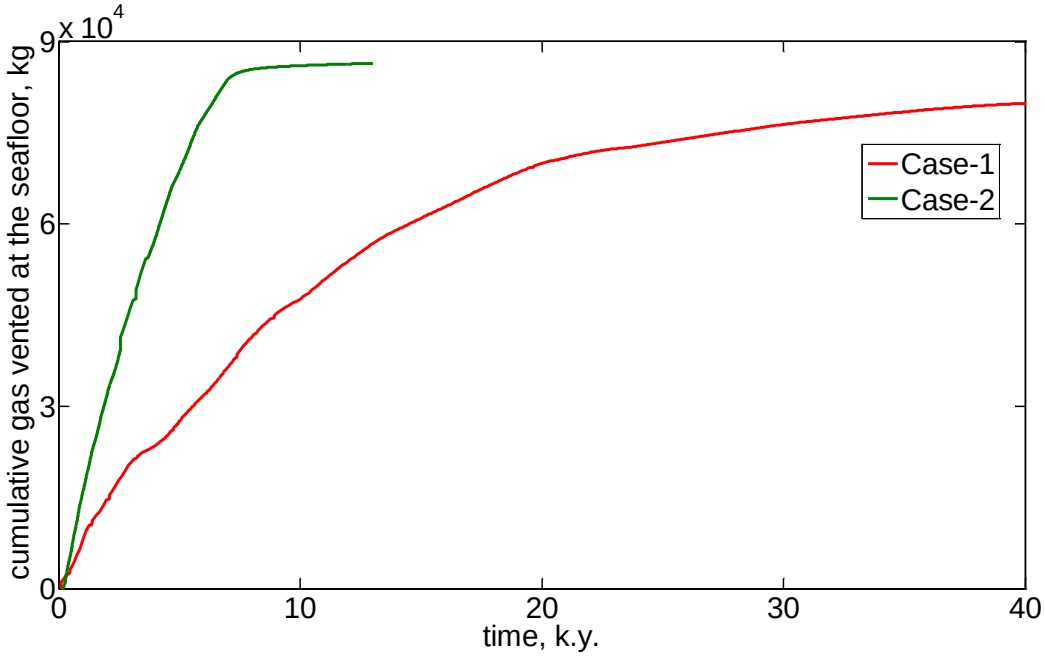

Figure 97: change of cumulative gas vented at the seafloor with time for Case-1 (red line) and Case-2 (green line), respectively.

3. Nomenclature Table

G	Free gas phase
H	Hydrate phase
L	Liquid phase
u	Pore pressure (MPa)
ρ_{sw}	Seawater Density (g/cm^3)
ρ_{pw}	Pore water density (g/cm^3)
ρ_f	Fluid density (g/cm^3)
ρ_b	Bulk density (g/cm^3)
ρ_m	Grain density (g/cm^3)
Z_{wd}	Water depth (m)
ΔZ	Depth within the GHSZ (m)
Z	GHSZ thickness (m)
g	Gravitational acceleration (m/s^2)
T_f	Formation temperature (ºC)
T_b	Seafloor temperature (ºC)
G_g	Geothermal gradient (ºC/km)
S_h	Hydrate saturation (dimensionless)
S_w	Water saturation (dimensionless)
$C_{in\text{-}situ}$	In-situ salinity (dimensionless)
C_0	Core-derived salinity (dimensionless)
C	Salinity (dimensionless)
N	Saturation exponent (dimensionless)
a	Tortuosity coefficient (dimensionless)
m	Cementation exponent (dimensionless)
n	Porosity (dimensionless)
ρ_w	Fluid resistivity (Ωm)
ρ_t	Formation resistivity (Ωm)
F	Formation factor (dimensionless)
M_g	gas molecular mass (g/mol)
M_h	hydrate molecular mass (g/mol)

M_w	water molecular mass (g/mol)
ΔS_g	change in gas saturation (V/V)
ΔS_h	change in hydrate saturation (V/V)
ΔS_w	change in water saturation (V/V)
ΔW	change in water mass (g)
ΔM	change in methane mass (g)
L	sample length (cm)
L_f	length of hydrate formation zone (cm)
V_{TOT}	total sample volume (mL)

MOC model

Superscript

a	downstream side of the leading shock
b	upstream side of the leading shock
c	downstream side of the trailing shock
d	upstream side of the leading shock
e	a position between the downstream side of the trailing shock and upstream side of leading shock

Subscript

B	the component of brine
M	the component of methane
W	the component of pure water
g	gas phase
h	hydrate phase
l	liquid water phase
β	phase index
κ	component index

Variables

cl_0	initial salinity (wt.%)

cl_e salinity at three phase equilibrium (wt.%)

D_s effective molecular diffusion coefficient of salt in sediment ($m^2\ s^{-1}$)

D_{s0} molecular diffusion coefficient of salt in free water ($m^2\ s^{-1}$)

f_g fractional flow of gas phase (dimensionless)

f_l fractional flow of liquid water phase (dimensionless)

g acceleration due to gravity ($m\ sec^{-2}$)

G_β overall dimensionless concentration of component β

H_β overall dimensionless flux of component β

k sediment intrinsic permeability (m^2)

k_0 sediment intrinsic permeability in absence of ice and hydrate (m^2)

$k_{r\beta}$ relative permeability of β phase (dimensionless)

L characteristic length (m)

L_s distance from the hydrate solidification front where salt diffusion changes the salinity (m)

P_c capillary pressure (Pa)

P_0 pressure (Pa)

q_{gi} gas injection rate ($m\ sec^{-1}$)

S_β^* effective saturation of β phase (dimensionless)

S_β saturation of β phase (dimensionless)

S_{gr} residual gas phase saturation (dimensionless)

S_{wr} residual water phase saturation (dimensionless)

t time (sec)

T_0 temperature (°C)

v total flux of the mobile phase (m sec^{-1})

v_D dimensionless total flux

$X_{\kappa,\beta}$ mass fraction of component κ in phase β (dimensionless)

θ dip angle of the system (rad)

ϕ porosity (dimensionless)

ρ_{lD} dimensionless density of liquid water phase

ρ_{gD} dimensionless density of gas phase

ρ_{hD} dimensionless density of hydrate phase

ρ_β density of β phase (kg m^{-3})

ρ_{gi} density of the injected gas (kg m^{-3})

μ_β dynamic viscosity of β phase (kg m^{-1} s^{-1})

λ_β mobility of phase β (W m^{-1} ^{o}C^{-1})

τ dimensionless time

ε dimensionless distance from gas inlet

ε_0 initial dimensionless position of the composition G_β

Λ_β^{ab} dimensionless leading shock velocity calculated by the component β

Λ^e dimensionless composition wave velocity for gas saturation of S_g^e

Numerical model

β	phase
e	energy component
g	gas phase
h	hydrate phase
κ	component

l	liquid phase
m	methane component
s	salt component
v	vapor phase
w	water component
C_R	heat capacity of the solid grain (J kg^{-1} oC^{-1})
D_{l0}^{κ}	molecular diffusion coefficient of component k in free water (m^2 s^{-1})
ϕ	porosity of the sediment (dimensionless)
ϕ_0	porosity in the absence of hydrate (dimensionless)
g	acceleration due to gravity (m s^{-2})
h_β	specific enthalpy of phase β (J kg^{-1})
k	intrinsic permeability (m^2)
k_0	permeability in the absence of hydrate (m^2)
$k_{r\beta}$	relative permeability of phase β (dimensionless)
λ	overall thermal conductivity of porous media (W m^{-1} ^{o}C^{-1})
λ_β	thermal conductivity of phase β (W m^{-1} ^{o}C^{-1})
λ_R	thermal conductivity of grain (W m^{-1} ^{o}C^{-1})
μ_β	viscosity of phase β (Pa s)
P_c	capillary pressure (Pa)
P_{c0}	capillary pressure in the absence of hydrate (Pa)
P_β	β phase pressure (Pa)
q^e	generation rate of energy (J m^{-3} s^{-1})
q^κ	generation rate of component κ (kg m^{-3} s^{-1})
ρ_β	density of phase β (kg m^{-3})
S_β	saturation of phase β (dimensionless)
T	temperature (^{o}C)
t	time (s)

u_β specific internal energy of phase β (J kg^{-1})

X_β^k mass fraction of component κ in phase β (dimensionless)

4. References

Archer, D., 2015, A model of the methane cycle, permafrost, and hydrology of the Siberian continental margin: Biogeosciences, v. 12, no. 10, p. 2953-2974.

Archer, D., Martin, P., Buffett, B., Brovkin, V., Rahmstorf, S., and Ganopolski, A., 2004, The importance of ocean temperature to global biogeochemistry: Earth and Planetary Science Letters, v. 222, p. 333-348.

Archie, G. E., 1942, The Electrical Resistivity Log as an Aid in Determining Some Reservoir Characteristics, Transactions of AIME, Volume 146, p. 4.

Arps, J. J., 1953, The Effect of Temperature on the Density and Electrical Resistivity of Sodium Chloride Solutions: Society of Petroleum Engineers, v. 5, p. 4.

Bader, S., and Kooi, H., 2005, Modelling of solute and water transport in semi-permeable clay membranes: comparison with experiments: Advances in Water Resources, v. 28, no. 3, p. 203-214.

Bangs, N. L. B., Hornbach, M. J., and Berndt, C., 2011, The mechanics of intermittent methane venting at South Hydrate Ridge inferred from 4D seismic surveying: Earth and Planetary Science Letters, v. 310, no. 1-2, p. 105-112.

Barbour, S. L., and Fredlund, D. G., 1989, Mechanisms of osmotic flow and volume change in clay soils: Canadian Geotechnical Journal, v. 26, no. 4, p. 551-562.

Bear, J., 1972, Dynamics of Fluids in Porous Media, Mineola, N. Y., Dover.

Behseresht, J., and Bryant, S., 2011a, Effect of Relative Permeability Characteristics and Gas/Water Flow on Gas-Hydrate Saturation Distribution, Society of Petroleum Engineers Annual Technical Conference and Exhibition: Denver, Colorado, USA, p. 14.

Behseresht, J., and Bryant, S. L., 2011b, Sedimentological Control on Hydrate Saturation Distribution in Arctic Gas-Hydrate-Bearing Deposits, Proceedings of the 7th International Conference on Gas Hydrates (ICGH 2011): Edinburgh, Scotland, United Kingdom.

Behseresht, J., Peng, Y., Prodanović, M., and Bryant, S., 2008a, Grain scale study of hydrate formation in sediments from methane gas: Role of capillarity, Proceedings of the 6th International Conference on Gas Hydrates (ICGH 2008): Vancouver, BC, Canada.

Behseresht, J., Peng, Y., Prodanović, M., Bryant, S., Jain, A., and Juanes, R., Mechanisms by Which Methane Gas and Methane Hydrate Coexist In Ocean Sediments, *in* Proceedings Proceedings of the 2008 Offshore Technology Conference, Houston, Texas, USA, 5-8 May 2008 2008b.

Bily, C., and Dick, J. W. L., 1974, Naturally occurring gas hydrates in the Mackenzie Delta, N.W.T: Bulletin of Canadian Petroleum Geology, v. 22, no. 3, p. 340-352.

Birkedal, K. A., Ersland, G., Hauge, L. P. O., and Graue, A., Electrical resistivity measurement of CH4 hydrate-bearing sandstone during formation, *in* Proceedings 7th International Conference on Gas Hydrates, Edinburgh, Scotland, United Kingdom, 2011.

Boswell, R., Collett, T. S., Frye, M., Shedd, W., McConnell, D. R., and Shelander, D., 2012, Subsurface gas hydrates in the northern Gulf of Mexico: Marine and Petroleum Geology, v. 34, no. 1, p. 4-30.

Bryant, S., and Juanes, R., 2012, Mechanisms Leading To Co-Existence Of Gas Hydrate In Ocean Sediments: U.S. Department of Energy, National Energy Technology Laboratory.

Circone, S., Kirby, S. H., and Stern, L. A., 2005, Direct Measurement of Methane Hydrate Composition along the Hydrate Equilibrium Boundary: The Journal of Physical Chemistry B, v. 109, no. 19, p. 9468-9475.

Clennell, M. B., Hovland, M., Booth, J. S., Henry, P., and Winters, W. J., 1999, Formation of natural gas hydrates in marine sediments 1. Conceptual model of gas hydrate growth conditioned by host sediment properties: Journal of Geophysical Research, v. 104, no. B10, p. 22985-23003.

Collett, T. S., and Dallimore, S. R., 1998, Quantitative assessment of gas hydrates in the Mallik L-38 well, Mackenzie Delta, NWT, Canada, *in* Lewkowicz, A. G. a. A., M., ed., Proceedings of the Eighth International Conference on Permafrost, June 23-27, 1998, Volume Bulletin 585: Quebec, Quebec, Centre d'etudes nordiques, p. 6.

Collett, T. S., and Ladd, J., 2000, Detection of gas hydrate with downhole logs and assessment of gas hydrate concentrations (saturations) and gas volumes on the Blake Ridge with electrical resistivity log data, Proceedings of the Ocean Drilling Program, Scientific Results, Volume 164: College Station, TX, Texas A & M University, Ocean Drilling Program, p. 179 -191.

Collett, T. S., Lee, M. W., Agena, W. F., Miller, J. J., Lewis, K. A., Zyrianova, M. V., Boswell, R., and Inks, T. L., 2011, Permafrost-associated natural gas hydrate occurrences on the Alaska North Slope: Marine and Petroleum Geology, v. 28, no. 2, p. 279-294.

Collett, T. S., Lee, M. W., Zyrianova, M. V., Mrozewski, S. A., Guerin, G., Cook, A. E., and Goldberg, D. S., 2012, Gulf of Mexico Gas Hydrate Joint Industry Project Leg II logging-while-drilling data acquisition and analysis: Marine and Petroleum Geology, v. 34, no. 1, p. 41-61.

Collett, T. S., Lewis, R. E., and Dallimore, S. R., 2005, JAPEX/JNOC/GSC et al. Mallik 5L-38 gas hydrate production research well downhole well-log and core montages, *in* Dallimore, S. R., and Collett, T. S., ed., Scientific Results from the Mallik 2002 Gas Hydrate Production Research Well Program, Mackenzie Delta, Northwest Territories, Canada, Volume Bulletin 585, Geological Survey of Canada, p. 23.

Cook, A. E., Anderson, B. I., Malinverno, A., Mrozewski, S., and Goldberg, D. S., 2010, Electrical anisotropy due to gas hydrate-filled fractures: Geophysics, v. 75, no. 6, p. F173-F185.

Cook, A. E., Anderson, B. I., Rasmus, J., Sun, K., Li, Q., Collett, T. S., and Goldberg, D. S., 2012, Electrical anisotropy of gas hydrate-bearing sand reservoirs in the Gulf of Mexico: Marine and Petroleum Geology, v. 34, no. 1, p. 72-84.

Crain, E. R., 2013, Crain's Petrophysical Handbook - Resistivity Basic.

Daigle, H., Bangs, N. L., and Dugan, B., 2011, Transient hydraulic fracturing and gas release in methane hydrate settings: A case study from southern Hydrate Ridge: Geochemistry Geophysics Geosystems, v. 12, no. 12.

Daigle, H., and Dugan, B., 2011, Capillary controls on methane hydrate distribution and fracturing in advective systems: Geochemistry, Geophysics, Geosystems, v. 12, no. 1, p. n/a-n/a.

Dallimore, S. R., and Collett, T. S., 2005, Summary and implications of the Mallik 2002 Gas Hydrate Production Research Well Program, Scientific Results from the Mallik 2002 Gas Hydrate Production Research Well Program, Mackenzie Delta, Northwest Territories, Canada, Geological Survey of Canada, Bulletin no. 585, 2005.

Dallimore, S. R., Uchida, T., and Collett, T., 1999, Summary, *in* Dallimore, S. R., Uchida, T., and Collett, T. S., eds., Scientific results from JAPEX/JNOC/GSC Mallik 2L-38 Gas Hydrate Production Research Well, Mackenzie Delta, Northwest Territories, Canada, Volume Bulletin 544, Geological Survey of Canada, p. 10.

Darnell, K. N., and Flemings, P. B., 2015, Transient seafloor venting on continental slopes from warming-induced methane hydrate dissociation: Geophysical Research Letters, p. n/a-n/a.

DiCarlo, D. A., Mirzaei, M., Aminzadeh, B., and Dehghanpour, H., 2012, Fractional Flow Approach to Saturation Overshoot: Transport in Porous Media, v. 91, no. 3, p. 955-971.

Dickens, G. R., 2003, Rethinking the global carbon cycle with a large, dynamic and microbially mediated gas hydrate capacitor: Earth and Planetary Science Letters, v. 213, no. 3–4, p. 169-183.

Duan, Z., Møller, N., Greenberg, J., and Weare, J. H., 1992, The prediction of methane solubility in natural waters to high ionic strength from 0 to 250°C and from 0 to 1600 bar: Geochimica et Cosmochimica Acta, v. 56, no. 4, p. 1451-1460.

Ellis, D. V., and Singer, J. M., 2007, Well Logging for Earth Scientists, 2nd ed., Springer, 692 p.:

England, W. A., Mackenzie, A. S., Mann, D. M., and Quigley, T. M., 1987, The movement and entrapment of petroleum fluids in the subsurface: Journal of the Geological Society of London, v. 144, no. 2, p. 327-347.

Expedition 311 Scientists, 2006, Site U1328, *in* Riedel, M., Collett, T. S., Malone, M. J., and Expedition 311 Scientists, eds., Proceedings of the Integrated Ocean Drilling Program, Volume 311: Washington, DC (Integrated Ocean Drilling Program Management International, Inc.).

Flemings, P. B., 2014a, October Quarterly Research Performance Progress Report (Period ending 9/30/2014), Controls on Methane Expulsion During Melting of Natural Melting of Natural Gas Hydrate Systems: Topic Area 2, DOE Award No.: DE-FE0010406.

-, 2014b, Phase 1 Progress Report (Period ending 3/31/2014), Controls on Methane Expulsion During Melting of Natural Melting of Natural Gas Hydrate Systems: Topic Area 2, DOE Award No.: DE-FE0010406.

-, 2015, January Quarterly Research Performance Progress Report (Period ending 12/31/2014), Controls on Methane Expulsion During Melting of Natural Melting of Natural Gas Hydrate Systems: Topic Area 2, DOE Award No.: DE-FE0010406.

Frederick, J. M., and Buffett, B. A., 2014, Taliks in relict submarine permafrost and methane hydrate deposits: Pathways for gas escape under present and future conditions: Journal of Geophysical Research: Earth Surface, v. 119, no. 2, p. 106-122.

Ginsburg, G. D., and Soloviev, V. A., 1997, Methane migration within the submarine gas-hydrate stability zone under deep-water conditions: Marine Geology, v. 137, p. 49-57.

Haacke, R. R., Hyndman, R. D., Park, K.-P., Yoo, D.-G., Stoian, I., and Schmidt, U., 2009, Migration and venting of deep gases into the ocean through hydrate-choked chimneys offshore Korea: Geology, v. 37, no. 6, p. 531-534.

Haberer, R. M., Mangelsdorf, K., Dieckmann, V., Fuhrmann, A., Wilkes, H., and Horsfield, B., 2005, Characterization of the organic matter in lignite layers of the Kugmallit Sequence (Oligocene) at the JAPEX/JNOC/GSC et al. Mallike 5L-38 gas hydrate production research well, *in* Dallimore, S. R., and Collett, T. S., ed., Scientific Results from the Mallik 2002 Gas Hydrate Production Research Well Program, Mackenzie Delta, Northwest Territories, Canada, Volume Bulletin 585, Geological Survey of Canada, p. 14.

Haeckel, M., Suess, E., Wallmann, K., and Rickert, D., 2004, Rising methane gas bubbles form massive hydrate layers at the seafloor: Geochimica et Cosmochimica Acta, v. 68, no. 21, p. 4335-4345.

Heeschen, K. U., Trehu, A. M., Collier, R. W., Suess, E., and Rehder, G., 2003, Distribution and height of methane bubble plumes on the Cascadia Margin characterized by acoustic imaging: Geophysical Research Letters, v. 30, no. 12.

Henninges, J., Schrotter, J., Erbas, K., and Huenges, E., 2005, Temperature field of the Mallik gas hydrate occurrence - implication on phase changes and thermal properties, *in* Dallimore, S. R., and Collett, T. S., eds., Scientific Results from the Mallik 2002 Gas Hydrate Production Research Well Program, Mackenzie Delta, Northwest Territories, Canada, Volume Bulletin 585, Geological Survey of Canada, p. 11.

Henry, P., Thomas, M., and Ben Clennell, M., 1999, Formation of natural gas hydrates in marine sediments 2. Thermodynamic calculations of stability conditions in porous sediments: Journal of Geophysical Research, v. 104, no. B10, p. 23005-23022.

Hesse, R., and Harrison, W. E., 1981, Gas hydrates (clathrates) causing pore-water freshening and oxygen isotope fractionation in deep-water sedimentary sections of terrigenous continental margins: Earth and Planetary Science Letters, v. 55, no. 3, p. 10.

Hodgman, C. D., 1960, Handbook of Chemistry and Physics, Cleveland, Ohio, Chemical Rubber Publishing Co.

Hubbert, M. K., 1953, Entrapment of Petroleum under Hydrodynamic Conditions: Bulletin of the American Association of Petroleum Geologists, v. 38, no. 8, p. 1954-2026.

Husebø, J., Ersland, G., Graue, A., and Kvamme, B., 2009, Effects of salinity on hydrate stability and implications for storage of CO2 in natural gas hydrate reservoirs: Energy Procedia, v. 1, no. 1, p. 3731-3738.

IOC, IHO, and BODC, 2003, Centenary Edition of the GEBCO Digital Atlas, published on CD-ROM on behalf of the Intergovernmental Oceanographic Commission and the International Hydrographic Organization as part of the General Bathymetric Chart of the Oceans: Liverpool, U.K., British Oceanographic Data Centre.

Katsuki, D., Ohmura, R., Ebinuma, T., and Narita, H., 2007, Methane hydrate crystal growth in a porous medium filled with methane-saturated liquid water: Philosophical Magazine, v. 87, no. 7, p. 1057-1069.

Kayen, R. E., and Lee, H. J., 1991, Pleistocene slope instability of gas hydrate-laden sediment on the Beaufort margin: Marine Geotechnology, v. 10.

Kennedy, W. D., and Herrick, D. C., 2003, Conductivity Anisotropy In Shale-Free Sandstone: Galveston, Texas, Society of Petrophysicists and Well-Log Analysts.

Kleinberg, R. L., Flaum, C., Griffin, D. D., Brewer, P. G., Malby, G. E., Peltzer, E. T., and Yesinowski, J. P., 2003, Deep sea NMR: Methane hydrate growth habit in porous media and its relationship to hydraulic permeability, deposit accumulation, and submarine slope stability: Journal of Geophysical Research: Solid Earth, v. 108, no. B10, p. 2508.

Kneafsey, T. J., Tomutsa, L., Moridis, G. J., Seol, Y., Freifeld, B. M., Taylor, C. E., and Gupta, A., 2007, Methane hydrate formation and dissociation in a partially saturated core-scale sand sample: Journal of Petroleum Science and Engineering, v. 56, no. 1–3, p. 108-126.

Kvenvolden, K. A., 1988, Methane Hydrate: A Major Reservoir of Carbon in the Shallow Geosphere?: Chemical Geology, v. 71, p. 11.

-, 1993, Gas hydrates-geological perspective and global change: Reviews of Geophysics, v. 31, p. 173-187.

Lake, L. W., 1989, Enhanced oil recovery, Prentice Hall.

Lederhos, J. P., Long, J. P., Sum, A., Christiansen, R. L., and Sloan Jr, E. D., 1996, Effective kinetic inhibitors for natural gas hydrates: Chemical Engineering Science, v. 51, no. 8, p. 1221-1229.

Lee, M. W., and Collett, T. S., 2009, Gas hydrate saturations estimated from fractured reservoir at Site NGHP-01-10, Krishna-Godavari Basin, India: Journal of Geophysical Research: Solid Earth, v. 114, no. B7, p. B07102.

Levitus, S., Boyer, T. P., Conkright, M. E., Brien, T. O., Antonov, J., Stephens, C., Stathoplos, L., Johnson, D., and Gelfeld, R., 1998, NOAA Atlas NESDIS 18,World Ocean Database 1998: VOLUME 1: INTRODUCTION: Wash., D.C., U.S. Gov. Printing Office, p. 346pp.

Li, F., Sun, C., Li, S., Chen, G., Guo, X., Yang, L., Pan, H., Li, S., and Zhang, K., 2012, Experimental studies on the evolvement of electrical resistivity during methane hydrate formation in sediments: Energy & Fuels, v. 26, no. 10, p. 6210-6217.

Li , S., Xia, X., Xuan, J., Liu, Y., and Li, Q., 2010, Resistivity in formation and decomposition of natural gas hydrate in porous medium: Chinese Journal of Chemical Engineering, v. 18, no. 1, p. 39-42.

Lide, D. R., 2004, CRC Handbook of Chemistry and Physics, 85th Edition, Taylor & Francis.

Liu, X., 2006, Dynamics of Shallow Marine Gas Hydrate and Free Gas Systems [Doctor of Philosophy: The Pennsylvania State University, 135 p.

Liu, X., and Flemings, P. B., 2006, Passing gas through the hydrate stability zone at southern Hydrate Ridge, offshore Oregon: Earth and Planetary Science Letters, v. 241, no. 1–2, p. 211-226.

-, 2007, Dynamic multiphase flow model of hydrate formation in marine sediments: Journal of Geophysical Research, v. 112, no. B3.

Liu, X., and Flemings, P. B., 2011, Capillary effects on hydrate stability in marine sediments: Journal of Geophysical Research-Solid Earth, v. 116, no. B07102, p. 24.

Lu, H., Dutrisac, R., Ripmeester, J., Wright, F., and Uchida, T., 2005, Measurements of gas hydrate saturation in sediment cores recovered from the JAPEX/JNOC/GSC et al. Mallik 5L-38 gas hydrate production research well, *in* Dallimore, S. R., and Collett, T. S., eds., Scientific Results from the Mallik 2002 Gas Hydrate Production Research Well Program, Mackenzie Delta, Northwest Territories, Canada, Volume Bulletin 585, Geological Survey of Canada, p. 11.

Lucia, F. J., 1983, Petrophysical Parameters Estimated From Visual Descriptions of Carbonate Rocks: A Field Classification of Carbonate Pore Space: Journal of Petroleum Technology, v. 35, no. 03, p. 629-637.

Majorowicz, J., Safanda, J., and Osadetz, K., 2012, Inferred gas hydrate and permafrost stability history models linked to climate change in the Beaufort-Mackenzie Basin, Arctic Canada: Clim. Past, v. 8, no. 2, p. 667-682.

Malinverno, A., Kastner, M., Torres, M. E., and Wortmann, U. G., 2008, Gas hydrate occurrence from pore water chlorinity and downhole logs in a transect across the northern Cascadia margin (Integrated Ocean Drilling Program Expedition 311): Journal of Geophysical Research: Solid Earth, v. 113, no. B8, p. B08103.

Malusis, M. A., Shackelford, C. D., and Olsen, H. W., 2003, Flow and transport through clay membrane barriers: Engineering Geology, v. 70, no. 3–4, p. 235-248.

Matsumoto, R., Tomaru, H., Chen, Y. F., Lu, H., and Clark, I. D., 2005, Geochemistry of the interstital waters of the JPAX/JNOC/GSC et al. Mallik 5L-38 gas hydrate production research well, *in* Dallimore, S. R., and Collett, T. S., ed., Scientific Results from the Mallik 2002 Gas Hydrate Production Research Well Program, Mackenzie Delta, Northwest Territories, Canada, Volume Bulletin 585, Geological Survey of Canada, p. 11.

Mazumdar, A., Dewangan, P., Joäo, H. M., Peketi, A., Khosla, V. R., Kocherla, M., Badesab, F. K., Joshi, R. K., Roxanne, P., Ramamurty, P. B., Karisiddaiah, S. M., Patil, D. J., Dayal, A. M., Ramprasad, T., Hawkesworth, C. J., and Avanzinelli, R., 2009, Evidence of paleo–cold seep activity from the Bay of Bengal, offshore India: Geochemistry, Geophysics, Geosystems, v. 10, no. 6, p. n/a-n/a.

McConnell, D. R., and Kendall, B. A., Images of the base of gas hydrate stability, Northwest Walker Ridge, Gulf of Mexico, *in* Proceedings Offshore Technology Conference, Houston, Texas, 6-9 May 2002 2002.

Medioli, B. E., Wilson, N., Dallimore, S. R., Pare, D., Brennan-Alpert, P., and Oda, H., 2005, Sedimentology of the cored interval, JAPEX/JNOC/GSC et al. gas hydrate production research well, *in* Dallimore, S. R., and Collett, T. S., eds., Scientific Results from the Mallik 2002 Gas Hydrate Production Research Well Program, Mackenzie Delta, Northwest Territories, Canada, Volume Bulletin 585, Geological Survey of Canada, p. 14.

Meyer, D. W., and Flemings, P. B., 2014, Thermodynamic State of Gas Hydrate in the Krishna-Godavari Basin Inferred From Well Log Analysis, Offshore Technology Conference.

Mienert, J., Vanneste, M., Bünz, S., Andreassen, K., Haflidason, H., and Sejrup, H. P., 2005, Ocean warming and gas hydrate stability on the mid-Norwegian margin at the Storegga Slide: Marine and Petroleum Geology, v. 22, no. 1–2, p. 233-244.

Milkov, A. V., 2004, Global estimates of hydrate-bound gas in marine sediments: how much is really out there?: Earth-Science Reviews, v. 66, no. 3–4, p. 183-197.

Milkov, A. V., Y.-J. Lee, Borowski, W. S., Torres, M. E., Xu, W., Tomaru, H., Trehu, A. M., Schultheiss, P., Dickens, G. R., and Claypool, G. E., 2004, Co-existence of gas hydrate, free gas, and brine within the regional gas hydrate stability zone at Hydrate Ridge (Oregon margin): Evidence from prolonged degassing of a pressurized core: Earth and Planetary Science Letters, v. 222, p. 829-843.

Moridis, G. J., 2008, TOUGH+Hydrate v1.0 User's Manual: A Code for the Simulation of System Behavior in Hydrate-Bearing Geologic Media.

Moridis, G. J., Seol, Y., and Kneafsey, T. J., 2005, Studies of Reaction Kinetics of Methane Hydrate Dissocation in Porous Media.

NGHP Expedition 01 Scientists, 2007, Sites NGHP-01-10, 12, and 13, *in* Collett, T. S., Reidel, M., Cochran, J., Boswell, R., Presley, J., Kumar, P., Sathe, A., Sethi, A., Lall, M., and the NGHP Expedition 01 Scientists, eds., National Gas Hydrate Program Expedition 01 Initial Reports, Directorate General of Hydrocarbon, Ministry of Petroleum and Natural Gas (India), p. 150.

Nixon, M. F., and Grozic, J. L. H., 2007, Submarine slope failure due to gas hydrate dissociation: a preliminary quantification: Canadian Geotechnical Journal, v. 44, no. 3, p. 314-325.

Orr, F. M., 2007, Theory of gas injection processes, Tie-Line Publications.

Paull, C. K., Buelow, W. J., Ussler, W., and Borowski, W. S., 1996, Increased continental-margin slumping frequency during sea-level lowstands above gas hydrate–bearing sediments: Geology, v. 24, no. 2, p. 143-146.

Paull, C. K., Dallimore, S., Hughes-Clarke, J., Blasco, S., Lundsten, E., III, W. U., Graves, D., Sherman, A., Conway, K., Melling, H., Vagle, S., and Collett, T., 2011, Tracking the Decomposition of Submarine Permafrost and Gas Hydrate Under the Shelf and Slope of the Beaufort Sea, 7th International Conference on Gas Hydrate, p. 12.

Pearson, C. F., Halleck, P. M., McGuire, P. L., Hermes, R., and Mathews, M., 1983, Natural gas hydrate deposits: a review of in situ properties: The Journal of Physical Chemistry, v. 87, no. 21, p. 4180-4185.

Phrampus, B. J., and Hornbach, M. J., 2012, Recent changes to the Gulf Stream causing widespread gas hydrate destabilization: Nature, v. 490, no. 7421, p. 527-530.

Rachold, V., Bolshiyanov, D. Y., Grigoriev, M. N., Hubberten, H.-W., Junker, R., Kunitsky, V. V., Merker, F., Overduin, P., and Schneider, W., 2007, Nearshore arctic subsea permafrost in transition: Eos, Transactions American Geophysical Union, v. 88, no. 13, p. 149-150.

Reagan, M. T., and Moridis, G. J., 2008, Dynamic response of oceanic hydrate deposits to ocean temperature change: Journal of Geophysical Research: Oceans, v. 113, no. C12, p. C12023.

Reagan, M. T., and Moridis, G. J., 2009, Large-scale simulation of methane hydrate dissociation along the West Spitsbergen Margin: Geophysical Research Letters, v. 36, no. 23, p. L23612.

Rees, E. V. L., Kneafsey, T. J., and Seol, Y., 2011a, Methane hydrate distribution from prolonged and repeated formation in natural and compacted sand samples: X-Ray CT observations: Journal of Geological Research, v. 2011.

Rees, E. V. L., Priest, J. A., and Clayton, C. R. I., 2011b, The structure of methane gas hydrate bearing sediments from the Krishna–Godavari Basin as seen from Micro-CT scanning: Marine and Petroleum Geology, v. 28, no. 7, p. 1283-1293.

Rehder, G., Brewer, P. W., Peltzer, E. T., and Friederich, G., 2002, Enhanced lifetime of methane bubble streams within the deep ocean: Geophysical Research Letters, v. 29, no. 15, p. 21-21-21-24.

Ren, S., Liu, Y., Liu, Y., and Zhang, W., 2010, Acoustic velocity and electrical resistance of hydrate bearing sediments: Journal of Petroleum Science and Engineering, v. 70, no. 1–2, p. 52-56.

Riedel, M., Collett, T. S., Kumar, P., Sathe, A. V., and Cook, A., 2010, Seismic imaging of a fractured gas hydrate system in the Krishna–Godavari Basin offshore India: Marine and Petroleum Geology, v. 27, no. 7, p. 1476-1493.

Ryu, B.-J., Collett, T. S., Riedel, M., Kim, G. Y., Chun, J.-H., Bahk, J.-J., Lee, J. Y., Kim, J.-H., and Yoo, D.-G., 2013, Scientific results of the Second Gas Hydrate Drilling Expedition in the Ulleung Basin (UBGH2): Marine and Petroleum Geology, v. 47, no. 0, p. 1-20.

Schmuck, E. A., and Paull, C. K., 1993, Evidence for gas accumulation associated with diaprisim and gas hydrates at the head of the Cape Fear Slide: Geo-Marine Letters, v. 13, p. 8.

Schneider, J., 2011, Compression and Permeability Behavior of Natural Mudstones [Doctor of Philosophy Doctor of Philosophy]: The University of Texas, 321 p.

Seol, Y., and Kneafsey, T. J., 2009, X-ray computed-tomography observations of water flow through anisotropic methane hydrate-bearing sand: Journal of Petroleum Science and Engineering, v. 66, no. 3–4, p. 121-132.

-, 2011, Methane hydrate induced permeability modification for multiphase flow in unsaturated porous media: Journal of Geophysical Research: Solid Earth, v. 116, no. B8, p. B08102.

Serra, O., 1984, Fundamentals of Well-log Interpretation: The interpretation of logging data, Elsevier, v. v. 2.

Shipboard Scientific Party, 2003, Site 1249, *in* Trehu, A. M., Bohrmann, G., Rack, F. R., Torres, M. E., and et al., eds., Proceedings of the Ocean Drilling Program, Initial Reports, Volume 204: College Station, Ocean Drilling Program.

Shipley, T. H., Houston, M. H., Buffler, R. T., Shaub, F. J., McMillen, K. J., Ladd, J. W., and Worzel, J. L., 1979, Seismic evidence for widespread possible gas hydrate horizons on continental slopes and rises: AAPG Bulletin, v. 63, no. 12, p. 2204-2213.

Skarke, A., Ruppel, C., Kodis, M., Brothers, D., and Lobecker, E., 2014, Widespread methane leakage from the sea floor on the northern US Atlantic margin: Nature Geosci, v. advance online publication.

Sloan, E. D., 1998, Clathrate Hydrates of Natural Gases, Third Edition, New York, NY, Marcel Dekker.

Sloan, E. D., and Koh, C., 2007, Clathrate Hydrates of Natural Gases, Third Edition, CRC Press.

Smith, A. J., Flemings, P. B., and Fulton, P. M., 2014, Hydrocarbon flux from natural deepwater Gulf of Mexico vents: Earth and Planetary Science Letters, v. 395, no. 0, p. 241-253.

Spangenberg, E., 2001, Modeling of the influence of gas hydrate content on the electrical properties of porous sediments: Journal of Geophysical Research: Solid Earth, v. 106, no. B4, p. 6535-6548.

Spangenberg, E., Kulenkampff, J., Naumann, R., and Erzinger, J., 2005, Pore space hydrate formation in a glass bead sample from methane dissolved in water: Geophysical Research Letters, v. 32, no. 24, p. L24301.

Sun, X., and Mohanty, K. K., 2006, Kinetic simulation of methane hydrate formation and dissociation in porous media: Chemical Engineering Science, v. 61, no. 11, p. 3476-3495.

Takahashi, H., Fercho, E., and Dallimore, S. R., 2005, Drilling and operations overview of the Mallik 2002 Production Research Well Program, *in* Dallimore, S. R., and Collett, T. S., ed., Scientific Results from the Mallik 2002 Gas Hydrate Production Research Well Program, Mackenzie Delta, Northwest Territories, Canada, Volume Bulletin 585, Geological Survey of Canada, p. 14.

Taylor, A. E., Dallimore, S. R., Hyndman, R. D., and Wright, F., 2005, Comparing the sensitivity of permafrost and marine gas hydrate to climate warming, Scientific Results from the Mallik 2002 Gas Hydrate Production Research Well Program, Mackenzie Delta, Northwest Territories, Canada, Geological Survey of Canada, Bulletin no. 585, 2005.

Torres, M. E., Kim, J. H., Choi, J. Y., Ryu, B. J., Bahk, J. J., Riedel, M., Collett, T. S., Hong, W. L., and Kastner, M., Occurrence of high salinity fluids associated with massive near-seafloor gas hydrate deposits, *in* Proceedings 7th International Conference on Gas Hydrates (ICGH 2011), Edinburgh; GB, July 17-21, 2011 2011, p. 1-19.

Torres, M. E., Wallmann, K., Tréhu, A. M., Bohrmann, G., Borowski, W. S., and Tomaru, H., 2004, Gas hydrate growth, methane transport, and chloride enrichment at the southern summit of Hydrate Ridge, Cascadia margin off Oregon: Earth and Planetary Science Letters, v. 226, no. 1–2, p. 225-241.

Tréhu, A. M., Flemings, P. B., Bangs, N. L., Chevallier, J., Gracia, E., Johnson, J. E., Liu, C. S., Liu, X. L., Riedel, M., and Torres, M. E., 2004, Feeding methane vents and gas hydrate deposits at south Hydrate Ridge: Geophysical Research Letters, v. 31, no. 23.

Weinberger, J. L., and Brown, K. M., 2006, Fracture networks and hydrate distribution at Hydrate Ridge, Oregon: Earth and Planetary Science Letters, v. 245, no. 1–2, p. 123-136.

Wright, J. F., Dallimore, S. R., Nixon, F. M., and Duchesne, C., 2005, In situ stability of gas hydrate in reservoir sediments of the JAPEX/JNOC/GSC et al. Mallik 5L-38 gas hydrate production research well: Geological Survey of Canada.

You, K., Kneafsey, T. J., Flemings, P. B., Polito, P., and Bryant, S. L., 2015, Salinity-buffered methane hydrate formation and dissociation in gas-rich systems: Journal of Geophysical Research: Solid Earth, v. 120, no. 2, p. 643-661.

You, Y., Flemings, P., Mohrig, D., and Germaine, J., 2014, How heterogeneity in the shear dilation of a deposit controls the mechanics of breaching slope failure: Journal of Geophysical Research: Earth Surface, p. n/a-n/a.

Yousif, M. H., 1994, The kinetics of hydrate formation, 69th Annual Technical Conference Soc. of Petrol. Eng.: New Orleans, LA.

Zatsepina, O. Y., and Buffett, B. A., 2003, Nucleation of gas hydrate in marine environments: Geophysical Research Letters, v. 30, no. 9, p. 1451.

5. Appendices

Appendix A: Mass Balance Equation Derivation

This derivation makes the following critical assumptions: A) constant brine density, B) gas and hydrate only exist within the MOC-defined hydrate formation zone (HFZ), and C) gas and hydrate phases are homogenously distributed within the HFZ. We begin with the following set of mass balance equations:

$$\Delta W = \Delta M_W^B + \Delta M_W^H = V_{TOT}\phi\rho_W \cdot \Delta S_W + \frac{V_{TOT}\phi\rho_H N M_W}{M_H} \cdot \Delta S_H \quad \text{Eq. 1A}$$

$$\Delta M = M_M^G + M_M^H = V_{TOT}\phi\rho_G \cdot \Delta S_G + \frac{V_{TOT}\phi\rho_H M_G}{M_H} \cdot \Delta S_H \quad \text{Eq. 2A}$$

$$0 = \Delta S_G + \Delta S_H + \Delta S_W \quad \text{Eq. 3A}$$

Where ΔM_W^B, ΔM_W^H, ΔM_M^G, and ΔM_M^H are the mass of water in the brine and hydrate phase and mass of methane in the gas and hydrate phase, respectively. These terms are expanded to show their relation to the phase saturations, such that we can solve for those instead of the masses. For simplicity, we reduce Eq.1A and 2A into Eq. 4A and 5A:

$$\Delta W = A \cdot \Delta S_W + B \cdot \Delta S_H \quad \text{Eq. 4A}$$

$$\Delta M = C \cdot \Delta S_G + D \cdot \Delta S_H \quad \text{Eq. 5A}$$

Where,

$$A = V_{TOT}\phi\rho_w$$

$$B = \frac{V_{TOT}\phi\rho_H N M_W}{M_H}$$

$$C = V_{TOT}\phi\rho_G$$

$$D = \frac{V_{TOT}\phi\rho_H M_G}{M_H}$$

Eliminate ΔS_H from Eq.1A and Eq. 2A by multiplying Eq. 4A by D and Eq.5A by B and then subtracting the two:

$$AD\Delta S_W - BC\Delta S_G = D\Delta W - B\Delta M \quad \text{Eq. 6A}$$

Eliminate ΔS_H from Eq.5A and Eq. 3A by multiplying Eq. 3A by D and then subtracting the two:

$$(C - D)\Delta S_G - D\Delta S_W = \Delta M \quad \text{Eq. 7A}$$

Eliminate ΔS_W from Eq. 6A and Eq. 7A by multiplying Eq. 7A by A and then subtracting the two:

$$[A(C - D) - BC]\Delta S_G = D\Delta W + (A - B)\Delta M \quad \text{Eq. 8A}$$

Solve for ΔS_G:

$$\Delta S_G = \frac{D\Delta W + (A-B)\Delta M}{[A(C-D) - BC]} = E \quad \text{Eq. 9A}$$

Substitute Eq.9A back into Eq. 10A and solve for ΔS_W:

$$\Delta S_W = \frac{(C-D)E + \Delta M}{D} = F \quad \text{Eq. 10A}$$

Substitute Eq. 9A and Eq. 10A back into Eq. 3A and solve for ΔS_H:

$$\Delta S_W = -(E + F) \quad \text{Eq. 11A}$$

Expand Eqs. 9A – 11A by substituting, A – F back into them:

$$\Delta S_G = \frac{\left[\left(\frac{V_{TOT}\phi\rho_H M_G}{M_H}\cdot\Delta W\right)+\left(\left(V_{TOT}\phi\rho_W - \frac{V_{TOT}\phi\rho_H N M_W}{M_H}\right)\cdot\Delta M\right)\right]}{\left[\left(V_{TOT}\phi\rho_W\cdot\left(V_{TOT}\phi\rho_G - \frac{V_{TOT}\phi\rho_H M_G}{M_H}\right)\right)-\left(\frac{V_{TOT}\phi\rho_H N M_W}{M_H}\cdot V_{TOT}\phi\rho_G\right)\right]} \quad \text{Eq. 12A}$$

$$\Delta S_W = \frac{\left[\left(\Delta S_G\cdot\left(V_{TOT}\phi\rho_G - \frac{V_{TOT}\phi\rho_H M_G}{M_H}\right)\right)-\Delta M\right]}{\frac{V_{TOT}\phi\rho_H M_G}{M_H}} \quad \text{Eq. 13A}$$

$$\Delta S_H = -(\Delta S_G + \Delta S_W) \quad \text{Eq. 14A}$$

Appendix B: Single Energy CT Saturation Equation Derivation

This derivation makes the following critical assumptions: A) the brine density does not change, B) gas density is negligible, C) the solid grains in the sample do not move, and D) hydrate only forms within the hydrate formation zone (HFZ) determined from the CT scan images. With these assumptions we begin with the following set of equations:

$$\rho_b^{dry} = \left((1-\phi)\cdot\rho_s\right)+\left(\phi\cdot\rho_G\right) \quad \text{Eq. 1B}$$

$$\rho_b^{wet} = \left((1-\phi)\cdot\rho_s\right)+\left(\phi\cdot\rho_W\right) \quad \text{Eq. 2B}$$

$$\rho_b^{exp} = \left((1-\phi)\cdot\rho_s\right)+\left(S_W\cdot\phi\cdot\rho_W\right)+\left(S_G\cdot\phi\cdot\rho_G\right)+\left(S_H\cdot\phi\cdot\rho_H\right) \quad \text{Eq. 3B}$$

$$S_W + S_H + S_G = 1 \quad \text{Eq. 4B}$$

Equations 1B – 3B define the bulk densities of the dry and saturated samples and during the experiment as a function of the saturations and densities of each individual phase present and the sample porosity. Where ρ_b^{dry}, ρ_b^{wet}, and ρ_b^{exp} are the dry, wet, and experimental bulk densities, respectively, ϕ is the porosity, S_W, S_G, and S_H and ρ_W, ρ_G, and ρ_H are the saturations and densities of water, gas, and hydrate, respectively. Equation 4B defines the fractional saturation of each phase in the sample.

Since the dry and saturated bulk density are considered the density endpoints of the system, the total saturation can be defined as the fractional change of the density between the endpoints (Eq. 5B):

$$S_T = \left(\frac{\rho_b^{exp} - \rho_b^{dry}}{\rho_b^{wet} - \rho_b^{dry}}\right) \quad \text{Eq. 5B}$$

This total saturation is equivalent to the water saturation if the system consisted of only two phases, gas and water. We incorporate the effect of hydrate as a third phase on the density and total saturation by substituting equations 1B – 3B into Equation 5B:

$$S_T = \left(\frac{\left((1-\phi)\cdot\rho_s\right)+\left(S_W\cdot\phi\cdot\rho_W\right)+\left(S_G\cdot\phi\cdot\rho_G\right)+\left(S_H\cdot\phi\cdot\rho_H\right)-\left((1-\phi)\cdot\rho_s\right)-\left(\phi\cdot\rho_G\right)}{\left((1-\phi)\cdot\rho_s\right)+\left(\phi\cdot\rho_W\right)-\left((1-\phi)\cdot\rho_s\right)-\left(\phi\cdot\rho_G\right)}\right) \quad \text{Eq. 6B}$$

As a result of the critical assumptions listed above, Equation 6B is further simplified (Eq. 7B):

$$S_T = \left(\frac{(S_W \cdot \phi \cdot \rho_W) + (S_H \cdot \phi \cdot \rho_H)}{(\phi \cdot \rho_W)}\right) = \frac{M_W + M_H}{M_{Wi}} \quad \text{Eq. 7B}$$

Where M_W, M_H, and M_{Wi} are the masses of water, hydrate, and initial water, respectively. Eq.7B can be rearranged in the following ways (Eqs. 8B and 9B):

$$S_T = \frac{M_W}{M_{Wi}} \cdot \left(1 + \frac{M_H}{M_W}\right) \quad \text{Eq. 8B}$$

$$S_T = \frac{M_H}{M_{Wi}} \cdot \left(1 + \frac{M_W}{M_H}\right) \quad \text{Eq. 9B}$$

From here, we need to determine the mass of water and hydrate in the system at any particular time. To do this we look to the following mass balance of water and hydrate in the sample:

$$M_W = M_{Wi} - XM_{Wi} - YM_{Wi} = (1 - X - Y)M_{Wi} \quad \text{Eq. 10B}$$

$$M_H = XfM_{Wi} \quad \text{Eq. 11B}$$

Equation 10B defines the mass of water remaining in the sample as a function of the initial water mass minus the fraction of initial water converted to hydrate (*X*) and the fraction of water removed from the sample (*Y*). Equation 11B defines the mass of hydrate in the sample as a function of initial water in the sample, the fraction of water converted into hydrate, and the mass ratio of hydrate to water in hydrate (*f*), equal to 1.15. Where *X* and *Y* are calculated with equations 12B and 13B:

$$X = (\Delta V_m - \Delta V_w) \cdot \frac{M_w \cdot N \cdot \rho_H}{V_{pore} \cdot \rho_w \cdot (1-C) \cdot M_H} \cdot \frac{L_{HFZ}}{L} \quad \text{Eq. 12B}$$

$$Y = \frac{\Delta V_w \cdot \rho_w}{V_{pore} \cdot \rho_w} \cdot \frac{L_{HFZ}}{L} \quad \text{Eq. 13B}$$

Where ΔV_m and ΔV_w are the changes in volume in the methane and brine pumps, respectively, V_{pore} is the pore volume ($V_{pore} = V_{TOT} \cdot \phi$), *C* is the initial salinity in weight percent, *L* is the total sample length, and L_{HFZ} is the length of the HFZ. *X* and *Y* are corrected for the location of the hydrate formation front using the ratio between *L* and L_{HFZ}. When processing CT slices beyond the HFZ, *X* and *Y* are both set equal to zero. Dividing Equation 10B by Equation 11B and Equation 11B by Equation 10B yields:

$$\frac{M_W}{M_H} = \frac{(1-X-Y)}{Xf} \quad \text{Eq. 14B}$$

$$\frac{M_H}{M_W} = \frac{Xf}{(1-X-Y)} \quad \text{Eq. 15B}$$

We define the saturations of water and hydrate as function of the volume of water and hydrate divided by the total volume, respectively:

$$S_W = \frac{V_W}{V_{TOT}} = \frac{M_W/\rho_W}{M_{Wi}/\rho_W} = \frac{M_W}{M_{Wi}} \cdot \frac{\rho_W}{\rho_W} \quad \text{Eq. 16B}$$

$$S_H = \frac{V_H}{V_{TOT}} = \frac{M_H/\rho_H}{M_{Wi}/\rho_W} = \frac{M_H}{M_{Wi}} \cdot \frac{\rho_W}{\rho_H} \quad \text{Eq. 17B}$$

Equations 16B and 17B can be simplified and rearranged into equations 18B and 19B:

$$\frac{M_W}{M_{Wi}} \cdot \frac{\rho_W}{\rho_W} = S_W \quad \text{Eq. 18B}$$

$$\frac{M_H}{M_{Wi}} = S_H \cdot \frac{\rho_H}{\rho_W} \quad \text{Eq. 19B}$$

Substituting equations 14B and 18B in Equation 8B and equations 16B and 19B into Equation 9B yields equations 20B and 21B:

$$S_T = S_W \cdot \left(1 + \frac{Xf}{(1-X-Y)}\right) \quad \text{Eq. 20B}$$

$$S_T = S_H \cdot \left(1 + \frac{(1-X-Y)}{Xf}\right) \cdot \frac{\rho_W}{\rho_H} \quad \text{Eq. 21B}$$

From here, we solve equations 17B, 20B and 21B for the gas, water, and hydrate saturations, respectively, to produce equations 22B – 24B:

$$S_w = \frac{S_T}{\left(1 + \frac{Xf}{(1-X-Y)}\right)} \quad \text{Eq. 22B}$$

$$S_H = \left[\frac{S_T}{\left(1 + \frac{(1-X-Y)}{Xf}\right)}\right] \cdot \left[\frac{\rho_w}{\rho_h}\right] \quad \text{Eq. 23B}$$

$$S_G = 1 - S_w - S_H \quad \text{Eq. 24B}$$

National Energy Technology Laboratory

626 Cochrans Mill Road
P.O. Box 10940
Pittsburgh, PA 15236-0940

3610 Collins Ferry Road
P.O. Box 880
Morgantown, WV 26507-0880

13131 Dairy Ashford Road, Suite 225
Sugar Land, TX 77478

1450 Queen Avenue SW
Albany, OR 97321-2198

Arctic Energy Office
420 L Street, Suite 305
Anchorage, AK 99501

Visit the NETL website at:
www.netl.doe.gov

Customer Service Line:
1-800-553-7681